Ultrafast Optical Control of Order Parameters in Quantum Materials

Thesis by
Honglie Ning

In Partial Fulfillment of the Requirements for the
Degree of
Doctor of Philosophy

CALIFORNIA INSTITUTE OF TECHNOLOGY
Pasadena, California

2023
Defended August 3rd 2022

Honglie Ning
ORCID: 0000-0003-4867-0751

ACKNOWLEDGEMENTS

First and foremost, the deepest gratitude goes to my PhD advisor David Hsieh. Dave has nurtured my attitude towards scientific challenges and has shaped my research tastes and perspectives. His vigor for innovations in experimental techniques and his insistence in solving important but not simple scientific questions are extremely inspiring and motivating. Dave endeavors to study the physics out of interest instead of popularity and always initiates a project with relatively clear purposes. Dave is also a really deep thinker. His sharp questions and honest critiques always push me to scrutinize and analyze my data and theories in a even deeper level and drive me to reexamine my prior knowledge which often gives rise to new insights. Despite his busy schedule, he is always available to meet and discuss and has been a constant source of encouragement. I still remember the numerous emails he sent in the early morning and the zoom meetings on late Saturday nights with him. My understanding about the underlying physics of strongly correlated materials and ultrafast physics would not reach today's level without his guidance and instructions. Furthermore, Dave masters the magic of presenting elusive physical concepts in a simple but rigorous way. My writing and presentation skills, although still far from outstanding, could not even have reached today's level without his patient instructions and insightful suggestions. The "v10" suffix of almost all my manuscripts not only reveals the number of versions that I have edited before submission but also reflects his tremendous selfless devotion of time and energy to improving the quality of my works.

My research experience in Hsieh lab has been very enjoyable because of my gifted colleagues. I owe my optical skills to Alberto de la Torre and Nicholas Laurita, who taught me "Optics Lab 101". I am indebted to Tejas Deshpande, John Harter, and Ryo Noguchi, who taught me every detail about angle-resolved photoemission spectroscopy, ultrahigh vacuum technology, cryogenic knowledges, and CAD modelling. I am thankful to Junyi Shan and Kyle Seyler, who have maintained the unimaginably productive second harmonic generation setups and taught me so much about analysis of nonlinear optics data. I want to thank my junior colleagues Chen Li, Yuchen Han, Daniel Van Beveren, and Mingyao Guo for providing technical support and enduring my endless talks at lab. I also enjoyed the discussions with the former group members Hao Chu, Liuyan Zhao, and Alon Ron. I am especially grateful to Xinwei Li, who worked with me on more than half of the projects included in this thesis.

He introduced me into the world of Keldysh tuning, excitonics, and optical study in semiconductors. His diligence and knowledgeability are mindblowing, making him a true role model. Last but not least, I am indebted to my close buddy Omar Mehio, who has worked with me on every single project during my PhD. Omar is not a just colleague but a true comrade and genuine friend for me. I remembered the countless days and nights during my whole PhD we spent struggling in the lab, debating about physics, discussing review comments, and chatting about random stuff beyond science like NBA and politics.

A diverse group of outstanding researchers both on and off campus also provide much-needed insights into surprising findings. I would like to first thank all my thesis committee members including Gil Refael, Marco Bernardi, Oskar Painter, and Scott Cushing. Their sharp questions during my oral candidacy exam and genuine suggestions afterwards helped me make correct choices on the next steps. As an experimentalist, theory supports are always highly desired. I am indebted to Michael Buchhold from University of Cologne, who magically constructed the exact microscopic model I need for almost all my projects from nowhere. The most astonishing part is that he can always explain the seemingly incomprehensible theories crystal-clearly. I am privileged to work with Chao Lian at University of Texas, Austin, who spearheads the TDDFT simulation which significantly enlightens my elemental tellurium project. I also appreciate the opportunity to collaborate with Zala Lenarčič at Jozef Stefan Institute, who pioneers the understanding of Hubbard excitons. High-quality samples are another prerequisite for successful experiments. In this regard, I am grateful to Eli Zoghlin, Zach Porter, and Stephen Wilson at Univeristy of California, Santa Barbara, Hendi Zhao and Gang Cao from Univeristy of Colorado Boulder, and Takashi Kurumaji and Joseph Checkelsky from Massachusetts Institute of Technology for the various samples. I appreciate the high-quality optical conductivity data from Min-Choel Lee and Kyungwan Kim from Korea and Fumihiko Nakamura and Yoshiteru Maeno from Japan. I am also constantly inspired by the helpful discussions about specific ultrafast topics with Gil Refael at Caltech, Richard Averitt at Univeristy of California San Diego, Eugene Demler at Harvard University, Martin Eckstein at University of Erlangen Nuremberg, Zhiyuan Sun at Harvard University, Daniel Podolsky at Technion, and Swati Chaudhary at The University of Texas at Austin. I am thankful to Sean Kung and Andrea Damascelli at The University of British Columbia, Guoqing Chang at Nanyang Technological University, Johnpierre Paglione at University of Maryland, and Halyna Hodovanets at Missouri University of Science and Technology for their

education on topological materials. The collaboration with so many top-notch groups has broadened my scientific horizon and forged long-lasting friendship that will be beneficial to the rest of my career.

Throughout the years as a graduate student, there were also other researchers that I often talked with or encountered at conferences: Matteo Mitrano, Fahad Mahmood, Shuolong Yang, Dao Xiang, Alfred Zong, Anita Verma, Yifan Su, Xuxin Huang, Ben Xu, Shaoxin Wang, Xirui Wang, Yingchao Zhang, and so on. I am very lucky to know these talented junior condensed matter physicists and look forward to meeting them again in the near future. I also enjoy the time with my friends, including Wenlong Ma, Fangzhou Xiao, Song Qi, Xichen Shi, Jiaqing Wang, Jin Sima, Hao Zhou, Weilai Yu, Ruru Zhang, Shixun Chen, Yue Ren, Siyi Wu, and Ye Qiu, who shared the countless Chinese delicacies with me in Los Angeles. A special note goes to Minglu Zhong, as her company and support in everyday life walked me through the unprecedented pandemic.

At last, my deepest gratitude goes to my parents Jundong Ning and Ruiqing Shi for their unconditional and unwavering patience, love, support, and wisdom, despite the 7500-mile distance. In the past 6 years, they have witnessed my every single struggle and achievement in research during our weekly meeting, which remained unnecessarily scientific and technical because of me. They shared every piece of my pain and joy with me. Hopefully their comprehension about condensed matter physics has also improved as mine has.

ABSTRACT

Developing protocols to realize quantum phases that are not accessible thermally and to manipulate material properties on demand is one of the central problems of modern condensed matter physics. Impulsive electromagnetic stimulus provides an extensive playground not only to exert desired control over the material macroscopic properties but also to optically detect the underlying microscopic mechanisms. Two indispensable components form the cornerstone to realize these goals: a meticulous comprehension of light-induced phenomena and a suitable and versatile platform.

Abundant photoinduced phenomena emerge upon light irradiation. A collective oscillation of order parameter can be launched and probed in the weak perturbation regime; further increasing light intensity can transiently modulate the free-energy landscape, inducing a suppression, enhancement, reversal, and switch of order parameters; in the strong non-perturbative excitation regime, the system can be driven nonlinearly with microscopic coupling parameters modified. Understanding these light driven emergent phenomena lays the foundation of optical control and novel functionalities.

Quantum materials, embodying a large portfolio of topological and strongly correlated compounds, afford an exceptional venue to realize optical control. Owing to the complex interplay between the charge, spin, orbital, and lattice degrees of freedom, a rich phase diagram can be generated with various phases that are selectively and independently accessible via optical perturbations. They hence offer a wealth of opportunities to not only improve our comprehension of the underlying physics but also develop the next generation of ultrafast technologies.

In Chapter I of this thesis, I will first cover a multitude of light-induced emergent phenomena in quantum materials under the framework of time-dependent Landau theory, Keldysh theory, and Floquet theory, and then introduce several canonical microscopic models to quantitatively rationalize the intra- and interactions between different degrees of freedom in quantum materials. As the necessary theoretical background is established, three main experimental techniques that have been extensively utilized in my research: time-resolved reflectivity and Kerr effect, time-resolved second harmonic generation rotational anisotropy, and coherent phonon spectroscopy will be introduced in Chapter II. In Chapter III, I will demonstrate that a light-induced topological phase transition can be engendered concomitant

with an inverse-Peierls structural phase transition in elemental Te. In Chapter IV, I will describe signatures of ultrafast reversal of excitonic order in excitonic insulator candidate Ta_2NiSe_5 and substantiate a manipulation of the reversal as well as the Higgs mode with tailored light pulses. In Chapter V, a light-induced switch of spin-orbit-coupled quadrupolar order in multiband Mott insulator Ca_2RuO_4 will be introduced. In Chapter VI, a Keldysh tuning of nonlinear carrier excitation and Floquet bandwidth renormalization in strongly driven Ca_2RuO_4 will be covered.

PUBLISHED CONTENT AND CONTRIBUTIONS

Li, Xinwei et al. (2022). "Keldysh Space Control of Charge Dynamics in a Strongly Driven Mott Insulator". In: *Phys. Rev. Lett.* 128 (18), p. 187402. DOI: 10.1103/PhysRevLett.128.187402.
H.N. performed the experiment, performed the simulation, and analyzed the data.

Ning, H. et al. (2020). "Signatures of Ultrafast Reversal of Excitonic Order in Ta_2NiSe_5". In: *Phys. Rev. Lett.* 125 (26), p. 267602. DOI: 10.1103/PhysRevLett.125.267602.
H.N. performed the experiment, performed the simulation, analyzed the data, and wrote the paper.

Ron, A. et al. (2020). "Ultrafast Enhancement of Ferromagnetic Spin Exchange Induced by Ligand-to-Metal Charge Transfer". In: *Phys. Rev. Lett.* 125 (19), p. 197203. DOI: 10.1103/PhysRevLett.125.197203.
H.N. performed the experiment and analyzed the data.

TABLE OF CONTENTS

LIST OF ILLUSTRATIONS

LIST OF TABLES

Chapter 1

Introduction

1.1 Light-Induced Emergent Phenomena

Discovering pathways to exert control over the microscopic phase of matter is a central goal of condensed matter physics, as it not only sheds light on steering the material properties on demand, but also holds promise for the next generation of electronic devices with currently inaccessible functionalities. Materials with multiple coexisting and competing phases are highly susceptible to external perturbations, providing an exceptional platform to explore the interplay of symmetry, topology, and strong correlations. Quantum materials represent a vast portfolio of strongly correlated and topological systems whose essential properties cannot be described by semi-classical or low-level quantum mechanics (Keimer and J. E. Moore, 2017). Arising from the complex interaction between the charge, orbital, spin, and lattice degrees of freedom (DoF), multiple phases and orders which exhibit remarkably different electrical, magnetic, and optical properties emerge in quantum materials and thus render quantum materials extremely sensitive to external stimuli. A wide range of tuning knobs are applied to engineer the material properties facilitated by both a deeper theoretical understanding of the underlying physics and rapid technological developments in lasers, precision control, and microscopy capacities. The multiple phases hosted by quantum materials can be independently accessed by applying external perturbations such as high magnetic fields, hydrostatic high pressure, uni- or bi-axial strain, chemical doping, electrostatic gating, heterostructuring, and, last but not least, impulsive electromagnetic field (Basov, Averitt, and D. Hsieh, 2017).

Remarkable progress in controlling the material properties has been made at the interface between traditionally separate fields: quantum materials, quantum optics, and laser physics. The strategy is based on the strong coupling between a quantum material and an ultrafast laser pulse whose frequency is resonant with the energy of a specific electronic or structural excitation or whose pulse duration is comparable to the timescale of particular microscopic dynamical process. A weak laser pulse with energy resonant with electronic transition can generate a nonequilibrium electronic redistribution within tens of femtoseconds (fs). The excess of kinetic energy will be imparted to the other DoF such as spins and lattice, and the different subsys-

tems will relax back to its original ground state on the timescale of picoseconds (ps), nanoseconds (ns), or even longer. By exciting the quantum materials with high-intensity laser pulses, on the other hand, we can exploit the competition and coexistence of multiple phases and steer the order from one to another that may not even exist in equilibrium (Orenstein, 2012). The new phase may be metastable until all DoF recover back to their ground states, or even stable and long-lived with distinct properties. More intriguingly, we gain a good opportunity to investigate the states that are inaccessible in equilibrium or that occur only during the duration of the light pulse.

The convergence of quantum materials and the cutting-edge laser technology not only enables us to change and manipulate the quantum material properties on demand but also equips us with novel probes with unprecedented time resolution as fast as attoseconds (as) to record the dynamical process upon light impingement. Employing a suite of ultrafast probes, we simultaneously obtain the spectroscopic and temporal information about the nonequilibrium states triggered by the optical excitation and the ground state the system relaxes back to. By further sweeping the probe energy ranging from less than a milli-electronvolt (meV) to hard X-ray (>1000 eV), we can selectively couple to different DoF and disentangle their complex collective dynamics (A. d. l. Torre, Dante M. Kennes, et al., 2021). A more comprehensive discussion about time-resolved techniques will be given in Chapter II.

A plethora of emergent phenomena including phase suppression, phase enhancement, and phase switching can be induced by the light pulse. A meticulous comprehension of phase transition is required to understand the light-induced emergent phenomena. The backbone of most non-topological phase transitions is the concept of spontaneous symmetry breaking. The symmetry breaking is parametrized by an order parameter (OP), a measure of orders across the phase transition boundary. In equilibrium, the most conventional pathway to induce a phase transition is through changing temperatures: the value of OP is zero in the high-temperature high-symmetry phase and onsets below a critical temperature T_c, where the low-temperature low-symmetry phase is realized. For instance, magnetization M can be used as the OP across the paramagnetic-to-ferromagnetic transition, which continuously decreases to zero as Curie temperature T_c is approached from below.

Over 80 years ago, Lev Landau formulated the celebrated Landau theory, a phenomenological and generalized mean-field theory, to describe the continuous (second-

order) phase transitions. This theory was later demonstrably adapted to systems under external stimuli or hosting discontinuous (first-order) transitions. Based on the symmetry of the system, an analytical expression for the free energy functional E can be written out as a Taylor expansion in the OP Φ. In most cases E is a function of even powers of Φ and can be expressed as:

$$E(\Phi, T) = E_0 + a(T)\Phi^2 + \frac{b(T)}{2}\Phi^4 + ... \tag{1.1}$$

Higher order terms are neglected for simplicity. For the system to be thermodynamically stable, the coefficient of the highest even power $b(T) > 0$. For simplicity, one can assume $b(T) = b_0 > 0$. Furthermore, $a(T)$ is required to change sign across T_c, and thus one can assume $a(T) = a_0(T - T_c), a_0 > 0$. With these assumptions, we can minimize the energy functional with respect to Φ and we have:

$$\Phi(T) = \begin{cases} 0, & T > T_c \\ \pm\sqrt{-\frac{a_0}{b_0}(T - T_c)}, & T < T_c \end{cases} \tag{1.2}$$

Therefore, the OP has a critical exponent $\beta = 1/2$ close to the critical temperature. The potential energy surface (PES) can be pictorially illustrated as function of OP and the system will stay in either of the global minima in equilibrium when $T < T_c$ and at zero when $T > T_c$. By further adding terms of odd powers such as $c(T)\Phi$, the PES will be tilted and a unique ground state will be reached below T_c (Figure 1.1).

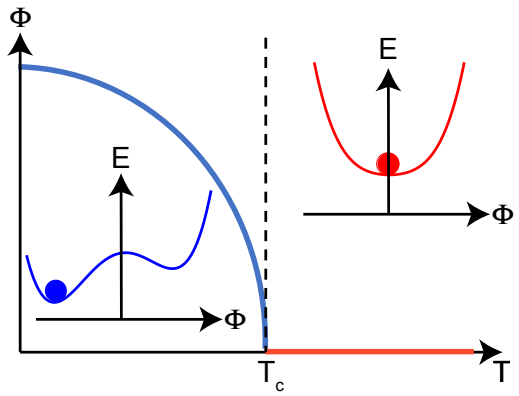

Figure 1.1: Schematic of the change of order parameter and potential energy surface around the phase transition.

The OP associated with the PES will be transiently modulated by the laser pulse in both thermal and nonthermal pathways. Depending on the strength of the impulsive light field, various emergent phenomena can be generated. In the weak

excitation regime, the PES will only be slightly perturbed and coherent oscillations of OP will be launched; further increasing the incident light intensity, which can be parametrized by the light fluence F, the PES can be drastically modified and the OP can transiently reach the region that are inaccessible in equilibrium. A restoration of higher symmetry, a reversal of order parameter, and a switch to a hidden state can be realized; finally an intense non-perturbative optical excitation can drive the system into nonlinear regimes and dynamically renormalize the microscopic couplings which govern the properties of the quantum material.

Coherent Mode Excitation Regime

The light can couple to different systems and launch the coherent motion of OP in multiple ways [Figure 1.2(a)]. If the photon energy of the pump pulse matches an infrared (IR)-active phonon mode, a direct resonant enhancement of such mode can be initiated (Först et al., 2011). Furthermore, the light pulse can effectively transfer sufficient kinetic energy to the lattice and impulsively launch Raman-active phonons (Dhar, Rogers, and Nelson, 1994) or exert a torque to each spin which generates a coherent spin precession, also known as magnon or spin wave (Kirilyuk, Alexey V. Kimel, and Rasing, 2010). Most commonly, the light irradiation can instantaneously quench the PES of the system while the OP still remains at its equilibrium position, so that a subsequent OP movement toward the new global minimum of PES can be generated (Zeiger et al., 1992). For instance, in systems with a spatial periodic charge distribution dubbed charge density wave (CDW), a CDW amplitude mode can be launched by light irradiation (Schmitt et al., 2008; R. V. Yusupov et al., 2008). Note that the coherent mode excitation regime typically but not necessarily indicates the cases where the system is weakly driven by the light pulse and the perturbation remains in a linear regime.

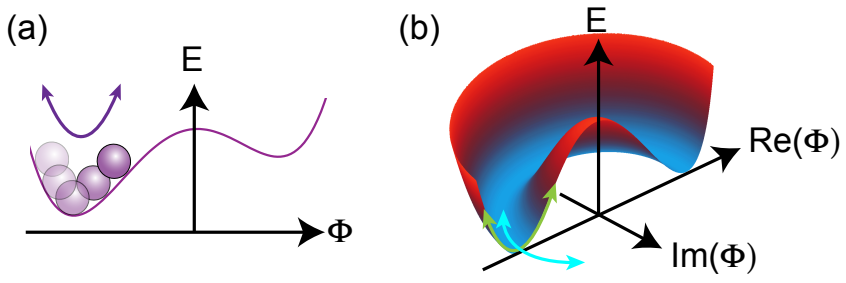

Figure 1.2: Schematic of (a) coherent mode excitation of a real order parameter and (b) Higgs (green) and Goldstone (cyan) mode excitations of a complex order parameter.

More intriguingly, in various systems with U(1) symmetry breaking such as superconductors, a complex OP is used to characterize both the strength and the coherence of the coupling and the PES resembles a "Mexican hat" [Figure 1.2(b)]. The system can undergo two orthogonal collective eigenmodes: one is the massive Higgs mode, which arises from amplitude fluctuations at constant phase and exhibits a finite energy even at $k = 0$ due to the radial curvature of the PES, and the other is the Goldstone mode, which arises from phase fluctuations at constant amplitude and hosts vanishing excitation energy at $k = 0$ due to the constant energy along the trough at the bottom of PES. The former has been coherently launched and detected by intense terahertz (THz) pulses (Matsunaga, Hamada, et al., 2013; Matsunaga, Tsuji, et al., 2014) while the latter has been detected by transient grating (Darius H. Torchinsky, Mahmood, et al., 2013).

Not only the dynamical recovery process but also the equilibrium properties can be inferred by analyzing the amplitude, frequency, lifetime, or coupling of these collective modes. For instance, weak pump excitation can reveal details about phase transitions (Harter, D. M. Kennes, et al., 2018), unveil the evolution of microscopic couplings (Ron et al., 2020), disentangle or unify the roles of charge, lattice, spin, or orbital DoF with multi-messenger approaches (Beaud, Caviezel, et al., 2014; Gerber et al., 2017), and uncover the existence of short-range orders (H. Chu et al., 2017). Furthermore, the achievement of enhancement and suppression of coherent excitations via multi-pulse tailoring demonstrates a universal and prototypical ultrafast means to manipulate the otherwise inaccessible collective excitations in diverse electronic and magnetic systems (A. M. Weiner et al., 1990; Kampfrath et al., 2011; M. Hase et al., 1996; Ning et al., 2020).

Order Parameter Manipulation Regime

Further increasing the incident light intensity above a critical value F_c, the quenching of PES can be so intense that a full suppression of OP to 0 accompanied by a transient restoration of higher symmetry can be achieved (Figure 1.3). This is analogous to the thermal case where a phase with higher symmetry is realized when $T > T_c$. Prominent examples include the light-induced complete suppression of charge order (Möhr-Vorobeva et al., 2011; Erasmus et al., 2012; Huber et al., 2014; Zong, Kogar, et al., 2019), excitonic order (Werdehausen, Takayama, Höppner, et al., 2018), ferroelectric (FE) order (Mankowsky, Hoegen, et al., 2017), magnetic order (Kirilyuk, Alexey V. Kimel, and Rasing, 2010; Petersen et al., 2011; Caviglia et al., 2013), orbital order (Beaud, Caviezel, et al., 2014; Tobey et al., 2008; Beaud, Johnson,

et al., 2009), and structural order (Teitelbaum et al., 2018). A more nontrivial case is the high-symmetry phase cannot be reached by simply increasing temperature, in which case a nonthermal phase transition with no equilibrium analogue is expedited by light. For example, in bismuth, a single element compound of $A7$ structure with symmetry lowering due to a Peierls distortion, an intense pulse with $F > 10$ mJ/cm^2 can create sufficiently large lattice displacement before the sample melts and a new high-symmetry phase can be restored (Fritz et al., 2007; Sokolowski-Tinten et al., 2003; Teitelbaum et al., 2018). In Chapter III of this thesis, I will introduce a novel system where an ultrafast restoration of higher crystalline symmetry associated with an electronic band topological transition can be generated.

If two phases coexist and compete with each other, collapse of one order may reinforce the other (Sun and Andrew J. Millis, 2020). The two competing orders can possess similar nature, like long-range CDWs developing along two crystallographic axes in transition metal tritellurides (Kogar, Zong, et al., 2020), or originate from different mechanisms, such as the competing stripe charge/spin order and superconductivity in doped lanthanum cuprates (Fausti et al., 2011). It has been experimentally demonstrated that suppression of the dominant OP can indeed generate an enhancement of the competing one in the aforementioned systems. These developments thus raise the possibility of "steering" the OP into a desired metastable state by dynamically suppressing one or more orders.

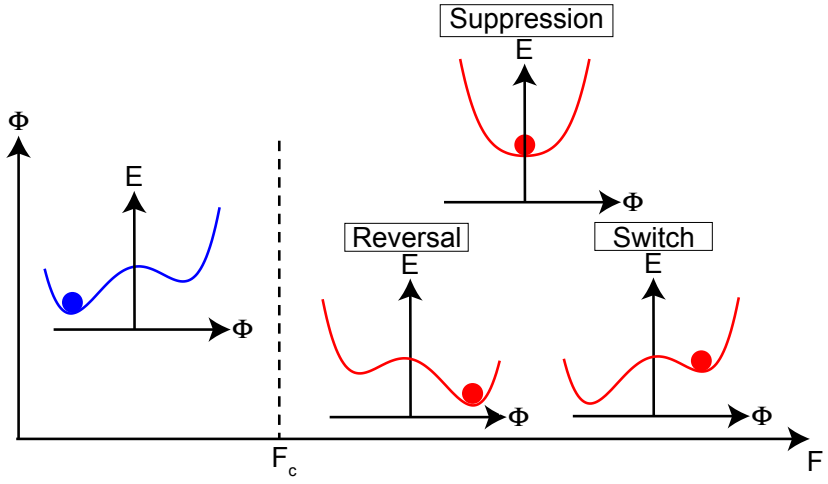

Figure 1.3: Schematic of light-induced suppression, reversal, and switch of order parameter.

Associated with the full suppression of OP, diverse dynamical critical behaviors emerge in diverse observables. At the melting critical fluence, the time needed to

melt the OP diverges (Zong, Dolgirev, Kogar, Erge çen, et al., 2019), the frequency of the coherent mode dramatically softens and may even redshift to zero (Möhr-Vorobeva et al., 2011; Teitelbaum et al., 2018), and the time needed to recover back to the equilibrium value diverges (Caviglia et al., 2013; Zong, Kogar, et al., 2019), owing to the flattening of the PES bottom as the order parameter is just fully suppressed. These phenomena showcase a dynamical critical slowing down akin to the static case in the vicinity of a second-order phase transition. Very recently, however, an ultrafast study reveals signatures of the decoupling between the divergence of the magnetic correlation length and the relaxation time, i.e. the critical fluences for the magnetic OP to be fully quenched and for the recovery time to fully diverge are not equivalent. The violation of conventional thermal critical behaviors stems from the photodoping-induced nonthermal magnon population (A. d. l. Torre, Seyler, et al., 2022). Therefore, out-of-equilibrium OP suppression provides a novel blueprint to understand the critical behavior both within and beyond conventional Landau theory.

In addition to suppression of OP and PES, other nonthermal pathways are available which bring the system to parts of the free-energy landscape that are inaccessible in equilibrium. For the systems with Ising-type OP, which harbor two degenerate ground states characterized by OPs of equal magnitude but opposite phase, like a ferromagnet with all spins pointing up or down, an ultrafast reversal of OP can be achieved when $F > F_c$ (Figure 1.3). Ensuing the transient quenching of PES, the inversion of OP is enabled by overshooting the opposite side of PES across $\Phi = 0$. The out-of-equilibrium protocols to reverse the OP have been realized in a variety of systems such as ferromagnetic (FM) systems with opposite magnetizations (Lambert et al., 2014; Tudosa et al., 2004; Gerrits et al., 2002), ferrimagnets and antiferromagnetic (AFM) systems with opposite staggered magnetizations (Stanciu et al., 2007; Vahaplar et al., 2009; Radu et al., 2011; A. V. Kimel et al., 2009; Manz et al., 2016; Schlauderer et al., 2019), ferroelectrics (FE) with opposite polarizations (Fahy and Merlin, 1994; Qi et al., 2009; Mankowsky, Hoegen, et al., 2017), and CDW with opposite spatial charge modulations (Zong, X. Shen, et al., 2018; Duan et al., 2021). Recently, the excitonic order in the presence of electron-phonon coupling was also found to be a dipolar order and thus a reversal can be achieved (Ning et al., 2020; Sun, Tatsuya Kaneko, et al., 2021). In Chapter IV, I will cover the mechanism underlying the reversal of excitonic order in an excitonic insulator candidate Ta_2NiSe_5 and demonstrate the controllability of the reversal on ultrashort timescales using appropriate laser pulse sequences.

A more general case is the existence of multiple local minima in PES and each state hosts entirely different properties and respects different symmetries. Without lack of generality, we assume the existence of another local minimum in the vicinity of the global equilibrium ground state with a slightly higher energy. An ultrafast laser pulse can steer the OP overcoming the energy barrier partitioning the two states, inducing an optical switch from the ground state to another metastable state that is potentially "hidden" in equilibrium (Figure 1.3). Seminal examples include the transition from insulating CDW into a long-lived metallic state in TaS_2 (Stojchevska et al., 2014), structural phase transition in FE SnSe (Huang et al., 2022), the Mott insulator-to-metal phase transition accompanied by a structural transition in VO_2 and V_2O_3 enabled by light with photon energy both resonant and off-resonant with electronic excitation (Cavalleri et al., 2001; M. Liu et al., 2012; Morrison et al., 2014; M. K. Liu et al., 2011; Singer et al., 2018), the simultaneous topological and structural transitions in type-II Weyl semimetals (W,Mo)Te_2 induced by IR and THz irradiation (Sie, Nyby, et al., 2019; M. Y. Zhang et al., 2019), and the charge-ordered AFM insulating phase to FM metallic phase transition in doped perovskite manganites (Ichikawa et al., 2011; T. Li et al., 2013; J. Zhang et al., 2016). Due to the universal coupling between different DoF in quantum materials and the induced rich phase diagrams, a light-induced switch between diverse states can be realized possibly without equilibrium analogue. In Chapter V, I will introduce a thermally inaccessible switch of exotic spin-orbit-coupled quadrupolar order, a field that remains largely underexplored, in multiband Mott insulator Ca_2RuO_4.

Nonlinear Excitation and Floquet Engineering Regime

Further increasing the light intensity, the nonlinear regime will be reached. In this non-perturbative regime, several different classes of nonlinear phenomena emerge including 1) nonlinear lattice driving, where phonon-phonon interactions arising from the anharmonicity of the PES kicks in, 2) nonlinear carrier generation with subgap light excitation, and 3) coherent modulation of microscopic couplings and effective interactions captured by Floquet engineering. To avoid the impulsive or static heating induced by intense light irradiation, pulse with photon energy off-resonant with electronic absorption peaks is preferred. Thanks to the rapid development of ultrafast laser technology, intense sub-bandgap pump with centered photon energies ranging from THz to mid-IR regime opens new opportunities to scrutinize the strong non-perturbative regime.

In lieu of depositing energy to electronic systems, the energy of the pump pulse can

be tuned to resonate with IR-active phonons such that a mode-selective enhancement of such phonon Q_{IR} can be realized. Constrained by symmetry, particular Raman active modes Q_R that directly couple to OPs can be launched by the anharmonic coupling ($Q_{IR}^2 Q_R$) to the IR modes [Figure 1.4(a)]. The so-called "nonlinear phononics" (Först et al., 2011) thus provide a unique platform where neither the charge, orbital, nor spin DoF, but the lattice, is primarily disturbed by light. Remarkable progress has been made using nonlinear phononic excitation in the past ten years including lattice-controlled insulator-to-metal transition (IMT) (Rini et al., 2007), light-induced superconductivity (SC) (Fausti et al., 2011; Mankowsky, Subedi, et al., 2014; Mitrano et al., 2016), light-enhanced FE in paraelectric (Nova, A. S. Disa, et al., 2019; Xian Li et al., 2019), polarized piezo-AFM (Ankit S. Disa et al., 2020), modulation of magnetic interaction (Afanasiev et al., 2021), and mapping of interatomic anharmonic PES (Hoegen et al., 2018).

Subgap electromagnetic field does not necessarily decouple to the electron reservoir. Strong AC field induced electron-hole pair production has been widely studied by a suite of nonequilibrium numerical techniques (Murakami and Werner, 2018; Tsuji et al., 2011; Oka, 2012; Imai, Ono, and Ishihara, 2020; Silva et al., 2018; Takahashi, Itoh, and Aihara, 2008; Tancogne-Dejean, Sentef, and Rubio, 2020). Different nonlinear carrier generation mechanisms dominate different regions in the parameter space, which can be characterized by the Keldysh adiabaticity parameter:

$$\gamma_K = \begin{cases} \frac{\hbar\omega}{eE\xi}, & \text{Mott insulator} \\ \frac{\omega\sqrt{m^* E_g}}{eE}, & \text{band insulator} \end{cases} \tag{1.3}$$

where ω is the photon energy, E is the electric field strength, ξ is the pair correlation length, m^* is the effective mass, Δ_{Mott} is the Mott gap, and E_g is the bandgap. Three regions can be classified depending on the value of γ_K: the adiabatic tunnelling region $\gamma_K \ll 1$, the multiphoton region $\gamma_K \gg 1$, and the Keldysh crossover region $\gamma_K \sim 1$. In the adiabatic tunneling regime, the carriers follow the slow change of the external field and "penetrate" potential barrier "horizontally", while in the multiphoton regime transitions occur "vertically" by absorbing multiple photons [Figure 1.4(b)]. These two limits smoothly crossover in the intermediate regime where diabatic tunneling occurs (Kruchinin, Krausz, and Yakovlev, 2018). The transition probability of the two limits for Mott insulator has unequivocally different mathematical forms:

$$P \propto \begin{cases} \exp\left(-\frac{\pi\Delta_{Mott}}{2E\xi}\right), & \gamma_K \ll 1 \\ \left(\frac{E\xi}{\hbar\omega}\right)^{\frac{2\Delta_{Mott}}{\omega}}, & \gamma_K \gg 1 \end{cases} \tag{1.4}$$

where a clear threshold behavior in the adiabatic tunneling regime evolves into a power law behavior in the multiphoton regime. Note that a large group of out-of-equilibrium nonlinear phenomena can be realized in the highly non-perturbative regimes of the Keldysh space, such as Wannier-Stark localization (Murakami and Werner, 2018), non-perturbative high-harmonic generation (Imai, Ono, and Ishihara, 2020; Silva et al., 2018; Murakami, Martin Eckstein, and Werner, 2018), dielectric breakdown (Martin Eckstein, Oka, and Werner, 2010; Giorgianni, J. Sakai, and Lupi, 2019; Mayer et al., 2015; Yamakawa et al., 2017), and dynamical Franz-Keldysh effect (Lucchini et al., 2016; Tancogne-Dejean, Sentef, and Rubio, 2020; Srivastava et al., 2004). In Chapter VI, I will show a Keldysh multiphoton-to-tunneling crossover is realized in Mott insulator Ca_2RuO_4.

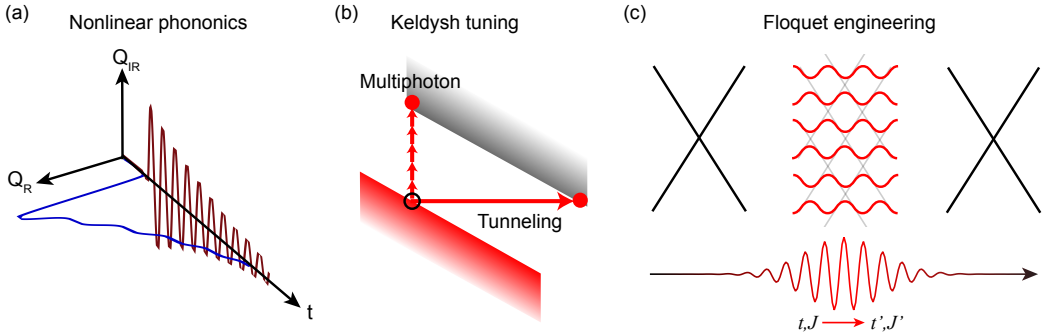

Figure 1.4: Schematic of (a) nonlinear phononics, (b) nonlinear carrier excitation Keldysh crossover, and (c) Floquet engineering.

Even without generating any real carrier or lattice excitation, the intense electromagnetic field of light pulse can still coherently modulate the spectrum of quantum materials. The Floquet formalism describes how a periodic-in-time optical field renormalizes the energy dispersion of the system and modulates its microscopic interaction parameters. Akin to the Bloch theorem which states that a spatially periodic crystal structure creates replicas of energy-momentum dispersion along the momentum axis, a temporally periodic light field creates replicas of the spectrum along the energy axis [Figure 1.4(c)]. Instead of solving the time-dependent Schrödinger equation, one can instead solve a time-independent Floquet Hamiltonian with each element simply a Fourier transform of the original Hamiltonian (or plus/minus an integer multiple of the photon energy) (Eckardt and Anisimovas, 2015; Rudner and Lindner, 2020b). The Floquet theory has been demonstrated to be correct in topological insulators by the pioneering photoemission experiments (Y. H. Wang et al., 2013; Mahmood et al., 2016).

Not only will the band structure be transiently dressed, but microscopic interactions and band topological properties will be coherently modulated by the temporally periodic optical field. Prominent examples include bandgap and exciton engineering (Shan et al., 2021; Sie, James W. McIver, et al., 2015; Sie, Lui, et al., 2017), magnetic exchange interaction modulation (Mentink, Balzer, and M. Eckstein, 2015; Hejazi, J. Liu, and Balents, 2019; Mikhaylovskiy et al., 2015; Batignani et al., 2015; Claassen et al., 2017), ultrafast topological Hall effect (J. W. McIver et al., 2020), and many body localization (Rudner and Lindner, 2020a).

Despite the spectacular theoretical progress, experimental achievements of Floquet engineering are much fewer. The main reason is Floquet engineering-induced effect is pronounced only when the Floquet parameter $\mathcal{E} = \frac{eEa}{\hbar\omega}$ (a is the lattice constant) is larger than unity. The major challenge experimentalists are faced with is that extremely intense light pulse ($\sim 10^9$ V/m) at THz or mid-IR frequencies is required to achieve reasonable microscopic coupling modulation by Floquet engineering. Therefore, a central question is how to choose ideal materials and develop proper driving protocols to minimize thermal heating such that the out-of-equilibrium state proximate enough to the ground state of an effective Floquet Hamiltonian can be experimentally realized (Oka and Kitamura, 2019). In terms of materials, compounds with large and clean bandgap are preferred due to less absorption; on the other hand, tailored drive pulses can be chosen to suppress heating at short times and reach a potentially long-lived "prethermalized" state (A. d. l. Torre, Dante M. Kennes, et al., 2021). A recently emerging field exploiting cavity quantum electrodynamics and integrating the target material with a vacuum cavity to enhance the light-matter interaction such that a less strong field is needed stands out as an alternative promising direction (Bloch et al., 2022).

1.2 Time Dependent Landau Theory

In the previous section where we show the three different cases of transient light-induced modulation of PES, we have implicitly extended the Landau theory to a time-dependent version. Time-dependent Landau theory (TDLT) has been widely used in various ultrafast studies and systems (Sun and Andrew J. Millis, 2020). In this prevailing mean-field description, the system is coarsely grained and simplified as an ensemble of time-dependent OP $\Phi(t)$ and PES $E(\Phi)$. It is assumed that light pulse transiently modulates the PES and exerts a force on the OP and the subsequent evolution of OP captures the pivotal dynamics. We now employ TDLT to simulate the dynamics of OP under the three aforementioned cases, i.e. suppression,

reversal, and switch, in three slightly different ways to show the universality of TDLT application.

TDLT Simulation of Order Parameter Suppression

Without loss of generality and simplicity, we consider the case that a single OP and the equilibrium functional form of $E(\Phi)$ is described by Eq1.1: a double-well potential at low temperature. The specific means to include the light excitation depends on the type of systems and orders. We assume that the light excitation will transiently quench the PES in a way similar to increasing temperature by modulating the term quadratic in Φ. Therefore, we have the following functional form for $E(\Phi, t)$:

$$E(\Phi, t) = \frac{1}{2}\omega^2[\eta(t) - 1]\Phi^2 + \frac{1}{4}b\Phi^4, \tag{1.5}$$

where ω is the eigenmode OP oscillation frequency determined by the curvature of the PES minimum, b is a constant of the fourth-order term, and $\eta(t)$ captures the light-induced modulation of the quadratic term. It has been extensively used in many studies that $\eta(t) = \alpha F * \frac{1+\mathrm{erf}\left(\sqrt{\frac{4\ln 2}{\sigma^2}}t\right)}{2} * \exp\left(-\frac{t}{\tau_0}\right)$, where α is a scaling factor, F is the fluence, σ is the full width at half maximum (FWHM) of the pulse duration and the error function represents the non-instantaneous onset of light perturbation due to the finite instrumental time resolution, and τ_0 is the recovery lifetime that PES relaxes back to its equilibrium form and is typically determined by the electronic, magnetic, or structural relaxation time. We also implicitly assume that the quenching is linearly proportional to F. Note that when $\eta(t) > 1$, the double-well PES transforms into a parabola, mimicking the high temperature case and featuring a full suppression of OP.

Considering that the functional derivative of free energy $E(\Phi, t)$ with respect to $\Phi(t)$ is a generalized force, the equation of motion of $\Phi(t)$ can in principle be derived as:

$$\frac{\partial^2\Phi(t)}{\partial t^2} + 2\gamma\frac{\partial\Phi(t)}{\partial t} + \frac{\partial E(\Phi, t)}{\partial\Phi(t)} = 0. \tag{1.6}$$

If we plug Eq1.5 in Eq1.6, we have:

$$\frac{\partial^2\Phi(t)}{\partial t^2} + 2\gamma\frac{\partial\Phi(t)}{\partial t} + \omega^2[\eta(t) - 1]\Phi(t)^2 + b\Phi(t)^4 = 0. \tag{1.7}$$

Note that we also add a damping term with constant γ to account for the dissipation of energy and damping of the coherent OP oscillation. In the overdamped case where γ is on par with or larger than ω, the coherent OP oscillation is suppressed and Φ will adiabatically follow the evolution of E.

For suppression, we define the critical fluence F_c as the fluence where a full melting of order occurs, i.e. $\eta(t) = 1$, and assume $\tau_0 \to \infty$ so that at $F > F_c$ the suppression lasts significantly longer than the time window we are interested in. We assume $\omega = (2\pi\times)3.6$ THz, $\gamma = 1$ THz and show the dynamics of $\Phi(t)$ in Figure 1.5(a). At all fluences an coherent oscillation corresponding to the excitation of the OP amplitude mode can be unambiguously resolved [Figure 1.5(a)]. At $F < F_c$, a gradual displacement of the quasi-equilibrium position from the equilibrium value $\Phi(t < 0)$ to 0 is evident, which arises from the ultrafast quenching of PES. At $F > F_c$, the quasi-equilibrium position saturates at 0, showcasing a complete suppression of OP.

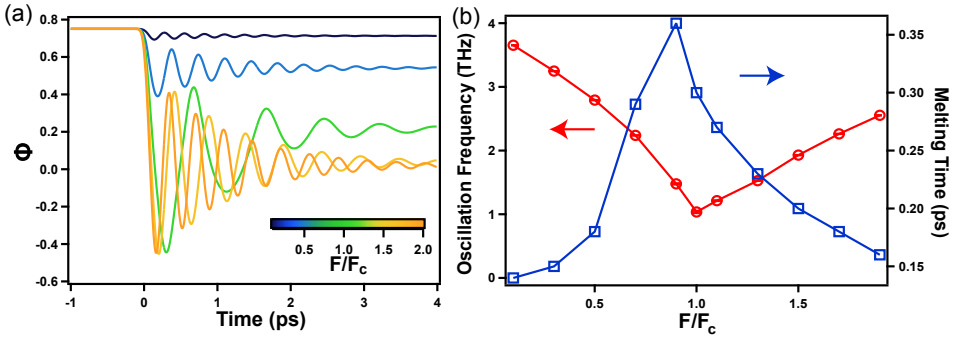

Figure 1.5: TDLT simulation of ultrafast OP suppression and critical behaviors. (a) Time evolution of OP at different fluences normalized by the critical fluence F_c where full melting of OP is just realized. (b) Fluence dependence of OP oscillation frequency and OP melting time.

The critical behaviors can also be elucidated by applying a damped cosine function fitting to the time traces of $\Phi(t)$. The frequency of the OP oscillation exhibits a pronounced softening at $F < F_c$, reaches a minimum at $F \sim F_c$, and blueshifts at $F > F_c$, reminiscent of the flattening of PES bottom at F_c. Simultaneously, an inverse behavior of the melting time can be seen, which shows a diverging behavior at $F \sim F_c$, suggesting the critical slowing down.

TDLT Simulation of Order Parameter Reversal

For reversal, we consider two coupled OPs Φ_1 and Φ_2, while only $E(\Phi_1)$ is directly modulated by light. This assumption can be generally applied to a lot of systems with an electronic OP Φ_1 and a lattice or magnetic OP Φ_2, in which the former is primarily excited by light. We assume (i) a double-well potential of Φ_1, (ii) a parabolic potential of Φ_2, and (iii) a linear coupling with coupling constant g between the two. The potential functional of the coupled system can be expressed

as:

$$E(\Phi,t)=\frac{1}{2}\omega_1^2[\eta(t)-1]\Phi_1^2+\frac{1}{4}b\Phi_1^4+\frac{1}{2}\omega_2^2\Phi_2^2+g\Phi_1\Phi_2. \tag{1.8}$$

We also assume the photo-excitation transiently shrinks the term quadratic in Φ_1 by $\eta(t)$ as defined before with a finite decay time same as electron depopulation time $\tau_0 = 1$ ps. We can then write out the equations of motion of the two OPs:

$$\begin{aligned}&\partial_t{}^2\Phi_1+2\gamma_1\partial_t\Phi_1+\omega_1^2[\eta(t)-1]\Phi_1+b\Phi_1^3+g\Phi_2=0,\\&\partial_t{}^2\Phi_2+2\gamma_2\partial_t\Phi_2+\omega_2^2\Phi_2+g\Phi_1=0,\end{aligned} \tag{1.9}$$

where again we add two different decay terms with different decay rates $\gamma_{1,2}$ to characterize the damping of two OPs.

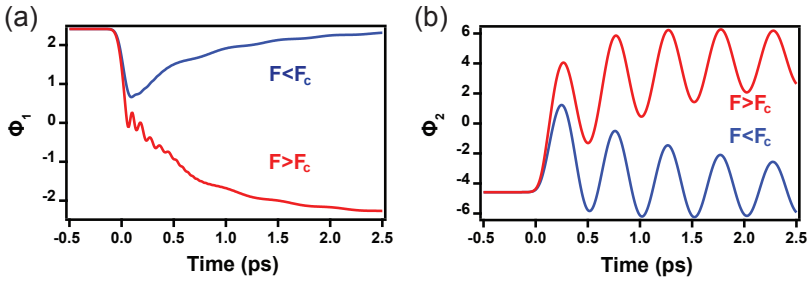

Figure 1.6: TDLT simulation of ultrafast reversal of two linearly coupled OPs.

We assume the OP oscillation of both OPs are underdamped but with generically different frequencies: $\omega_2 = (2\pi\times)2$ THz, $\gamma_2 = 0.3$ THz, $\omega_1 = (2\pi\times)40$ THz, $\gamma_1 = 5$ THz, $g = 300$, $b = 5000$. The critical fluence F_c is defined as the fluence where reversal occurs, which is larger than the fluence where the full suppression occors. The TDLT simulation clearly suggests a reversal of both OPs at $F > F_c$, as the magnitude of quasi-equilibrium position of both parameters at $F > F_c$ is equivalent to the values of equilibrium values, but the sign flips (Figure 1.6). Another interesting feature is that Φ_1 only exhibits evident oscillation at ω_1 only when the reversal occurs, but shows oscillation at ω_2 at all fluences. In contrast, Φ_2 only shows oscillation at ω_2.

TDLT Simulation of Order Parameter Switch

To simulate the ultrafast switch to a hidden state, we again consider a single OP Φ and add a term linear in Φ with coupling k such that the double-well is tilted. Thereby, the ground state is unique and another local minimum of PES slightly elevated in energy is the hidden state in equilibrium.

$$E(\Phi,t)=-\frac{1}{2}\omega_1^2\Phi_1^2+\frac{1}{4}b\Phi_1^4+k\Phi_1. \tag{1.10}$$

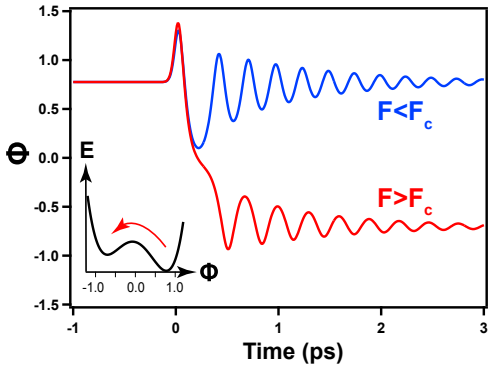

Figure 1.7: TDLT simulation of ultrafast switch of OP to an hidden state. The inset shows the tilted PES.

We assume the light directly exert a force to the OP and transfer kinetic energy, which can be characterized as a Gaussian driving force $f(t) = F \exp\left[-4\ln(2)t^2/\sigma^2\right]$ and the dynamical equation reads:

$$\frac{\partial^2\Phi(t)}{\partial t^2} + 2\gamma\frac{\partial\Phi(t)}{\partial t} - \omega^2\Phi(t)^2 + c\Phi(t)^4 + k = f(t). \tag{1.11}$$

The simulation result indeed shows that above a critical fluence F_c, a switch to the hidden can be realized (Figure 1.7).

Despite the ignorance of microscopic couplings and simplicity, the phenomenological TDLT based on symmetry analysis has succeeded in explaining a myriad of experimental observations in CDWs (R. Yusupov et al., 2010; Zong, Dolgirev, Kogar, Erge çen, et al., 2019; Duan et al., 2021), FEs (Mankowsky, Hoegen, et al., 2017; Kozina et al., 2019), magnets (Chuang et al., 2013; Nova, Cartella, et al., 2016; Gorobtsov et al., 2021), superconductors (Mankowsky, Subedi, et al., 2014), and nonlinear phononic setups (Först et al., 2011; Hoegen et al., 2018). Note that we only show the simplest examples of TDLT application in this section, but to more quantitatively understand the experimental data a great number of ingredients can be added such as complex OPs (Chuang et al., 2013), time-dependent damping rate (Huber et al., 2014), Langevin spatial fluctuation (Zong, Dolgirev, Kogar, Erge çen, et al., 2019; Zong, Dolgirev, Kogar, Su, et al., 2021), spatial dependence (R. Yusupov et al., 2010; Trigo et al., 2021; Duan et al., 2021), nonlinear OP coupling (Harter, D. M. Kennes, et al., 2018; Gorobtsov et al., 2021; Yoshikawa et al., 2021), and higher-order anharmonic terms (Hoegen et al., 2018).

Although the majority of ultrafast phase transitions can be interpreted in this framework, the IMT in VO_2 which originates from the spatially inhomogeneous atomic

disorders may not be correctly captured by TDLT (Perez-Salinas et al., 2022). Since the mean-field dynamics predict that the local distribution of OP is close to its mean value, it remains unclear whether TDLT can describe these possibly first-order disorder-order transitions with significant spatial heterogeneity.

1.3 Degrees of Freedom and their Interactions

Despite the achievements of the Landau theory, the microscopic origin of different phenomenological parameters defined in the Landau theory remains elusive. In this section, a handful of basic microscopic models of strongly correlated quantum materials will be introduced. Strongly correlated materials (SCMs) represent a large portfolio of compounds whose electronic behaviors cannot be effectively described by a non-interacting picture. Each electron can no longer be considered as moving freely in a "sea" of Fermi gas but has a complex influence on its neighbors. Typically, SCMs have incompletely filled $d-$ or $f-$electron shells and host a vast variety of unconventional electronic and magnetic properties, such as IMT, SC, colossal/giant magnetoresistance, magnetism, CDW, heavy fermionic behavior, large thermoelectric power, and multiferroic (Keimer and J. E. Moore, 2017; Tokura and N. Nagaosa, 2000).

The fascinating phenomena in SCMs originate from the complex intra- and interactions between the charge, orbital, spin, and lattice DoF (Figure 1.8). Especially in a paradigmatic group of SCMs, transition metal oxides (TMOs) with $d-$orbital electrons ranging from $3d$ cuprates to $5d$ iridates, a multitude of exotic phenomena such as high-T_c SC, pseudogap (PG), strange metal, orbital magnetism, and quantum spin liquid emerge from the strong (multi-orbital) electronic correlation and magnetic exchange interaction, electron-phonon coupling (EPC), spin-orbit coupling (SOC), and orbital-lattice coupling dubbed Jahn-Teller (JT) interaction. In the following, I will briefly cover the fundamental microscopic models of these interactions in paradigmatic $d-$orbital TMOs, which form the backbone of the systems covered in Chapters III-VI.

Crystal Field Splitting

Without including the spin DoF, a transition metal ion respects SO(3) symmetry in the free space and harbors a five-fold degenerate $d-$orbital (orbital angular momentum $l = 2$). A free atom electronic wave-function respecting spherical symmetry has orbital eigenstates described by spherical harmonics:

$$\psi_{nlm_l}(r, \theta, \phi) = R_{nl}(r, \theta, \phi) Y_l^{m_l}(\theta, \phi), \tag{1.12}$$

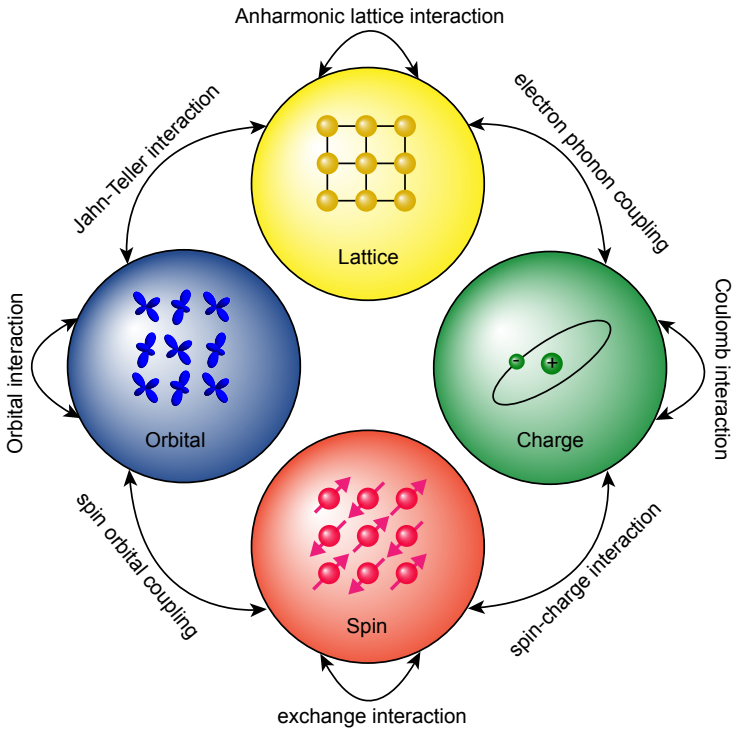

Figure 1.8: Schematic of charge, orbital, spin, and lattice degrees of freedom and their intra- and interactions.

where R is the radial distribution, $Y_l^{m_l}$ is the spherical harmonic, and n, l, m_l are quantum numbers.

In crystal, however, the ionic potential is no longer spherical. Instead, it is reduced to discrete rotational symmetries. For most of TMOs, the transition metal ion is constrained in a octahedral cage surrounded by six oxygen ligands at the apeces, and the local symmetry is reduced to cubic point group O_h. Consequently, the $d-$orbital degeneracy is lifted and its energy level is split into a two-fold degenerate e_g manifold and a three-fold degenerate t_{2g} manifold. Since the charge distribution of t_{2g} is in between the metal-ligand bond, while the e_g charge distribution lies along the direction of the metal-ligand bond, the energy level of the latter is higher than the former by a large cubic crystal field $10Dq$ on the order of several eV. The cubic splitting is commonly the largest energy scale in TMOs ($\sim$ 3 eV) and thus determines the orbital distribution at relatively large energy scales compared to the other interactions.

The d_{xz}, d_{yz}, and d_{xy} orbitals from t_{2g} manifold and $d_{3z^2-r^2}$ and $d_{x^2-y^2}$ orbitals from the e_g manifold are formed by the linear combinations of spherical harmonics

functions $Y_l^{m_l}$ with $l = 2$ and magnetic quantum number m_l from $-l$ to l:

$$\begin{aligned} d_{xz} &= \frac{1}{\sqrt{2}}(Y_2^{-1} - Y_2^1), d_{yz} = \frac{i}{\sqrt{2}}(Y_2^{-1} + Y_2^1), d_{xy} = \frac{i}{\sqrt{2}}(Y_2^{-2} - Y_2^2), \\ d_{3z^2-r^2} &= Y_2^0, d_{x^2-y^2} = \frac{1}{\sqrt{2}}(Y_2^{-2} + Y_2^2). \end{aligned} \tag{1.13}$$

Since $Y_2^{m_l}$ and $Y_2^{-m_l}$ equally contribute to these states, these states possess zero orbital angular momentum $L_z = 0$, which explains the missing orbital magnetic moment for most of transition metal ions with $d-$electrons in the absence of SOC.

Based on the above formulas and the recurrence relationships $\hat{L_z} Y_l^{m_l} = m_l Y_l^{m_l}$, $\hat{L_\pm} Y_l^{m_l} = \sqrt{(l \mp m)(l \pm m + 1)} Y_l^{m_l \pm 1}$, and $\hat{L_x} = \frac{1}{2}(\hat{L_+} + \hat{L_-})$, $\hat{L_y} = \frac{1}{2i}(\hat{L_+} - \hat{L_-})$, we can write out the matrix representation of the orbital angular momentum operators $\hat{L}_x$, $\hat{L}_y$, and $\hat{L}_z$ in the basis of $\{d_{xz}, d_{yz}, d_{xy}, d_{3z^2-r^2}, d_{x^2-y^2}\}$:

$$\begin{aligned} \hat{L}_x &= \begin{pmatrix} 0 & 0 & i & 0 & 0 \\ 0 & 0 & 0 & -\sqrt{3}i & -i \\ -i & 0 & 0 & 0 & 0 \\ 0 & \sqrt{3}i & 0 & 0 & 0 \\ 0 & i & 0 & 0 & 0 \end{pmatrix}, \\ \hat{L}_y &= \begin{pmatrix} 0 & 0 & 0 & \sqrt{3}i & -i \\ 0 & 0 & -i & 0 & 0 \\ 0 & i & 0 & 0 & 0 \\ -\sqrt{3}i & 0 & 0 & 0 & 0 \\ i & 0 & 0 & 0 & 0 \end{pmatrix}, \\ \hat{L}_z &= \begin{pmatrix} 0 & -i & 0 & 0 & 0 \\ i & 0 & 0 & 0 & 0 \\ 0 & 0 & 0 & 0 & 2i \\ 0 & 0 & 0 & 0 & 0 \\ 0 & 0 & -2i & 0 & 0 \end{pmatrix}. \end{aligned} \tag{1.14}$$

From the above formulas, we note that the angular momentum inside the e_g orbital is always 0. Since the crystal splitting $10Dq$ is usually much larger than the other energy scales, one can also ignore the off-diagonal elements between the e_g and t_{2g} manifolds and obtain the abbreviated effective angular momentum operators for the t_{2g} manifold:

$$\hat{L}_x = \begin{pmatrix} 0 & 0 & i \\ 0 & 0 & 0 \\ -i & 0 & 0 \end{pmatrix}, \ \hat{L}_y = \begin{pmatrix} 0 & 0 & 0 \\ 0 & 0 & -i \\ 0 & i & 0 \end{pmatrix}, \ \hat{L}_z = \begin{pmatrix} 0 & -i & 0 \\ i & 0 & 0 \\ 0 & 0 & 0 \end{pmatrix}. \tag{1.15}$$

One can check the angular momentum operators for the p orbital with $l = 1$ and find an easy relation, dubbed the T-P equivalence (Stamokostas and Fiete, 2018):

$$\hat{\mathbf{L}}(t_{2g}) = -\hat{\mathbf{L}}(p). \tag{1.16}$$

This can be understood by checking the effective angular momentum of the t_{2g} orbitals, by which one can easily demonstrate that the eigenstates of the truncated operators (Eq1.16) are linear combinations of d_{xz},d_{yz}, and d_{xy} orbitals:

$$|m_l = 1\rangle = -\frac{id_{xz} - d_{yz}}{\sqrt{2}}, \ \ |m_l = -1\rangle = -\frac{id_{xz} + d_{yz}}{\sqrt{2}}, \ \ |m_l = 0\rangle = d_{xy}. \tag{1.17}$$

Therefore, the t_{2g} manifold constructs a $l_{eff} = 1$ state, which can be mapped directly to the $l = 1$ p orbital.

It is universal that further distortion of octahedron arise from the formation of corner- or edge-shared octahedral network in real TMO lattices. These distortions belonging to E_g or T_{2g} irreproducible representations will further decrease the cubic symmetry to tetragonal, orthorhombic, trigonal, or even lower symmetries, part of which will be later elucidated in the JT interaction subsection.

Electronic Correlation and Magnetic Exchange Interaction

Despite the success in understanding the transport properties of conventional metal and semiconductors, single-particle band theory fails to describe the electronic state of TMOs with partially filled $d-$shell characterized by strong correlations. Specifically, many insulating TMOs such as NiO with partially filled electronic bands with strong Coulomb interaction between electrons turn out to be electrically insulating, posing serious challenge to the conventional band theory. Mott insulator (MI) is later coined to identify a class of solids violating the fundamental expectations of band theory. The behavior of MI can be understood with Hubbard model. Based on the tight-binding model, the Hubbard Hamiltonian adds the short-range Coulomb interaction U to the kinetic term parametrized by the hopping integral t:

$$\hat{H}_U = -\sum_{i,j,\sigma} t_{ij}\hat{c}^{\dagger}_{i\sigma}\hat{c}_{j\sigma} + U\sum_{i} n_{i\uparrow}n_{i\downarrow}, \tag{1.18}$$

where $\hat{c}^{\dagger}_{i\sigma}$ and $\hat{c}_{i\sigma}$ are the creation and annihilation operators for an electron with spin σ at lattice site i, $n_{i\sigma} = \hat{c}^{\dagger}_{i\sigma}\hat{c}_{i\sigma}$ is the number operator.

A metal-to-Mott-insulator transition can be realized by tuning the ratio U/t from zero to infinity when the band is half-filled: when $U = 0$, a simple tight-banding

band theory predicts a metallic ground state with incompletely filled band, while at $t = 0$ each site is singly occupied with localized spin because the penalty U for double occupancy at a single site is heavy. In the limit of large U/t, it can be shown that the effective Hamiltonian can be transformed into the Heisenberg model:

$$\hat{H}_J = -J \sum_{\langle ij \rangle} \hat{\mathbf{S}}_\mathbf{i} \cdot \hat{\mathbf{S}}_\mathbf{j}, \tag{1.19}$$

where $\langle ij \rangle$ denotes nearest neighbour, $\hat{\mathbf{S}}_\mathbf{i}$ is the spin vector at site i, and $J = 4t^2/U$ is the magnetic exchange interaction. An AFM ground state is reached in the MI where the spins on the nearest neighbours are anti-parallel so that a virtual hopping is possible.

MI with localized electrons due to strong Coulomb repulsion and reduced bandwidth is the central paradigm in the study of SCMs. The parent phase of high-T_c cuprate superconductors is MI albeit with a charge-transfer type. The SC, PG, strange metal, and Fermi liquid phases all arise from doping MI with carriers. The Heisenberg model, on the other hand, lays the foundation of magnetism, where abundant magnetic orders and excitations can be modelled by further introducing anisotropic spin interaction ($J_{xx} \neq J_{yy} \neq J_{zz}$) and antisymmetric Dzyaloshinskii–Moriya interaction (DMI) with the form of $\hat{H}^{ij}_{DM} = \mathbf{D_{ij}} \cdot (\hat{\mathbf{S}}_\mathbf{i} \times \hat{\mathbf{S}}_\mathbf{j})$.

In contrast to cuprate in which a single active electronic band is near the Fermi level, most of TMOs are multi-band SCMs. Many multi-orbital compounds such as ruthenates and iron pnictides are strongly correlated metal not in proximity to MI, which may be accounted for by Hund's coupling. Hund's coupling J_H represents the intra-atomic exchange energy scale, which favors two electrons in different orbitals with parallel spin as opposed to two electrons in the same orbital with opposite spins. Hund's coupling thus plays a crucial role in correlated metals with intermediate U. On the one hand, it reduces the energy cost of adding electron when the shell is not half filled and thus drives the system away from MI; on the other hand, it strongly lowers the quasi-particle coherence scale and makes the metallic state more correlated.

Hund's coupling is based on the atomic case, where Friedrich Hund formulated the three famous rules that are used to determine the ground-state electronic configuration of a multi-electron atom. For N electrons in a shell, the rules state that:

1. Total spin angular momentum S should be maximized.

2. For a given S, total orbital angular momentum L should be maximized.

3. For a less than half-filled shell, total angular momentum $J = |L - S|$ should be minimized; for a more than half-filled shell, $J = L + S$ should be maximized.

The origin of these rules can be attributed to the minimization of the Coulomb interaction. The importance of including Hund's coupling in incoherent metallic systems with itinerant electrons, broad bands, and moderate Coulomb repulsion like $4d$ and $5d$ TMOs and iron pnictides and chalcogenides highlights the consequences of atomic physics (Georges, Medici, and Mravlje, 2013).

To more quantitatively illustrate the role of both Coulomb repulsion U and Hund's coupling J_H in the presence of multiple orbitals, the many-body atomic Hamiltonian for t_{2g} manifold can be captured by the Kanamori multi-orbital electronic interaction model (Georges, Medici, and Mravlje, 2013):

$$\begin{aligned}\hat{H}_K =& U \sum_i \hat{n}_{i\uparrow}\hat{n}_{i\downarrow} + U' \sum_{i\neq i'} \hat{n}_{i\uparrow}\hat{n}_{i'\downarrow} + (U' - J_H) \sum_{i<i',\sigma} \hat{n}_{i\sigma}\hat{n}_{i'\sigma} \\ & - J_H \sum_{i\neq i'} \hat{c}^\dagger_{i\uparrow}\hat{c}_{i\downarrow}\hat{c}^\dagger_{i'\downarrow}\hat{c}_{i'\uparrow} + J_H \sum_{i\neq i'} \hat{c}^\dagger_{i\uparrow}\hat{c}^\dagger_{i\downarrow}\hat{c}_{i'\downarrow}\hat{c}_{i'\uparrow}\end{aligned} . \tag{1.20}$$

These terms represent the interaction U between electrons with opposite spins in the same orbital, the interaction $U' < U$ between electrons with opposite spins in different orbitals, and the interaction $U' - J_H$ between electrons with parallel spins in different orbitals, the spin exchange between different orbitals, and pair hopping between different orbitals, respectively. With $U' = U - 2J$ and rotational invariance, the Kanamori Hamiltonian takes a simplified form:

$$\hat{H}_U = (U - 3J_H)\frac{\hat{N}(\hat{N} - 1)}{2} + \frac{5}{2}J_H\hat{N} - J_H(2\hat{S}^2 + \hat{L}^2/2), \tag{1.21}$$

where $\hat{L}$ and $\hat{S}$ are the total orbital and spin angular momentum operators, and $\hat{N}$ is the total number of electrons operator. Note that in this form, Hund's first two rules are explicitly fulfilled.

Electron Phonon Coupling

Aside from the electronic correlation, EPC is one of the most fundamental and essential interactions in solids. The electronic excitation around meV energy scale in the vicinity of Fermi level can be strongly modified by EPC, which induces a variety of exotic phenomena including SC, CDW, Peierls distortion, polaron, band dispersion kink, and so on.

The most fundamental electron-phonon scattering process is absorption/emission of one phonon from one electron with a vertex coupling g and conserving both momentum and energy. Frölich Hamiltonian quantitatively captures this process:

$$\hat{H}_F = \hat{H}_e + \hat{H}_{ph} + \hat{H}_{e-ph}. \tag{1.22}$$

The electronic term captures the non-interacting band structure:

$$\hat{H}_e = \sum_{k\nu\sigma} \epsilon_{\nu\sigma}(k)\hat{c}^\dagger_{k\nu\sigma}\hat{c}_{k\nu\sigma}, \tag{1.23}$$

where the non-interacting electron possesses a band with dispersion $\epsilon(k)$, band index ν, momentum k, and spin σ.

The lattice term is expressed in terms of quantized non-interacting phonons:

$$\hat{H}_{ph} = \sum_{q\mu} \omega_\mu(q)(\hat{b}^\dagger_{q\mu}\hat{b}_{q\mu} + \frac{1}{2}), \tag{1.24}$$

where $\hat{b}^\dagger_{q\mu}$ and $\hat{b}_{q\mu}$ are the creation and annihilation operators for a phonon mode with momentum q, branch index μ, and energy $\omega_\mu(q)$.

The linear interaction term considers the lowest-order scattering process respecting the conservation of momentum and energy:

$$\hat{H}_{e-ph} = \sum_{k\nu\nu'\sigma} \sum_{q\mu} g^{q\mu}_{k+q\nu',k\nu}\hat{c}^\dagger_{k+q\nu'\sigma}\hat{c}_{k\nu\sigma}(\hat{b}^\dagger_{-q\mu} + \hat{b}_{q\mu}). \tag{1.25}$$

EPC can generate new quasiparticles (QPs) dubbed polarons which induces pronounced band dispersion renormalization. The concept of polaron was proposed by Lev Landau and Solomon Pekar which describes an electron moving in a phonon cloud where the atoms displace from their equilibrium positions to effectively screen the charge of the electron. Due to the electron-phonon scattering, the electronic state acquires finite lifetime and exhibits an abrupt change in dispersion, dubbed as kink, in the vicinity of the phonon energy, which can be captured by photoemission spectroscopy in various TMOs (Damascelli, Hussain, and Z.-X. Shen, 2003; Sobota, He, and Z.-X. Shen, 2021). This QP velocity change can be equivalently interpreted as an enhancement of the effective mass m^*. In the systems with very strong EPC such as titanates and iron chalcogenides, shake-off replicas of the original bands separated by the energy of a particular optical phonon branch can be resolved (J. J. Lee et al., 2014; Z. Wang et al., 2016; Rebec et al., 2017). On the other hand, EPC reciprocally modifies the phonon dispersion and linewidth. The phonon linewidth

which can be measured by inelastic neutron or X-ray scattering provides information about the degree of coupling to electrons of a particular phonon mode.

A vast variety of phenomena involving alteration of both electronic and structural properties emerge from the EPC. Peierls distortion arises when electrons in partially filled states are strongly coupled to vibrational modes along whose coordinates the distortions occur. Since the energy cost of lattice rearrangement is compensated by the splitting of degenerate electronic states, a bandgap opens accompanied by a periodic lattice distortion (Teitelbaum et al., 2018). Peierls distortion naturally leads to the formation of CDW where a spontaneous spatial modulation of charge density accompanied by the periodic ionic distortion occurs.

Stronger interest was developed in SC, where analogous to CDW the instability of electrons around Fermi level produces a new ground state. Two bound electrons with opposite spins and momenta undergo Bose-Einstein condensation showing superfluidity with zero electrical resistance. In the seminal work by Bardeen, Cooper, and Schrieffer (BCS), the attraction between the two paired electrons was proposed to be assisted by EPC. The BCS theory successfully explains behavior of most conventional superconductors such as the OP-like onset of SC gap at T_c, the isotope effect, an exponential raise of specific heat at T_c, and the expulsion of a magnetic field from the superconductor dubbed Meissner effect (Damascelli, Hussain, and Z.-X. Shen, 2003). Although alternative mechanisms including order fluctuations are proposed to explain the high-T_c SC which cannot be fully understood within BCS theory, EPC is still pivotal to understanding these novel superconducting systems.

Jahn Teller Interaction

JT interaction, originating from the coupling between the orbital degree of freedom and the lattice vibration, is one of the paradigmatic mechanism shows the spontaneous symmetry breaking induced by EPC in TMOs. The JT theorem essentially states that any nonlinear polyatomic system with a degenerate electronic ground state will undergo a geometrical lattice distortion that removes the electronic degeneracy and lowers the overall energy with a gain of E_{JT}. It usually drives the structural phase transition concomitant with the orbital ordering.

The JT effect of d orbital is of particular interest. The selection rule dictates the following: $e_g \otimes e_g = a_{1g} \oplus e_g$ and $t_{2g} \otimes t_{2g} = a_{1g} \oplus e_g \oplus t_{2g}$. Hereafter, we label the lattice irreproducible representation with capital letters to distinguish from the elec-

tronic channel, and drop the subscript for simplicity. Therefore, the e_g orbital can be coupled to 1 fully symmetric A_1 mode and 2 tetragonal/orthorhombic E lattice distortions, and the t_{2g} orbital can interact with 1 A_1 mode, 2 E modes, and 3 trigonal T vibration modes. A more widely-used routine is denoting $\{d_{yz}, d_{xz}, d_{xy}, d_{3z^2-r^2}, d_{x^2-y^2}\}$ as $\{\xi, \eta, \zeta, \theta, \epsilon\}$ (Bersuker, 2006). Accordingly, the general JT Hamiltonian can be written as followed (Iwahara, Vieru, and Chibotaru, 2018):

$$\hat{H}_{JT} = \sum_k \sum_{n\Lambda\lambda} \sum_{\Lambda_1\Lambda_2\cdots\Lambda_k} \frac{1}{k!} g_{n\Lambda}^{\Lambda_1\Lambda_2\cdots\Lambda_k} \times \{Q_{\Lambda_1} \otimes Q_{\Lambda_2} \otimes \cdots \otimes Q_{\Lambda_k}\}_{n\Lambda\lambda} \hat{\tau}_{\Lambda\lambda}. \tag{1.26}$$

Here $\Lambda(\Lambda_i)$ is e_g or t_{2g}, λ is its component, n distinguishes the repeated representation, $\hat{Q}_{\Lambda\lambda}$ is the normal coordinate, $\{Q_{\Lambda_1} \otimes Q_{\Lambda_2} \otimes \cdots \otimes Q_{\Lambda_k}\}_{\Lambda\lambda}$ is the symmetrized product of coordinates, g is the $k-$th order orbital-lattice coupling parameter, and $\hat{\tau}_{\Lambda\lambda}$ are the matrices of Clebsch-Gordan coefficients, which can be written out based on the quadrupolar angular momentum operators. The spatial configurations of the six normal modes that can be coupled to the t_{2g} orbitals with respect to an octahedron are illustrated in Figure 1.9.

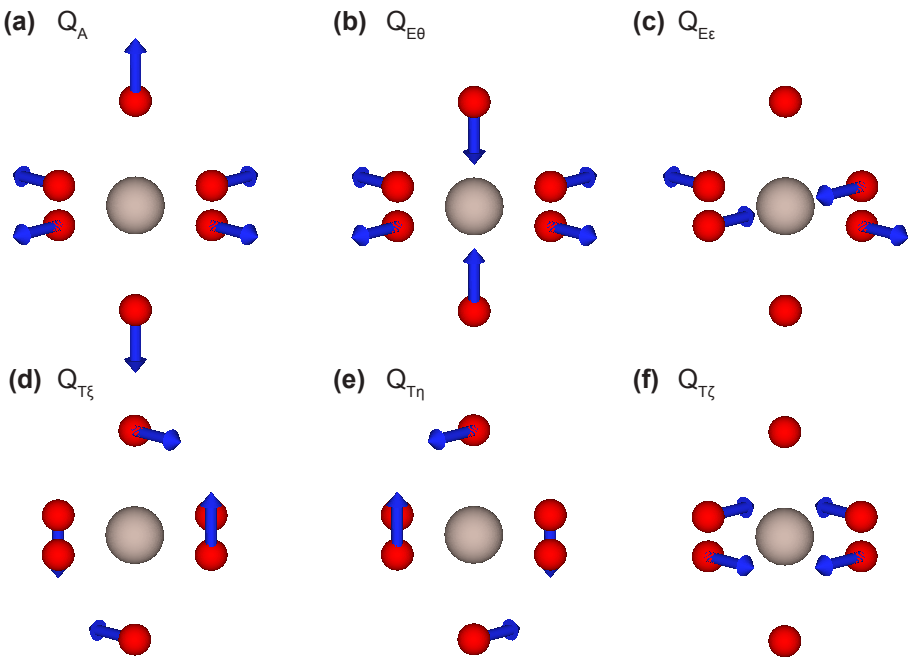

Figure 1.9: Schematic of orthonormal eigenmodes of an octahedron that can couple to $d-$orbital electrons.

Only keeping the linear coupling terms, we have a much simplified version:

$$\hat{H}_{JT} = \sum_{\gamma=\theta,\epsilon} g_E Q_{E\gamma} \hat{\tau}_{E\gamma} + \sum_{\gamma=\xi,\eta,\zeta} g_T Q_{T\gamma} \hat{\tau}_{T\gamma}. \tag{1.27}$$

With the harmonic lattice energy:

$$\hat{H}_{Lat} = \sum_{\gamma=\theta,\epsilon} \frac{1}{2} B_E Q_{E\gamma}^2 + \sum_{\gamma=\xi,\eta,\zeta} \frac{1}{2} B_T Q_{T\gamma}^2. \tag{1.28}$$

The quadrupolar tensors $\hat{\tau}$ can be written out based on their basis function symmetry as a function of orbital angular momentum operators: $\hat{\tau}_{\mu\nu} = \frac{1}{2}(\hat{L}_\mu \hat{L}_\nu + \hat{L}_\nu \hat{L}_\mu) - \frac{L(L+1)}{3}\delta_{\mu\nu}$. Specifically, we have:

$$\begin{aligned}
\hat{\tau}_{E\theta} &= -\frac{1}{2}(2\hat{L}_z^2 - \hat{L}_x^2 - \hat{L}_y^2), \\
\hat{\tau}_{E\epsilon} &= -\frac{\sqrt{3}}{2}(\hat{L}_x^2 - \hat{L}_y^2), \\
\hat{\tau}_{T\xi} &= -\frac{1}{\sqrt{2}}(\hat{L}_y \hat{L}_z + \hat{L}_z \hat{L}_y), \\
\hat{\tau}_{T\eta} &= -\frac{1}{\sqrt{2}}(\hat{L}_x \hat{L}_z + \hat{L}_z \hat{L}_x), \\
\hat{\tau}_{T\zeta} &= -\frac{1}{\sqrt{2}}(\hat{L}_x \hat{L}_y + \hat{L}_y \hat{L}_x).
\end{aligned} \tag{1.29}$$

Again, for t_{2g} manifold, both E and T vibronic modes are coupled, while for e_g orbital only E is interacting. For the latter case, the PES is simply a "Mexican hat" respecting $U(1)$ symmetry (Bersuker, 2006). We consider the t_{2g} manifold with possible coupling to both E and T vibronic modes. The general JT Hamiltonian with both distortions can be expressed as:

$$\hat{H}_{JT} = \begin{pmatrix} -g_E(\frac{1}{2}Q_{E\theta} - \frac{\sqrt{3}}{2}Q_{E\epsilon}) & \frac{1}{\sqrt{2}}g_T Q_{T\zeta} & \frac{1}{\sqrt{2}}g_T Q_{T\eta} \\ \frac{1}{\sqrt{2}}g_T Q_{T\zeta} & -g_E(\frac{1}{2}Q_{E\theta} + \frac{\sqrt{3}}{2}Q_{E\epsilon}) & \frac{1}{\sqrt{2}}g_T Q_{T\xi} \\ \frac{1}{\sqrt{2}}g_T Q_{T\eta} & \frac{1}{\sqrt{2}}g_T Q_{T\xi} & g_E Q_{E\theta} \end{pmatrix}. \tag{1.30}$$

We first consider the full Hamiltonian including both $\hat{H}_{Lat}$ and $\hat{H}_{JT}$ with only E distortion:

$$\hat{H}_E = \begin{pmatrix} -g_E(\frac{1}{2}Q_{E\theta} - \frac{\sqrt{3}}{2}Q_{E\epsilon}) + \frac{B_E}{2}(Q_{E\theta}^2 + Q_{E\epsilon}^2) & 0 & 0 \\ 0 & -g_E(\frac{1}{2}Q_{E\theta} + \frac{\sqrt{3}}{2}Q_{E\epsilon}) + \frac{B_E}{2}(Q_{E\theta}^2 + Q_{E\epsilon}^2) & 0 \\ 0 & 0 & g_E Q_{E\theta} + \frac{B_E}{2}(Q_{E\theta}^2 + Q_{E\epsilon}^2) \end{pmatrix}. \tag{1.31}$$

The eigenvalues are straightforward and characterize the PES of the system as the function of the two Q_E coordinates. Three paraboloids shifted away from origin in three directions with an included angle of 120° in-between [Figure 1.10(a)]. The

three minima are at $(Q_{E\theta}, Q_{E\epsilon}) = (-\frac{g_E}{B_E}, 0), (\frac{g_E}{2B_E}, \frac{\sqrt{3}}{2B_E}), (\frac{g_E}{2B_E}, -\frac{\sqrt{3}}{2B_E})$ with $E_{JT,E} = -\frac{g_E^2}{2B_E}$. These states correspond to tetragonal compression along $z-$, $y-$, and $x-$axes, and the electronic wavefunctions harbor the d_{xy}, d_{xz}, and d_{yz} characters, respectively. Here, the $U(1)$ symmetry is broken into Z_3.

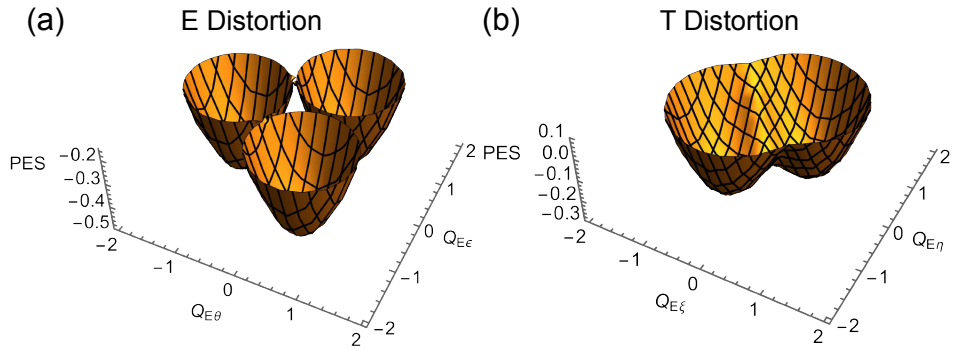

Figure 1.10: Calculated PES of (a) E and (b) T distortion. The unit of the horizontal axes is $g_{E/T}/B_{E/T}$ and the unit of the vertical axis is in $g_{E/T}^2/B_{E/T}$. Zero energy is defined as the case with no distortion $Q_i = 0$.

With only T distortion we have:

$$\hat{H}_T = \begin{pmatrix} \frac{B_T}{2}(Q_{T\xi}^2 + Q_{T\eta}^2 + Q_{T\zeta}^2) & \frac{1}{\sqrt{2}}g_T Q_{T\zeta} & \frac{1}{\sqrt{2}}g_T Q_{T\eta} \\ \frac{1}{\sqrt{2}}g_T Q_{T\zeta} & \frac{B_T}{2}(Q_{T\xi}^2 + Q_{T\eta}^2 + Q_{T\zeta}^2) & \frac{1}{\sqrt{2}}g_T Q_{T\xi} \\ \frac{1}{\sqrt{2}}g_T Q_{T\eta} & \frac{1}{\sqrt{2}}g_T Q_{T\xi} & \frac{B_T}{2}(Q_{T\xi}^2 + Q_{T\eta}^2 + Q_{T\zeta}^2) \end{pmatrix}. \tag{1.32}$$

We get four minima at $(Q_{T\xi}, Q_{T\eta}, Q_{T\zeta}) = (-\frac{\sqrt{2}g_T}{3B_T}, -\frac{\sqrt{2}g_T}{3B_T}, -\frac{\sqrt{2}g_T}{3B_T}), (-\frac{\sqrt{2}g_T}{3B_T}, \frac{\sqrt{2}g_T}{3B_T}, \frac{\sqrt{2}g_T}{3B_T}), (-\frac{\sqrt{2}g_T}{3B_T}, \frac{\sqrt{2}g_T}{3B_T}, \frac{\sqrt{2}g_T}{3B_T}), (\frac{\sqrt{2}g_T}{3B_T}, \frac{\sqrt{2}g_T}{3B_T}, -\frac{\sqrt{2}g_T}{3B_T})$ corresponding to $E_{JT,T} = -\frac{g_T^2}{3B_T}$ [Figure 1.10(b)]. These states correspond to elongation along the four trigonal axes of the octahedron.

With both distortions the general Hamiltonian with be the summation of Eq.(1.31) and (1.32). The PES in the five-dimensional space is rather complicated. Depending on the relative values of energy gain between $E_{JT,E}$ and $E_{JT,T}$, the extrema points can be categorized into three different groups (Bersuker, 2006): (1) when $E_{JT,E} = -\frac{g_E^2}{2B_E} < E_{JT,T} = -\frac{g_T^2}{3B_T}$, in other words, $\frac{g_T}{g_E} < \sqrt{\frac{3B_T}{2B_E}}$, the minima are realized at the three tetragonal distortion points and the trigonal distortion minima are saddle points; (2) when $E_{JT,E} = -\frac{g_E^2}{2B_E} > E_{JT,T} = -\frac{g_T^2}{3B_T}$, in other words, $\frac{g_T}{g_E} > \sqrt{\frac{3B_T}{2B_E}}$, the minima are realized at the four trigonal distortion points and the tetragonal distortion minima are saddle points; (3) six equivalent orthorhombic saddle points. One Q_T

and one Q_E are individually displaced at each of these saddle points. The total energy reads $E_{JT} = \frac{1}{4}E_{JT,T} + \frac{3}{4}E_{JT,T}$. The results are summarized as follows:

Number of extrema points	Nature of extrema points	$(Q_{E\theta},Q_{E\epsilon},Q_{T\xi},Q_{T\eta},Q_{T\zeta})$ in the unit of $(\frac{g_E}{B_E}, \frac{g_E}{B_E}, \frac{g_T}{B_T}, \frac{g_T}{B_T}, \frac{g_T}{B_T})$
3	Tetragonal minima or saddle points	$(-1,0,0,0,0)$ $(\frac{1}{2}, \frac{\sqrt{3}}{2}, 0, 0, 0)$ $(\frac{1}{2}, -\frac{\sqrt{3}}{2}, 0, 0, 0)$
4	Trigonal minima or saddle points	$(0,0,-\frac{\sqrt{2}}{3}, -\frac{\sqrt{2}}{3}, -\frac{\sqrt{2}}{3})$ $(0,0,-\frac{\sqrt{2}}{3}, \frac{\sqrt{2}}{3}, \frac{\sqrt{2}}{3})$ $(0,0,\frac{\sqrt{2}}{3}, -\frac{\sqrt{2}}{3}, \frac{\sqrt{2}}{3})$ $(0,0,\frac{\sqrt{2}}{3}, \frac{\sqrt{2}}{3}, -\frac{\sqrt{2}}{3})$
6	Orthorhombic saddle points	$(\frac{1}{2},0,0,0,-\frac{1}{\sqrt{2}})$ $(\frac{1}{2},0,0,0,\frac{1}{\sqrt{2}})$ $(-\frac{1}{4}, \frac{\sqrt{3}}{4}, 0, -\frac{1}{\sqrt{2}}, 0)$ $(-\frac{1}{4}, \frac{\sqrt{3}}{4}, 0, \frac{1}{\sqrt{2}}, 0)$ $(-\frac{1}{4}, -\frac{\sqrt{3}}{4}, -\frac{1}{\sqrt{2}}, 0, 0)$ $(-\frac{1}{4}, -\frac{\sqrt{3}}{4}, \frac{1}{\sqrt{2}}, 0, 0)$

Table 1.1: Summary of JT distortion in different cases.

Spin Orbit Coupling

The SOC is a relativistic interaction of a particle's spin with its angular motion. In atomic physics, a key result of SOC is electronic energy level shift and splitting. The SOC Hamiltonian takes a general form with the coupling constant λ:

$$\hat{H}_{SOC} = \lambda \hat{\mathbf{L}} \cdot \hat{\mathbf{S}}. \tag{1.33}$$

The effect of SOC in noninteracting semiconductors has been extensively studied, leading to a number of interesting phenomena including the anomalous Hall effect, Rashba and Dresselhauss effects, and control of spin current through spin-orbit torque (Rau, E. K.-H. Lee, and Kee, 2016). More recently, SOC-induced band inversion has led to a flourishing field of topological phases (Lv, Qian, and Ding, 2021).

Not until recently was it realized that SOC plays a vital role in correlated $d-$ orbital systems especially with high atomic numbers like $4d$ and $5d$ transition

metal ions. Upon descending the periodic table from $3d$ to $5d$, the electronic correlation decreases as the d-orbital becomes more extended, while SOC increases dramatically as the atom gets heavier. The cooperative interplay between correlation and SOC generates rich phase diagrams in $d-$orbital TMOs. Considerable SOC in the presence of intermediate correlation gives rise to a plethora of new topological phases including topological insulator, topological semimetal, axionic insulator, and topological Mott insulator. In the presence of strong electronic correlation, the spin-orbit entanglement removes orbital degeneracy and reduces Jahn-Teller effect, promoting spin-orbit coupled Mott insulator, quantum spin liquid, and multipolar ordered phases (Witczak-Krempa et al., 2014).

We now consider the microscopic model of SOC for TMOs with $d-$orbital electrons in the basis $\{d_{xz\uparrow}, d_{yz\uparrow}, d_{xy\downarrow}, d_{3z^2-r^2\downarrow}, d_{x^2-y^2\downarrow}, d_{xz\downarrow}, d_{yz\downarrow}, d_{xy\uparrow}, d_{3z^2-r^2\uparrow}, d_{x^2-y^2\uparrow}\}$ so that its matrix representation is block-diagonalized (Stamokostas and Fiete, 2018):

$$\hat{H}_{SOC} = \frac{\lambda}{2}\left(\begin{array}{ccccc|ccccc} 0 & -i & i & \sqrt{3} & -1 & & & & & \\ i & 0 & -1 & -\sqrt{3}i & -i & & & & & \\ -i & -1 & 0 & 0 & -2i & & & 0 & & \\ \sqrt{3} & \sqrt{3}i & 0 & 0 & 0 & & & & & \\ -1 & i & 2i & 0 & 0 & & & & & \\ \hline & & & & & 0 & i & i & -\sqrt{3} & 1 \\ & & & & & -i & 0 & 1 & -\sqrt{3}i & -i \\ & & 0 & & & -i & 1 & 0 & 0 & 2i \\ & & & & & -\sqrt{3} & \sqrt{3}i & 0 & 0 & 0 \\ & & & & & 1 & i & -2i & 0 & 0 \end{array}\right). \quad (1.34)$$

The SOC within e_g manifold is zero due to its quenched orbital angular momentum. Considering the large energy scale of $10Dq$, hereafter we neglect the e_g manifold and the $e_g - t_{2g}$ mixing and focus on the SOC effect within the t_{2g} orbitals. Now we have t_{2g} SOC Hamiltonian in the basis of $\{d_{xz\uparrow}, d_{yz\uparrow}, d_{xy\downarrow}, d_{xz\downarrow}, d_{yz\downarrow}, d_{xy\uparrow}\}$:

$$\hat{H}^{t_{2g}}_{SOC} = \frac{\lambda}{2}\left(\begin{array}{ccc|ccc} 0 & -i & i & & & \\ i & 0 & -1 & & 0 & \\ -i & -1 & 0 & & & \\ \hline & & & 0 & i & i \\ & 0 & & -i & 0 & 1 \\ & & & -i & 1 & 0 \end{array}\right). \quad (1.35)$$

The eigenvalues are $\{\lambda, \lambda, -\lambda/2, -\lambda/2, -\lambda/2, -\lambda/2\}$. Therefore the 6-fold degenerate t_{2g} manifold is split due to SOC. One can further label these states by calculating

their eigenvalues of the effective angular momentum operator $\hat{\mathbf{J}}_{\mathbf{eff}} = -\hat{\mathbf{L}}_{\mathbf{eff}} + \hat{\mathbf{S}}$ and get the well-known two-fold degenerate $J_{eff} = 1/2$ state which lies λ above the original degenerate t_{2g} orbital and four-fold degenerate eigenstate $J_{eff} = 3/2$ state which lies $-\frac{\lambda}{2}$ below: (Stamokostas and Fiete, 2018):

$$
\begin{aligned}
\left|J_{eff}=\frac{1}{2},m_j=-\frac{1}{2}\right\rangle &= -\frac{i}{\sqrt{3}}\left|d_{xz\uparrow}\right\rangle + \frac{1}{\sqrt{3}}\left|d_{yz\uparrow}\right\rangle - \frac{1}{\sqrt{3}}\left|d_{xy\downarrow}\right\rangle \\
\left|J_{eff}=\frac{1}{2},m_j=\frac{1}{2}\right\rangle &= \frac{i}{\sqrt{3}}\left|d_{xz\downarrow}\right\rangle + \frac{1}{\sqrt{3}}\left|d_{yz\downarrow}\right\rangle + \frac{1}{\sqrt{3}}\left|d_{xy\uparrow}\right\rangle \\
\left|J_{eff}=\frac{3}{2},m_j=\frac{3}{2}\right\rangle &= -\frac{i}{\sqrt{2}}\left|d_{xz\uparrow}\right\rangle - \frac{1}{\sqrt{2}}\left|d_{yz\uparrow}\right\rangle \\
\left|J_{eff}=\frac{3}{2},m_j=-\frac{3}{2}\right\rangle &= -\frac{i}{\sqrt{2}}\left|d_{xz\downarrow}\right\rangle + \frac{1}{\sqrt{2}}\left|d_{yz\downarrow}\right\rangle \\
\left|J_{eff}=\frac{3}{2},m_j=-\frac{1}{2}\right\rangle &= -\frac{i}{\sqrt{6}}\left|d_{xz\uparrow}\right\rangle + \frac{1}{\sqrt{6}}\left|d_{yz\uparrow}\right\rangle + \frac{2}{\sqrt{6}}\left|d_{xy\downarrow}\right\rangle \\
\left|J_{eff}=\frac{3}{2},m_j=\frac{1}{2}\right\rangle &= -\frac{i}{\sqrt{6}}\left|d_{xz\downarrow}\right\rangle - \frac{1}{\sqrt{6}}\left|d_{yz\downarrow}\right\rangle + \frac{2}{\sqrt{6}}\left|d_{xy\uparrow}\right\rangle .
\end{aligned}
\tag{1.36}
$$

Specifically for t_{2g} manifold, different occupancy of electrons will generate ground states with distinct effective angular momentum (Takayama, Jiřì Chaloupka, et al., 2021). Here, we consider the case with a relatively large Hund's coupling so that the Hund's rules apply. The resulting spin-orbit energy level diagram and the total angular momentum spatial configuration for different occupancy are shown in Figure 1.11. The ground state properties and the relationship between JT interaction and SOC for t_{2g} manifold with different electron filling numbers n are introduced as follows:

- d^1: without SOC, the single electron occupies d_{xy} orbital and generates a JT effect with a compressed $z-$axis. Including SOC, $J_{eff} = \frac{3}{2}$ state is singly occupied and thus t_{2g}^1 possesses $J = \frac{3}{2}$ with parallel $S = \frac{1}{2}$ and $L = 1$. $J = \frac{3}{2}$ is JT-active and can be further split into two doublets which are both similar to e_g manifold. JT distortion will be suppressed by SOC asymptotically to half of its value without SOC (Streltsov and Khomskii, 2020). $J = \frac{3}{2}$ can also host novel FM state, AFM octopolar state, quadrupolar-ordered spin nematic state, quantum spin liquid state, and valence-bond solid state (G. Chen, Pereira, and Balents, 2010).

- d^2: without SOC and due to the Hund's rule, the two parallel electrons occupy $d_{xz/yz}$ orbitals and the octahedron thus shows a $z-$axis elongation.

In the presence of SOC, $J_{eff} = \frac{3}{2}$ is doubly occupied. Since $L = 1$ and $S = 1$ are parallel, $J = 2$ is the ground state with $J = 1, 0$ at higher energies. $J_{eff} = \frac{3}{2}$ is JT-active and will be split into two doublets and one singlet. JT distortion will approach zero asymptotically only when $\lambda \rightarrow \infty$ (Streltsov and Khomskii, 2020). Significant fourth and sixth order $J - J$ interactions lead to a rich ground-state phase diagram with multiple novel dipolar FM and AFM states and spin-nematic quadrupolar ordered intermediate states (G. Chen and Balents, 2011).

- d^3: without SOC and due to Hund's rule, the three electrons share the same spin polarization direction and occupy all the three orbitals. The orbital momentum is completely quenched and the system is JT-inactive. Turning on the SOC will make the $J_{eff} = \frac{3}{2}$ quartet singly hole-occupied similar to d^1. Therefore, SOC can induce JT-distortion at large λ (Streltsov and Khomskii, 2020).

- d^4: without SOC and due to the Hund's rule, two electrons with oppsite spins occupy d_{xy} orbital and the other two electrons occupy d_{xz} and d_{yz} orbitals. The octahedron thus exhibits compression along $z-$axis. Turning on SOC will make the $J_{eff} = \frac{3}{2}$ quartet fully occupied. Therefore a $J = 0$ ground state with anti-parallel $L = 1$ and $S = 1$ will be reached, which is JT-inactive and magnetic-silent. Simulation shows that JT distortion is abruptly quenched when λ is larger than a critical value (Streltsov and Khomskii, 2020). When λ is not so large and comparable to the exchange interaction J, a virtual excitation to $J = 1$ state from $J = 0$ can generate excitonic magnetism and the magnetic gap is of intra-atomic nature determined by λ (Khaliullin, 2013; Jain et al., 2017). Simultaneously, the JT-activity of $J = 1$ state can be inherited by $J = 0$ state and a spin-nematic quadrupolar ordered state can be realized at an intermediate temperature (H. Liu and Khaliullin, 2019).

- d^5: without SOC and due to the Hund's rule, both d_{xz} and d_{yz} orbitals are fully occupied while d_{xy} orbital is singly occupied, hence the octahedron shows a $z-$axis elongation. Turning on SOC will make the $J_{eff} = \frac{3}{2}$ quartet fully occupied and $J_{eff} = \frac{1}{2}$ doublet singly occupied, thus giving rise to a $J = \frac{1}{2}$ state with anti-parallel $L = 1$ and $S = \frac{1}{2}$. The ground state is thus a Kramers doublet echoing a $S = \frac{1}{2}$ system and is JT-inactive when λ is larger than a critical value (Streltsov and Khomskii, 2020). Exotic states such as quantum spin liquid and topological Mott insulator have been proposed in the

strong-SOC and intermediate-SOC regimes, respectively (Witczak-Krempa et al., 2014).

- d^6: with or without SOC, t_{2g} bands are fully occupied and both magnetic- and JT-inactive.

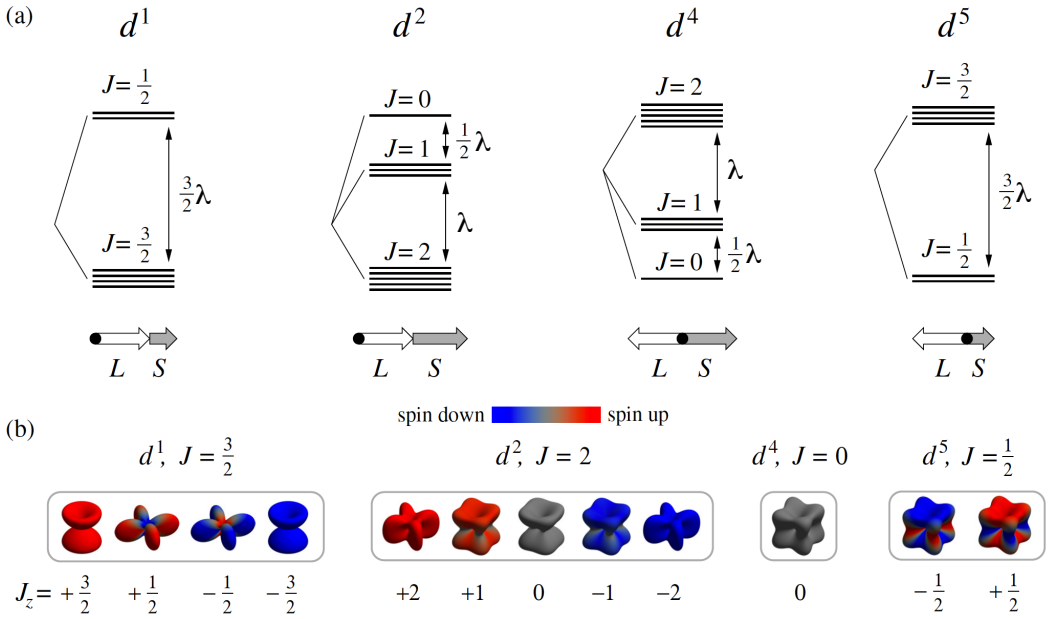

Figure 1.11: Spin orbital energy level diagram and the total angular momentum spatial configuration. (a) Low-energy levels of d^1, d^2, d^4, and d^5 filling cases for t_{2g} manifold. The degeneracy of different levels is characterized by the number of lines. (b) Spatial shape of the ground state J. The spatial shape reflects the angular distribution of the electron (hole) density for less (more) than half-filled case. The color of the surface indicates normalized spin polarization ranging from -1 to 1. The figure is adopted from Takayama, Jiří Chaloupka, et al., 2021.

Chapter 2

Experimental Techniques

Ultrafast laser technology plays an instrumental role in understanding the underlying physics of quantum materials in the past decade. State-of-the-art laser technology can now reliably produce light pulses with time duration ranging from as to ps and centered energy ranging from far-IR to ultraviolet (UV). The recent development of table-top extreme UV source based on high-harmonic generation (HHG) and national lab-based X-ray free electron laser (XFEL) creates tunable ultrafast laser pulses even in the X-ray regime. These advances open unprecedentedly abundant opportunities to interrogate the non-equilibrium emergent phenomena and implement nonthermal control of macroscopic properties of quantum materials.

A typical ultrafast experiment is technically composed of two critical ingredients: a stronger "pump" pulse which photo-excites the material and initiates the nonequilibrium process, and a relatively weaker "probe" which directly or indirectly couples to different DoF and monitors their ultrafast dynamics as a function of time delay with respect to the pump pulse. A number of experimental tools can be leveraged as the probe to investigate the ultrafast behaviors of quantum materials (A. d. l. Torre, Dante M. Kennes, et al., 2021):

- Time- and angle-resolved photoemission spectroscopy (tr-ARPES) probes momentum-resolved electronic dynamics by directly measuring the evolution of single-particle spectral function upon photo-excitation;
- Time-resolved X-ray diffraction (tr-XRD) and ultrafast electron diffraction (UED) selectively track the dynamics of structural, charge, orbital, and spin orders at different Bragg peaks with fs time resolution;
- Time-resolved resonant inelastic X-ray scattering (tr-RIXS) and electron energy loss spectroscopy (tr-EELS), as complementary probes of tr-ARPES, directly map the transient bosonic excitation (phonon, magnon, plasmon, etc) spectra;
- Time-resolved microscopy, including scanning near-field optical microscopy (SNOM), scanning tunneling microscopy (STM), electron microscopy, momentum microscopy, and X-ray microscopy, are capable of measuring the

electronic and OP dynamics down to nanometer (nm) length scale with outstanding temporal and spectral resolutions;

- Time-resolved transport, albeit with ps resolution, directly probes the transient photoconductivity and photocurrent in microstructured devices that are not accessible with far-field measurements;
- Time-resolved optical spectroscopy, one of the simplest yet most extensively utilized ultrafast techniques, probes diverse aspects of a quantum material's optical properties as a function of time with fs resolution.

Time-resolved optical spectroscopy include various forms. Time-resolved absorption and reflectivity measurements detects the carrier excitation and subsequent relaxation dynamics. Time-resolved IR, visible, and UV broadband spectroscopy simultaneously yield temporal and spectral information. Time-resolved magneto-optical Kerr and Faraday effect induced by magneto-optical effect can be used to track the dynamics of magnetic OP. Time-resolved nonlinear spectroscopy detects the underlying symmetry change of quantum materials upon photo-excitation. Transient grating spectroscopy, in which a pair of beams are interfered on the sample surface to form a periodic intensity modulation, can probe the propagation of QPs in real space. Time-resolved time-domain THz spectroscopy (tr-TDTS) enables a phase- and frequency-resolved measurements of transient complex optical conductivity in the THz regime. Coherent oscillation of phonon, magnon, or Higgs mode may also emerge in various optical spectroscopy techniques, the measurement of which is dubbed coherent mode spectroscopy. In the following, I will introduce time-resolved reflectivity and magneto-optical Kerr effect, time-resolved nonlinear spectroscopy, and coherent mode spectroscopy in more detail, since they have been mainly used in the experiments shown in Chapter III-VI.

2.1 Time-Resolved Reflectivity and Magneto-Optical Kerr Effect

Due to the versatility and simplicity, time-resolved reflectivity (tr-ΔR/R) has been widely applied to a multitude of non-interacting and strongly correlated systems to study their carrier and OP dynamics (Orenstein, 2012). By tracking the differential reflectivity intensity change upon light impingement, not only the relaxation of excited carriers but also the temporal evolution of band structure can be retrieved. On the other hand, by measuring the polarization change of reflection light, time-resolved magneto-optical Kerr effect (tr-MOKE) whose value is linearly proportional to the change in magnetic OP reflects the dynamics of the spin DoF.

Physical Mechanism

To begin with, we calculate the complex optical conductivity $\tilde{\sigma} = \sigma_1 + i\sigma_2$ using a quantum mechanical model based on fluctuation-dissipation theorem and Fermi's Golden rule (Armitage, 2009). The real part σ_1, which is also referred to as the Kubo-Greenwood formula, basically reflects the interband transitions with initial state i to final state f:

$$\sigma_1(\omega) = \frac{e^2}{4\pi^2 m^2 \omega} |\langle f|p|i\rangle|^2 D_{fi}(\omega), \tag{2.1}$$

where $\langle f|p|i\rangle$ is the dipole matrix element incorporating symmetry constraints and selection rules, and $D_{fi}(\omega) = \frac{2}{(2\pi)^3} \int \delta(\hbar\omega - \hbar\omega_{fi}) dk$ is the so-called joint density of states (JDOS), which is determined by the band structure and carrier distribution. The imaginary part σ_2 follows the Kramers-Kronig relation, which is given by σ_1:

$$\sigma_2(\omega) = -\frac{2\omega}{\pi} \int_0^\infty \frac{\sigma_1(\omega')}{\omega'^2 - \omega^2} d\omega'. \tag{2.2}$$

The complex dielectric constant and refractive index can then be calculated through $\tilde{\epsilon} = \frac{i\tilde{\sigma}}{\epsilon_0 \omega}$ and $\tilde{n} = \sqrt{\tilde{\epsilon}}$.

For light with electric field polarized parallel (p) or perpendicular (s) to the scattering plane (Figure 2.1), the amplitude reflection coefficient $\tilde{r}$ is determined by $\tilde{n}$ and the incident (reflection) angle θ_i:

$$\begin{aligned} \tilde{r}_p &= \frac{-\tilde{n}^2 \cos\theta_i + \sqrt{\tilde{n}^2 - \sin^2\theta_i}}{\tilde{n}^2 \cos\theta_i + \sqrt{\tilde{n}^2 - \sin^2\theta_i}}, \\ \tilde{r}_s &= \frac{\cos\theta_i - \sqrt{\tilde{n}^2 - \sin^2\theta_i}}{\cos\theta_i + \sqrt{\tilde{n}^2 - \sin^2\theta_i}}. \end{aligned} \tag{2.3}$$

The reflectance $R_{s/p} = |r_{s/p}|^2$ can thus be calculated. Therefore, if the symmetry of the bands and the light polarization do not change over time, the change in transient reflectivity reflects the evolution of JDOS, which can be generated either by photo-carrier redistribution or light-induced band structure modulation. By performing broadband spectroscopy, the full spectrum of $\tilde{\sigma}(\omega)$ of the corresponding energy range can be retrieved through Kramers-Kronig transformation, thus showing a frequency-resolved change of JDOS. A specific example of Kramers-Kronig transformation is shown in Chapter VI.

The MOKE, on the other hand, describes the change in both polarization and reflected intensity of the light reflected from a magnetized surface. Similar to the

Faraday effect, which describes the change of light transmission through a magnetic material, MOKE originates from the anti-symmetric off-diagonal components of the dielectric tensor ϵ_{ij}^{A}, which yields an anisotropic permittivity that changes the phase and absorption of polarized incident light (Němec et al., 2018). The MOKE-induced polarization change include two complementary effects that are both linearly proportional to M, namely the Kerr rotation θ_K, where the reflected light polarization angle rotates with respect to the incident light, and the Kerr ellipticity η_K, where the reflected light becomes elliptical (Figure 2.1).

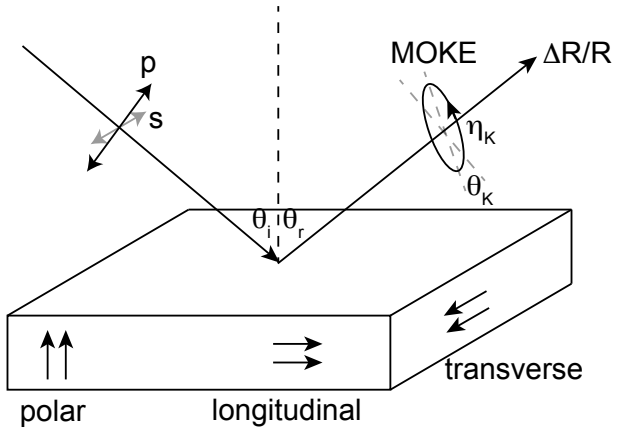

Figure 2.1: Schematic of the time-resolved reflectivity and MOKE of different types.

There are three types of MOKE depending on the relative direction of the magnetization **M** with respect to the scattering plane and sample surface normal (Figure 2.1): polar MOKE, with **M** parallel to the scattering plane and to the surface normal, gives rise to a considerable polarization change; longitudinal MOKE, with **M** parallel to the scattering plane but perpendicular to the surface normal, induces an ellipticity change. The longitudinal MOKE signal is conventionally smaller than the polar configuration and vanishes when the incident angle is zero; transverse MOKE, with **M** perpendicular to both the scattering plane and the surface normal, only modulates the reflected light intensity linear in **M** without generating any polarization change and is thus hard to be distinguished from transient reflectivity.

Tr-MOKE can also be used to study AFM materials despite its lack of averaged **M**. The first reason is that many antiferromagnets still possess net magnetic moment due to spin canting induced by DMI. The other reason is that coherent dynamics of **M** can be generated by $\mathbf{L} \times \frac{d\mathbf{L}}{dt}$, where **L** is the AFM OP staggered magnetization (Němec et al., 2018). In addition, the polarization change of the reflected light can also arise from transient lattice change. For instance, materials with a chiral

structure like elemental tellurium can also generate gyrotropic and optical anisotropy mimicking MOKE (Shalygin et al., 2016; Zhong, Joel E. Moore, and Souza, 2016; Tsirkin, Puente, and Souza, 2018). Furthermore, magneto-optical effect that scale quadratically with M or L like Cotton-Mutton or Voigt effect can also alter the polarization of reflected light (Němec et al., 2018).

Experimental Setup

A typical time-resolved reflectivity setup is shown in Figure 2.2, which is composed of two main parts: the pump arm and the probe arm. In the pump arm, we use two irises to align the incident beam pointing so that later it goes straightly into the translation delay stage. We use a pair of lenses as telescope to collimate the beam and change the beam spot size on the sample. We use a half-waveplate (HWP) and linear polarizer (LP) pair, both of which are placed on a rotation mount, to tune either the pump light polarization with a constant incident fluence (by rotating the LP) or the pump fluence with a fixed polarization (by rotating the HWP). An additional quarter wave plate (QWP) can be placed after the polarizer to create a circularly polarized light. The pump beam then goes through a retroreflector placed on a motorized translation delay stage so that the time delay between the pump and probe can be tuned, and finally goes through the objective lens nearly perpendicularly to the sample surface. Note that depending on the pump energy, different achromatic WP and LP should be chosen correspondingly.

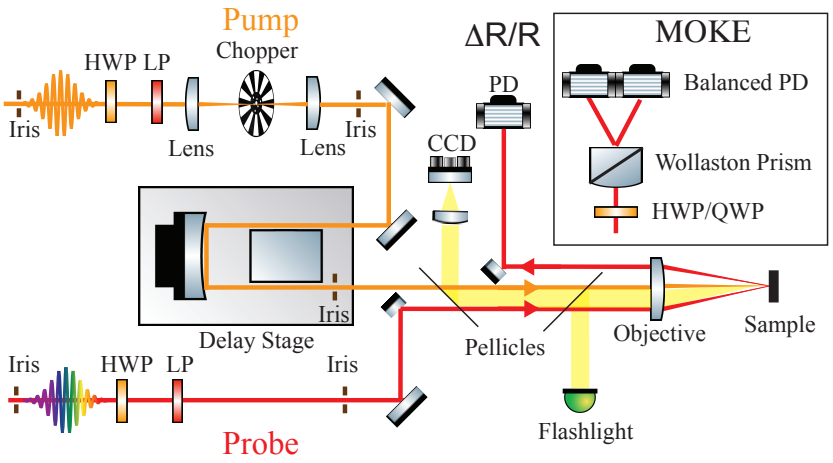

Figure 2.2: Schematic of the time-resolved reflectivity and MOKE experimental setup.

The probe arm also goes through a HWP-LP pair and two irises to achieve the same aforementioned goals. It goes through the objective lens off-center so that

the reflected beam can be picked up by another small D-mirror and then directed into the photo-diode (PD) that is connected to the lock-in amplifier. An additional bandpass filter to block the pump scattering can be put before the PD. Also note that nonlinear response of PD may emerge when the probe signal is too strong. A neutral density (ND) filter should be placed in front of the PD if the PD reading indeed shows nonlinear behavior. Depending on the probe energy, Si (1 eV to 3 eV) or InGaAs PD (0.5 eV to 1.4 eV) should be selected correspondingly.

We detected the differential reflectivity using a lock-in amplifier. A chopper is placed near the focus of the telescope in the pump arm to chop the pump pulse at half of the laser repetition rate (500 Hz). Therefore, half of the detected probe pulses are modulated by pump while the other half are not. By taking the difference between these two, we can get the differential reflectivity ΔR. We can measure R by setting the frequency of the lock-in amplifier to be equal to the laser repetition rate.

To detect the polarization change in a MOKE experiment, a single PD is not enough. Instead, a balanced detector should be used. After the probe beam reflected from the sample surface, a HWP (QWP) is placed to measure the Kerr rotation (ellipticity). Then one should put a Wollaston prism to separate the probe into two orthogonally polarized outputs in two directions. The Wollaston prism should be placed at the correct position and rotation angle such that the two beams hit the two PDs on the balanced detector. The balanced detector then subtracts the two inputs from each other. In the absence of pump, one should first rotate the WP in front of the Wollaston prism such that the two outgoing beams after the Wollaston prism have identical intensity and thus the output of the balanced detector is minimized. Then the pump-induced magnetism change will unbalance the two arms and a transient signal Δx can be recorded. By further measuring R by blocking one of the two PD, one can get $\Delta\theta_K = \frac{\Delta x}{2R}$.

The sample, whose surface normal is aligned to the optical axis of the objective, is placed at the focus of the objective lens inside a cryostat. A simple white light microscopy setup can be incorporated into the setup to image the sample surface. Two pellicle beamsplitters are placed close to the objective, with one for directing the flashlight beam into the objective to illuminate the sample surface and the other for directing the reflected beam into a webcam to image the sample surface as well as the position of the pump and probe beams if their energies are adequate. One can then look at the real-time image of the sample surface on the webcam and finely tune the sample position and tilting angle so that the sample image is clear and both the

pump and probe are spatially overlapped on a smooth region of the sample surface free of domains or terraces.

Data Analysis

A prototypical time-resolved reflectivity trace upon overgap pumping is shown in Figure 2.3(a). Time zero is defined as the time when the peak intensity of pump and probe pulses overlap temporally. A prompt onset of signal emerges before time zero and peaks after. Ensuing the onset, one exponential decay or two exponential decays with different decay times representing the carrier relaxation through different channels can be observed. Without loss of generality, we consider the double-decay case here and $\Delta R/R(t)$ can thus be fit with a convolution of a Gaussian representing the instrumental response function (IRS) with a double-exponential decay:

$$\Delta R/R(t) = e^{-\frac{4\ln 2 t^2}{\sigma^2}} * H(t)(A_1 e^{-t/\tau_1} + A_2 e^{-t/\tau_2} + C), \tag{2.4}$$

where σ is the finite time resolution, $H(t)$ is the Heaviside function representing the instantaneous onset of signal due to electron-electron scattering (~fs) that occurs within the pulse duration, A_i and τ_i are the amplitude and time constant of the two decays, C is the constant background representing long-time heat dissipation away from the excited region, which may take ns. The two decaying channels can be either intra- and interband relaxation (Xinwei Li et al., 2022), strongly and weakly coupled phonon baths (Laurita et al., 2019), or two distinct DoF such as spin and lattice (Beaurepaire et al., 1996). The temperature-, fluence-, polarization-, and wavelength-dependent measurements of A_i, τ_i, and C can provide rich information about the evolution of photo-carriers and band structure, expediting a comprehensive understanding of the ultrafast dynamics of quantum materials.

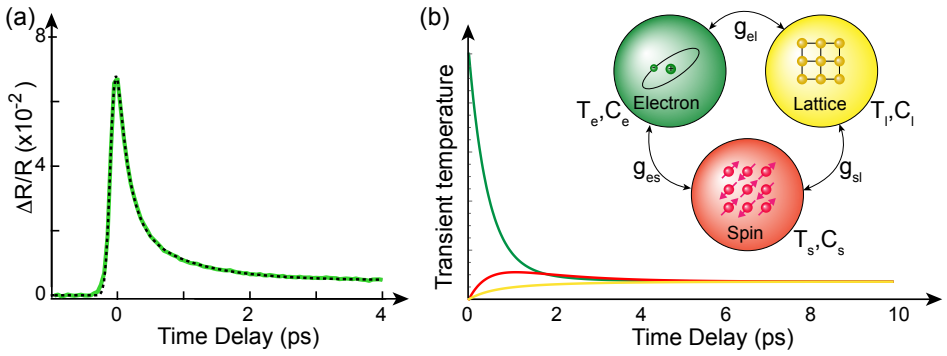

Figure 2.3: (a) A typical differential reflectivity transients overlaid with a fit with Eq.2.4. (b) Simulation of the 3T model.

Another phenomenological way to understand the double-exponential behavior is through the three-temperature (3T) model, which assumes that the material is divided in three subsystems: electrons, spins and lattice, and each subsystem relaxes to equilibrium with coupling to each other g_{es}, g_{el}, g_{sl}. Transient temperatures T_e, T_s, T_l can be defined and each system has temperature-dependent heat capacity C_e, C_s, C_l. Also, only the electronic degree of freedom is excited by light with a source term $P(t)$. Thermalization of each system is thus described by three differential equations (Beaurepaire et al., 1996):

$$\begin{aligned} C_e \frac{dT_e}{dt} &= -g_{es}(T_e - T_s) - g_{el}(T_e - T_l) + P(t), \\ C_s \frac{dT_s}{dt} &= -g_{es}(T_s - T_e) - g_{sl}(T_s - T_l), \\ C_l \frac{dT_l}{dt} &= -g_{el}(T_l - T_e) - g_{sl}(T_l - T_s). \end{aligned} \tag{2.5}$$

A typical solution to the above differential equations exhibits double-exponential form, representing the interaction between different DoF [Figure 2.3(b)]. Based on the rough assumption that $\Delta R/R \propto n \propto T_e$, it would be expected that $\Delta R/R$ also shows the double-exponential decay. Although the 3T model was originally proposed for the interplay between electron, spin, and lattice, it can have many variations. For example, the spin and lattice DoF can be replaced by a set of phonons that are strongly coupled to electrons and another set of phonons that are not (Laurita et al., 2019). In addition, if one channel is shut off, the 3T model goes back to a two-temperature model with single-exponential decay solution. Also note that the assumption of the 3T model that different systems are in internal equilibrium so that a temperature can be defined may not always hold true. A number of recent ultrafast experiments have demonstrated the breakdown of the 3T model in various systems where a nonthermal manipulation of OP is realized (A. d. l. Torre, Dante M. Kennes, et al., 2021).

2.2 Time-Resolved Second Harmonic Generation Rotational Anisotropy

Second harmonic generation (SHG) is the lowest-order degenerate nonlinear optical generation process that can be used to directly determine the symmetry of electronic order and lattice structure by measuring the sample's second order nonlinear optical susceptibility tensor χ (Boyd, 2020; Manfred Fiebig, Pavlov, and Pisarev, 2005; Y. R. Shen, 2003). To experimentally determine the χ tensor elements, a SHG rotational anisotropy (RA) experiment was recently developed, where the whole scattering plane rotates about the sample surface normal and the intensity of the

reflected SHG beam is recorded as a function of the rotation angle ϕ (Darius H. Torchinsky, Hao Chu, et al., 2014; Harter, Niu, et al., 2015). In the past few years, SHG-RA experiments in SCMs not only demonstrated the power of nonlinear optics in refining subtle structural distortions (D. H. Torchinsky et al., 2015) but also uncovered unexpected symmetry breaking induced by exotic electronic orders hidden to other techniques (L. Zhao et al., 2017; Harter, Z. Y. Zhao, et al., 2017).

Physical Mechanism

Electromagnetic waves of an incident light beam propagating through a medium induces electric dipole $\mathbf{P}$, magnetic dipole $\mathbf{M}$, and electric quadrupole $\tilde{\mathbf{Q}}$ moments which can irradiate light to the far field. The source term for radiation is composed of these three terms:

$$\mathbf{S} = \mu_0 \frac{d^2\mathbf{P}}{dt^2} + \mu_0 \bigtriangledown \times \frac{d\mathbf{M}}{dt} - \mu_0 \bigtriangledown \frac{d^2\tilde{\mathbf{Q}}}{dt^2}. \tag{2.6}$$

The leading-order electric dipolar term ($\propto \mathbf{P}$) is typically $\lambda/a \sim 10^3$ times stronger than the magnetic dipolar ($\propto \mathbf{M}$) and electric quadrupolar ($\propto \tilde{\mathbf{Q}}$) terms, where λ and a are the fundamental wavelength of the light and the lattice constant of the crystal.

The induced multipolar moments can be expressed as expansion with respect to the electric $\mathbf{E}$ and magnetic field $\mathbf{H}$ of the incident fundamental light:

$$\begin{aligned}
\mathbf{P}(\omega, \mathbf{2}\omega, ...) \propto & \chi^{PE}\mathbf{E}(\omega) + \chi^{PH}\mathbf{H}(\omega) + \chi^{PEE}\mathbf{E}(\omega)\mathbf{E}(\omega) + \\
& \chi^{PEH}\mathbf{E}(\omega)\mathbf{H}(\omega) + \chi^{PHH}\mathbf{H}(\omega)\mathbf{H}(\omega) + O[(\mathbf{E}(\omega), \mathbf{H}(\omega))^3], \\
\mathbf{M}(\omega, \mathbf{2}\omega, ...) \propto & \chi^{ME}\mathbf{E}(\omega) + \chi^{MH}\mathbf{H}(\omega) + \chi^{MEE}\mathbf{E}(\omega)\mathbf{E}(\omega) + \\
& \chi^{MEH}\mathbf{E}(\omega)\mathbf{H}(\omega) + \chi^{MHH}\mathbf{H}(\omega)\mathbf{H}(\omega) + O[(\mathbf{E}(\omega), \mathbf{H}(\omega))^3], \\
\tilde{\mathbf{Q}}(\omega, \mathbf{2}\omega, ...) \propto & \chi^{QE}\mathbf{E}(\omega) + \chi^{QH}\mathbf{H}(\omega) + \chi^{QEE}\mathbf{E}(\omega)\mathbf{E}(\omega) + \\
& \chi^{QEH}\mathbf{E}(\omega)\mathbf{H}(\omega) + \chi^{QHH}\mathbf{H}(\omega)\mathbf{H}(\omega) + O[(\mathbf{E}(\omega), \mathbf{H}(\omega))^3].
\end{aligned} \tag{2.7}$$

Different χs in the above formulas are optical susceptibility tensors correspond to different linear and nonlinear optical harmonic generation processes. Neumann's principle dictates that the symmetry of the property tensors like χ must contain the symmetry elements of the point group of the crystal (Birss, 1966). By enforcing symmetry constraints on the tensor elements, the number of independent non-zero tensor elements is significantly reduced. Consequently, the underlying electronic and structural symmetries of quantum materials are encoded in the susceptibility tensors. Susceptibility tensors corresponding to the linear process have limited sensitivity to the underlying symmetry because different point groups corresponding to

the same crystal family harbor identical tensor form. On the contrary, albeit empirically weaker, nonlinear responses with higher-rank susceptibility tensors possess much better symmetry resolution because different point groups harbor different tensor forms. SHG, as the leading-order nonlinear process, is thus powerful in determination of crystalline and electronic symmetries.

Among all SHG radiation processes as shown in Eqs.2.6 and 2.7, the leading-order term is electric dipolar (ED) radiation:

$$P_i(2\omega) = \chi_{ijk}^{PEE} E_j(\omega) E_k(\omega). \tag{2.8}$$

Note that the ED process vanishes in the systems that respect inversion symmetry: an inversion operation in these systems will flip the direction of both polar vectors P and E but leave χ the same. Therefore, the above formula becomes $-P = \chi EE$ and the only possible solution is that all the elements of χ vanish. The extreme sensitivity to inversion symmetry makes ED SHG an adequate probe for surfaces or interfaces where the inversion symmetry is naturally broken. ED SHG is also a sensitive probe to phase transitions with spontaneous inversion symmetry breaking like paraelectric-to-FE transition.

The χ_{ijk}^{PEE} can also be calculated in a quantum mechanic picture through second-order time-dependent perturbation theory (Boyd, 2020):

$$\chi_{ijk}^{PEE} \propto \sum_k \sum_{mf} \frac{\langle g|P_i|f\rangle\langle f|P_j|m\rangle\langle m|P_k|g\rangle}{(E_f - E_g - 2\hbar\omega - i\gamma_{fg})(E_m - E_g - \hbar\omega - i\gamma_{mg})} + \ldots \tag{2.9}$$

which involves two ED transitions at $\hbar\omega$ from the initial state g to the intermediate state m and then to the final state f. Ensuing the two-photon adsorption, a single-photon ED emission at $2\hbar\omega$ from f to g occurs. The energy difference between different levels are given by $E_{m,f} - E_g$, and the damping rate for different transitions are represented by $\gamma_{mg,fg}$. With known band structure, the tensor can be calculated and resonant optical transitions dominate the response when $E_f - E_g = 2\omega$. Due to the existence of damping terms near resonance, all the tensor elements are in general complex.

Although ED SHG vanishes in the presence of inversion symmetry, higher-order SHG processes are not hindered. There are four terms in the absence of bulk ED process that can produce SHG radiation. The first one is the magnetic dipolar radiation of the first kind (MD1) that still comes from the the electric dipole term in Eq.2.7 but involves both magnetic and electric fields:

$$P_i(2\omega) = \chi_{ijk}^{PEH} E_j(\omega) H_k(\omega). \tag{2.10}$$

The second one is the magnetic dipolar radiation of the second kind (MD2) which arises from the magnetic dipole term in Eq.2.7:

$$P_i(2\omega) \propto [\nabla \times \mathbf{M}(2\omega)]_i = \epsilon_{iab}\partial_a \chi^{MEE}_{bjk} E_j(\omega) E_k(\omega). \tag{2.11}$$

where ϵ_{ijk} is the Levi-Civita symbol. The above two terms exist in the presence of inversion symmetry because both $\mathbf{M}$ and $\mathbf{H}$ are axial-vector and thus remain unchanged under inversion operation.

The third possibility is the electric quadrupolar (EQ) radiation which in general comes from the electric quadrupole term in Eq.2.7:

$$P_i(2\omega) \propto [\nabla \tilde{\mathbf{Q}}(2\omega)]_i = \chi^{QEE}_{ijkl} E_j(\omega) \partial_k E_l(\omega). \tag{2.12}$$

However, note that this process also include MD1, since the antisymmetric part with regard to the last two indices k, l, $\partial_k E_l(\omega) - \partial_l E_k(\omega)$ gives $H(\omega)$, and thus only the symmetric part with regard to the last two indices corresponds to the EQ process:

$$P_i(2\omega) = \chi^{QEE}_{ij[kl]} E_j(\omega) \partial_{[k} E_{l]}(\omega). \tag{2.13}$$

The fourth possible source is the surface ED term, which takes the exactly same form of Eq.2.8, arising from the necessary inversion symmetry-breaking at the sample surface. The surface ED term is in principle orders of magnitude smaller than the bulk ED term, because the surface effect is only evident in topmost layers but the measured bulk ED contribution is contributed by all the layers within the penetration depth of the fundamental or SHG light.

The SHG intensity of the four different sources can be in principle comparable, but one can distinguish them by measuring the RA pattern since the susceptibility tensor is different for distinct processes.

SHG can also be applied to magnetic systems with time-reversal (TR) symmetry breaking. For the nonmagnetic 32 point groups, the tensors are even under TR operation and are called $i-$type tensors. On the other hand, among the 122 magnetic point groups, if the tensors couple linearly to the magnetic OP, they will change sign under TR operation and are called $c-$type tensors (Boyd, 2020). For one point group, its structural $i-$type tensors and magnetic $c-$type tensors usually have different forms. Also note that all the aforementioned processes can be both $i-$type or $c-$type. In magnetic materials, the interference between the magnetic and structural SHG can be exploited to determine the magnetic moment direction and image magnetic domains (Manfred Fiebig, Pavlov, and Pisarev, 2005; Darius H. Torchinsky and David Hsieh, 2017)

Experimental Setup

SHG-RA experiments were traditionally carried out by rotating the sample about its surface normal with fixed optics. The new approach to rotating the scattering plane with fixed sample overcomes several problems include beam walking on the sample and precession of the reflected beam. Furthermore, it enables the experiment to be carried out at cryogenic temperatures, in magnetic fields, under high pressure, etc (Darius H. Torchinsky, Hao Chu, et al., 2014; Harter, Niu, et al., 2015).

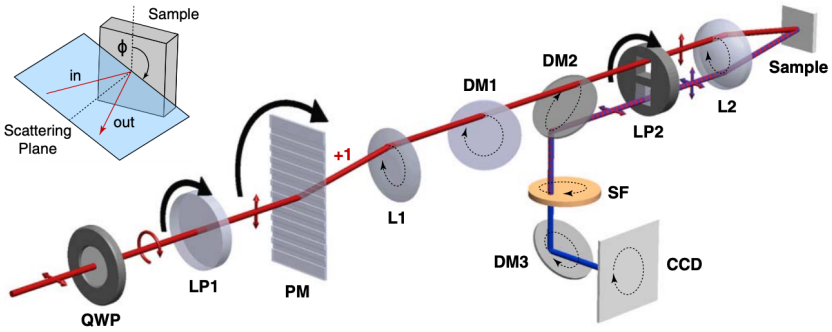

Figure 2.4: Schematic layout of the SHG-RA experimental setup. The figure is adopted from Harter, Niu, et al., 2015.

The principle of SHG-RA remains the same: recording the specular reflected SHG signal intensity as a function of the rotation azimuth angle ϕ. Since the light polarization can be either parallel (P) or perpendicular (S) to the scattering plane, a total of four different polarization geometries including $P_{in} - P_{out}$, $P_{in} - S_{out}$, $S_{in} - P_{out}$, and $S_{in} - S_{out}$ can be chosen. With global fitting of a single susceptibility tensor in four channels, the underlying symmetry of the material can be uniquely determined.

A schematic layout of the new SHG-RA setup is shown in Figure 2.4 (Harter, Niu, et al., 2015). Before entering the setup, the probe beam goes through a HWP and a LP for power control. The linearly-polarized probe beam first goes through a well-aligned QWP and becomes perfectly circularly-polarized. It then goes through a LP1 so that either P_{in} or S_{in} is selected and later goes through a telescope with a fused silica binary phase mask (PM) lying slight off-focus, which works like a diffraction grating. PM splits the beam into many diffracted order and the +1 order is selected. It is later collimated by a lens L1 and propagates parallel to the optical axis of the whole setup, while the other diffracted beams are blocked. The probe beam is focused onto the sample by an objective lens L2. The sample should be placed at the focal point of the objective with its surface normal coinciding with

the optical axis to ensure a constant incident angle θ_i when the scattering plane is rotated. The specular reflected probe beam goes through LP2 such that either P_{out} or S_{out} is selected. Note LP2 is placed on a special mount with two off-centered holes: one for accommodating LP2 and the other for transmission of the incident light. The reflected beam is later picked up by two dichroic mirrors (DM2 and DM3) in a periscope geometry and the unwanted fundamental signal is filtered out by a pair of longpass filters and a pair of bandpass filters before going into the electron multiplying CCD camera. Note that an additional DM1 is placed in the beam line. This is because the incident fundamental beam also transmits through DM2, whose intensity will oscillate as the scattering plane rotates in accordance with the Fresnel equations. DM1 is required to compensate for this effect.

LP1, PM, and the special mount holding LP2 are simultaneously rotated to achieve a rotation of scattering plane. The incident beam will sweep out a cone after the PM and draw circles on the optics and CCD as it rotates. Instead of stepping and holding ϕ at discrete values and recording the SHG intensity, we rotate the whole setup with a motor at 2 Hz to avoid long-time low-frequency noise stemming from fluctuations in laser power and beam pointing and record the full SHG-RA pattern at each time delay.

A pump beam can be incorporated into the setup similar to the time-resolved reflectivity measurement but at oblique incidence with incident angle larger than θ_i, otherwise the directing mirror of the pump may block the probe beam as the setup rotates. Note that wise choices of pump incident angle and additional spectral filters may be needed to avoid pump-induced SHG and pump-probe sum frequency generation getting into CCD. The white light imaging setup can also be included in the setup identical to the time-resolved reflectivity measurement to assist the alignment.

Data Analysis

A normal dataset we obtain with SHG-RA measurement is polar plots of SHG intensity as a function of ϕ in four different polarization configurations. To fit the data, we need to first determine a point group the quantum material potentially respects. Normally by investigating its lattice and magnetic structure, a structural and a magnetic point group can be individually fixed. Note that if unknown symmetry breaking occurs, a subgroup of the structural or magnetic point group should be used.

After the underlying point group is known, we should determine the susceptibility

tensor elements. Tensors for different point group and SHG processes can be found on Bilbao crystallographic server: https://www.cryst.ehu.es/. Note that additional symmetry constraints of different SHG processes render part of the tensor elements interchangeable. More specifically, for ED (including surface ED) process, the last two indices are interchangeable, i.e. $\chi^{PEE}_{ijk} = \chi^{PEE}_{ikj}$ because the two $E-$field share the same source. Using the language of Jahn symbols, the intrinsic symmetry of ED process is denoted as $V[V2]$, where V indicates the polar vector ($\mathbf{P}, \mathbf{E}$); for MD1, no additional symmetry is applied and the symmetry is $V2eV$, where eV indicates the axial vector ($\mathbf{M}, \mathbf{H}$); for MD2, the last two indices are interchangeable, i.e. $\chi^{MEE}_{ijk} = \chi^{MEE}_{ikj}$, and the intrinsic symmetry is $eV[V2]$; for EQ, in most cases, we can substitute ∂_j with k_j where $\mathbf{k}$ is the propagation vector. Note that this substitution is not valid in the rare cases where the incident beam contains both S or P polarization and ∂_j is taken along z and the material is anisotropic (Bloembergen and Pershan, 1962). Then the second and fourth indices are interchangeable, i.e. $\chi^{QEE}_{ijkl} = \chi^{QEE}_{ilkj}$. Since the last two indices are also interchangeable, the intrinsic symmetry of EQ is $V[V3]$. For magnetic point groups, if the tensors are $c-$type, an additional time-reversal constant a should be added in front of the Jahn symbols. By choosing the correct symmetry symbols on Bilbao server, the corresponding tensor to different SHG processes can be obtained. Bilbao normally set the $z-$ axis to the axis with the highest rotation symmetry of the point group, but note that especially for point groups with low symmetries, this may not remain true. Therefore, it would be safer to apply symmetry operations included in the point group to the tensor and check if it remains the same. If not, $x-$, $y-$, and $z-$axes may need to be swapped.

Note that not all the sample surface we measured are the surface harboring the highest symmetry. The next step is thus to rotate the tensor from the crystallographic coordinates to lab coordinates, where the surface normal is along $\mathbf{z} = (0, 0, 1)$. Assume the surface normal is along $[hkl]$, a normal unit vector can be defined as $\mathbf{u} = \mathbf{r}/|\mathbf{r}|$, where $\mathbf{r} = h\mathbf{a} + k\mathbf{b} + l\mathbf{c}$. We can write out the rotation matrix as:

$$R = I + v_{\times} + \frac{1 - \mathbf{z} \cdot \mathbf{u}}{|v|^2} v_{\times}^2, \tag{2.14}$$

where $\mathbf{v} = \mathbf{z} \times \mathbf{u}$, and the skew-symmetric cross product matrix of $\mathbf{v}$ is expressed as

$$v_{\times} = \begin{pmatrix} 0 & -v_3 & v_2 \\ v_3 & 0 & -v_1 \\ -v_2 & v_1 & 0 \end{pmatrix}. \tag{2.15}$$

So the tensor (e.g. a rank-3 tensor) can be expressed as

$$\chi^{lab}_{ijk} = R_{ii'}R_{jj'}R_{kk'}\chi^{crst}_{i'j'k'}. \tag{2.16}$$

Then we can write out the tensor as the scattering plane rotates with a rotation matrix:

$$R^{\phi} = \begin{pmatrix} \cos\phi & -\sin\phi & 0 \\ \sin\phi & \cos\phi & 0 \\ 0 & 0 & 1 \end{pmatrix}. \tag{2.17}$$

So the tensor (e.g. a rank-3 tensor) can be expressed as

$$\chi_{ijk} = R^{\phi}_{ii'}R^{\phi}_{jj'}R^{\phi}_{kk'}\chi^{lab}_{i'j'k'}. \tag{2.18}$$

Then with $\mathbf{k} = (\sin\theta_i, 0, -\cos\theta_i)$, the incident $P-$polarized light with $E_{P,in} = (\cos\theta_i, 0, \sin\theta_i)$, $H_{P,in} = (0, -1, 0)$, and incident $S-$polarized light with $E_{S,in} = (0, 1, 0)$, $H_{S,in} = (\cos\theta_i, 0, \sin\theta_i)$, we can calculate $P_i(2\omega)$ in each channel of different SHG processes. The conversion from $\mathbf{P}(2\omega)$ to $\mathbf{E}(2\omega)$ at the sample-vacuum interface requires solving the Fresnel and Maxwell's equations under correct boundary conditions (Bloembergen and Pershan, 1962). For simplicity, we assume our measured reflected SHG intensity $I(2\omega)_{S,out} \propto |P_y(2\omega)|^2$ and $I(2\omega)_{P,out} \propto |-P_x(2\omega)\cos\theta_i + P_z(2\omega)\sin\theta_i|^2$. After obtaining the functional form of $I(2\omega)$ in all the four polarization geometries with SHG-RA, we can global-fit these four channels simultaneously. Note that an additional angle ϕ_0 may be needed to account for the misalignment between the lateral crystal axis and lab coordinates. To get absolute values of different tensor elements, a comparison with SHG intensity of a standard sample like GaAs under the exactly same condition is needed.

2.3 Coherent Phonon Spectroscopy

As we discussed in Chapter I Section 1.1, coherent OP oscillation occurs in a large variety of systems with different orders. Coherent OP vibration modulates $\tilde{n}$ periodically, so such motion can be monitored in many optical observables and measured with time-resolved diffraction, trARPES, time-resolved reflectivity and absorption, time-resolved MOKE, transient grating, time-resolved nonlinear spectroscopy, and so on. In this section, we focus on the most ubiquitous collective excitation of lattice, Raman-active phonon. The method to monitor and investigate coherent phonon oscillations is known as coherent phonon spectroscopy.

Physical Mechanism

Raman-active phonons can be launched in general with at least four methods:

- Ionic Raman scattering (IRS), where a particular Raman active mode is excited due to the anharmonic coupling to an IR active phonon that is resonantly excited by a mid-IR pulse (Först et al., 2011).

- Transient depletion field screening (TDFS), where in III-V semiconductors like GaAs, photo-excited electrons and holes in the depletion region drift in opposite directions which induces a screening of the depletion field. The change of the electric field launches motion of positive and negative ions (Pfeifer et al., 1992).

- Displacive excitation of coherent phonon (DECP), where the creation of photo-carriers instantaneously quenches the PES and shifts its minimum. Since the lattice cannot adiabatically follow the prompt change of PES and remains at its equilibrium value, an effective displacive force will be imparted to the lattice and a coherent oscillation of the fully symmetric $A_{1(g)}$ mode will be initiated (Zeiger et al., 1992; Kuznetsov and Stanton, 1994). Some variations include spin-DECP (Ron et al., 2020), where the ultrafast enhancement of magnetic exchange interaction displacively excites phonons.

- Impulsive stimulated Raman scattering (ISRS), where a stimulated Raman scattering occurs so any phonon that satisfies Raman selection rule can be triggered. To realize ISRS, the pulse duration is required to be shorter than the phonon period such that the bandwidth of the pump is larger than the phonon energy (Dhar, Rogers, and Nelson, 1994).

Since the latter two mechanisms driven by EPC govern the coherent phonon generation in most materials, we will elaborate on the similarity and disparity of these two mechanisms in the following.

A general equation of motion of phonon Q can be expressed as a driven damped harmonic oscillation:

$$\frac{d^2Q(t)}{dt^2} + 2\gamma\frac{dQ(t)}{dt} + \omega_0^2 Q(t) = F(t). \tag{2.19}$$

Phonons have finite lifetime $1/\gamma$ on the order of several to hundreds of ps after light excitation. The scattering to lower-energy phonons through anharmonic coupling, scattering with impurities, and scattering to electrons near the Fermi level in metals compose the main decaying channels of optical phonons.

If one assumes a displacive force with $F(t) = I_0 H(t)$, we have (O. V. Misochko and Lebedev, 2016):

$$Q(t) \propto Im(\epsilon) I_0 H(t) \{1 - e^{-\gamma t} [\cos\left(\sqrt{\omega_0^2 - \gamma^2} t\right) + \frac{\gamma}{\sqrt{\omega_0^2 - \gamma^2}} \sin\left(\sqrt{\omega_0^2 - \gamma^2} t\right)]\}. \tag{2.20}$$

If one assumes an impulsive force $F(t) = I_0 \delta(t)$, we have:

$$Q(t) \propto \chi^R I_0 H(t) e^{-\gamma t} \sin\left(\sqrt{\omega_0^2 - \gamma^2} t\right), \tag{2.21}$$

where the Raman tensor χ^R is proportional to the partial derivative of the dielectric tensor with respect to the phonon coordinate $\frac{\partial \tilde{\epsilon}}{\partial Q}$ and can be expressed as (Stevens, Kuhl, and Merlin, 2002):

$$\chi^R(\omega, \omega \pm \omega_0) \propto g[\frac{dRe(\epsilon)}{d\omega} + 2i\frac{Im(\epsilon)}{\omega_0}], \tag{2.22}$$

where g is the EPC constant. When the pump photon energy is in the transparent region, $\frac{dRe(\epsilon)}{d\omega} \gg \frac{Im(\epsilon)}{\omega_0}$ and the force is purely impulsive, while if the pump energy is resonant with absorption peaks, $\frac{dRe(\epsilon)}{d\omega} \ll \frac{Im(\epsilon)}{\omega_0}$ and the force can be both impulsive and displacive.

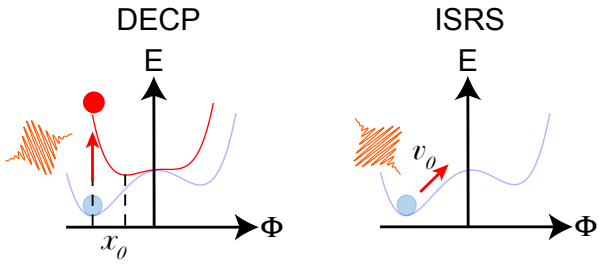

Figure 2.5: Schematic of DECP and ISRS mechanisms.

Several aspects are revealed by the above formulas. First, DECP depends on carrier excitation and thus only dominates when resonant electronic transition occurs. On the other hand, ISRS can occur with any pump energy but exclusively dictates the generation of optical phonons when the pulse photon energy is off-resonant or transparent to the material. Second, DECP imparts a displacive force with shift in PES minimum, while ISRS imparts an impulsive force with finite momentum transfer (Figure 2.5). Third, only $A_{1(g)}$ modes at $q = 0$ can be launched by DECP, while all Raman-active phonons whose energy is smaller than the bandwidth of the pump pulse can be generated by ISRS. Fourth, the DECP-launched phonon

exhibits a $\cos(\omega_0 t)$ oscillation if the damping γ is infinitesimal, while ISRS-driven phonon possesses a $\sin(\omega_0 t)$ form (O. V. Misochko and Lebedev, 2016). Fifth, the amplitude of the phonons generated by both mechanisms scale linearly with the pump intensity I_0. Owing to the similarities and differences, the community has not reached a consensus on whether Raman formalism constitutes a unified picture to describe both impulsively and displacively launched phonons. (Kuznetsov and Stanton, 1994; Garrett et al., 1996; Stevens, Kuhl, and Merlin, 2002; Melnikov, O. Misochko, and Chekalin, 2011; O. V. Misochko and Lebedev, 2016)

Since $\Delta R \propto \frac{\partial R}{\partial \tilde{\epsilon}} \frac{\partial \tilde{\epsilon}}{\partial Q} Q$, and $\chi^R = \frac{\partial \tilde{\epsilon}}{\partial Q}$ determines the Raman scattering amplitude at the probe frequency ω, the coherent phonon will induce a periodic modulation of transient reflectivity on top of the electronic response and thus can be measured in time-domain techniques. The amplitude, frequency, lifetime, and phase measured in transient reflectivity also reflect their true values.

The validity of the aforementioned discussion can also be applied to a broadband probe with tunable photon energies resonant with different charge-excitation peaks, illustrating the energy-dependent Raman tensor elements of different phonon modes.

According to the symmetry of different Raman modes, they can be also measured with probes of different polarization configurations. For conventional (isotropic) transient reflectivity measurement, only the phonons with nonzero diagonal Raman tensor elements can be detected, and in most cases the $A_{1(g)}$ modes dominate. To measure the low-symmetry Raman phonons, anisotropic transient reflectivity measurement is required, which can be conducted in a way similar to an optical Kerr effect measurement.

Data Analysis

An example of differential reflectivity traces with multiple coherent phonon oscillation is displayed in Figure 2.6(a). After one subtracts the electronic background by fitting it with a double-exponential decay, the oscillatory part can be isolated [Figure 2.6(b)]. The beating pattern suggests the coexistence of multiple phonons.

To study the phonon amplitude, frequency, lifetime, and phase, in principle we can fit the time traces with multiple damped oscillations:

$$\frac{\Delta R}{R} = \sum_i B_i \exp\left(-\frac{t}{\tau_i}\right) \cos\left(2\pi \nu_i t + \phi_i\right), \tag{2.23}$$

where B_i, $\tau_{ph,i}$, ν_i, and ϕ_i are the amplitude, lifetime, frequency, and phase of the $i-$th phonon [Figure 2.6(b)].

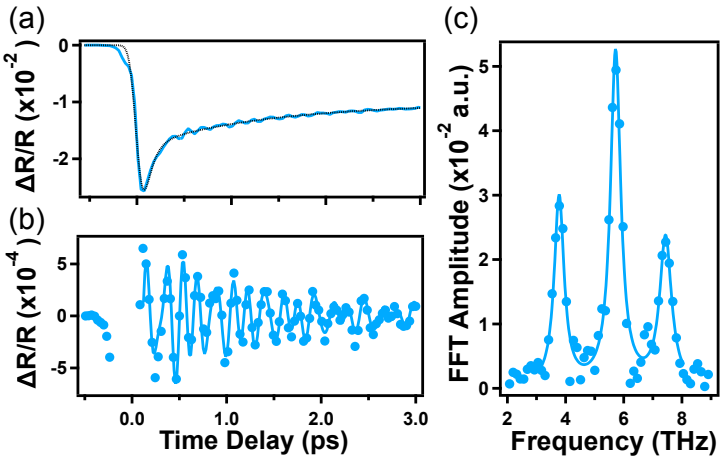

Figure 2.6: Example of coherent phonon spectrum obtained from transient reflectivity measurement. (a) Transient reflectivity curve with double-exponential fit to the background overlaid. (b) Background-subtracted transient reflectivity curve with multi-sinusoid fit overlaid. (c) FFT spectrum of (b) with multi-Lorentzian fit overlaid.

However, in many cases, the number of coexisting phonons surpasses the threshold where a time-domain fitting is reliable. Equivalently, we can perform fast Fourier transform (FFT) to the background-subtracted reflectivity transient and fit the peaks in the FFT spectrum [Figure 2.6(c)]. A damped sinusoidal oscillation in the time domain transforms into a Lorentzian in the frequency domain. Thus, we can fit the FFT data with multiple Lorentzians with the corresponding parameters as defined above:

$$\sum_i \frac{B_i}{(\nu - \nu_i)^2 + (\frac{1}{2\pi\tau_i})^2}. \tag{2.24}$$

Note that although the phase information is missing in FFT amplitude, it can be retrieved through a complex FFT analysis.

The symmetry of different mode can be determined by a RA measurement reminiscent of the SHG-RA. The difference is that long time traces at select angles are taken instead of scanning angles at discrete time delays. Also normal incidence of probe is favored and thus only two polarization geometries exist: the incident probe is parallel or crossed to the reflected probe. By recording reflectivity transients at each angle and applying FFT, the peak intensity of different modes as a function of scattering angle is recorded. The Raman tensor of different modes of different point groups can be found on Bilbao Crystallographic Server. With similar fitting procedures similar to SHG-RA analysis, the Raman tensor of different modes can

be determined.

2.4 Miscellaneous

Apart from powerful ultrafast probes, many factors will determine the success of an ultrafast experiment. In this section, details of generation of pump light, general sample preparation procedures, spot size measurement, pulse duration and spectrum measurement, pulse stretching and compression techniques, and calibration of optical heating will be discussed.

Multi-Color Pump Light Generation

To generate multi-chromatic light pulses, a state-of-the-art Ti:sapphire femtosecond ultrafast laser (Coherent Astrella) is used for the majority of the projects covered in this thesis. The output light is centered at 800 nm at 1 kHz repetition rate with a pulse duration around 35 fs. Out of the maximal power of 5 W, 3.5 W is dumped into an optical parametric amplifier (OPA1, Light Conversion TOPAS), which can generate pump light ranging from 1160 nm to 2600 nm. The rest 1.5 W is split into two arms, with 1 W dumped into another OPA2 to generate probe light with the same wavelength range and another 0.5 W is used to generate THz pulse ranging from 0.5-6 THz with nonlinear crystal ZnTe and GaP (Figure 2.7). The maximal efficiency of the pump OPA1 occurs at around 1400 nm with a peak power of 1 W. The OPA1 beam can alternatively go through a differential frequency generation (DFG) module to generate mid-IR pump with wavelength up to 15 μm.

The core part of the laser is the regenerative amplifier based on Coherent Legend Elite, where weak pulses are amplified within a Ti:sapphire gain medium. Two significant beams enter the regenerative amplifier: the seed laser beam with the weak pulses to be amplified and the pump laser beam which induces the population inversion and generates lasing. Coherent Vitara serves as the seed laser. This mode-locked oscillator with a repetition rate of 80 MHz is pumped by the Coherent Verdi-G series, a continuous-wave (cw) diode-pumped green laser centered at 532 nm. Revolution is the diode-pumped, intra-cavity doubled, Q-switched Nd:YLF pump laser. Operating at 527 nm and 1 kHz repetition rate, it provides power to the amplifier module.

Note that before the seed pulse is sent to amplification, it is stretched temporally using a pair of diffraction gratings. This technique, dubbed chirped pulse amplification (CPA), decreases the pulse peak intensity to avoid damage or nonlinear effect in the gain medium. After the stretched pulse is sent into the amplifier, an electro-optical

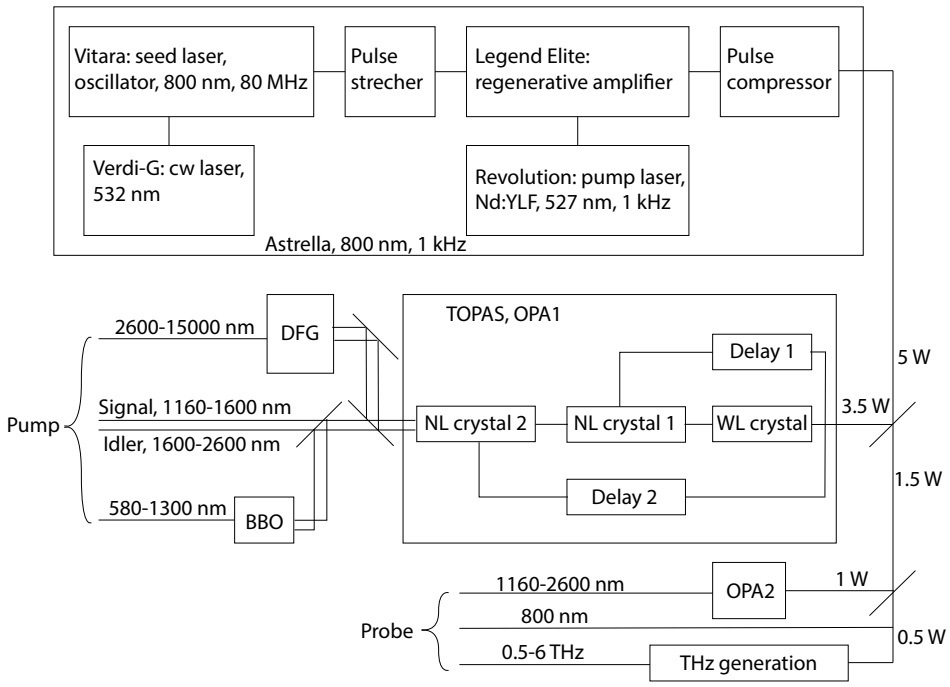

Figure 2.7: Schematic layout of the Te:sapphire laser and OPA.

device called a Pockels cell, which can rotate the light polarization by $\pi/2$ when activated by voltage, controls the cycle number of amplification and reduces the repetition rate to 1 kHz. The amplified pulse is compressed back with another pair of diffraction gratings to reach short time duration and high peak intensity after it exits the amplifier.

The majority of laser power enters OPA1. The principle of OPA is optical parametric generation process $\omega_0 = \omega_s + \omega_i$, where one photon of fundamental frequency ω_0 is down-converted into a signal beam of a relatively higher frequency ω_s and an idler beam of a relatively lower frequency ω_i. The output frequency is controlled by tuning the phase matching condition and time delay between pulses in nonlinear (NL) crystals. Practically in our setup, the incident pulse is split into three beams. 4% of the beam is focused on a white-light (WL) generation crystal (sapphire) which produces WL continuum whose bandwidth contains the signal wavelength. 16% of the beam and the WL are then focused on NL crystal 1 where pre-amplification occurs. The output signal and idler wavelengths can be controlled by varying the time delay between the 800 nm and the WL (Delay 1) and by rotating the NL crystal 1 to satisfy the phase matching condition. After the pre-amplification, only the pre-amplified signal is selected and directed to NL crystal 2, where it meets the rest

80% of 800 nm beam and the main amplification occurs. Again Delay 2 and rotation of NL crystal 2 can control the amplification efficiency.

Either signal or idler beam can be used as the pump. Alternatively, they can enter the non-collinear differential frequency generation (NDFG) to generate mid-IR pumps through $\omega_{DFG} = \omega_s - \omega_i$. The two beams are split by a dichroic mirror and focused non-collinearly onto a GaSe NL crystal. To change the DFG wavelength, both the angle between the signal and the idler beams and the angle of the DFG crystal need to be changed.

We can also use NL crystal like $\beta-BaB_2O_4$ (BBO) to double the frequency of the signal and idler to extend our pump wavelength lower limit from 1160 nm down to 580 nm. However, note that only when the type-I phase-matching condition is met, i.e. $n_o(\omega) = n_e(2\omega, \theta)$, where o and e represents ordinary and extraordinary light, the SHG process is most efficient. Therefore, a correct cut θ of the BBO crystal is needed. Given a specific cut, one can also change the angle of incidence and the azimuthal angle of BBO to optimize the SHG output power.

Sample Preparation

The sample is mounted on customized copper sample holders using Torr Seal epoxy or silver epoxy for good thermal contact. To cure the epoxy, the sample should either be heated at a moderate temperature (better no higher than 100 °C) for 1 h or kept at room temperature for over 12 h depending on the sample sensitivity and epoxy type.

For most of the samples we studied, we cleave or polish the sample just before putting it into the cryostat to get a fresh and smooth surface for optical measurement. For quasi-2D or 1D materials, one can gently stick a piece of scotch tape on the top surface of the sample and quickly remove the top layers to get a shiny surface; for 3D materials, one can stick a small ceramic post on the top of the sample surface with silver epoxy. After the epoxy cures, one should quickly knock the post off to get a fresh surface; for uncleavable materials, the sample can still be polished. The sample holder should be first mounted on a specific polishing pack with wax. Polishing diamond lapping films with diamond grit of 10 micron (μm), 5 μm, and 1 μm are used in sequence to get a mirror-like finish of the sample surface. We then melt the wax to retrieve the sample holder.

The customized sample holder has two “lips” sticking out on the face where we mount sample. Immediately after the fresh surface of the sample is prepared, we

normally stick a cover slip on top of these lips with N grease for low temperature measurement, because according to our experience significant absorbate condensation occurs below 250 K in various SCMs which may dramatically modulate the sample's optical response. The existence of the cover slip can dramatically reduce the condensation. Note that the N grease should not be used (and is not needed) in high temperature measurement to avoid contamination caused by its evaporation. Also note that the DFG pump pulses may not transmit the cover slip.

We then screw the sample holder onto the cryostat (Janis ST-500) coldfinger with indium foil between them for better thermal contact. Before pumping down, one can further put some N grease on the O-ring between the window and the cryostat to get a better seal. The cryostat chamber is then pumped down to 10^{-8} – 10^{-7} torr overnight by a vacuum pump (Pfeiffer HiCube 80 Eco). The whole cryostat is placed on a customized 5-axis mount, which can be used to align the sample surface normal direction with 2 rotation DoF and sample position with 3 translation DoF. The transfer lines to transfer cryogenic liquid is then connected to the cryostat.

Spot Size Measurement

To get the correct fluence, the spot size of the pump and probe beams at the focal point where the sample is placed should be accurately measured using a knife edge. We mount a knife edge on a 2-axis translation stage with one for moving the knife edge along the optical (z-) axis to find the sample location and another for moving the knife edge laterally parallel to the sample surface (x-axis) to cut the beam. A power meter is placed after the knife edge. One should first quickly move the translation stage along the z-axis until the pump and probe disappear simultaneously when moving x-axis. This indicates the current z-axis position is the focal point of the objective and the position where the sample is measured. One should then slowly move the translation stage along x-axis and record the transmitted power of both pump and probe beams as a function of the lateral position of the knife edge as it cuts the beam. Assuming a Gaussian beam profile of the intensity at focus $I = I_0 \exp\left[\frac{(x-x_0)^2}{2\sigma^2}\right]$, the measured power can be fit with an error function $P = P_0 \frac{1+\mathrm{erf}\,(\frac{x-x_0}{\sqrt{2}\sigma})}{2}$ and the FWHM is given by $2\sqrt{2\ln 2}\sigma$. A typical spot FWHM ranges from 50 to 150 μm.

Pulse Duration and Spectrum Measurement

Both the temporal and spectral profile of the pump and probe beams can be measured using frequency-resolved optical gating (FROG). FROG is based on a spectrally-resolved autocorrelation method and a phase-retrieval algorithm. Since a SHG medium only produces signal when both pulses are temporally and spatially overlapped (i.e. "optical gating"), varying the delay between the pulse and its copy and measuring their sum-frequency generation (SFG) signal at each delay yields an estimate of the pulse length. Instead of just recording the intensity, FROG measures the spectrum of the SFG signal at each time delay (Andrew Marc Weiner, 2009):

$$I_{SFG}(\omega, t) = |\int_{-\infty}^{+\infty} E(\tau)E(\tau - t)e^{-i\omega\tau}d\tau|^2. \tag{2.25}$$

Technically, the incident beam is split into two arms with a 50:50 beam splitter when it gets into the FROG. One arm has a fixed optical path and the other arm goes through a retroreflector on a translation stage so the time delay between the two arms can be tuned. The two reflected beams are then focused at the same spot on a BBO crystal, and their SFG intensity is measured by a spectrometer as a function of time delay. Using a phase-retrieval algorithm, the temporal and spectral information of the beam can be retrieved. For a pulse with Gaussian time intensity profile, the product of its pulse duration and bandwidth has a minimum of $\Delta t \Delta \nu \geq 0.44$. For a 50 fs beam centered at around 800 nm, its minimal bandwidth is around 20 nm.

Pulse Stretching and Compression

Angular dispersion of a multicolor light can be enabled by a prism, which is a first-order dispersive effect since the difference in deflection angle is determined by $\frac{dn}{d\lambda}$. When a multicolor light transmits any medium, a second-order dispersive effect called group velocity dispersion $GVD = \frac{d(1/v_g)}{d\omega} = \frac{d^2k}{d\omega^2} = \frac{\lambda^3}{2\pi c^2}\frac{d^2n}{d\lambda^2}$ will occur. Because the relatively "red" light moves faster than the relatively "purple" light, which is also called positively chirped, a phase delay characterized by group delay dispersion $GDD = \frac{d^2\psi}{d\omega^2} = GVD \cdot L$ can be generated, where L is the light propagation distance inside the medium. For a Gaussian pulse, the time-stretching can be calculated by $\sigma_{out} = \sigma_{in}\sqrt{1 + (\frac{4ln2 \cdot GDD}{\sigma_{in}^2})^2}$ (Andrew Marc Weiner, 2009).

Since almost all the materials will cause a positive chirp, the pulse will be dramatically broadened in time after it transmits several optics and the time resolution is reduced. Fortunately, a negative chirp can be produced with the help of a pair of prisms or gratings, dubbed pulse compressor. The principle is based on the

angular dispersion: the relatively "red" light will go through a longer optical path than the relatively "purple" light inside the compressor to generate a negative chirp compensating the positive chirp induced by the other optics.

The prism compressor is composed of two identical prisms (P1 and P2) that are placed parallel to each other on two rotation mounts. The second prism should also be placed on two translation stages so that the relative position between the two prisms can be tuned. A folding mirror (M) is placed after the second prism to reflect the beam back into the prism pairs such that the final beam leaves the setup almost at the same spot where it comes in. The schematic layout of the whole setup can be found in Figure 2.8.

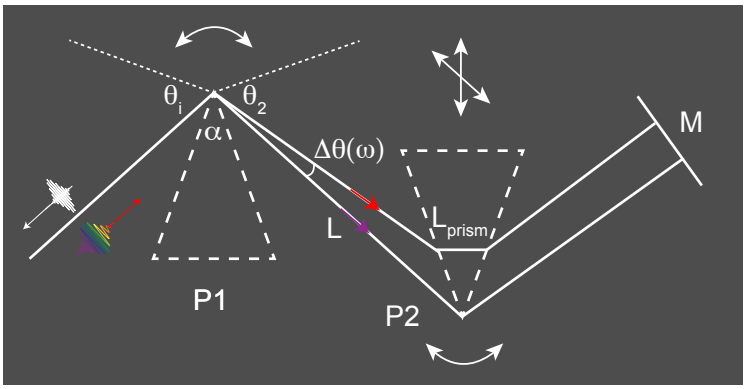

Figure 2.8: Schematic layout of a prism compressor.

We assume that the light pulse goes into the first prism at θ_i around the apex of the first prism with an apex angle α. Light of different colors will have a slight different outgoing angle $\theta_2(\omega)$ with a difference $\Delta\theta(\omega)$. By rotating P1, we can have $\theta_2 = \theta_i$, where the minimal deviation angle is reached. If the prism apex angle can be chosen to satisfy $\alpha = 2\arcsin(\sin(\arctan(n))/n)$, a Brewster's angle for both input and output beams, i.e. $\tan(\theta_2) = \tan(\theta_i) = n(\omega)$, can be realized simultaneously, yielding the least loss with $p-$polarized incident light and the least astigmatism. We then rotate P2 in the downstream with the same requirement and make the light reflect back in the same optical path after it hits M by rotating M. Based on these experimental conditions, the phase compensation generated by the prism pair is expressed as: $GDD = -\frac{2\lambda^3}{2\pi c^2}\{4L\cos\Delta\theta(\frac{dn}{d\lambda})^2 - 2L\sin\Delta\theta[\frac{d^2n}{d\lambda^2} + (2n - \frac{1}{n^3})(\frac{dn}{d\lambda})^2]\}$, where L is the apex-to-apex distance (Andrew Marc Weiner, 2009). Since $\Delta\theta$ is small, the formula can be simplified as: $GDD = -\frac{\lambda^3}{\pi c^2}4L(\frac{dn}{d\lambda})^2$. Also recall that in the previous calculation we ignore the GDD inside the prisms which will induce a positive chirp. Including this factor we have: $GDD = -\frac{\lambda^3}{\pi c^2}[4L(\frac{dn}{d\lambda})^2 + \frac{d^2n}{d\lambda^2}L_{prism}]$,

where L_{prism} is the distance light travels inside one pair of prisms. By further tuning L and L_{prism} with the two translation stages that controls the position of P2, we are able to compensate the positive chirped.

Note that a pair of gratings can also fulfill the same function with a slightly different compensation formula $GDD = \frac{m^2\lambda^3 L}{2\pi c^2 d^2 \cos^2\theta_D}$, where L is the distance between the two gratings, m is the diffraction order, d is the grating periodicity, and θ_D is the diffraction angle satisfying the grating function $\sin\theta_D = \sin\theta_i + \frac{m\lambda}{d}$. Grating compressor needs much smaller L compared with prism pairs, but has higher energy loss. Also note that the third-order dispersion plays an important role when GVD is nearly completely compensated on the second-order and needs to be taken account.

Calibration of the Impulsive and Cumulative Heating

Light impingement will generate heating and create an effective temperature increase at the sample surface with respect to the measured cryostat temperature. There are two types of optical heating: impulsive heating and cumulative heating. To estimate the heating induced by a single laser pulse we use the equation $\Delta T = \frac{(1-R)F}{C\rho\delta}$ (Harter, D. M. Kennes, et al., 2018), where ρ is the sample density in g/cm^3, F is the fluence in mJ/cm^2, R is the reflectivity, δ is the optical penetration depth of pump, and C is the heat capacity in mJ (g K)$^{-1}$. Although R, δ and C are all dependent on temperature, their temperature dependence can be ignored if the effective temperature increase is not dramatic. Typical values can range from several to hundreds of K depending on the experimental parameters.

The second kind of heating, cumulative heating of a laser pulse with Gaussian profile, can cause a static temperature increase that can be estimated to be $\Delta T = \sqrt{\frac{\ln 2}{\pi}}\frac{P}{d\kappa}$ (A. d. l. Torre et al., 2021), where P is the input power, d is the FWHM of the pump spot size, and κ is the thermal conductivity, which should in principle be a function of temperature. Typical values can range from several to tens of K depending on the experimental parameters.

Chapter 3

Light-Induced Topological Phase Transition in Te

3.1 Introduction

The emergence of topological quantum materials initiated a colossal tide of research due to their fascinating properties such as exotic band structures and dissipationless electronic states. These unique properties highlight the need to develop experimental protocols that can controllably tune the topological characteristics of a material on demand. Traditionally, there have been attempts to induce topological phase transition (TPT) in equilibrium via the application of strain, doping, electric field, or simply changing temperature (Xiao et al., 2020; Ying Wang et al., 2017; B. Xu et al., 2018; Mutch et al., 2019), but more promising opportunities lie within the out-of-equilibrium regime. In contrast to Floquet engineering, which only allows for a coherent switch of band topology within the pulse duration (Lindner, Refael, and Galitski, 2011; Y. H. Wang et al., 2013; Mahmood et al., 2016; J. W. McIver et al., 2020), driving a lattice displacement can change the electronic topology through electron-phonon coupling and possibly engender metastable states with a distinct topological property (Sie, Nyby, et al., 2019; M. Y. Zhang et al., 2019; Vaswani et al., 2020; Luo et al., 2021).

Weyl nodes are topologically stable crossing points between non-degenerate bands in a crystal, which impart unconventional properties including ultrahigh charge mobility and chiral magneto-transport (B. Yan and Felser, 2017). The possibility to create or annihilate Weyl nodes *in situ* using ultrashort light pulses has been broadly explored theoretically (Hübener et al., 2017; Chan et al., 2016; Z. Yan and Zhong Wang, 2016; Topp et al., 2018; Guan et al., 2021; Ebihara, Fukushima, and Oka, 2016) and was recently demonstrated experimentally in Dirac and type-II Weyl semimetal materials via impulsively driven lattice symmetry changes (Vaswani et al., 2020; Luo et al., 2021; Sie, Nyby, et al., 2019; M. Y. Zhang et al., 2019). However, efforts have so far focused on binary switching between semi-metallic states with and without Weyl nodes. In this chapter, we identify a three-state switch from Weyl semiconductor to Weyl metal to non-Weyl metal in chiral Peierls-distorted tellurium crystals as a function of the chiral chain radius. By performing time-dependent density functional theory calculations, we demonstrate that these

states can be transiently stabilized via a light-induced inverse-Peierls distortion. Predicted signatures of the inverse-Peierls distortion are experimentally reproduced using time-resolved optical second harmonic generation rotational anisotropy (tr-SHG-RA).

The Peierls instability is a spontaneous symmetry-lowering lattice deformation that lifts the degeneracy of electronic states at the Fermi level in order to reduce the overall system energy [Figure 3.1(a)]. Elemental tellurium (Te) is a prototypical strongly spin-orbit coupled Peierls-distorted system, which crystallizes in a non-centrosymmetric trigonal structure composed of chiral chains of Te atoms oriented along the c-axis, with space group $P3_121$ or $P3_221$ depending on the chain chirality [Figure 3.1(c) depicts $P3_121$ structure]. Each atom has two intra-chain nearest-neighbors (NNs) and four inter-chain next-nearest-neighbors (NNNs). This structure can be regarded as arising from the Peierls distortion of an achiral centrosymmetric rhombohedral structure (space group $R\bar{3}m$) in which the NN and NNN distances are equal [Figures 3.1(d),(f)] (Tangney and Fahy, 2002). The structural evolution is parameterized by the chain radius x, expressed in units of the lattice constant or inter-chain distance a, which is a displacement along the A_1 phonon coordinate. In the equilibrium phase $x_{eq} = 0.269$ and at the structural phase transition into the rhombohedral phase $x_{SPT} = 0.333$, amounting to a difference of approximately 0.26 Å.

3.2 Density Functional Theory Simulation

To understand the evolution of the electronic structure with x, we performed fully relativistic density functional theory (DFT) calculations using QUANTUM ESPRESSO package with plane wave and fully relativistic norm-conserving pseudopotentials. To calculate the equilibrium band structure, we relieve the stress in the structure and obtain the equilibrium lattice constant in agreement with previous results (Tangney and Fahy, 1999; Tangney and Fahy, 2002; Gatti et al., 2020). For the intermediate structures, we displace the Te atom along the x at several values between $x_{eq} = 0.269$ and $x_{SPT} = 0.333$ and obtain the electronic structure with the new lattice structures. Within the frozen-phonon approximation, these intermediate states reflect the metastable structure of the photo-induced states at different excitation levels.

In the equilibrium phase ($x_{eq} = 0.269$), we find that Te is a semiconductor with non-degenerate bands harboring Weyl nodes below the Fermi level along the H-K line

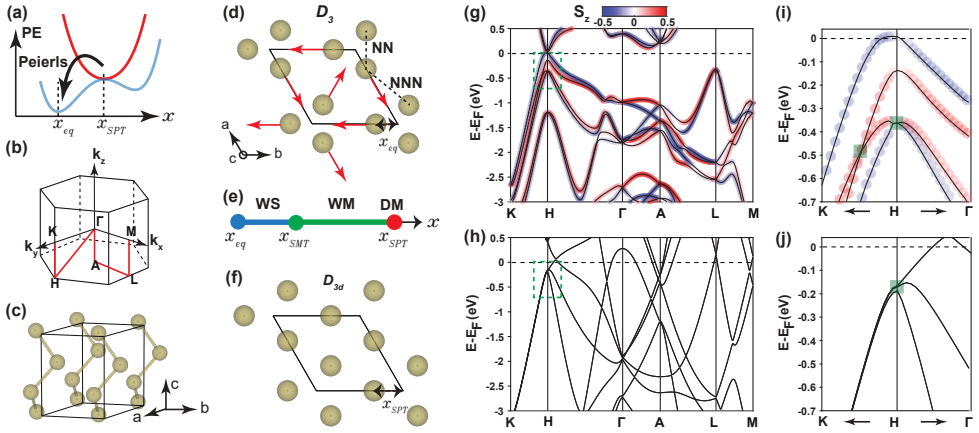

Figure 3.1: Band evolution of Te across the Peierls transition. (a) Schematic evolution of the potential energy (PE) surface across a Peierls transition. (b) Brillouin zone and (c) unit cell of bulk Te. (d) Equilibrium structure of Te (D_3 point group). Black rhombus denotes the unit cell and red arrows point along the A_1 phonon coordinate x. (e) Phase diagram as a function of x determined from DFT calculations (WS: Weyl semiconductor; WM: Weyl metal; DM: Dirac metal). (f) Peierls un-distorted structure of Te (D_{3d} point group). (g) DFT calculated band structure of Te in the equilibrium and (h) Peierls un-distorted structure respectively. Red and blue colors encode the spin polarization along k_z. (i),(j) Zoom-in of the region enclosed by the dashed rectangles in panels (g) and (h). The Weyl and Dirac nodes are denoted by green squares.

in the Brillouin zone [Figures 3.1(g),(i)], as well as Kramers-Weyl nodes (Chang, Wieder, et al., 2018) at the time-reversal invariant momenta Γ, M and A. These results are consistent with previous reports (Nakayama et al., 2017; Sakano et al., 2020; Gatti et al., 2020; N. Zhang et al., 2020; Hirayama et al., 2015) classifying Te as a Weyl semiconductor (WS). Upon increasing x, Te undergoes a semiconductor-to-metal transition (SMT) at $x_{SMT} \approx 0.283$ [Figure 3.1(e)] due to the sinking of the conduction bands at A, realizing an intermediate Weyl metal (WM). Finally, on reaching the rhombohedral phase ($x_{SPT} = 0.333$), band degeneracy is restored and the merger of Weyl nodes into Dirac nodes is accompanied by a closing of the direct gap at H [Figures 3.1(h),(j)], giving rise to a Dirac metal (DM). Tuning x therefore provides a mechanism for simultaneous Weyl node and band gap control.

Previous DFT studies have shown that trigonal Te can be driven into topological Weyl semimetal, three-dimensional topological insulator or WM phases by applying either hydrostatic pressure, shear or uniaxial strains to alter its structure (Agapito et al., 2013; Hirayama et al., 2015; Xue et al., 2018). However, no equilibrium

pathway to directly invert the Peierls distortion by tuning x, either through thermal or mechanical deformation (Rodriguez et al., 2020; Ideue et al., 2019), is known to exist.

3.3 Time-Dependent Density Functional Theory Simulation

Impulsive excitation by an intense laser pulse offers a potential out-of-equilibrium pathway to induce an inverse Peierls transition. By optically de-populating states near the Fermi level, the energy increase due to the lattice distortion is no longer balanced by the energy decrease due to the lifting of band degeneracy. This causes a sudden change in the potential energy surface of the lattice, generating a restoring force that drives coherent atomic motion reversing the Peierls distortion. For underdamped motion, a totally symmetric $A_{1(g)}$ Raman active mode is expected to be coherently launched through this displacive excitation mechanism (Zeiger et al., 1992) [Figure 3.1(a)]. Light-induced inverse Peierls transitions are accessible in a variety of systems including A7-structured semimetals (Teitelbaum et al., 2018), VO_2 (S. Wall, Wegkamp, et al., 2012) and charge density wave materials (Simone Wall et al., 2012; Huber et al., 2014; Beaud, Caviezel, et al., 2014). However, this mechanism has so far not been explored for ultrafast control of band topology.

To study the possibility of a light-induced inverse Peierls distortion in Te, we carried out time-dependent (TD) DFT calculations based on the time-dependent Kohn-Sham equation in the plane-wave basis to simulate the real-time lattice dynamics following impulsive optical excitation (Runge and Gross, 1984):

$$i\hbar\frac{\partial\psi_{\gamma\mathbf{k}}(\mathbf{G},t)}{\partial t} = \mathcal{H}_{\mathbf{k}}(t)\psi_{\gamma\mathbf{k}}(\mathbf{G},t), \tag{3.1}$$

where $\psi_{\gamma\mathbf{k}}(\mathbf{G},t)$ is the TDKS orbital, γ denotes the band index, and $\mathbf{k}$ is the reciprocal momentum index. $\mathcal{H}_{\mathbf{k}}(t)$ is the Hamiltonian expanded in a plane-wave basis with matrix element

$$\begin{aligned}\mathcal{H}_{\mathbf{k}}(\mathbf{G},\mathbf{G}',t) =& T_{\mathbf{k}}(\mathbf{G},\mathbf{G}',t) + V(\mathbf{G},\mathbf{G}',t)\\ =& \frac{\hbar^2}{2m}|\mathbf{k}+\mathbf{G}+\mathbf{A}(t)|^2\delta_{\mathbf{G},\mathbf{G}'} + V(\mathbf{G},\mathbf{G}',t),\end{aligned} \tag{3.2}$$

where $T_{\mathbf{k}}(\mathbf{G},\mathbf{G}') = \frac{\hbar^2}{2m}|\mathbf{k}+\mathbf{G}+\mathbf{A}(t)|^2\delta_{\mathbf{G},\mathbf{G}'}$ is the kinetic term. $\mathbf{A}$ is the velocity gauge potential (Bertsch et al., 2000):

$$\mathbf{A}(t) = -\int_0^t \mathbf{E}(t')dt', \tag{3.3}$$

where $\mathbf{E}$ is the electric field. $V(\mathbf{G}, \mathbf{G}')$ is the potential term calculated within the corresponding module QUANTUM ESPRESSO, including ion-electron potential, Hartree potential, and exchange-correlation potential.

Once the self-consistency in charge density evolution is satisfied, post-processing including the calculation of total energy, Hellmann-Feynman forces, and the ionic trajectory are invoked. For instance, the forces acting on the ions can be calculated through

$$\mathbf{F}_{\mathbf{R}_I} = \sum_{\gamma\mathbf{k}} \left\langle \psi_{\gamma\mathbf{k}} | \nabla_{\mathbf{R}_I} \mathcal{H} | \psi_{\gamma\mathbf{k}} \middle| \psi_{\gamma\mathbf{k}} | \nabla_{\mathbf{R}_I} \mathcal{H} | \psi_{\gamma\mathbf{k}} \right\rangle , \tag{3.4}$$

where $\mathbf{R}_I$ and $\mathbf{F}_{\mathbf{R}_I}$ are the position and force of the $I-$th ion.

With $\mathbf{R}_I$ and $\mathbf{F}_{\mathbf{R}_I}$, we utilize the Ehrenfest theorem for evolving ions according to the equation of motion

$$M_I \frac{d^2\mathbf{R}_I}{dt^2} = \mathbf{F}_{\mathbf{R}_I}, \tag{3.5}$$

where M_I is the mass of $I-$th ion. The velocity $v_I(t) = d\mathbf{R}_I/dt$ and the temperature $T(t) = \sum_I^{N_I} M_I v_I^2(t)/2N_I$ are also calculated, where N_I is the total number of ions. Also note that the Ehrenfest dynamics describe a microcanonical system where only electron-electron energy transfer and electron-phonon scattering are allowed. We neglected radiative recombination and heat radiation. Moreover, since periodic boundary conditions are utilized in the simulation, the whole crystal is homogeneously excited when the laser pulse is present and there is no driven mechanism for thermal transport. Thus, the total energy of the system is conserved after pumping.

Our method provides a fully *ab initio* description of the electronic, phononic and photonic degrees of freedom on equal footing. Using an advanced evolutionary algorithm, the velocity-gauge formalism, and symmetry-reduced momentum space sampling, we efficiently calculate the periodic Te system up to an unprecedented 3 ps, providing comprehensive information about not only the fast electronic response but also the long-time structural dynamics. The pump pulse is chosen to have a Gaussian profile of 100 fs width, a linear polarization with electric field perpendicular to the c-axis, and a photon energy centered at 1 eV, which is above the 0.3 eV band gap of Te. Otherwise, there are no adjustable parameters. For all pump fluences sampled, we resolved atomic motion exclusively along the A_1 phonon coordinate. Specifically, pumping excites sinusoidal displacement oscillations in t about a new value of x that is shifted higher than x_{eq} [Figure 3.2(a)]. Since the lifetime of photo-carriers deduced from our simulations well exceeds our sampled time window of several

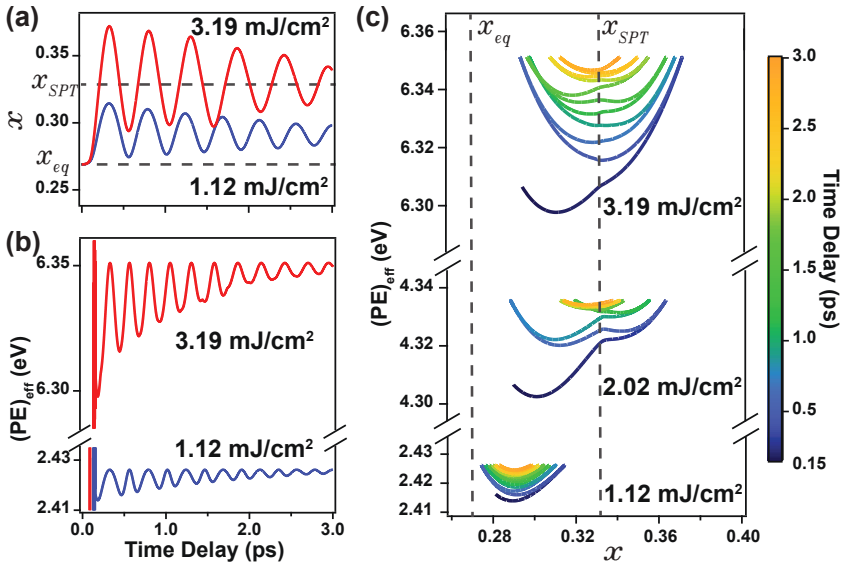

Figure 3.2: Light-induced lattice and effective potential energy dynamics. TDDFT calculated temporal evolution of (a) x and (b) the effective potential energy (see text) following impulsive optical excitation at a fluence below (blue) and above (red) F_c. (c) Spatio-temporal trajectories of the effective potential energy at fluences below, near, and above F_c. Color scales with the time delay.

picoseconds, this new position (x_0) is metastable. With increasing fluence (F), both the magnitude of the oscillations and x_0 increase. At sufficiently high fluence x_0 is able to reach x_{SPT}, signifying complete reversal of the Peierls distortion. An effective potential energy $(PE)_{eff}$ can be determined by evaluating $E_{total}[x(t),t] - E_{kin}[x(t),t]$, which is the difference between the total energy — including both lattice and electronic degrees of freedom — and ionic kinetic energy [Figure 3.2(b)]. To better visualize the dynamics of the inverse Peierls transition, we plot the spatio-temporal trajectory of $(PE)_{eff}$ for select fluences in Figure 3.2(c). For a fixed fluence, we observe that $(PE)_{eff}$ generally increases with time because $E_{total}[x(t),t]$ is fixed while $E_{kin}[x(t),t]$ is gradually damped out. But within each oscillation period there are local minima marking metastable x positions. In the low fluence regime, the trajectories are parabolic and share a single minimum displaced slightly towards x_{SPT} from x_{eq}. As fluence increases, this minimum monotonically shifts to larger x and, near a critical value $F_c \approx 2$ mJ/cm^2 (0.03 V/Å peak field), the trajectories become flattened and highly non-parabolic. Above F_c, parabolic trajectories are restored about a new minimum fixed at x_{SPT}. The fluence dependence of the curvature and local minima of $(PE)_{eff}$ are signatures of a dynamical phase transition across F_c that can be quantitatively tested experimentally.

Our TDDFT simulations are consistent with several previously reported experiments. Time-resolved pump-probe x-ray diffraction measurements on Te showed that the lattice undergoes transient deformation predominantly along the A_1 coordinate (Johnson et al., 2009), characterized by periodic oscillations about a position positively offset from x_{eq}. However, low fluences were used for this experiment, which only induced changes in x of order 0.01. Time-resolved optical reflectivity measurements demonstrated displacive excitation of coherent A_1 phonon oscillations, which undergo red-shifting and chirping with increasing fluence (Dekorsy et al., 1995; Hunsche, Wienecke, Dekorsy, et al., 1995; Kamaraju et al., 2010), as well as an anomalous blue-shift at higher fluence possibly due to overshooting a high symmetry point, although no explicit claim of an inverse Peierls distortion was made (Y.-H. Cheng, Teitelbaum, et al., 2018). Transient broadband optical spectroscopy measurements on Te thin films revealed slow photo-carrier recombination times ranging from tens to hundreds of picoseconds, possibly bottlenecked by weak inter-valley scattering (Iyer et al., 2019; Jnawali et al., 2020), giving rise a metastable excited state. Finally, evidence of a semiconductor-to-metal transition (A. M.-T. Kim, Roeser, and Mazur, 2003) was revealed by time-resolved ellipsometry measurements, which may be related to our predicted sinking of the A point conduction band at x_{SMT}. However, no ultrafast inverse Peierls transition in Te has been experimentally reported to date.

Based on the adiabatic approximation, in which the electrons are conjectured to instantaneously adjust to the new lattice position, the time-dependent electronic structure as a function of $x(t)$ can be reproduced by the static DFT calculation as a function of x Sie, Nyby, et al., 2019. Accordingly, as the inversion symmetry is restored, a WS-to-DM transition must follow. In this regard, to demonstrate the three-state switch, an experimental corroboration of the ultrafast SPT is prerequisite.

3.4 Experimental Results

To quantitatively test our TDDFT predictions, we performed tr-SHG-RA measurements (Darius H. Torchinsky, Hao Chu, et al., 2014). SHG-RA has been extensively applied to measuring the structure of topological materials both with and without inversion center (Appendix A). Since the leading order electric-dipole contribution to SHG directly couples to the inversion odd structural order parameter of Te (M. Cheng et al., 2019), this technique is simultaneously sensitive to the metastable x coordinate and the A_1 phonon properties under identical experimental conditions. Static SHG-RA patterns were measured using 1.5 eV incident probe light on Te

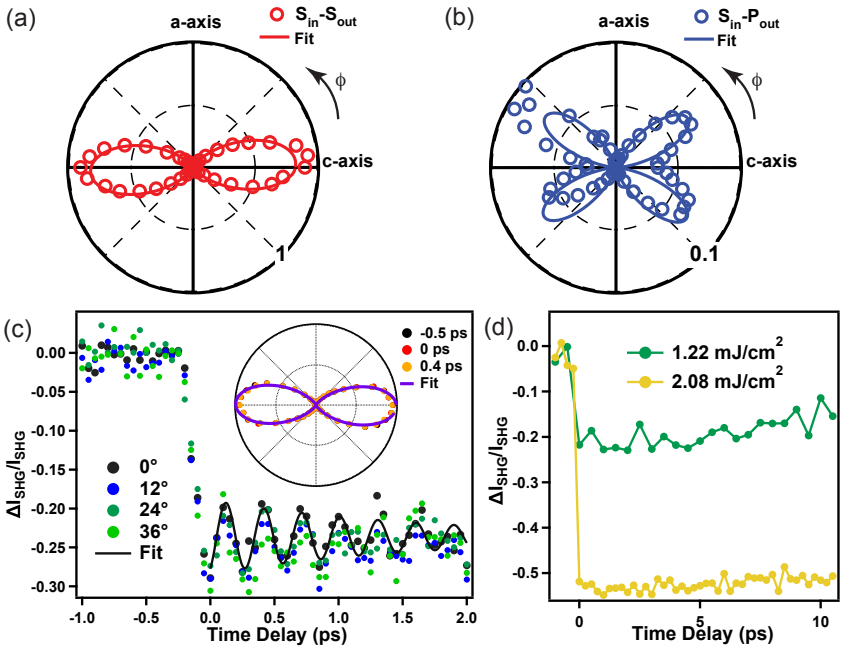

Figure 3.3: Static and time-resolved SHG-RA results. Static SHG-RA patterns in the (a) S_{in}-S_{out} and (b) S_{in}-P_{out} channels. The intensity is normalized to the peak intensity in the S_{in}-S_{out} channel. (c) Temporal evolution of SHG-RA intensity at select angles in the S_{in}-S_{out} channel with an absorbed pump fluence of around 1.22 mJ/cm^2 at various scattering angles normalized to their equilibrium value. The data for each angle is well-fit by a single decaying sinusoidal function, shown as a solid black curve. The inset shows scaled SHG-RA patterns at t = -0.5 ps, 0 ps and 0.4 ps, which can all be fit with the same curve. (d) Temporal evolution of SHG intensity at two characteristic fluences for a fixed ϕ in the S_{in}-S_{out} channel at long timescales.

single crystals polished with the c-axis parallel to the surface plane. By acquiring patterns in both parallel (S_{in}-S_{out}) and perpendicular (S_{in}-P_{out}) configurations, we verified that the entire signal is attributable to a bulk electric-dipole SHG susceptibility tensor respecting D_3 symmetry [Figures 3.3(a),(b)]:

$$\begin{aligned} I_{SP}(2\omega,\phi) &\propto \left[-2\chi_{xyz}\sin(\theta)\sin(\phi)\cos(\phi) + \chi_{xxx}\cos(\theta)\cos(\phi)\sin^2(\phi)\right]^2, \\ I_{SS}(2\omega,\phi) &\propto \chi_{xxx}^2\sin^6(\phi), \end{aligned} \tag{3.6}$$

where $\chi_{xxx} = -\chi_{xyy} = -\chi_{yyx} = -\chi_{yxy}$, and $\chi_{xyz} = \chi_{xzy} = -\chi_{yxz} = -\chi_{yzx}$ are the only two independent nonzero tensor elements. The ratio between χ_{xxx} and χ_{xyz} obtained from fitting is 1:0.05, in agreement with a recent theoretical SHG simulation (M. Cheng et al., 2019).

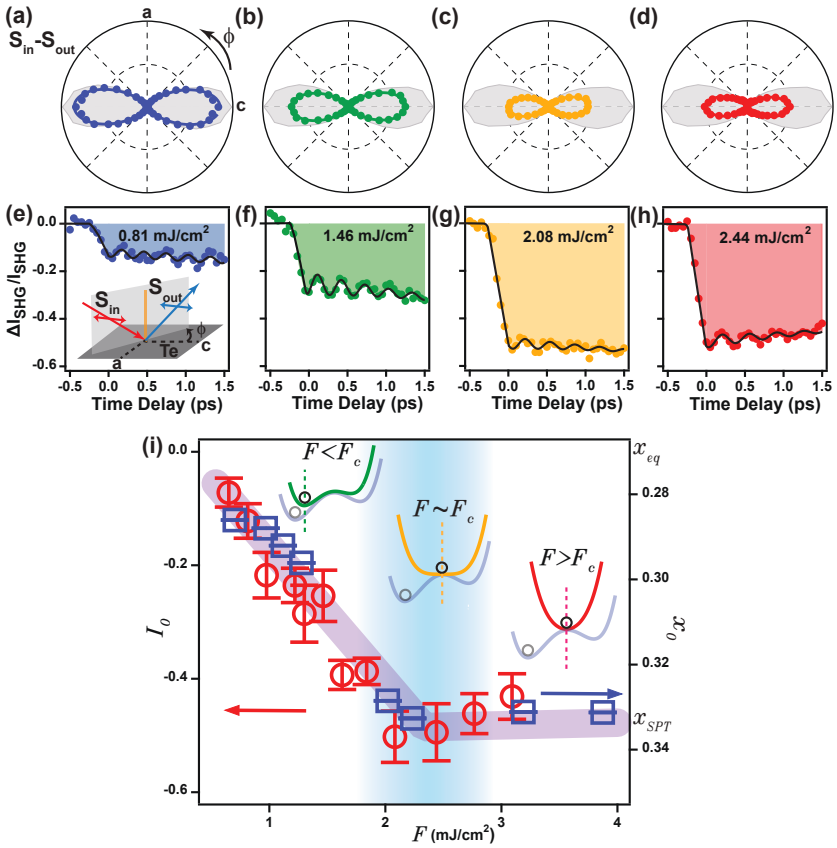

Figure 3.4: Fluence dependence of SHG dynamics. (a)-(d) Instantaneous SHG-RA patterns measured at t = 50 fs for different absorbed pump fluence values. The static (t < 0) pattern is overlaid and shaded gray. (e)-(h) Normalized differential SHG intensity transients acquired at the angle of maximum intensity (ϕ = 0°) in the S_{in}-S_{out} pattern for each fluence. Solid lines are fits to an exponential decaying oscillation plus a constant offset. A weak linear background was introduced in some traces to account for laser power drift. The inset in panel (e) shows a schematic of the SHG-RA setup. The scattering plane angle ϕ is measured with respect to the crystallographic c-axis. Red, blue and orange lines represent the incident, reflected SHG and pump beams, respectively. (i) Pump fluence dependence of the measured SHG offset term (red circles) and TDDFT calculated metastable x position (blue squares). The blue shaded bar indicates the critical fluence regime. Insets show schematics of the transient potential energy surface in the low, critical, and high fluence regimes, illustrating the shift in the metastable x position from equilibrium (gray curves).

Pump Fluence Dependence of SHG Dynamics

Figures 3.4(a)-(d) show instantaneous SHG-RA patterns in the S_{in}-S_{out} channel measured immediately after exciting with a 1 eV pump pulse of 100 fs duration — matching our TDDFT parameters — for different absorbed fluence levels. Note that

the absorbed fluence is lower than the applied fluence by a factor of 1 - R, where R is the reflectance at 1 eV. The instantaneous patterns exhibit a uniform (independent of scattering plane angle ϕ) decrease in intensity relative to the equilibrium pattern, indicating that all electric-dipole susceptibility tensor elements are suppressed by the same scale factor [Figure 3.3(c)]. Since each tensor element is proportional to the structural order parameter, this confirms that pump excitation acts simply to reduce the structural order parameter and does not induce any symmetry breaking. The patterns subsequently undergo uniform oscillations about the reduced intensity value, consistent with a totally symmetric A_1 breathing mode [Figure 3.3(c)]. By tracking the time dependence of the SHG intensity at $\phi = 0°$ [Figures 3.4(e)-(h)], we clearly resolve an intensity drop upon pump excitation on the timescale of a half cycle of the A_1 mode, followed by A_1 mode oscillations. While the oscillations are damped out after approximately 2 ps, the intensity offset persists out to at least 10 ps [Figure 3.3(d)]. We also note a SHG intensity drop and oscillation with similar amplitude can be seen in crossed polarization channels, which further confirms that all the SHG susceptibility tensor elements are suppressed by the same scale factor.

To directly compare the predicted and measured structural dynamics, we fit both $x(t)$ obtained from our TDDFT simulations [Figure 3.2(a)] as well as the differential SHG transients [Figures 3.4(e)-(h)] for $t > 0$ to the function $Ae^{-t/\tau}\cos(2\pi\nu t + \varphi) + B$. This expression includes the phonon amplitude A, damping time τ, phase φ, frequency ν, and a constant offset of the x coordinate ($B = x_0$) or SHG intensity ($B = I_0$).

Focusing first on the offset term, we plot in Figure 3.4(i) the fitted values of x_0 for multiple fluences. In the weak excitation regime, x_0 increases monotonically with fluence, indicating a shift of potential energy minimum towards the centrosymmetric position. At a critical fluence near 2 mJ/cm^2, the Peierls non-distorted structure is reached and the potential energy surface becomes parabolic with a minimum at x_{SPT}. Further increasing the fluence alters the curvature of the parabola but leaves x_0 fixed at x_{SPT}. The fitted values of I_0 acquired over a similar fluence range are overlaid [Figure 3.4(i)], which not only obeys a qualitatively akin trend to x_0 but also shows a quantitatively matching critical fluence value. These results strongly suggest an experimental realization of a light-induced inverse Peierls transition.

Several other plausible scenarios can be excluded. Photo-bleaching can be ruled out because only $\sim$ 1% of electrons have been excited. This number is too small to bleach the possible transitions given the large absorption peak centered at 1 eV

in the previous infrared spectroscopy measurements and simulations (Rodriguez et al., 2020; M. Cheng et al., 2019). We then consider the possibility of a thermal phase transition. Accounting for both impulsive and static heating, which give a temperature increase of 190 K and 0.6 K, respectively, we reach an effective temperature at 500 K pumped with a critical fluence of 2 mJ/cm^2 at 300 K. According to the equilibrium phase diagram of Te, there is no structural phase transition under ambient pressure until liquefaction at around 700 K (Hejny and McMahon, 2003; Hejny and McMahon, 2004) and the rhombohedral centrosymmetric phase of Te only exists above room temperature at high pressures of order 20 GPa (compressing the lattice volume by 15%) (Hejny, Falconi, et al., 2006). Therefore we can rule out a thermally driven transition into the D_{3d} phase. Another photo-thermal induced melting transition was previously reported in single crystalline Te based on the loss of optical anisotropy upon pumping with 100 fs long 1.5 eV pulses (Ashitkov et al., 2002). This transition was observed above approximately 15 mJ/cm^2 and occurs over ps timescale that decreases with fluence. In contrast, our experiments are performed at much lower fluence and the timescale over which our SHG signal drops is less than 0.2 ps and almost fluence independent. The fourth possibility is a reversible transition between crystalline and amorphous phases that can be realized in Te via optical illumination. We rule out this optically induced order-to-disorder transitions for two reasons. First, the amorphous phase of Te exhibits a broad mode centered at 4.7 THz in its spontaneous Raman spectrum, which is absent in the FFT spectrum of our signal (Brodsky et al., 1972). Second, a recent single-shot transient reflectivity measurement on a polycrystalline Te thin film using 60 fs long 1.5 eV pulses reported laser-induced amorphization above a threshold fluence of around 3 mJ/cm^2 (Y.-H. Cheng, Teitelbaum, et al., 2018). Preceding this transition, inflections were observed in the fluence dependence of both the A_1 phonon amplitude and frequency, reminiscent of our reported TDDFT and SHG results. After excluding these possibilities and considering the good match between theory and experiment, we believe a light-induced inverse Peierls transition is the most plausible explanation.

Despite the reasonable agreement between TDDFT simulation and tr-SHG-RA results, note that the comparison is not exact because the SHG intensity saturates to a non-zero value. Such residual signals are commonly observed across photo-induced phase transitions (Kogar, Zong, et al., 2020; Huber et al., 2014; Caviglia et al., 2013; M. Y. Zhang et al., 2019). They may be attributed to incomplete order parameter suppression within the probed volume due to quench-induced spatial

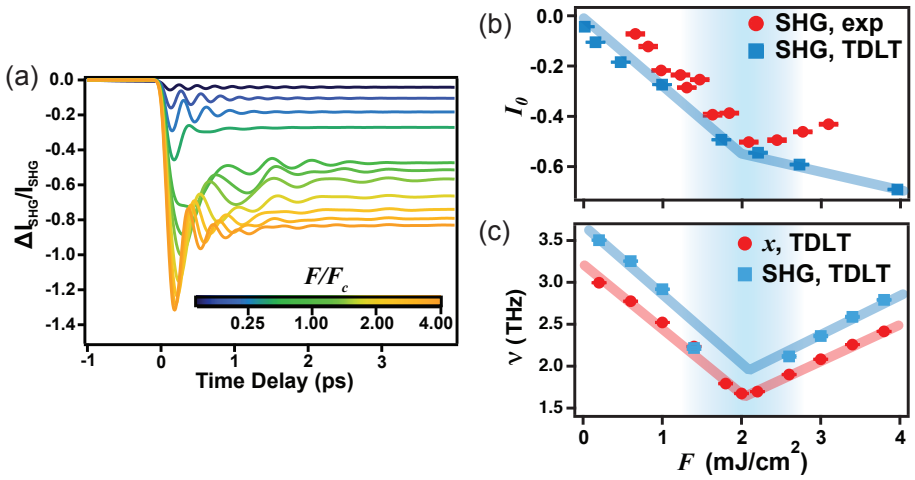

Figure 3.5: TDLT simulation of SHG offset intensity and phonon frequency mismatch induced by pump-probe penetration depth mismatch. (a) TDLT simulation of relative SHG change as a function of time at different pump fluences. (b) TDLT simulation of SHG background intensity as a function of pump fluence with the experimental results overlaid. (c) Phonon frequencies as a function of fluence obtained from fitting to TDLT-simulated $\Delta I_{SHG}/I_{SHG}(t)$ and $x(t)$. Both are scaled by a same factor to match the TDDFT-calculated phonon frequencies.

domains and defects (R. Yusupov et al., 2010), penetration depth mismatch between pump and probe beams (Kogar, Zong, et al., 2020), spatial non-uniformity of the pump intensity (M. Y. Zhang et al., 2019), or higher multipole SHG radiation processes, all of which are not accounted for by our TDDFT simulations.

To more quantitatively simulate the effects of a penetration depth mismatch between the pump and probe light on the transient SHG response, we used a phenomenological time-dependent Landau theory (TDLT) model based on a dynamical double-well potential of the form Eq.1.6 and the dynamical equation of the form Eq1.7 introduced in Chapter I Section 1.2. Due to the pump-probe penetration depth mismatch, different depths z below the sample surface experience a different level of quenching of the potential. The reported pump and probe penetration depths are δ_{pu} =76 nm and δ_{pr} =38 nm, respectively, giving rise to an approximate two-fold difference (Tutihasi et al., 1969). We assume that the sample is composed of thin layers and an exponential z-dependence of light-induced modulation of PES arises from the exponentially decaying photo-carrier distribution. We then solve $x(z,t)$ for each layer. The depth integrated value of x_{int} is evaluated by summing over each layer weighted by the probe penetration depth as $x_{int}(t) = \sum_{z=0}^{\infty} \exp(-z/\delta_{pr}) x(z,t)$. The relative SHG intensity change is then defined as $\Delta I_{SHG}/I_{SHG} = [x_{int}(t) - x_{int}(0)]/x_{int}(0)$

[Figure 3.5(a)]. By fitting the simulated $\Delta I_{SHG}/I_{SHG}(t)$ curves with the same formula used for the experimental $\Delta I_{SHG}/I_{SHG}$ curves, we obtain the simulated I_0 as a function of pump fluence [Figure 3.5(b)]. A decrease in slope is most pronounced near F_c, suggesting that the penetration depth mismatch may be partially responsible for the observed saturation-like behavior in the SHG intensity at F_c. The difference between simulation and experiment, which is most obvious above 2.2 mJ/cm^2, may be caused by the other factors as previously mentioned.

Pump Fluence Dependence of A_1 Phonon Dynamics

The dynamics of the coherent A_1 phonon can serve as an additional diagnostic as schematically depicted in Figures 3.6(a)-(c). For an ultrafast inverse Peierls distortion, one expects that as the fluence increases towards F_c, the potential energy minimum should be displaced further away from x_{eq} and its curvature should decrease as the landscape evolves from being locally parabolic to locally quartic. As illustrated in Figure 3.6(a), the former causes the phonon amplitude to increase while the latter causes the phonon frequency to decrease. At F_c, the displacement reaches its maximum value of $x_{SPT} - x_{eq}$ and so the phonon amplitude saturates [Figure 3.6(b)]. On the other hand, the landscape becomes parabolic again above F_c and so the curvature starts to increase with fluence, corresponding to an increasing phonon frequency [Figure 3.6(c)].

Figures 3.6(d) and (e) show the fluence dependence of A_{th} and ν_{th} extracted from fits to the TDDFT simulations. Subscripts on the phonon parameters denote theoretical (th) or experimental (exp) values. The anticipated saturation behavior of A_{th} and softening and re-hardening behavior of ν_{th} are clearly borne out. Turning to the transient SHG data, we resolve coherent phonon oscillations both below and above F_c [Figures 3.4(e)-(h)], indicating that Te remains crystalline over our measured fluence range. As shown in Figure 3.6(f), A_{exp} increases with fluence in the weak excitation regime and then abruptly changes slope just below F_c, reminiscent of A_{th}. However, unlike A_{th}, A_{exp} does not saturate above F_c but instead exhibits a slightly downward slope. Although the origin of this discrepancy with TDDFT is unclear, a similar downward trend has been reported above other ultrafast structural phase transitions (M. Y. Zhang et al., 2019) and may be related to cumulative heating, electronic diffusion, and changes in the Raman scattering cross section of probe photons, which are not accounted for in TDDFT. Figure 3.6(g) shows that ν_{exp} decreases with fluence from its 3.6 THz equilibrium value in the weak excitation regime. This is quantitatively consistent with previous studies on Te (Dekorsy et al.,

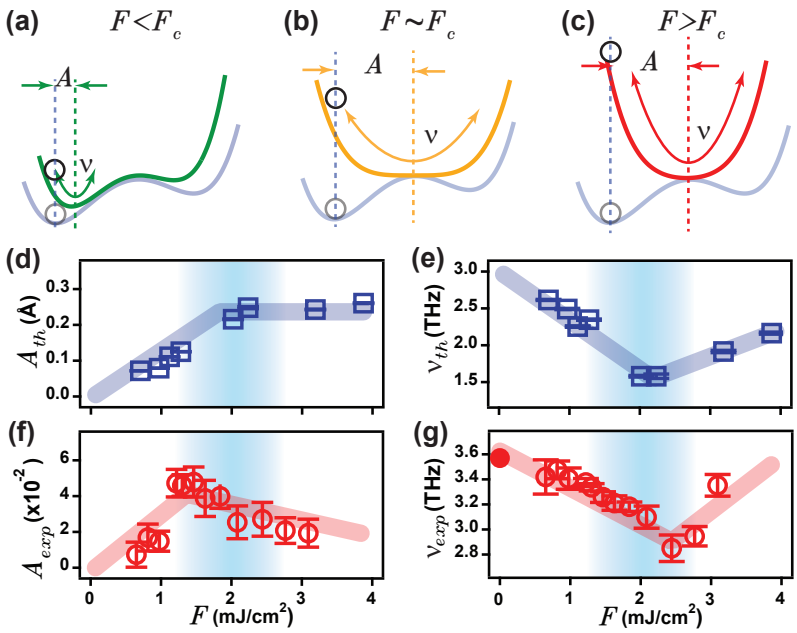

Figure 3.6: Fluence dependence of the coherent A_1 phonon dynamics. (a)-(c) Schematics of the metastable potential energy surface at select fluences. The separation between the vertical dashed lines sets the phonon amplitude A and the curvature of the potential minimum sets the phonon frequency ν. (d) Simulated pump fluence dependence of the phonon amplitude and (e) frequency obtained from TDDFT. (f) Experimentally measured fluence dependence of the phonon amplitude and (g) frequency obtained by fitting the SHG transients in Figures 3.6(e)-(h). The solid circle at $F = 0$ in panel (g) is measured with Raman scattering. The shaded blue bars mark the critical regime.

1995; Teitelbaum et al., 2018) and indicates that TDDFT slightly underestimates the frequency. Above approximately 2 mJ/cm^2, there is an abrupt change in slope from negative to positive, closely following the behavior of ν_{th}.

Despite the reasonable agreement, we also note a quantitative mismatch between the TDDFT-calculated and experimental phonon frequencies, which can be partially induced by the penetration depth mismatch between pump and probe and quantitatively simulated by our aforementioned TDLT model. We obtained the fluence dependence of phonon frequency by fitting both $x(t)$ and $\Delta I_{SHG}/I_{SHG}(t)$ curves, and find that the former always has a lower value than the latter [Figure 3.5(c)]. The reason is straightforward: the deeper probed region is irradiated with a lower fluence effectively, and thus the laser-induced phonon frequency softening of the deeper region is less than the surface which can be characterized by $x(t)$. Since our TDDFT calculation directly simulates $x(t)$ while our SHG experiment measures

$\Delta I_{SHG}/I_{SHG}(t)$, the latter should always exhibit a higher phonon frequency than the former. Following the same direction, one would expect that the thin-film samples should exhibit a more pronounced frequency softening than the bulk samples, which is indeed the case as shown by previous experimental results on both thin-film (Y.-H. Cheng, Teitelbaum, et al., 2018) and bulk samples (Hunsche, Wienecke, and Kurz, 1996; Kudryashov et al., 2007; Kamaraju et al., 2010).

3.5 Discussion and Outlook

The consistency between our TDDFT simulations and time-resolved SHG experiments across multiple observables establishes that impulsive excitation can drive Te across an inverse Peierls transition. Our TDDFT results show that the inverse Peierls transition concurrently induces an ultrafast switching from WS to metastable WM and DM states, which may be directly verifiable in the future using high-resolution extreme ultraviolet time- and angle-resolved photoemission spectroscopy. Moreover, our work showcases the effectiveness of TDDFT in predicting impulsively driven out-of-equilibrium structural phase transitions. More generally, our results suggest that three-dimensional Peierls systems are a vast and fertile playground for exploring the interplay of ultrafast insulator-to-metal transitions and ultrafast band topology control, two hitherto disparate areas of research. As embodied by Te, this research possibly paves the way towards multi-state-switchable and multifunctional ultrafast Weyl devices.

Chapter 4

Ultrafast Reversal of Excitonic Insulating Order in Ta_2NiSe_5

4.1 Introduction

Exploring new pathways to optically switch Ising-type electronic order parameters is a major theme of current ultrafast science. In recent years, a variety of out-of-equilibrium protocols have been developed for rapidly switching ferromagnetic (Lambert et al., 2014; Tudosa et al., 2004; Gerrits et al., 2002), ferrimagnetic (Stanciu et al., 2007; Vahaplar et al., 2009; Radu et al., 2011), antiferromagnetic (A. V. Kimel et al., 2009; Manz et al., 2016; Schlauderer et al., 2019), and ferroelectric (Fahy and Merlin, 1994; Qi et al., 2009; Mankowsky, Hoegen, et al., 2017) order parameters. However, far less is understood about the mechanisms for switching more exotic order parameters that are not of magnetic and charge dipolar type.

A particularly interesting case is the excitonic insulator (EI), a strongly correlated electronic phase realized through condensation of bound electron-hole pairs (Jérome, Rice, and Kohn, 1967). EI was theoretically proposed to be realized in a semiconductor (semimetal) with a tiny (negative) band gap E_g. The weakly screened Coulomb interaction between a hole and an electron leads to a bound state dubbed exciton. If the exciton binding energy E_B exceeds the magnitude of E_g, the semiconducting or semimetallic ground state becomes unstable against the formation of excitons, and an EI ground state forms. A semiconductor undergoes a Bose-Einstein condensation of excitons to an EI, while the transition from a semimetal to EI can be captured by BCS theory (Wakisaka et al., 2009). Currently, promising intrinsic EI candidates include $TmSe_0.45Te_0.55$ (Bucher, Steiner, and Wachter, 1991), $1T-TiSe_2$ (Kogar, Rak, et al., 2017), Ta_2NiSe_5 (Wakisaka et al., 2009), and mono- or double-layer transition metal dichalcogenides (Ma et al., 2021; Jia et al., 2022).

Based on Ginzburg-Landau theory, the free energy landscapes of the complex electronic order parameter and the real lattice order parameter of an EI are typically characterized by a Mexican hat with continuous U(1) symmetry and a parabola, respectively [Figure 4.1(a)]. However, strong electron-phonon coupling (EPC) induces a tilting of both the lattice and electronic potentials (Lian et al., 2020; Larkin et al., 2017; T. Kaneko et al., 2013; Nakano et al., 2018; Takeshi Suzuki

et al., 2021), reducing the U(1) symmetry to a discrete Z_2 Ising-type symmetry. Like in magnetic or charge dipole ordered ferroic materials, this leads to two degenerate ground states characterized by order parameters of equal magnitude but opposite phase [Figure 4.1(b)].

There is currently no experimental method to switch nor directly measure the phase of an EI order parameter on ultrashort timescales. An alternative strategy is to measure the phase of the coupled structural order parameter. However, existing time-resolved x-ray and electron diffraction techniques are not phase sensitive. Optical phase-resolved second harmonic generation measurements (Mankowsky, Hoegen, et al., 2017; Manfred Fiebig, Thomas Lottermoser, et al., 2004; M. Fiebig, Fröhlich, Sluyterman v. L., et al., 1995) have been used to measure the phase of structural order parameters in noncentrosymmetric ferroic materials (M. Fiebig, Fröhlich, Krichevtsov, et al., 1994; M. Fiebig, Th. Lottermoser, et al., 2002; Van Aken et al., 2007; Matsubara et al., 2015), but all known EI candidates are centrosymmetric (Kogar, Rak, et al., 2017; Wakisaka et al., 2009). The possible presence of 180° EI domains further complicates such measurements because domain averaging would cause overall signal cancellation.

In this chapter, we demonstrate via theory and experiment a pathway to optically switch an EI order parameter and probe this reversal through a coherent EI order-parameter-coupled phonon (OPCP). The time evolution of the coupled EI and structural order parameters following impulsive laser excitation are derived from modeling a prototypical system Ta_2NiSe_5, which we assume to harbor an EI phase, with an elementary spinless two-band Hamiltonian. Our simulations reveal that the EI order parameter is stably reversed above a critical laser fluence, identifiable indirectly via a saturation of the coherent OPCP amplitude. Our comprehensive time-resolved coherent phonon spectroscopy measurements experimentally verify this scenario. We also demonstrate how switching can be controlled through the relative timing between successive laser excitation pulses. Eventually, we theoretically explore the possibility of amplifying the EI Higgs mode in Ta_2NiSe_5.

4.2 Microscopic Model and Dynamical Simulation

The quasi-one-dimensional (1D) direct band-gap semiconductor Ta_2NiSe_5 is reported to undergo an EI transition at a critical temperature $T_c = 328$ K (Wakisaka et al., 2009; Seki et al., 2014), accompanied by a weak orthorhombic-to-monoclinic structural distortion due to EPC (T. Kaneko et al., 2013). Impulsive laser excitation

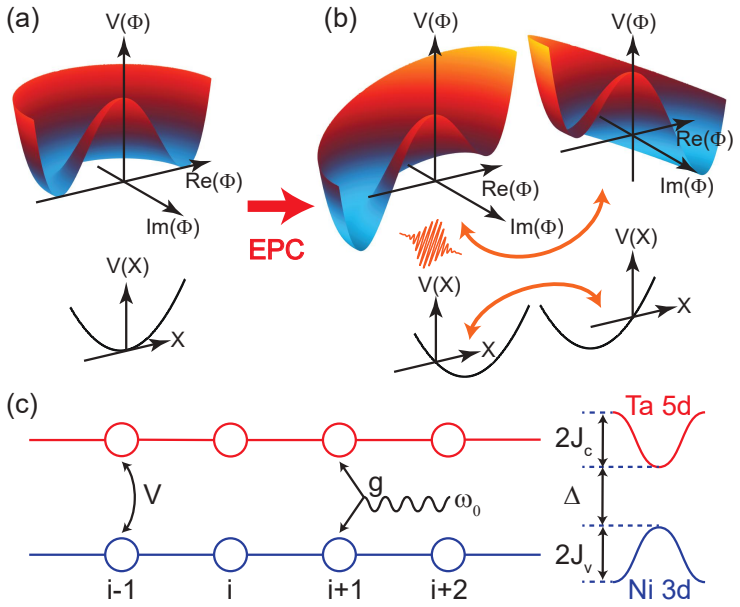

Figure 4.1: Schematic of the electronic and structural free energy landscapes (a) without and (b) with EPC. In the latter case, pulsed excitation can drive the system between two degenerate ground states. (c) Schematic of the 1D spinless two-band model. Red (blue) circles on each site i denote Ta $5d$ conduction band (Ni $3d$ valence band) states. The microscopic parameters discussed in the main text are defined pictorially.

below T_c has been shown to coherently excite at least five distinct Raman-active phonons with frequencies near 1, 2, 3, 3.7, and 4 THz. The 1, 2, and 4 THz modes are sensitive to the EI transition at T_c (Werdehausen, Takayama, Höppner, et al., 2018; Mor, Herzog, Noack, et al., 2018; Takeshi Suzuki et al., 2021; Tangwei Tang et al., 2020) and thus constitute the OPCPs, while the 3 and 3.7 THz modes are reportedly not coupled to the EI order parameter and thus serve as a control. However, recent results also suggest that these modes may potentially couple to EI Goldstone mode (Bretscher, Andrich, Murakami, et al., 2021).

Microscopic Model

The low energy electronic structure of Ta_2NiSe_5 consists of a conduction band with Ta $5d$ orbital character and a valence band with Ni $3d$-Se $4p$ hybridized orbital character. The EI instability is well captured by a 1D spinless two-band Hamiltonian with EPC (Zenker, Fehske, and Beck, 2014; Tanaka, Daira, and Yonemitsu, 2018; Murakami, Gole ž, Martin Eckstein, et al., 2017; Tanabe, Sugimoto, and Ohta,

2018) [Figure 4.1(c)],

$$H = \sum_k (\epsilon_k {c_k}^\dagger c_k + \mu_k {v_k}^\dagger v_k) + \sum_i [V {c_i}^\dagger c_i {v_i}^\dagger v_i + \omega_0 {b_i}^\dagger b_i + g({b_i}^\dagger + b_i)({c_i}^\dagger v_i + {v_i}^\dagger c_i)], \tag{4.1}$$

where ${c_k}^\dagger, c_k$ and ${v_k}^\dagger, v_k$ are the fermionic creation and annihilation operators for conduction and valence band electrons with momentum k, respectively, and ${b_i}^\dagger, b_i$ are the bosonic creation and annihilation operators for an OPCP mode of energy ω_0 at site i. The conduction and valence band dispersions are given by $\epsilon_k = \frac{\Delta}{2} + 2J_c \sin(ka/2)^2$ and $\mu_k = -\frac{\Delta}{2} - 2J_v \sin(ka/2)^2$, respectively, where $2J_c$ and $2J_v$ are their bandwidths and Δ is the band gap (Murakami, Gole ž, Martin Eckstein, et al., 2017; Tanabe, Sugimoto, and Ohta, 2018). An on-site interband electron-electron interaction term V drives the excitonic pairing, and an EPC term g couples the electronic and phononic subsystems. These microscopic parameters have been experimentally determined (Murakami, Gole ž, Martin Eckstein, et al., 2017; Tanabe, Sugimoto, and Ohta, 2018).

From Eq.4.1, we derive the equations of motion for the EI and structural order parameters, defined as $\Phi_i = \langle {c_i}^\dagger v_i \rangle$ and $X_i = \langle {b_i}^\dagger + b_i \rangle$, respectively, in two steps. We first derive the exact expression for the nonequilibrium free energy functional of Φ and X in the Keldysh path integral framework, where we include the light excitation via Peierls substitution. Then we obtain the equations of motion as the saddle point of the free energy, ignoring population in the conduction bands, spatial fluctuations of the order parameter field, and higher-order contributions $O(\Phi^6)$,

$$iZ\partial_t \Phi = (-\tilde{D}(\nabla - iqA)^2 + \tilde{m} + \tilde{U}|\Phi|^2)\Phi + \frac{2g}{V}X, \tag{4.2}$$

$${\partial_t}^2 X = -({\omega_0}^2 + \frac{2g^2\omega_0}{V})X - 2g\omega_0 \,\mathrm{Re}(\Phi), \tag{4.3}$$

with the parameters $\tilde{D}, \tilde{m}, \tilde{U}, Z$ depending on integrals over Green's functions and therefore on the band structure of the material and the temperature T of the system. Assuming $k_B T < \Delta$, i.e. negligible population in the conduction bands, we can write

out these parameters based on the parameters that determine the band structure

$$\tilde{m} = 1 - \frac{2V}{\sqrt{\Delta(2J_c + 2J_v + \Delta)}}, \tag{4.4}$$

$$\tilde{D} = \frac{2J_c J_v V}{\sqrt{\Delta(2J_c + 2J_v + \Delta)}^3}, \tag{4.5}$$

$$Z = V\left(\frac{2J_c + 2J_v + 2\Delta}{\sqrt{\Delta(2J_c + 2J_v + \Delta)}^3}\right), \tag{4.6}$$

$$\tilde{U} = \left(\frac{2(3(J_c + J_v)^2 + 4\Delta(J_c + J_v) + 2\Delta^2)}{\sqrt{\Delta(2J_c + 2J_v + \Delta)}^5}\right)V^3. \tag{4.7}$$

Applying the following transformation relationships $m = \tilde{m}/Z$, $U = \tilde{U}/Z$, and $D = \tilde{D}/Z$, $g' = g/(ZV)$, and introducing two phenomenological constants γ_e and γ_{ph} to account for damping of electronic and structural modes due to thermal fluctuation, we obtain the simplified equations of motion:

$$i\partial_t\Phi = ((-D(\nabla - iqA)^2 + m + U|\Phi|^2)\Phi + 2g'X)(1 - i\gamma_e), \tag{4.8}$$

$$\partial_t{}^2X = -\omega_0{}^2X - 2g\omega_0\phi - 2\gamma_{ph}\partial_t X. \tag{4.9}$$

Here D is an effective diffusion coefficient, q is the electron charge, A is the light vector potential, g' is the renormalized EPC coefficient for the electronic channel, and m and U are the second- and fourth-order expansion coefficients of the electron-electron interaction term, respectively.

Simulation Results

We first present a qualitative picture of how order parameter reversal occurs in our model. In equilibrium the electronic potential $V(\Phi) = \frac{1}{2}m\Phi^2 + \frac{1}{4}U\Phi^4 + 2g'X\Phi$ has either a tilted parabolic ($m > 0$) or tilted Mexican-hat ($m < 0$) form capturing the absence or presence of exciton condensation. For homogeneous optical excitation, one can ignore spatial derivatives of Φ. For pulsed excitation with infrared light, whose frequency well exceeds the electronic Higgs-Goldstone (Murakami, Gole ž, Martin Eckstein, et al., 2017; Murakami, Gole ž, Tatsuya Kaneko, et al., 2020) and OPCP mode frequencies, one can also average out the fast oscillations of the perturbation and retain only its Gaussian envelope. Under these conditions one can make the simplification $m(t) = -D(\nabla - iqA)^2 + m \triangleq f(t) + m$, where $f(t) = \alpha F \exp\left\{(-\frac{4\ln(2)t^2}{\sigma^2})\right\}$. Here σ is the temporal width of the Gaussian pulse, α is a positive constant scaling factor, and F is the pump fluence, the only tunable

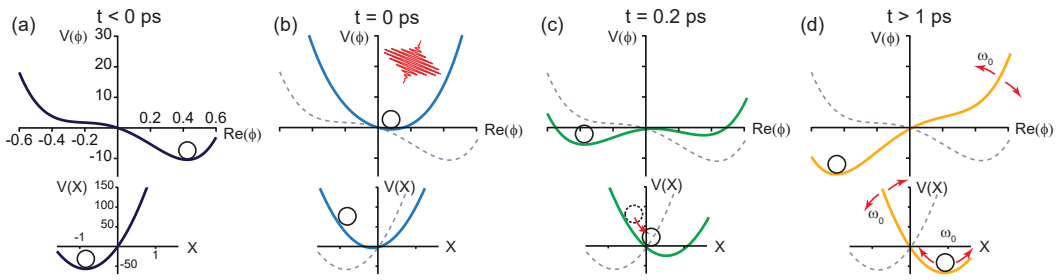

Figure 4.2: Simulation results of $V(\Phi)$ and $V(X)$ for $F > F_c$ with experimentally determined parameters. Snapshots of the potential landscapes (solid lines) and the electronic and structural order parameters (circles) are shown (a) in the equilibrium state (reproduced as dashed lines in (b)-(d)), (b) at the moment of excitation, (c) during transit into the reversed state, and (d) in the reversed state before equilibration, where both potentials are modulated at the phonon frequency (red arrows). Axes' scales are the same in all panels.

parameter in our model. In the EI phase ($m < 0$), optical excitation therefore acts to instantaneously increase $m(t)$. The subsequent reduction of the EI order parameter, which occurs on a timescale much shorter than $2\pi/\omega_0$, results in a sudden shift in the lattice potential $V(X) = \frac{1}{2}{\omega_0}^2 X^2 + 2g\omega_0 \,\mathrm{Re}(\Phi)X$ due to EPC, launching coherent oscillations through displacive excitation. In the low fluence regime, where the phonon oscillation amplitude is small enough such that X does not change sign, the direction of tilt of both $V(\Phi)$ and $V(X)$ remains unchanged and so no switching occurs. However, above a critical fluence F_c, where the phonon oscillation amplitude becomes large enough to change the sign of X, the tilting of both potentials is reversed and the system can relax into the switched state.

Numerical simulations of our model using experimentally determined material parameters for Ta_2NiSe_5 and $\sigma = 100$ fs were carried out in the EI phase. Figure 4.2 displays simulation results for F slightly greater than F_c. At the moment of excitation $t = 0$ [Figure 4.2(b)], there is an instantaneous change in $V(\Phi)$ from Mexican-hat to parabolic form caused by the light-induced enhancement of $m(t)$. The EI order parameter evolves rapidly to the new potential minimum with overdamped dynamics and is quenched within the pulse duration. This leads to a rapid shift in $V(X)$, launching coherent oscillations of the underdamped OPCP, which shakes the electronic potential via EPC at the phonon frequency. Once the pulsed excitation is over, $V(\Phi)$ recovers a Mexican-hat form. However, as X crosses zero within the first half period of oscillation [Figure 4.2(c)], the tilting of $V(\Phi)$ is reversed with respect to

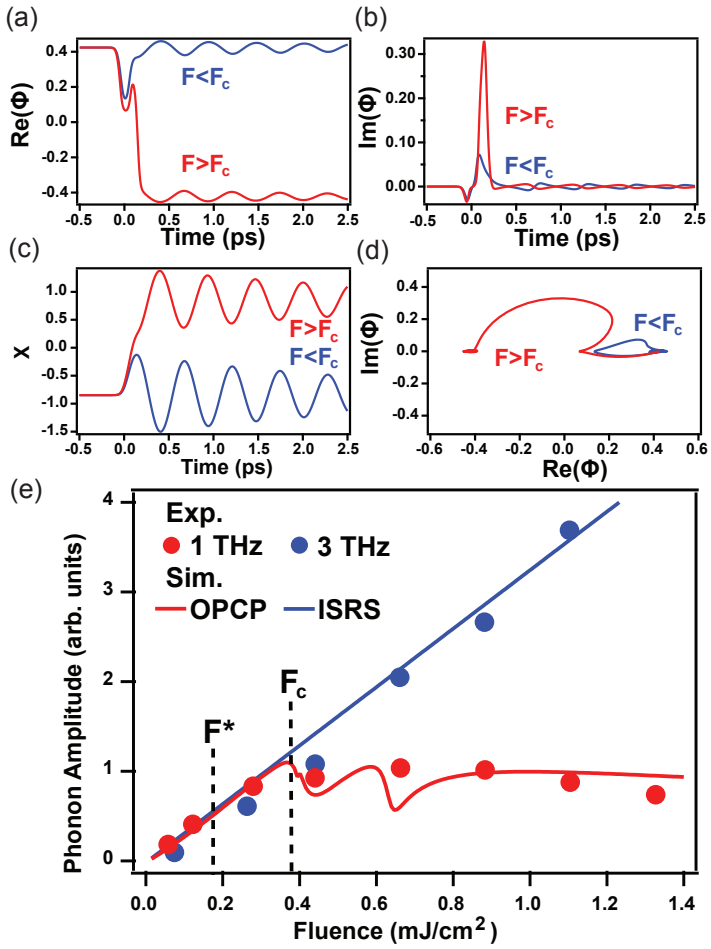

Figure 4.3: Simulated time evolution of (a) the real part of the electronic order parameter, (b) the imaginary part of the electronic order parameter, and (c) the lattice order parameter. (d) Trajectory of the electronic order parameter. (e) Experimental pump fluence dependence of the 1 THz (red circles) and 3 THz (blue circles) coherent phonon amplitudes in Ta_2NiSe_5 reproduced from Ref.(Werdehausen, Takayama, Höppner, et al., 2018). Simulation results for an OPCP (red line) and a conventional ISRS phonon (blue line) are overlaid and horizontally scaled to match the experimental data. Vertical dashed lines mark the calculated F_c and F^*.

the pre-pumped ($t < 0$) case [Figure 4.2(a)], sending Φ toward the new minimum on the negative side. As Φ crosses zero, the tilt of $V(X)$ is also reversed due to EPC, thus pushing X to the new minimum on the positive side. The system then continues to oscillate about the reversed minima at the phonon frequency until the OPCP is damped out [Figure 4.2(d)]. Note that this model treats light as a coherent drive without considering heating- and cooling-induced changes in $m(t)$. However, accounting for the latter merely shifts F_c.

We show the time evolution of the complex electronic order parameter Φ (real in equilibrium) and the real structural order parameter X in Figure 4.3(a)-(d) for two characteristic fluences: $F > F_c$ and $F < F_c$. A clear sign change of Re(Φ) and of X that occurs within 0.2 ps can be found with $F > F_c$, indicating the reversal of the EI order. Φ also transiently becomes complex during the process of reversal. Aside from sign change, a clear coherent oscillation reflecting OPCP can be identified in every channel. By taking the fast Fourier transform (FFT) of X in the time interval from 0 ps to 20 ps with different pumping fluence values, we obtain the pump fluence dependence of the OPCP amplitude defined as the peak height in the FFT spectra [Figure 4.3(e)]. A nonlinear behavior of the OPCP amplitude as a function of F is evident.

In lieu of probing the phase of X and Φ, we propose that the reversal can be identified via the pump fluence dependence of the OPCP amplitude. A conventional Raman-active phonon is coherently launched through either displacive excitation or impulsive stimulated Raman scattering (ISRS) (Stevens, Kuhl, and Merlin, 2002; Melnikov, O. Misochko, and Chekalin, 2011) with an amplitude that is linearly proportional to F. For $F < F_c$, the amplitude of an OPCP also scales linearly with F. In this regime the structural order parameter simply oscillates about the initial potential minimum and thus behaves like a conventional phonon. But once the initial displacement of $V(X)$ is large enough to enable escape to the opposite minimum ($F > F_c$), the amplitude ceases to grow. Order parameter reversal is thus marked by a saturation in the amplitude versus fluence curve.

Discussion

We argue that experimental evidence for this phenomenon already exists in published studies of Ta_2NiSe_5. Werdehausen *et al*. (Werdehausen, Takayama, Höppner, et al., 2018) performed ultrafast optical reflectivity measurements at T = 120 K using a pump photon energy of 1.55 eV and observed clear coherent oscillations of the 1 THz OPCP as well as the uncoupled 3 THz phonon (ISRS). The pump fluence dependence of these two mode amplitudes is reproduced in Figure 4.3(e). The 3 THz mode scales linearly with F, consistent with its assignment as a conventional phonon. In contrast, the 1 THz mode scales linearly with F only at low fluences and then saturates above ~0.4 mJ/cm^2, consistent with an order parameter reversal. By overlaying our simulation results atop these experimental curves, we find close agreement [Figure 4.3(e)].

Our theory also predicts that the exciton condensate should be transiently quenched $[m(t) \rightarrow 0]$ above a critical fluence $F = F^*$ where the condition $f(t) = |m|$ is satisfied. Eqs. 4.8 and 4.9 do not constrain F^* to coincide with F_c and our simulation shows that F^* is clearly lower than F_c in Ta_2NiSe_5 [Figure 4.3(e)]. Recently Tang *et al*. (Tangwei Tang et al., 2020) performed time- and angle-resolved photoemission spectroscopy (tr-ARPES) measurements on Ta_2NiSe_5 at $T = 30$ K and tracked the dynamics of the charge gap, a measure of Φ, immediately after pumping with 1.77 eV light polarized perpendicular to the chain direction. They found that the instantaneous gap size decreases linearly with increasing pump fluence and saturates above 0.29 mJ/cm^2, which was interpreted as the point where Φ transiently collapses. The fact that this fluence is lower than 0.4 mJ/cm^2, and is expected to be even lower if the experiment were conducted at 120 K, is consistent with our theory.

Also note that the OPCP amplitude as a function of pump fluence shows a non-monotonic behavior when $F > F_c$ [Figure 4.3(e)]. The amplitude of the "wiggles" and the fluence where they emerge are dependent on the specific values of the microscopic parameters. This behavior can arise from two factors: the strong feedback between the electronic and structural order parameter dynamics immediately after excitation and the back-and-forth reversal. In terms of the feedback between electronic and structural channels, because Φ always responds more rapidly than X, the subtle mismatch of the time when the two order parameters cross zero will influence the phonon amplitude [Figures 4.3(a) and (c)]. After careful examination of the dynamics of both channels at each pump fluence, we find that this temporal mismatch occurs twice as the pump fluence is increased, yielding the two "dips" above F_c in the overdamped case. On the other hand, as we show later in Figure 4.9, if the electronic channel is underdamped and a Higgs mode is launched, the order parameters can now also oscillate back-and-forth between the minima on either side of zero and gives rise to an even stronger non-monotonic behavior.

Our field theory description of the EI order parameter goes beyond the phenomenological time-dependent Landau theory (Huber et al., 2014; Zong, Dolgirev, Kogar, Erge çen, et al., 2019; R. Yusupov et al., 2010; Harter, D. M. Kennes, et al., 2018) in that it allows the order parameter to explore the tilted Mexican-hat potential in the complex plane and can be naturally linked to microscopic parameters of the underlying lattice model. While more details including extension beyond the mean-field limit ($\nabla \neq 0$), temperature dependence with $T > 0$, diffusion perpendicular to the surface (R. Yusupov et al., 2010), time-dependent damping (Huber et al., 2014),

and anharmonic phonon coupling (Muneaki Hase, Kitajima, et al., 2002) can be added to refine the simulations, our minimal microscopic theory already captures the most salient physics and experimental features. These ideas and dynamical protocols apply not only to excitonic insulators, but also to any system featuring a continuous-symmetry-breaking electronic order parameter induced by coupling to a structural order parameter, such as a charge ordered system coupled to a Peierls distortion or an orbital ordered system coupled to a Jahn-Teller distortion. Therefore the OPCP behavior revealed here may be a general fingerprint of electronic order parameter switching.

4.3 Experimental Results

To test our simulation results and thoroughly investigate the phonon modes, we conducted coherent phonon spectroscopy by measuring the time-resolved reflectivity of Ta_2NiSe_5. We impinged the sample with a pump (probe) pulse centered at 0.9 eV (1.55 eV) of 80 fs duration, since near-infrared light has been demonstrated to both efficiently launch and detect phonons (Werdehausen, Takayama, Höppner, et al., 2018; Mor, Herzog, Noack, et al., 2018; Bretscher, Andrich, Telang, et al., 2021; Bretscher, Andrich, Murakami, et al., 2021; Q. M. Liu et al., 2021; Mor, Herzog, Gole ž, et al., 2017; Okazaki et al., 2018; Takeshi Suzuki et al., 2021; Tianwei Tang et al., 2020; Baldini et al., 2020). Since our sample is monoclinic (orthorhombic) below (above) T_c, a and c axes are nonequivalent and thus features in-plane anisotropy. However, as shown later in Figure 4.7, our experiment results demonstrate that the phonons are insensitive to the pump polarization but very sensitive to the probe polarization. We thus fixed the pump polarization along the crystallographic a-axis and probe the reflectivity change along the direction bisecting a- and c-axes in our experiment without further specification.

Pump Fluence Dependence of Phonon Dynamics

Figure 4.4(a) shows the differential reflectivity transients for different pump fluence levels. Ensuing an instantaneous intensity increase upon pump excitation, the reflectivity transients exhibit a clear beating pattern overlaid with a decaying background. We fit the background with a double-exponential decaying function characterizing the electronic scattering (Werdehausen, Takayama, Albrecht, et al., 2018) and isolate the beating patterns characterizing the coexistence of multiple phonon modes [Figure 4.4(b)]. After performing a fast Fourier transform (FFT) to these background-subtracted curves, we found in total ten Raman-active phonon

modes centered around 1, 2, 3, 3.7, 4, 4.4, 5.3, 5.8, 6.5, and 7 THz [Figure 4.4(c)]. Previous Raman spectroscopy results have resolved all these modes and identified the 2, 4, and 4.4 THz phonons as B_{2g}-symmetry modes and the other seven modes as A_g-symmetry modes in the high temperature orthorhombic phase, while all these modes are assigned to A_g-symmetry in the low temperature monoclinic phase (K. Kim et al., 2021; Volkov et al., 2021; M.-J. Kim et al., 2020). Despite this static characterization, to the best of our knowledge, this is the first time that ten different phonon modes are clearly identified in time-resolved measurements of Ta_2NiSe_5, possibly due to a higher quality of our synthesized samples or a larger (smaller) bandwidth (time duration) of the pump pulse we employed in our experiments.

To distinguish whether different modes are EI-coupled or uncoupled, we investigate the pump fluence of frequency and amplitude of each mode. Owing to the clear separation of the ten modes in the frequency domain, we analyzed the FFT spectra at different pump fluences to obtain their fluence dependence [Figure 4.4(d)]. We fit the FFT spectra with multiple Lorentzian peaks representing different phonon modes to obtain their amplitude and frequency as a function of fluence. As the pump fluence is swept up from zero, different phonons exhibit distinct fluence dependence of amplitude and frequency. The amplitude of 1 and 2 THz phonon modes features a quasi-linear increase below 2 mJ/cm^2 but exhibits a saturation above [Figures 4.4(d) and (e)], consistent with the previous experimental results and the assignment of an OPCP (Ning et al., 2020). The saturation of OPCP amplitude thus unambiguously signifies the reversal of the EI order with F_c ~2 mJ/cm^2 at 80 K. On the contrary, the amplitude of 4, 4.4, 5.3, 5.8, 6.5, and 7 THz modes increases linearly with pump fluence, indicating their potentially uncoupled nature [Figures 4.4(d) and (f)]. We want to note that although 4 and 4.4 THz modes respect B_{2g} symmetry, identical to the symmetry that breaks at T_c, they do not show amplitude saturation like 1 and 2 THz modes.

We can compare the calculated F_c with the experimental value. To get the value of the simulated critical fluence F_c in real units, we explicitly write out the scaling factor $\alpha = \frac{8Dq^2d^2(1-R)}{\hbar^2\omega_{ph}{}^2c\epsilon_0\sigma}$, where D is the parameter defined in Section 4.2, q is electron charge, d is the lattice constant, R is the reflectance, $\hbar$ is the reduced Planck's constant, ω_{ph} is the pump light frequency, c is the speed of light, ϵ_0 is the vacuum permittivity, σ is the pulse duration. We obtained a simulated $F_c \sim 6$ mJ/cm^2, qualitatively matching the real experimental F_c. Possible factors that can give rise to this discrepancy include the uncertainties in determination of microscopic

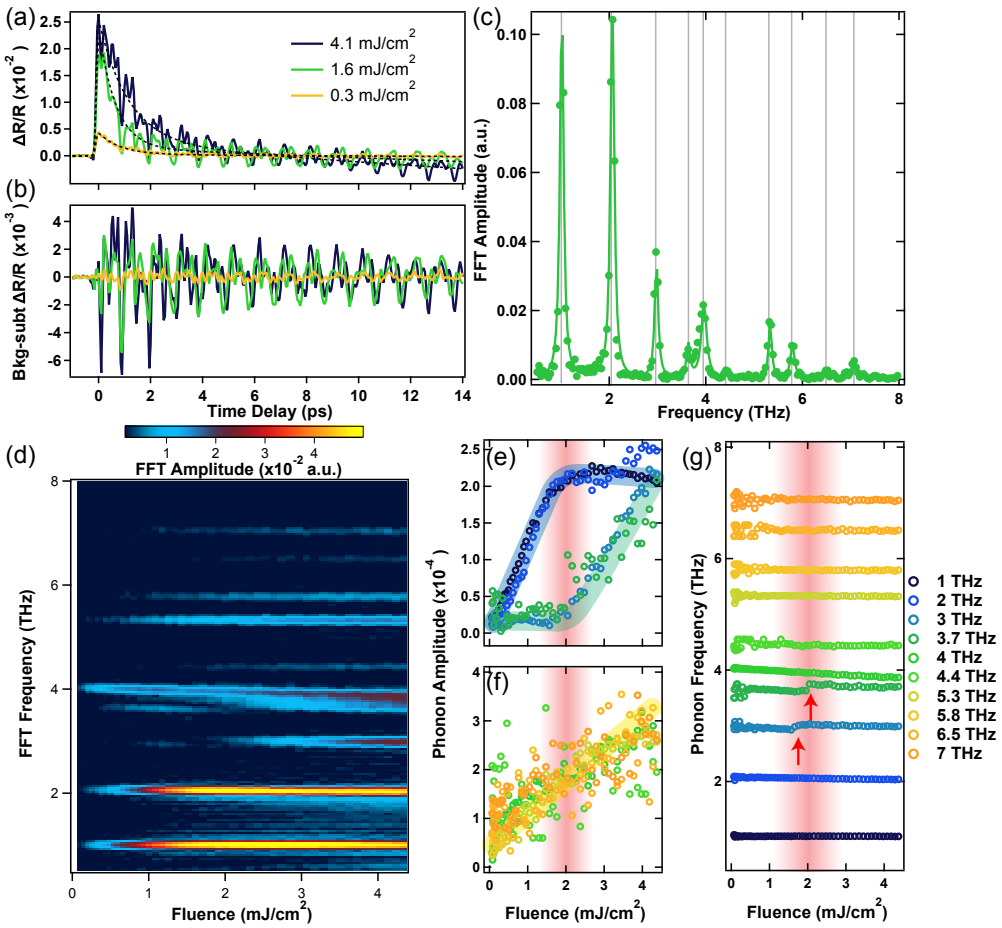

Figure 4.4: Pump fluence dependence of phonon amplitudes and frequencies. (a) Differential transient reflectivity curves at select pump fluences with pump along a-axis at 80 K. The dashed lines are fits to a double-exponential decay. (b) Background-subtracted curves of reflectivity transients in (a). (c) FFT spectrum of the background-subtracted reflectivity transient with 1.6 mJ/cm^2 pump as shown in (b) overlaid by multi-Lorentzian fits. The gray lines denote the position of the ten phonon modes. (d) Pump fluence dependent FFT spectra. (e),(f) Pump fluence dependence of the amplitude of different phonon modes obtained by Lorentzian fitting to FFT spectra in (d). The thick lines are guide to eye. (g) Pump fluence dependence of the frequency of different phonon modes by Lorentizain fitting to FFT spectra in (d). The red arrows denote the frequency blueshift. The red shaded bar indicates the critical fluence regime.

parameters, temperature dependence of F_c, transient heating, and other possible factors that are not accounted for in our microscopic model.

However, inconsistent with the previous assignment of an uncoupled phonon, the amplitude of 3 and 3.7 THz modes exhibit a threshold-like superlinear increase with the pump fluence at F_c [Figure 4.4(e)]. We note that this behavior almost

exclusively occurs at low temperatures and at specific probe polarization angles. In the other cases, a linear increase of amplitude of the two modes as a function of fluence is resolved. The superlinear increase of 3 THz mode has been observed before (Werdehausen, Takayama, Höppner, et al., 2018) but without interpretation. Recent experiments suggest the 3 and 3.7 THz mode can couple to the Goldstone mode of the EI condensate, which may indicate the superlinear behavior of these two modes may be a reflection of EI order reversal as well. This hypothesis goes beyond the scope of our microscopic model and further investigation is needed to quantitatively understand the behavior of these two modes.

More intriguingly, we notice that accompanied by the amplitude anomaly at F_c, a sudden frequency blueshift of 3 and 3.7 THz modes can be clearly identified, while the other modes just show a moderate softening over fluence without any abrupt change at F_c [Figure 4.4(g)]. Due to the hardening of the 3.7 THz mode and the softening of the 4 THz mode, the two modes merge into one at around F_c [Figure 4.4(d)]. This has also been observed before (Q. M. Liu et al., 2021) but without interpretation. The merger of phonons usually indicates a structural change, which is consistent with the picture of EI order reversal but beyond the scope of our microscopic model.

Our time-resolved measurement can not only track the fluence dependence of the phonon amplitude and frequency but also provide information about the phase of different modes as a function of pump fluence. As aforementioned, due to the coexistence of multiple modes, it is challenging to directly fit the background-subtracted reflectivity transients with damped sinusoidal functions to get the phonon phase. Instead, two complementary approaches can be applied to obtain the phonon phase. The first method is applying a bandpass filter centered around the target phonon frequency (± 0.15 THz) to the background-subtracted reflectivity traces, enabling us to isolate a single phonon mode in the time domain. We can then check the phase of this mode as a function of fluence. The second method is based on complex FFT. Phonons with different phases will show distinct shapes in the real and imaginary FFT components [Figure 4.5(e)]. A simultaneous fit of the real and imaginary spectra enables an accurate determination of phonon phase.

Since phonons are in general launched via displacive excitation or impulsively stimulated Raman scattering (Chapter II, Section 2.3), we round the phonon phase to the closest multiples of $\pi/2$ to understand their generation mechanism and summarize the phase of different phonons in the following table. Based on the cross-check

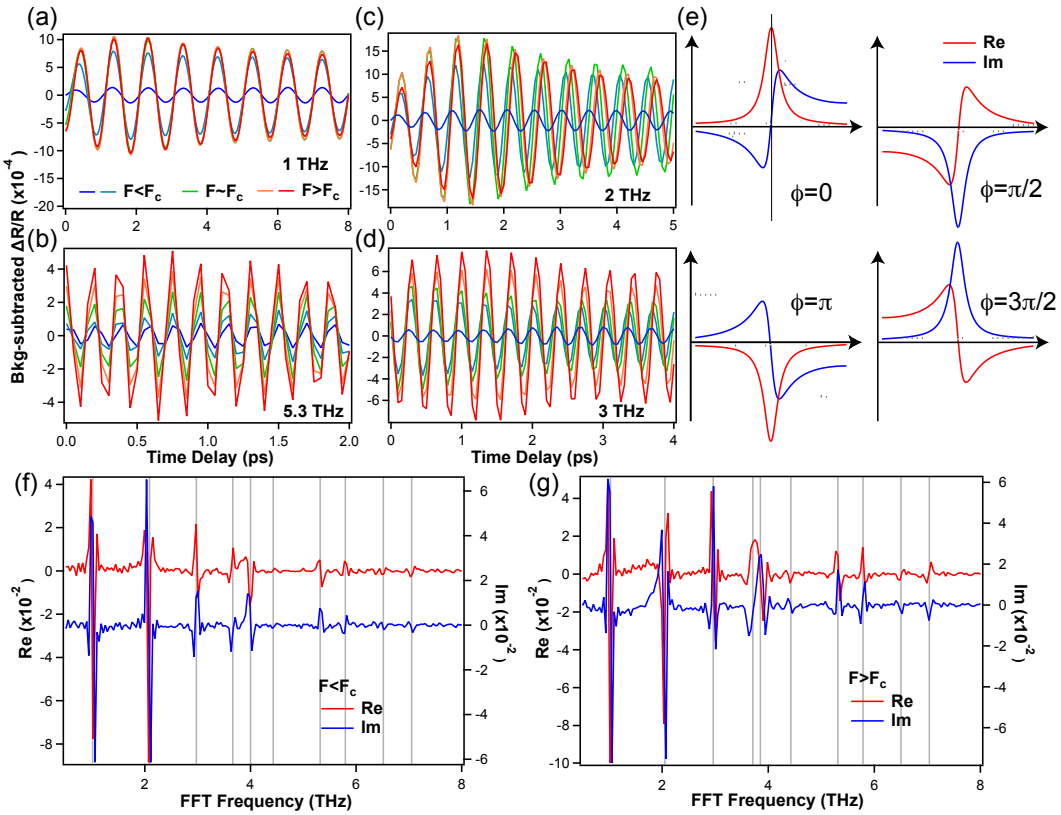

Figure 4.5: Fluence dependence of phonon phases. (a)-(d) 1, 5.3, 2, and 3 THz bandpass-filtered background-subtracted reflectivity transients at select fluences. (e) Complex FFT spectra of a damped cosine function with different characteristic phase shift ϕ. The grey line denotes the phonon frequency. (f),(g) Complex FFT spectra of two background-subtracted reflectivity transients with pump fluence below and above F_c. The grey lines denote the phonon frequencies.

through the aforementioned two methods, we found the phase of most of phonons do not change dramatically with fluence [Figures 4.5(a),(b),(f),(g)]. However, the phase of 2, 3 and 4.4 THz phonons show a change as can be clearly seen in both the filtered time traces and the shape change in complex FFT spectra [Figure 4.5(c),(d),(f),(g)], where 2 and 3 THz phonons exhibit a $\pi/2$ change at low and high fluences, while 4.4 THz phonon undergoes a π change. Note that across the F_c regime the phase of these phonons indeed shows an obvious change, although their phase also changes with fluence in the rest of fluence regimes moderately. Previous ultrafast measurements reported that the phonon phase may change across thermal phase transitions arising from the competition between diverse generation mechanisms (Ron et al., 2020; M.-C. Lee, C. H. Kim, Kwak, J. Kim, et al., 2018; M.-C. Lee, C. H. Kim, Kwak,

Seo, et al., 2019). In our case, an reversal of order cannot be directly considered as a phase transition since the microscopic parameters dictating the physical properties of the system do not alter. The phase shift is not predicted by our microscopic model and further theoretical modelling is needed to understand this phenomenon.

Phonon	$F < F_c$	$F > F_c$
1 THz	π	π
2 THz	π	$\pi/2$
3 THz	0	$3\pi/2$
3.7 THz	0	$3\pi/2$
4 THz	π	π
4.4 THz	0	π
5.3 THz	$3\pi/2$	$3\pi/2$
5.8 THz	0	0
6.5 THz	$\pi/2$	$\pi/2$
7 THz	$\pi/2$	$\pi/2$

Table 4.1: Phonon phases below and above the critical fluence measured at 80 K.

Temperature Dependence of Phonon Dynamics

To further demonstrate the amplitude saturation of 1 and 2 THz phonons is indeed induced by EI order reversal, we conducted the pump fluence dependent coherent phonon spectroscopy at several temperatures across T_c. We first check the temperature dependence of the transient reflectivity at a fixed pump fluence. The electronic background of the transient reflectivity curves exhibits a transformation from double-exponential decay at low temperature into an exponential increase followed by an exponential decay at $T > T_c$ [Figure 4.6(a)]. Moreover, as the temperature increases, the amplitude, lifetime, and frequency of different phonons show a systematic change: the amplitude of the 1, 2, 4, and 4.4 THz modes display a strong suppression, while the amplitude of the 3 and 3.6 THz modes shows a nonmonotonic change against temperature increase [Figure 4.6(b)], consistent with the previous reports (Mor, Herzog, Noack, et al., 2018; Bretscher, Andrich, Telang, et al., 2021; Q. M. Liu et al., 2021). The amplitude of the rest uncoupled phonons also show a decrease over temperature. In terms of phonon lifetime, the 2 THz mode shows a much more pronounced broadening than the other modes as temperature increases, corroborating its strong coupling to the EI order. With regard to frequency, the 2 THz phonon also exhibits a considerable redshift over 0.4 THz, while the other modes only show moderate softening.

We then interrogate the fluence dependence of the amplitude of different modes

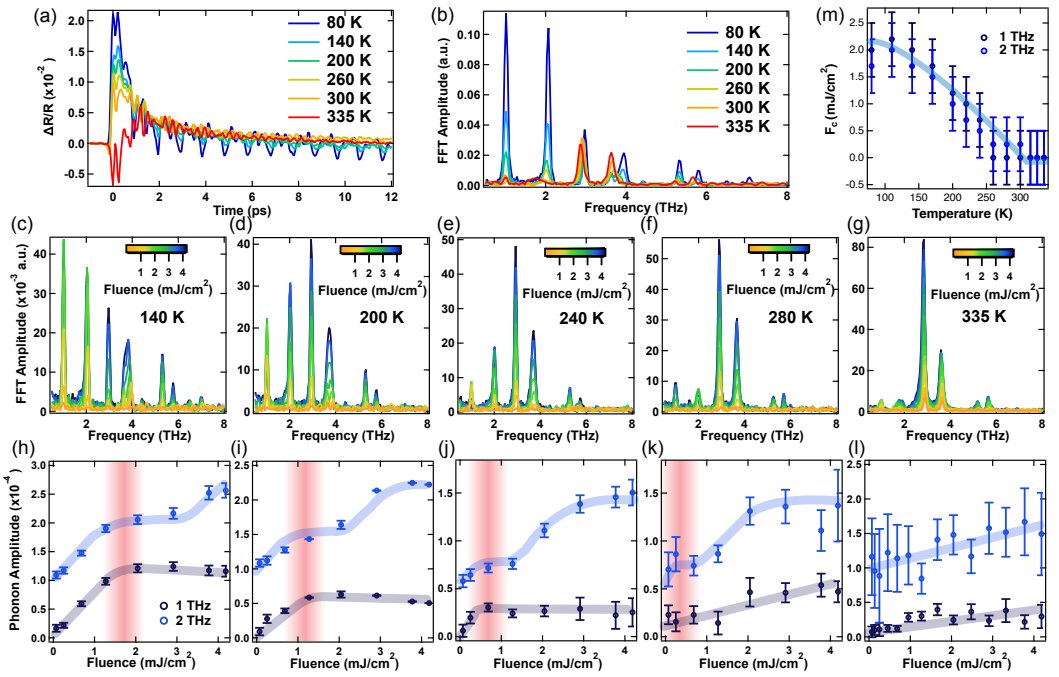

Figure 4.6: Temperature dependence of the phonons. (a) Differential transient reflectivity curves at select temperatures with pump at 2 mJ/cm^2 along a axis. (b) FFT spectra of background-subtracted transient reflectivity curves in panel (a). (c)-(g) Pump-fluence dependent FFT spectra at select temperatures. (h)-(l) Pump fluence dependence of the amplitude of 1 and 2 THz phonon modes obtained by fitting to FFT spectra in panels (c)-(g). The amplitude of 2 THz mode is vertically offset for clarity. (m) Temperature dependence of the critical fluence for 1 and 2 THz phonons. All the thick lines are guide to eye.

across a large temperature range. The FFT spectra are displayed in Figures 4.6(c)-(g). At all temperatures, the amplitude of 3, 3.7, 5.3, and 6 THz show increase with fluence without saturation akin to 80 K. The amplitude of 1 THz phonon, on the other hand, saturates at a critical fluence F_c at all temperatures below 280 K. Above 280 K, the amplitude of 1 THz mode increases with fluence quasi-linearly like an uncoupled phonon. More intriguingly, F_c displays an apparent decrease as the temperature increases [Figures 4.6(h)-(l)]. This is expected as according to our theory, the value of F_c is determined by the shape of $V(\Phi)$. As temperature approaches T_c from below, the EI order is suppressed and $V(\Phi)$ will gradually recover a parabolic form. Accordingly, the minimum of $V(\Phi)$ will become shallower and Φ_0 will get closer to $\Phi = 0$ and so the reversal of the EI order is expedited more easily. A finer scan of temperature shows that F_c almost follows an order-parameter-like onset at around 300 K, substantiating our expectation. Note that the disappearance

of saturation is not strictly at T_c = 325 K. An estimate of temperature increase of about 30 K with 2 mJ/cm^2 incident pump fluence in the whole temperature range we investigated indicates that laser heating can effectively raise the sample surface temperature above T_c at around 300 K.

It is noteworthy that the amplitude of 2 THz mode depict a nontrivial nonlinear dependence over fluence at different temperatures. With a more careful check on Figure 4.4(e), we find that the amplitude of 2 THz mode increases again at around 3.5 mJ/cm^2 after the saturation at 2 mJ/cm^2. The revival of amplitude increase above F_c is more evident at 140 K [Figure 4.6(h)]. A second saturation emerges at 200 K and becomes an apparent plateau at 240 and 280 K [Figures 4.6(i)-(k)]. At 335 K above T_c, however, the double-saturation behavior vanishes, demonstrating its direct relevance to EI ordering. Analogous to the first saturation critical fluence F_c which closely follows F_c of 1 THz as a function of temperature [Figure 4.6(m)], the second saturation fluence also shows a salient decrease with temperature and vanishes at around 300 K.

We notice that although the double-saturation behavior is not explicitly captured by our microscopic model, our model indeed predicts the non-monotonic amplitude "wiggles" as a function of pump fluence when $F > F_c$ in Section 4.2. If we assume the EI order does not adiabatically follow the evolution of $V(\Phi)$, a high-frequency electronic oscillation also known as Higgs mode can be generated. In this underdamped case, the order parameters can now oscillate back and forth between the minima of potentials on both sides of zero, rendering a strong non-monotonic behavior. The order parameter is more susceptible to reversal upon small changes in pump fluence as temperature approaches T_c and the back-and-forth reversal will disappear when $T > T_c$. All of these predictions match our experimental observation. Moreover, recent ultrafast photoemission results highlighted that the electronic spectral weight, which is an observable of charge density wave order parameter, shows similar non-monotonic wiggles over fluence when the charge density wave is inverted and domain wall forms (Duan et al., 2021). These results lead us to tentatively attribute our double-saturation behavior of 2 THz phonon to the back-and-forth reversal of EI order.

Pump and Probe Polarization Dependence of Phonon Dynamics

Note that there existed inconsistency in the previous experiments about whether the transient reflectivity and EI condensate are sensitive to the pump and probe

polarizations (Werdehausen, Takayama, Höppner, et al., 2018; Bretscher, Andrich, Telang, et al., 2021). We thus performed pump- and probe-polarization dependent measurements to reconcile the controversy. We first fixed the probe polarization to be along the direction bisecting $a-$ and $c-$axes and changed the pump polarization to be either parallel to $a-$ or $c-$axis with a constant fluence at around 2 mJ/cm^2. We notice that other than a moderate change in the electronic background no obvious change in phonon frequency and amplitude can be detected [Figure 4.7(a)]. This observation is consistent with one of the recent time-resolved reflectivity results (Bretscher, Andrich, Telang, et al., 2021) but in contrast to a previous one (Werdehausen, Takayama, Höppner, et al., 2018). We then swept the pump fluence up and a saturation of amplitude of the 1 and 2 THz phonons are present in both pumping cases, although a slightly larger F_c for pump parallel to $a-$axis is obtained. This observation is in line with our theory. According to our theory, F_c is determined by the the effective scaling factor α. Because d and $1-R$ are both larger for $c-$axis, while the other parameters for the two pump polarization directions, α is larger for $c-$axis. Therefore, with the same nominal fluence F, pump along $c-$axis can generate a larger quench to the EI condensate and thus F_c should be reached sooner.

The phonons are yet very sensitive to the probe polarization. We fixed the pump polarization along $a-$axis with a constant fluence at around 0.9 mJ/cm^2 ($<F_c$ at 80 K) and finely tuned the probe polarization. A clear two-fold symmetry of all phonon modes can be evidently seen in the FFT spectra [Figure 4.7(b)] with the local maxima or minima along either $a-$ or $c-$axis. We fit the FFT spectra in Figure 4.7(b) with multi-Lorentzians and polar-plotted the amplitude of different modes as a function of probe polarization angle [Figures 4.7(c)-(l)]. It is evident that the 1, 2, 3, and 3.6 THz phonons exhibit four petals and four nodes, while the high-frequency modes are nodeless. We found that the phase of these low-frequency modes flips when the probe is polarized along $a-$ and $c-$axes, further demonstrating the presence of nodes.

The symmetry of different phonons is captured by the Raman tensors: (K. Kim et al., 2021), where in our experimental coordinate we have:

$$\chi^R_{A_g,T<T_c} = \begin{pmatrix} a & d & 0 \\ d & b & 0 \\ 0 & 0 & c \end{pmatrix}, \chi^R_{A_g,T>T_c} = \begin{pmatrix} a & 0 & 0 \\ 0 & b & 0 \\ 0 & 0 & c \end{pmatrix}, \chi^R_{B_{2g},T>T_c} = \begin{pmatrix} 0 & d & 0 \\ d & 0 & 0 \\ 0 & 0 & 0 \end{pmatrix}. \quad (4.10)$$

Note that the all the phonons at $T < T_c$ respect A_g symmetry and thus can be fit with a single Raman tensor, while the 2 THz phonon (as well as 4 and 4.4 THz

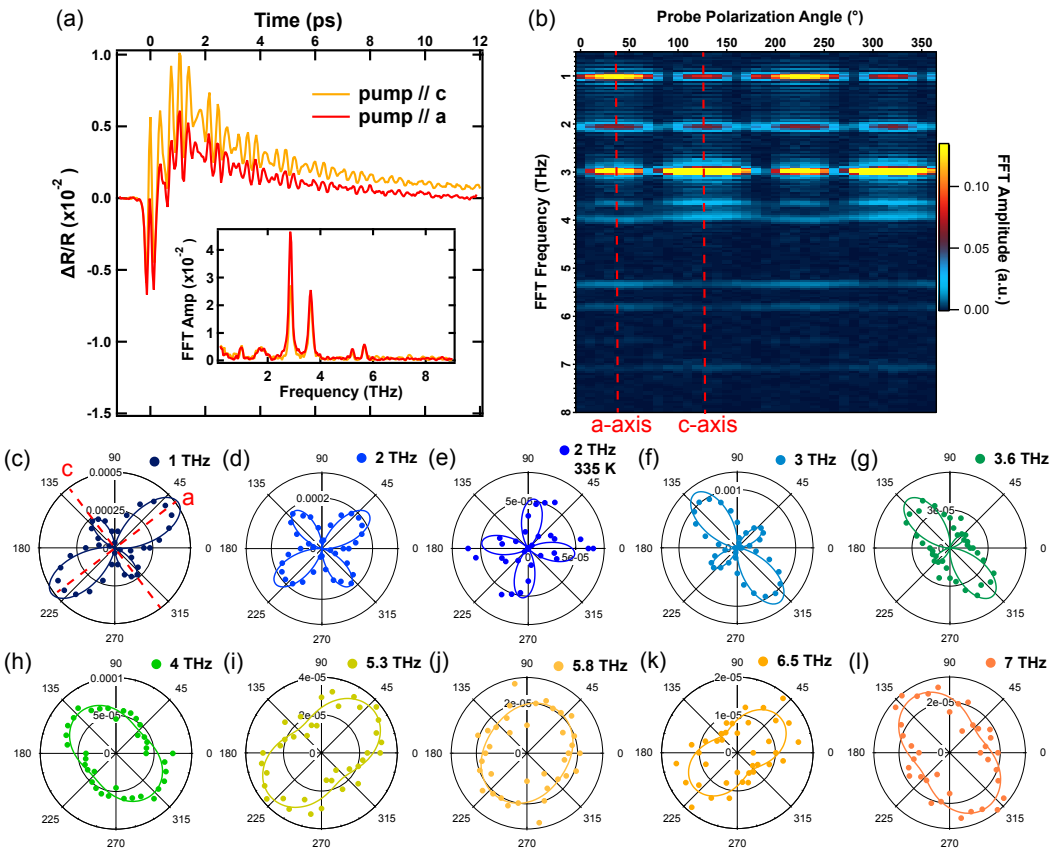

Figure 4.7: Pump and probe polarization dependence of different phonons. (a) Pump polarization dependent reflectivity transients measured at 335 K with a fluence of 2 mJ/cm^2. The inset shows their FFT spectra. (b) Probe polarization dependence of FFT spectra measured at 80 K with pump polarization parallel to a axis and fluence at 0.9 mJ/cm^2. The red dashed line denotes the a and c axes of the sample. (c)-(l) Probe polarization dependence of the amplitude of 1 THz, 2 THz, 2 THz at 335 K, 3 THz, 3.7 THz, 4 THz, 5.3 THz, 5.8 THz, 6.5 THz, and 7 THz phonons, respectively, overlaid with fits to corresponding Raman tensors. The data from 180 to 360 ° is symmetrized from the data taken from 0 to 180 °.

modes, although they cannot be detected in our experiment at $T > T_c$) respects B_{2g} symmetry at $T > T_c$. The change in the petal direction from along to away from crystallographic axes can be clearly observed across T_c in 2 THz mode [Figure 4.7(e)]. On the contrary, no qualitative change in shape and rotation angle can be observed in the other modes. This is in accord with the extremely subtle structural symmetry breaking at T_c but at odds with the recent Raman spectroscopy results where the polar pattern of multiple modes exhibits a noticeable change in both shape and rotation across T_c (K. Kim et al., 2021).

In summary, our comprehensive coherent phonon spectroscopy measurements reveal a myriad of rich phenomena of OPCPs in Ta_2NiSe_5. Our pump fluence dependent measurements corroborate the previous reported amplitude saturation of 1 and 2 THz modes at low temperature and thus confirm their OPCP nature. We also found that the amplitude of 3 and 3.6 THz modes may show a superlinear increase at F_c, the frequency of 3 and 3.6 THz modes exhibits a sudden blueshift at F_c, 3.6 and 4 THz modes merge into one at high fluence, and the phase of 2, 3 and 4.4 THz modes exhibits a remarkable shift around F_c. We further for the first time demonstrate that the 5.3, 5.8, 6.5, and 7 THz modes are conventional uncoupled phonons due to their lack of anomaly at F_c. Our temperature-dependent results reveal that the amplitude of the 2 THz mode exhibits multiple nonlinearity which may reflect the multiple reversal of EI order as temperature gets close to T_c. Our polarization dependent measurements showcase the insensitivity of phonon dynamics to pump polarization and sensitivity to probe polarization. Although more experimental studies and theory development are needed to fully understand the nature of 3, 3.6, 4, and 4.4 THz phonons, our experimental results not only corroborate the OPCP amplitude saturation at F_c reversal but uncover a multitude of new phonon anomalies accompanying the EI order reversal.

4.4 Control of the Excitonic Order Reversal via Two-Pulse Pumping

The dynamical nature of the order parameter reversal process suggests that it can be controlled not merely by the total pump energy deposited, but also by its distribution in time. To show this, we consider a situation where the sample is pumped by two identical pulses separated by time δt, with individual fluences $F < F_c$ but $2F > F_c$. For $\delta t \rightarrow 0$ the system is effectively pumped by a single pulse exceeding F_c and so reversal occurs, while for $\delta t \rightarrow \infty$, the system relaxes back to the initial ground state before the second pulse arrives and so no reversal occurs. To qualitatively understand the behavior at intermediate δt values where the system is still dynamically evolving when the second pulse arrives, we recall that in the single pulse case, switching occurs once the OPCP amplitude is large enough to change the sign of X. Therefore, in the two-pulse case, switching possibly occurs if coherent oscillations of the OPCP induced by the first pulse can be sufficiently amplified by the second time-delayed pulse.

Previous studies have shown that impulsively and displacively excited conventional Raman-active phonons can be coherently amplified (suppressed) by a second pump pulse when δt is an integer (half-integer) multiple of the phonon period (M. Hase

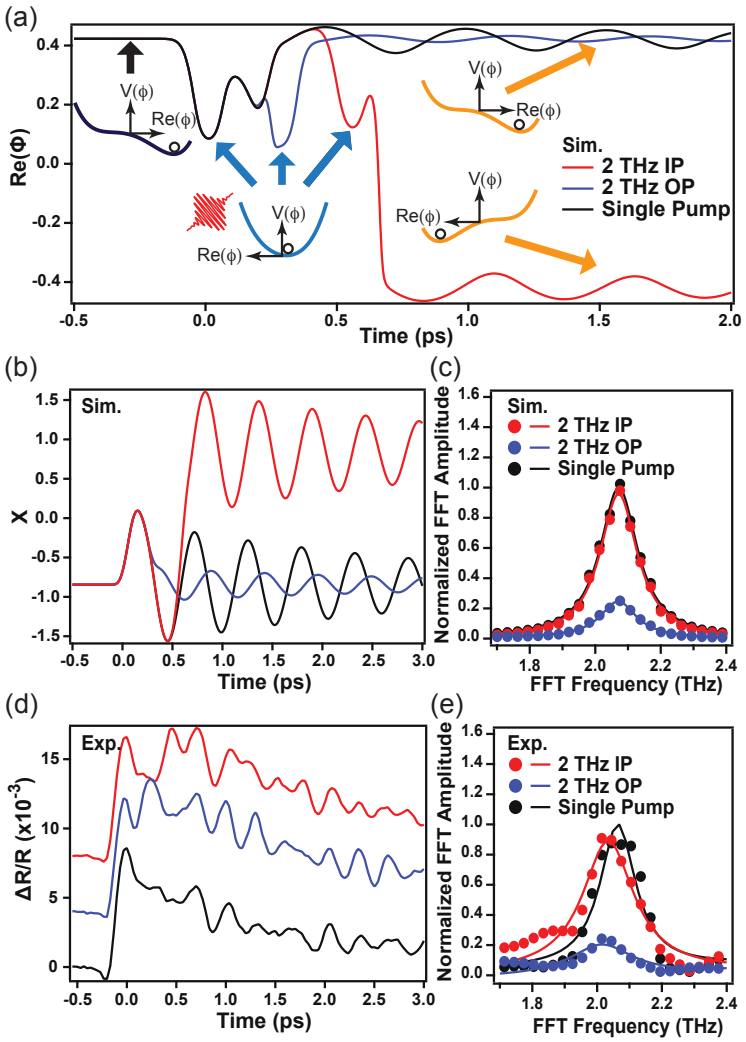

Figure 4.8: Control of EI reversal via two-pulse pumping. Simulated time evolution of (a) Re(Φ) and (b) X following single-pulse pumping (black) and two-pulse OP (blue) and IP (red) pumping of the 2 THz phonon using $F = 0.96F_c$ and the same microscopic parameters as in Figs. 2 and 3. The calculated instantaneous electronic potential is displayed at several select times. (c) Normalized FFT of the traces shown in (b). Each curve is normalized by the peak value of the single-pulse pumping curve. (d) Reflectivity transients measured from Ta_2NiSe_5 under the same pumping conditions used in the simulations. Curves are vertically offset for clarity. (e) Normalized FFT of the traces shown in (d).

et al., 1996; Muneaki Hase, Itano, et al., 1998; Murray et al., 2005; O V Misochko et al., 2007; Wu and X. Xu, 2007; Y.-H. Cheng, F. Y. Gao, et al., 2017), dubbed in-phase (IP) and out-of-phase (OP) pumping respectively. Therefore we simulated the effects of both IP and OP pumping on the order parameters of Ta_2NiSe_5 using the same material parameters as before. We chose to simulate the OPCP at $\omega_0/2\pi$

= 2 THz rather than at 1 THz because recent tr-ARPES data show that the most pronounced modulations of the valence band maximum occur at 2 THz, suggesting strong coupling to Φ (Takeshi Suzuki et al., 2021). As shown in Figure 4.8(a), pumping by a single pulse with F slightly less than F_c causes a rapid but incomplete reduction of Φ, followed by a slower recovery back to its original value on a timescale set by the damping of the 2 THz phonon. For the two-pulse case, OP pumping of the 2 THz phonon similarly leads to partial suppression of Φ without reversal, but reversal is achieved with IP pumping. This phenomenon is again manifested through an unconventional behavior of the OPCP. As shown in Figures 4.8(b) and (c), OP pumping leads to suppression of the 2 THz phonon amplitude relative to the single pump case, resembling a conventional phonon because the oscillation is around the initial potential minimum. But, in contrast to conventional behavior, IP pumping does not lead to further amplification once X is excited to the opposite minimum.

To verify this prediction, we performed transient optical reflectivity measurements on Ta_2NiSe_5 single crystals using two identical pump pulses (σ = 80 fs) with variable δt. The light was polarized perpendicular to the chain direction and the fluence of each pulse was tuned slightly below F_c to match our simulations. We chose a pump photon energy of 1 eV to enhance the 2 THz oscillations. Figure 4.8(d) shows the fractional change in reflectivity ($\Delta R/R$) versus time for both IP and OP pumping of the 2 THz phonon, as well as for pumping with only a single pulse. All three curves exhibit fast (~1 ps) exponential decay following pump excitation, corresponding to the charge relaxation process. Oscillations from the beating of several coherently excited phonons are also clear. A FFT of the data shows the most pronounced peaks at 2, 3, and 3.8 THz. A focus on the 2 THz mode reveals that OP pumping strongly suppresses its amplitude relative to the single-pump case whereas IP pumping does not amplify it [Figure 4.8(e)], in quantitative agreement with our simulations [Figure 4.8(c)]. We thus demonstrate a temporal control of the EI order reversal.

4.5 Resonant Amplification of the Higgs mode

Spontaneous breaking of continuous U(1) symmetry in the EI transition can induce two types of collective electronic excitations. One is the gapless phase mode dubbed the Nambu-Goldstone mode, and the other is the gapped amplitude mode dubbed the Higgs mode. Due to the further lowering of symmetry to Z_2 stemming from the strong EPC in Ta_2NiSe_5, however, the Goldstone mode also gains mass and gaps out. The amplitude mode typically located in the THz range can be coherently excited by an impulsive or displacive light stimulus, and has been observed extensively

in multiple superconductors upon THz pump (Matsunaga, Hamada, et al., 2013; Matsunaga, Tsuji, et al., 2014; Katsumi et al., 2018) and CDW systems upon overgap excitation (R. Yusupov et al., 2010; Zong, Kogar, et al., 2019). A recent theory also demonstrates that Higgs mode can mediate a parametric amplification of incident radiation through nonlinear coupling (Buzzi et al., 2021).

However, to date, no direct evidence of Higgs mode has been demonstrated in the EI candidate Ta_2NiSe_5. The reason can be threefold: first, based on our microscopic model, the predicted Higgs mode frequency ω_{Higgs} is around $2\pi\times17$ THz ($\sim|m|$). According to the Nyquist–Shannon sampling theorem, we need a pulse with duration shorter than 25 fs to probe such quick dynamics. Second, similar to the superconductors, THz pump with energy at half of the Higgs mode frequency is required to generate the Higgs mode, because Higgs mode is Raman-active and thus a two-photon absorption is needed to resonantly excite this mode. However, intense light source in this frequency range is challenging to realize technically and so far no THz pump experiment has been reported on Ta_2NiSe_5. Third, the Higgs mode can decay into a pair of Goldstone modes with half of the Higgs mode energy and opposite momenta. Therefore, the Higgs mode can be very short-lived in time domain. If its decay rate is larger than its frequency, the Higgs mode will be overdamped and not emerge as a coherent oscillation in time domain.

We thus theoretically investigate the amplification of Higgs mode to shed light on future experiments. Based on the equations of motion Eqs.4.8 and 4.9, we can obtain the dynamics of the Higgs mode as a function of both pump photon energy and fluence. Note that two new treatments are required: first, we need to set γ_e smaller than ω_{Higgs} so that the Higgs oscillation is underdamped. A large γ_e describes the overdamped case where the electronic subsystem adiabatically evolves into the transient free energy minimum, while a small γ_e captures the underdamped case which explores a larger region of the Mexican-hat potential via rapid Higgs oscillations upon light excitation; second, we need to retain the the oscillatory part in the light induced modulation $f(t) = \alpha F \exp\left(-\frac{4\ln(2)t^2}{\sigma^2}\right)\sin^2(\omega t)$ to characterize the light with different energies. Also, α at different photon energies needs to be rescaled by $\frac{1}{\omega^2}$ to ensure an identical light field strength for all the pump energies.

We show the dynamics of the complex electronic order parameter Φ and the real structural order parameter X in Figure 4.9(a)-(d) for two characteristic fluences above and below F_c for a pump energy $\omega = 2\pi \times 240$ THz, much larger than Δ and representing the overgap excitation case. Compared with Fig 4.3(a)-(d), the clear

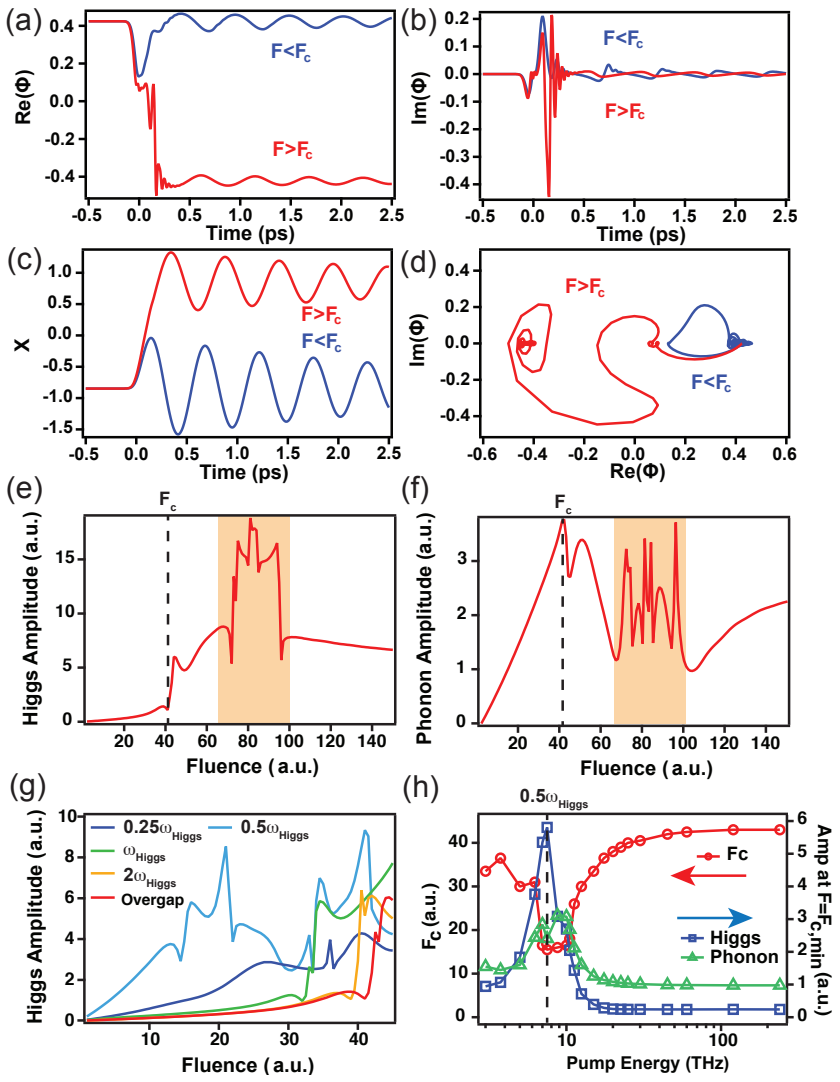

Figure 4.9: Simulation of Higgs mode dynamics. Simulated time evolution of (a) the real part of the electronic order parameter, (b) the imaginary part of the electronic order parameter, and (c) the lattice order parameter, in the underdamped case with overgap pumping. (d) Trajectory of the electronic order parameter. (e) Pump fluence dependence of the Higgs mode amplitude with overgap pumping. (f) Pump fluence dependence of the OPCP amplitude with overgap pumping. Vertical dashed lines mark the calculated F_c. The orange shaded region characterize the unstable reversal region where multiple reversals occur. (g) Pump fluence dependence of the Higgs mode amplitude with several characteristic pump photon energy. (h) Pump photon energy dependence of F_c and amplitude of Higgs and OPCP at the lowest $F_c = 13$. Vertical dashed line marks the frequency around half of the Higgs mode.

reversal is realized when $F > F_c$ independent of the value of γ_e. However, aside from the slow oscillation which exists in both Φ and X representing the coherent phonon, a fast oscillation emerges upon light excitation exclusively in the electronic

channel and quickly damps out within 0.25 ps, which is the Higgs mode. By applying FFT to the amplitude $|\Phi(t)|$, we find the Higgs mode peaks at around 15 THz and spans from 5 to 30 THz range. We define the Higgs amplitude as the area between 5 to 35 THz of the Higgs mode in the FFT spectra. The phonon amplitude is defined in the same way as aforementioned.

We first keep $\omega = 2\pi \times 240$ THz and sweep the fluence. The amplitude of the Higgs mode and OPCP is shown in Figures 4.9(e) and (f). Compared with the overdamped case, alteration of γ_e has a minimal affect on F_c. However, the non-monotonic behavior in X is stronger for the underdamped case due to the Higgs oscillations in Φ. The feedback between the two channels also lasts longer, creating more complicated dynamics. In addition to the mismatch between the time when X and Φ cross zero as discussed in the overdamped case, the order parameters can now also oscillate back-and-forth between the minima on either side of zero. This makes the final state more sensitive to pump fluence compared to the overdamped case. In other words, the order parameter is more susceptible to reversal upon small changes in pump fluence, leading to sharper modulations of the phonon amplitude especially in a fluence region around $2F_c$. Moreover, unlike X, the Higgs amplitude does not show saturation but exhibits nonlinear enhancement when $F \sim 2F_c$.

We now change ω to several characteristic values and investigate the pump fluence dependence of Higgs amplitude [Figure 4.9(g)]. Notably, as ω is close to ω_{Higgs}, the reversal is more easily facilitated, i.e. F_c is smaller, compared with the overgap excitation. By finely sweeping ω, we find F_c is lowest when $\omega = 0.5\omega_{Higgs}$ [Figure 4.9(h)]. Moreover, if we track the Higgs mode amplitude at this specific fluence $F_{c,min} = 13$ with different ω, we find it also resonantly peaks at $\omega = 0.5\omega_{Higgs}$ [Figure 4.9(h)]. Similar maximum is observed in phonon amplitude as well. This coincidence demonstrates that the Higgs mode is most efficiently generated and the EI order parameter is most efficiently reversed at $\omega = 0.5\omega_{Higgs}$, revealing the strong coupling between the electronic and structural DoF in EI. This is expected since our light field is coupled to m quadratically, in agreement with the Raman symmetry of the Higgs mode. Also notice that only little variance can be found when $\omega > \omega_{Higgs}$.

In summary, our simulation systematically explores pump photon energy and fluence dependence of the Higgs mode amplitude and reversal critical fluence. We demonstrate that the most efficient amplification of Higgs mode accompanied by the most efficient reversal of EI order can be realized with a pump photon energy at half

of the Higgs mode energy. Further measurements conducted with short probe pulse ($\sigma < 20$ fs) and intense pump pulse in THz range are required to experimentally prove our theory.

Chapter 5

Ultrafast Switch of Quadrupolar Order in Ca_2RuO_4

5.1 Introduction

Impulsive optical excitation provides nonthermal pathways to bring the system to parts of the potential energy surface that are inaccessible in equilibrium. Ultrafast switch of order parameter to its nonequilibrium "hidden" counterpart has been demonstrated in a plethora of systems with structural order (Teitelbaum et al., 2018; Sie, Nyby, et al., 2019; Q. M. Liu et al., 2021), charge order (Stojchevska et al., 2014; Kogar, Zong, et al., 2020), magnetism (J. Zhang et al., 2016; T. Li et al., 2013), superconductivity (Mitrano et al., 2016), orbital order (Ichikawa et al., 2011), and ferroelectricity (Nova, A. S. Disa, et al., 2019; Xian Li et al., 2019). However, a variety of exotic orders with multipolar moment are conjectured to exist in strongly correlated transition metal oxides in the presence of considerable spin-orbit coupling but are challenging to detect with conventional probes (G. Chen, Pereira, and Balents, 2010; G. Chen and Balents, 2011; Witczak-Krempa et al., 2014; Takayama, Jiřì Chaloupka, et al., 2021). Experimental evidence of ultrafast switch of such spin-orbit coupled multipolar order to a hidden phase remains elusive (J. Li, Strand, et al., 2018). In this chapter, we demonstrate that in $4d$ transition metal oxide multiband Mott insulator Ca_2RuO_4, an ultrafast switch of spin-orbit-coupled quadrupolar order can be impulsively stimulated by sub-gap light excitation and probed by broadband energy-resolved coherent phonon spectroscopy. The amplitude of a particular 3.7 THz phonon exhibits a temperature- and probe-energy-dependent nonlinearity over pump fluence accompanied by the switch to another hidden quadrupolar order, which can be qualitatively reproduced by a microscopic model.

Electric quadrupolar order (QO) preserves the time-reversal symmetry and parity but breaks rotational symmetry. As the QO in electronic sector is intimately tied to lattice, a structural distortion (Q) can be employed as the order parameter to describe the QO phase transition. We now consider a single-ion model to illustrate the change of local structural and electronic configuration associated with quadrupolar ordering. Because the d-electron transition metal oxides normally form structures composed of corner- or edge-shared octahedra with each transition metal ion caged by six

oxygen atoms, we isolate a single-ion octahedron unit and show a prototypical case of QO of t_{2g} electrons (d_{xy},d_{yz},d_{xz}) accompanying a tetragonal distortion of octahedron ($Q > 0$ corresponds to elongation along $c-$axis). When temperature is higher than the critical temperature $T > T_{QO}$, the potential energy surface (PES) can be pictorially illustrated as a parabola and the ground state is centered at $Q_0 = 0$ with zero orbital polarization [Figure 5.1(a)]. This is shown by the harmonic lattice Hamiltonian $\hat{H}_{Lat} = \sum_\gamma \frac{1}{2} B Q_\gamma^2$, where B determines the curvature of PES bottom and γ runs over all the octahedron distortion eigenmodes. As $T < T_{QO}$, a Jahn-Teller (JT) coupling onsets $\hat{H}_{JT} = \sum_\gamma g Q_\gamma \hat{\tau}_\gamma$, where g is the JT coupling constant and $\hat{\tau}$ is the quadrupolar operator respecting the same symmetry as the corresponding Q. Adding this term will shift the parabola along different Q coordinates and endow the new PES with multiple local minima corresponding to QOs with different orbital polarizations and lattice distortions. Specifically for the tetragonal distortion case, the PES exhibits a tilted double-well configuration with the lower valley corresponding to a d_{xy}-dominated orbital occupation with $Q_0 < 0$ and the higher valley corresponding to a $d_{xz/yz}$-dominated orbital occupation with $Q_0 > 0$ [Figure 5.1(b)]. A moderate spin-orbit coupling (SOC), $\hat{H}_{SOC} = \lambda \hat{\mathbf{L}} \cdot \hat{\mathbf{S}}$, where λ is SOC constant and $\hat{L}$ and $\hat{S}$ are the total orbital and spin angular momentum operators, will render the QO made of pseudospin in lieu of orbital and slightly compromise the JT distortion (Streltsov and Khomskii, 2020). Owing to the existence of multiple local minima, a switch of spin-orbit-coupled QO from the ground state to a state inaccessible in equilibrium is potentially realizable.

Despite the ubiquity of spin-orbit-coupled QO, an ultrafast switch of QO remains elusive, mainly due to the lack of susceptible ultrafast probes. The absence of magnetic dipolar moment renders the QO hidden to conventional probes such as neutron scattering and hard to probe even in equilibrium. Although resonant X-ray scattering (RXS) has been largely applied to determine the pseudospin rotational symmetry breaking, it is usually limited to high-symmetry compounds where the multipolar ordering is accompanied by a global symmetry breaking (Santini et al., 2009) and may not apply to the candidates where no ostensible symmetry breaks at T_{QO} or the change is too subtle (Takayama, Jiri Chaloupka, et al., 2021; S. Gao et al., 2020; Nilsen et al., 2021). The alternative strategy to measure the symmetry breaking in structural sector is also challenging, as QO may host very small moment whose induced symmetry change is sub-resolutional to conventional X-ray diffraction (Lu et al., 2017).

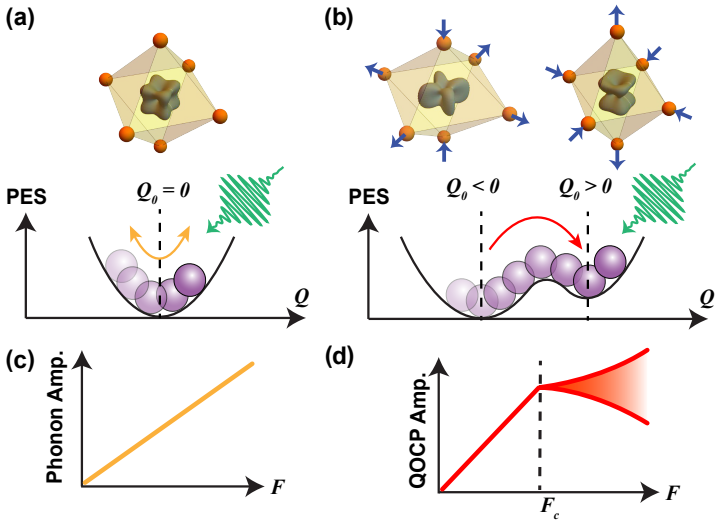

Figure 5.1: Schematic of ultrafast switch of QO. (a),(b) Schematic of PES without and with QO. The corresponding real-space pseudospin distribution of the transition metal atom and octahedron distortion for each valley are shown on top. The shapes of the surface plot reflects the ground-state orbital angular distribution and the grayish color indicates the unpolarized spin. The orange spheres stand for the oxygen atoms. The blue arrows show the eigenvector of Q. (c),(d) Schematic of pump fluence dependence of conventional phonon and QOCP.

Due to the intimate coupling between QO and lattice, an ultrafast switch of QO can be not only induced but also detected through the structural channel. An optical excitation can exert an impulsive force and transfer sufficient kinetic energy to the system. If the optical stimulus triggers a lattice distortion along the Q-coordinate so large that the QO parameter transiently surpasses the potential barrier partitioning different valleys, an ultrafast switch of QO is realized (Figure 5.1b). Simultaneously, phonons are coherently launched via impulsive stimulated Raman scattering (Stevens, Kuhl, and Merlin, 2002), and thus coherent phonon spectroscopy can serve as a susceptible ultrafast probe to detect the switch of QO. Normally, the amplitude of an impulsively launched phonon without coupling to any order increases linearly with pump fluence F [Figure 5.1(c)] (Stevens, Kuhl, and Merlin, 2002). In contrast, the amplitude of a QO-coupled phonon (QOCP) will only scale linearly with F when it is lower than the critical fluence, F_c, where the switch occurs; once $F > F_c$ and the state is steered from one valley to the other, the amplitude of QOCP will deviate from linearity due to the non-parabolic PES [Figure 5.1(d)]. On the other hand, the frequency of QOCP may not show pronounced change as the switch occurs if the two valleys of PES have identical shape and curvature. Therefore,

the switch of the QO is signified by the nonlinear behavior of QOCP amplitude. This method is complementary to and different from other phonon critical behaviors including frequency softening and relaxation time diverging, which instead unveil an order parameter suppression concomitant with higher-symmetry restoration (S. Wall, Wegkamp, et al., 2012; Teitelbaum et al., 2018).

Ca_2RuO_4 is a $4d^4$ perovskite multiband Mott insulator below $T_{MIT} = 357$ K. It possesses a $J = 0$ ground state and inherits a QO from the $J = 1$ excited state through SOC excitation at $T_{QO} = 260$ K (Khaliullin, 2013; Jain et al., 2017). Dubbed as spin-nematic, this phase is a SOC analogue of an orbital-ordered state (H. Liu and Khaliullin, 2019). A dipolar antiferromagnetism subsequently develops at $T_N = 110$ K. The quadrupolar moment of the intermediate state is quite small, as shown by the RXS results where subtle intensities of several particular magnetic Bragg peaks remain up to T_{QO} (Zegkinoglou et al., 2005; Porter et al., 2018). Moreover, the structure of Ca_2RuO_4 respects a rather low orthorhombic symmetry at all temperatures and show no clear anomaly around T_{QO}, indicating the QO is hidden to probes that are sensitive to global structural symmetry change (Friedt et al., 2001). On the other hand, a recent study shows that the 3.7 THz phonon, whose eigenvector is parallel to the direction of octahedral deformation across T_{QO}, exhibits a $\pi-$phase shift at T_{QO} (M.-C. Lee, C. H. Kim, Kwak, J. Kim, et al., 2018). Therefore, Ca_2RuO_4 serves as a paradigm with small quadrupolar moment and low symmetry to investigate the possibility of revealing QO switch through nonlinear phonon dynamics.

5.2 Experimental Results

We harnessed broadband coherent phonon spectroscopy to exhaustively study all the phonons potentially coupled to QO since the relative amplitudes of different phonons can sensitively depend on the probe energy. We scanned our probe energy from 0.5 eV to 2.1 eV, covering the absorption peaks dominated by $d_{xy}\rightarrow d_{xz/yz}$ transition at around 1 eV and by $d_{xz/yz}\rightarrow d_{xz/yz}$ transition at around 2 eV (Jung et al., 2003; Fang, Naoto Nagaosa, and Terakura, 2004). To impulsively excite coherent phonons with minimal carrier excitation, we employ a mid-IR pump centered at 0.3 eV, 2 times smaller than the charge gap of Ca_2RuO_4 (J. S. Lee et al., 2002), and scan F up to 30 mJ/cm^2. This method based on sweeping probe energy is different from the nonlinear phononic setup which selectively generates phonons by changing pump energy and polarization (Först et al., 2011). Compared with conventional coherent phonon spectroscopy performed with time-resolved diffraction or monochromatic optical

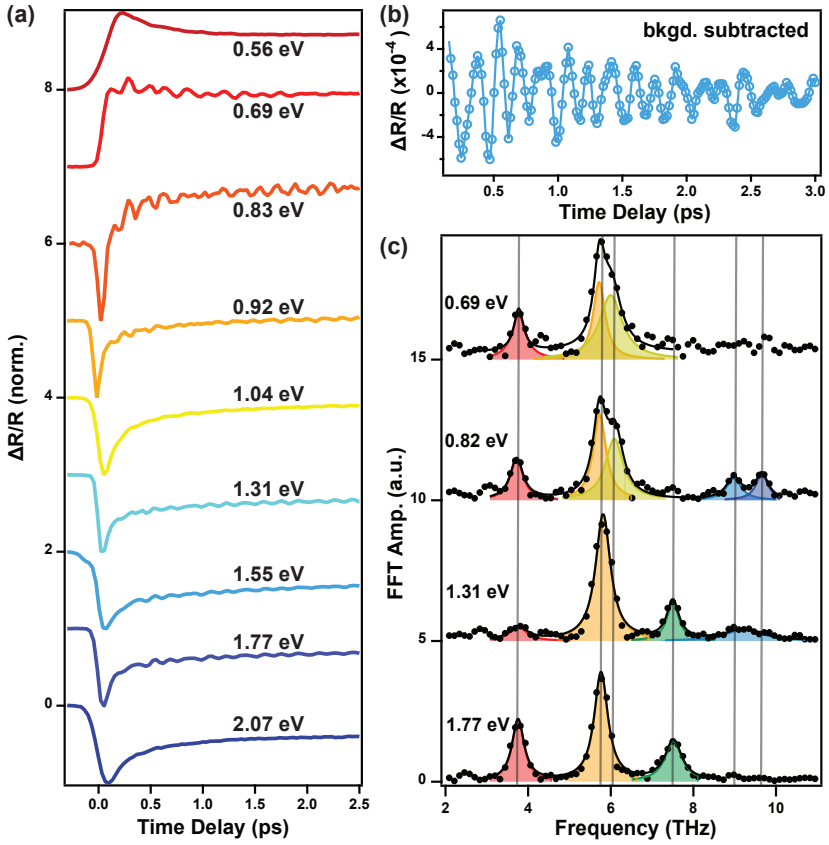

Figure 5.2: Probe-energy-dependent transient reflectivity. (a) Normalized transient reflectivity pumped at 15 mJ/cm^2 and probed at several energies. Each curve is vertically offset for clarity. (b) Transient reflectivity curve subtracted by the double-exponential decaying background and probed at 1.55 eV (Section 5.4). (c) FFT phonon spectra of background-subtracted curves probed at different energies. The multi-Lorentzian fit is shown by black lines. Each phonon is shown by a shaded Lorentzian whose center frequency is denoted by gray lines. Each curve is vertically scaled and offset for clarity.

probe, this technique further provides an orbital-transition-sensitive information of the collective phonon modes as shown later.

Pump Fluence Dependence of QOCP Dynamics

The transient differential reflectivity curves measured at 80 K and probed at selected energies are shown in Figure 5.2(a). Depending on the probe energy, each reflectivity curve can be fit with either a double-exponential decay or an exponential increase followed by an exponential decay, which characterizes the charge relaxation upon pumping: $\frac{\Delta R}{R} = g(\sigma, t) * [\sum_{i=1,2} A_i \exp\left(-\frac{t}{\tau_i}\right) + C)]$, where for

$g(\sigma, t) = \exp\left(-\frac{4\ln(2)t^2}{\sigma^2}\right)$ is a Gaussian kernel that captures the instrumental response function with temporal resolution σ = 0.1 ps, A_i denotes the amplitude of the decay background, t_i represents the decay time, and C characterizes the constant background within our time window, which may represent the long-time heating diffusion. We note that the sign of the amplitude of the electronic background (A_i, C) is dependent on the probe energy and fluence. In general, we have the following dependence:

Probe energy (eV)	A_1	A_2	C
1.2 - 2.2	< 0	< 0	< 0
0.8 - 1.1	< 0	< 0	> 0
0.55 - 0.7	< 0	> 0	> 0

We also realize that the amplitude of A_i and C increases with pump fluence, and C shows a monotonic negative-to-positive change as the probe energy decreases. The fluence dependence of A_i will be discussed further in Chapter VI. Since the sign and magnitude of the background exponential terms are determined by the band structure and transient electronic distribution, many multi-band systems exhibit similar strong energy-dependent transient reflectivity (Bretscher, Andrich, Telang, et al., 2021; Dal Conte et al., 2015).

After subtracting the background, evident beating patterns stemming from the coexistence of multiple phonons can be resolved [Figure 5.2(b)]. By performing a fast Fourier transform (FFT) to the background-subtracted reflectivity at various energies, we found in total six Raman-active phonon modes centered around 3.7, 5.7, 6.1, 7.5, 9.0, and 9.7 THz, whose relative amplitudes are indeed strongly dependent on probe energy [Figure 5.2(c)]. These phonons can all be assigned as A_g modes according to Raman spectroscopy results (Rho et al., 2005).

By varying F and performing multi-Lorentzian fit to the corresponding peaks, we can trace the $F-$dependence of the amplitude of each mode at different probe energies [Figure 5.3(a)]. Strikingly, the amplitude of the 3.7 THz mode reveals a clear deviation from linearity when F >15 mJ/cm^2, while the amplitude of the other modes scales linearly with F up to 30 mJ/cm^2 as predicted for conventional uncoupled phonons [Figure 5.3(b)]. On the other hand, the frequency of different modes is nearly fluence-independent [Figure 5.4(a)].

We now examine several possible causes of the 3.7 THz phonon amplitude nonlinearity. Absorption saturation can be ruled out because the amplitude of transient

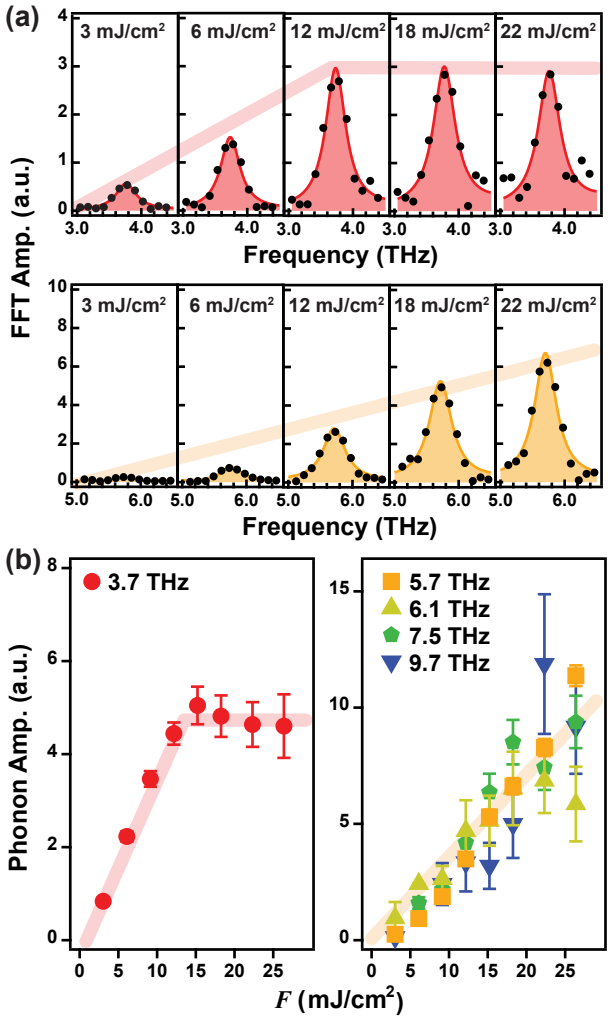

Figure 5.3: Pump-fluence-dependent coherent phonon spectroscopy. (a) FFT spectra of 3.7 THz and 5.7 THz phonon modes pumped at various F and probed at 1.55 eV. The data are fit with Lorentzians. The thick lines are guide to eye. (b) Pump fluence dependence of amplitude of different phonons. The thick lines are guide to eye.

reflectivity and of the other modes increases without saturation in the same pump fluence range [Figure 5.3(b)]. Given that Ca_2RuO_4 undergoes a MIT, a QO transition, and an AFM transition, it is important to interrogate the possibilities of light-induced phase transitions. Thermal phase transitions are not possible because the 3.7 THz phonon frequency exhibits a dramatic redshift with temperature (M.-C. Lee, C. H. Kim, Kwak, J. Kim, et al., 2018), in contrast to its fluence independence [Figures 5.4(a) and (b)]. A photo-induced MIT can also be excluded, since the differential optical conductivity obtained from the transient reflectivity spectrum,

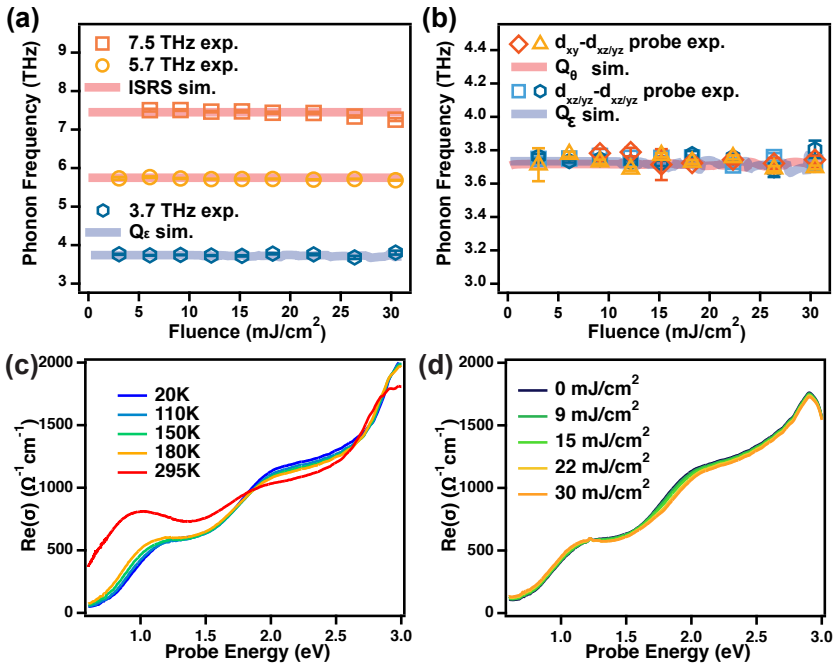

Figure 5.4: Fluence dependence of phonon frequencies and transient optical conductivity. (a),(b) Experimental and simulational fluence dependence of frequencies of QOCP and ISRS phonons. The simulation results are shifted vertically to match the experimental frequency without scaling. (c) Static optical conductivity as a function of temperature. (d). Transient optical conductivity at $t = 0$ as a function of pump fluence.

which reflects the light-induced change in electronic structure, is at least one order of magnitude smaller than the difference of static optical conductivity between the insulating phase at 80 K and the metallic phase at 357 K [Figures 5.4(c) and (d)]. The remaining possibility is a transient modification of either the AFM or the QO, both of which strongly couple to lattice.

Temperature Dependence of QOCP Dynamics

To test whether this phonon amplitude anomaly is associated with quadrupolar ordering, we carried out a F-dependence measurements of the 3.7 THz phonon with 1.55 eV probe, where this mode is most easily resolved, at various temperatures across T_N and T_{QO}. Three features signify the direct coupling between the 3.7 THz mode and the QO. First, the nonlinear $F-$dependence disappears at T_{QO} but not at T_N [Figure 5.5(a)], excluding magnetic order switch as a possible cause. Furthermore, as the temperature increases, F_c shows a concomitant decrease and vanishes at T_{QO} [Figure 5.5(b)], which can be understood in the QO switch scenario: as temperature

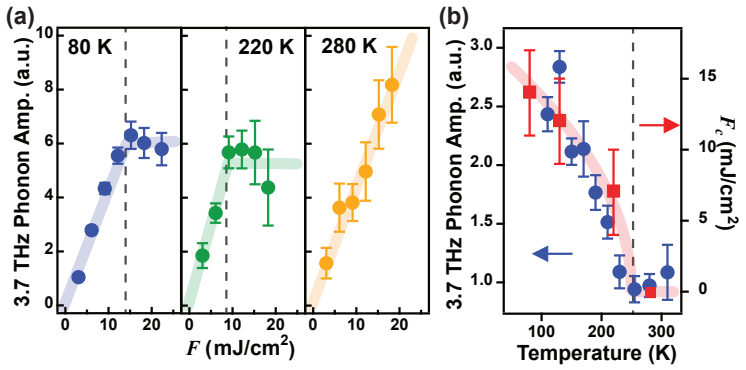

Figure 5.5: Temperature dependence of the 3.7 THz phonon mode. (a) Pump fluence dependence of the 3.7 THz phonon amplitude measured at selected temperatures. Thick colored lines are guide to eye and the dashed lines denote F_c. (b) Temperature dependence of F_c and the 3.7 THz phonon amplitude pumped at 15 mJ/cm^2. $F_c = 0$ indicates no nonlinearity is observed. The theoretical temperature dependence of F_c calculated from the microscopic model is shown by the thick colored line and is scaled vertically to match the experimental values. The pump-induced temperature increase was taken into account. The dashed line denotes T_{QO}.

increases, the QO is suppressed and so the PES will gradually recover a parabolic form. Accordingly, the discrete minima of PES will get closer to each other and so the switch of the QO is expedited more easily. Third, we track the temperature dependence of the 3.7 THz mode amplitude pumped at a fixed F =15 mJ/cm^2, and find an order-parameter like upturn of phonon amplitude at T_{QO} [Figure 5.5(b)], in good agreement with the temperature dependence of F_c. The onset of 3.7 THz phonon amplitude and of F_c at T_{QO} hence benchmarks the direct connection between the nonlinearity of the 3.7 THz mode and the QO.

Probe Energy Dependence of QOCP Dynamics

To understand the phonon nonlinearity with electronic band resolution, we investigate the F-dependence of the 3.7 THz mode amplitude with various probe energies at 80 K. Optical conductivity depicts a $d_{xy}\rightarrow d_{xz/yz}$ transition peak between 0.5-1.3 eV and a $d_{xz/yz}\rightarrow d_{xz/yz}$ transition peak between 1.3-2.1 eV within our probe energy range (Jung et al., 2003; J. S. Lee et al., 2002; Fang, Naoto Nagaosa, and Terakura, 2004). The former transition is more susceptible to tetragonal distortion of octahedron, Q_θ, since this mode can modulate the splitting between d_{xy} and $d_{xz/yz}$. On the other hand, $d_{xz}\rightarrow d_{yz}$ (or vice versa) transition is more sensitive to the orthorhombic mode, Q_ϵ, which breaks the in-plane degeneracy and thus swaps the orbital occupation of d_{xz} and d_{yz} bands without involving d_{xy} [Figure 5.6(b) insets]. Therefore,

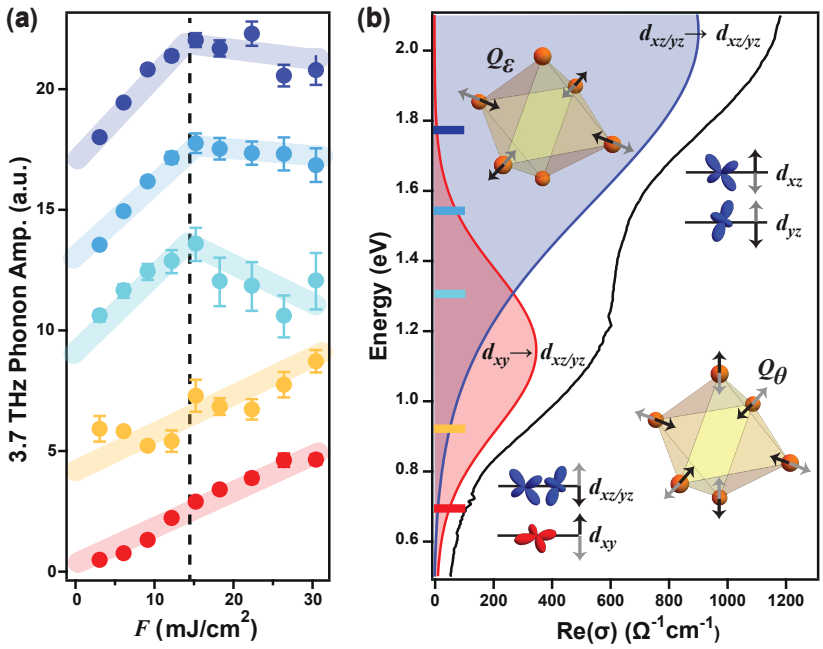

Figure 5.6: Probe-energy dependence of the 3.7 THz phonon mode. (a) Pump fluence dependence of the 3.7 THz phonon amplitude probed at selected wavelengths as denoted by the color bar in panel (b). The thick lines are guides to eye and the dashed line denotes F_c. Each curve is vertically scaled and offset for clarity. (b) Optical conductivity digitized from Ref.(Jung et al., 2003) with Lorentzian fits corresponding to $d_{xy}\rightarrow d_{xz/yz}$ (red) and $d_{xz/yz}\rightarrow d_{xz/yz}$ (blue) transitions. The insets show the real space configuration of the two orthonormal eigenmodes, Q_θ and Q_ϵ, and the induced modulation of orbital levels.

scanning the probe energy from $d_{xy}\rightarrow d_{xz/yz}$ to $d_{xz/yz}\rightarrow d_{xz/yz}$ orbital transition enables a selective coupling to Q_θ and Q_ϵ modes, respectively. Intriguingly, with probe energies resonant with $d_{xy}\rightarrow d_{xz/yz}$ transition leading edge, the amplitude of the 3.7 THz mode reflecting the Q_θ component depicts quasi-linearity up to 30 mJ/cm^2; in contrast, with probe energies resonant with $d_{xz/yz}\rightarrow d_{xz/yz}$ transition leading edge, the amplitude of this mode which reflects the Q_ϵ component displays a clear deviation from linearity at an identical F_c =15 mJ/cm^2 [Figure 5.6(a)].

We emphasize here that the Q_θ and Q_ϵ modes are two orthonormal eigenfunctions of octahedron distortion with E_g-symmetry. More generally, any global phonon that can couple to d-shell electrons of a perovskite lattice can be viewed as a superposition of 6 orthonormal eigenmodes respecting either A_g, E_g, or T_{2g} symmetry with reference to each octahedron. E_g-symmetry components dominate in transition metal oxides that host tetragonal (Q_θ) or orthorhombic (Q_ϵ) distortion in equilibrium

due to a stronger electron-phonon coupling. First principle calculations suggested that all the A_g phonons in Ca_2RuO_4 involve rotation or tilting of octahedra (M.-C. Lee, C. H. Kim, Kwak, J. Kim, et al., 2018), which inevitably changes the Ru-O bond length and generates E_g-symmetry modulation of each octahedron. Therefore, the clear dichotomy shows that Q_θ and Q_ϵ eigenmodes of 3.7 THz phonon exhibit distinct behaviors as the QO is manipulated by light.

5.3 Microscopic Model and Dynamical Simulation

Microscopic Model

To quantitatively understand the underlying physics, we developed a microscopic model and then conducted dynamical simulations. To capture the d^4 multi-orbital configuration and the interactions, in addition to $\hat{H}_{JT}$, $\hat{H}_{Lat}$, and $\hat{H}_{SOC}$ as mentioned before, our Hamiltonian also contains the generalized Kanamori parametrized electronic correlation term $\hat{H}_U = (U - 3J_H)\frac{\hat{N}(\hat{N}-1)}{2} + \frac{5}{2}\hat{N} - J_H(2\hat{S}^2 + \hat{L}^2/2)$, where J_H is the intra-atomic Hund's exchange and U is the intraorbital Coulomb interaction (Streltsov and Khomskii, 2020). Performing exact diagonalization to the total Hamiltonian, we can calculate the PES as a function of the two E_g eigenmodes, Q_θ and Q_ϵ. The PES depicts three minima when $T < T_{QO}$: the d_{xy}-orbital-dominated ground state with tetragonal compression along z axis demonstrated by optical and X-ray spectroscopy measurements (Jung et al., 2003; Mizokawa et al., 2001), and two local minima with d_{xz}- or d_{yz}-orbital-dominated character with compression along y or x axis, respectively, that do not exist in equilibrium [Figure 5.7(a)]. Accordingly, a nonthermal switch from the spin-orbit-coupled QO ground state characterized by d_{xy}-dominated orbital polarization to another hidden QO can be potentially facilitated by impulsive stimulus.

We then derive the equations of motion for Q_θ and Q_ϵ coordinates and show their temporal evolution. Since our pump photon energy (0.3 eV) is 2 times smaller than the gap, we assume an impulsive instead of displacive excitation occurs at time zero which initiates the time evolution of Q_θ and Q_ϵ. This is further corroborated by two facts: first, the 3.7 THz phonon shows a sinusoidal instead of cosinusoidal oscillation, consistent with ISRS mechanism; second, the transient optical conductivity spectrum shows faint difference from the equilibrium one, revealing a minor modulation of PES and contradicting the displacive excitation scenario. Also because the pump light frequency is one order of magnitude larger than any observable phonons, we can safely average out the sinusoidal oscillatory part of the pump and model the pump as a Gaussian function centered at time zero with time duration σ of 0.1 ps

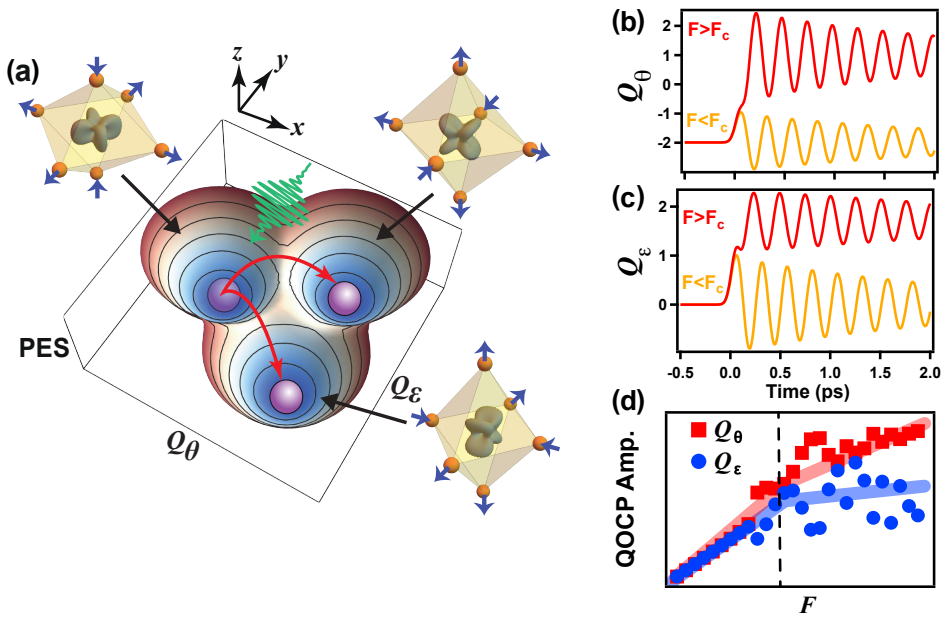

Figure 5.7: Microscopic model simulation results. (a) Schematic of PES of the quadrupolar ordered phase calculated from the microscopic model (Methods). The corresponding real-space pseudospin distribution and lattice distortion for each valley are shown by side. (b)(c) Time evolution of Q_θ and $Q_epsilon$ with pump fluence lower and higher than the critical fluence. (d) Pump fluence dependence of amplitude of QOCP along Q_θ (red) and Q_ϵ (blue) coordinates calculated based on the dynamical simulation. The dashed line denotes the first switching critical fluence.

and amplitude proportional to the fluence F with a scaling factor A. By further including a damping term with constant γ which can be experimentally determined, we can write out the equation of motion of Q_θ and Q_ϵ:

$$\frac{d^2Q_{\theta/\epsilon}(t)}{dt^2} + 2\gamma\frac{dQ_{\theta/\epsilon}(t)}{dt} + \frac{dV(Q_\theta(t), Q_\epsilon(t))}{dQ_{\theta/\epsilon}(t)} = AF\exp\left\{\frac{4\ln(2)t^2}{\sigma^2}\right\}. \quad (5.1)$$

Simulation results

The time evolution of the structural order parameters Q_θ and Q_ϵ pumped with two characteristic fluences ($F > F_c$ and $F < F_c$) are shown in Figures 5.7(b) and (c). As $F > F_c$, a clear change of sign in offset of both Qs can be unambiguously observed, which underlines a switch of QO from the initial valley to another hidden valley. By performing FFT to time traces after the system is stabilized as we vary the only free parameter F, we can track the fluence dependence of the amplitude of Q_θ and Q_ϵ modes. As expected, when $F < F_c$, the amplitude of both Q_θ and Q_ϵ coordinates exhibits the same linear dependence akin to a conventional phonon;

as the system transiently evolves into the two excited states accompanied by the QO switching ($F > F_c$), phonons along both coordinates display an deviation from perfect linearity and the nonlinearity of Q_ϵ is more drastic than Q_θ [Figure 5.7(d)]. Not only does this result suggest that the nonlinear behavior of the coupled phonon signifies the ultrafast switch of QO, but it reproduces the probe-energy-dependent measurements in Figure 5.6, where Q_ϵ-sensitive probes indeed show a more dramatic deviation from linearity than the Q_θ-sensitive probes.

Note that there is an aperiodic oscillation of QOCP amplitude over fluence as $F > F_c$. The nonmonotonic behavior arises from the back-and-forth switching between different valleys as F increases. This indicates F_c corresponds to the fluence where the first reversal occurs $F_{c,i=1}$. When F is slightly higher than F_{c1}, the system relaxes to and stays in the x/y-compressed valley. When $F > F_{c2}$, the system will relax back to the original valley. With even higher F, the system can switch between different valleys back and forth transiently before it settles into one valley. Now we provide an explanation on why the switch between valleys will generate the aperiodic oscillation. Let us consider two fluences: $F_1 = F_{c1} - \delta$ and $F_2 = F_{c1} + \delta$, where δ is a small positive value. Since $F_2 > F_1$, the system will roll over the barrier and move to the new valley, which obviously travels a longer distance and thus the damping will decrease the amplitude for F_2 case more than F_1 case. Thus we will find the phonon amplitude at F_2 is smaller than F_1. As F further increases, the larger energy dumped into the system will compensate the damping loss and the phonon amplitude will slowly increase until it reaches the boundary between the two valleys again at $F = F_{c2}$. Then the new reversal occurs and the phonon amplitude will drop again. Therefore, the QOCP amplitude will show a sudden change at each $F_{c,i}$ and thus depicts an oscillatory behavior as a function of F.

Also note that in the minimal model we neglect the intrinsic energetic difference between d_{xy} and the nearly degenerate $d_{xz/yz}$-dominated states, which arises from noncubic environment induced by the octahedron distortion and the planar cornered-shared lattice structure. We can include the tetragonal splitting by phenomenologically adding a linear term $k_E Q_{E\theta}$ to tilt the PES so that the ground state of compressed $z-$axis is uniquely favored. Based on this assumption, the JT effect will become pseudo-JT effect due to the energetic nondegeneracy in the parent phase (Bersuker, 2006). After including the tetragonal splitting, we find that the original d_{xy}-dominated valley will almost always be reached eventually after about 3 ps in-

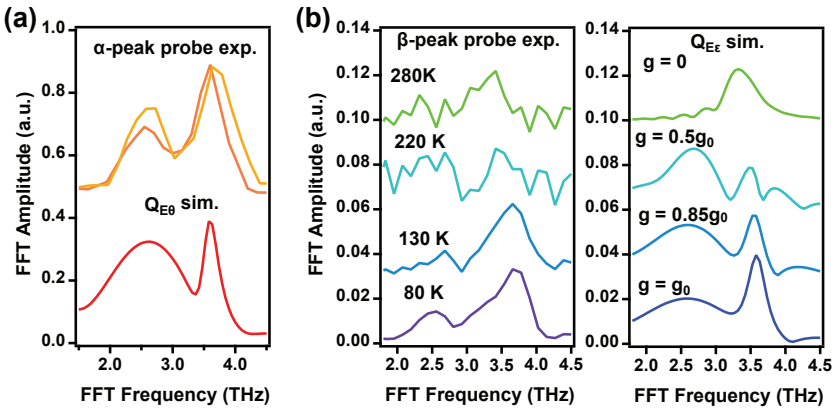

Figure 5.8: Illustration of the 2.5 THz hump. (a) Comparison of FFT spectra of QOCP between experiment and simulation with two $d_{xy}\rightarrow d_{xz/yz}$-peak probes (0.69, 0.92 eV) at 80 K. b. Comparison of FFT spectra of QOCP between experiment and simulation with 1.55 eV $d_{xz/yz}\rightarrow d_{xz/yz}$-peak probe at various temperatures. All the experimental data were taken at a pump fluence of 15 mJ/cm^2. The simulated FFT spectra are calculated by changing g in a form of $\sqrt{1-T/T_{QO}}$. The relative value of g at each temperature is denoted. The data are scaled and offset vertically for better comparison.

dependent of F, but a transient switch between different QOs still occurs. We note that F_c in the presence of tetragonal splitting is larger than that without tetragonal splitting because d_{xz} and d_{yz} valleys are elevated and thus harder to reach. However, despite the discrepancy, the fluence dependence of QOCP amplitude and frequency is qualitatively identical to the case with tetragonal splitting ignored.

We can also simulate the temperature dependence of QOCP amplitude and F_c by assuming that microscopically the JT coupling constant g, which determines the spacing and depth of different valleys, decreases as temperature increases in an order-parameter form $\sqrt{1-T/T_{QO}}$. By introducing a temperature dependence of g, our model confirms a primary order-parameter-like behavior $\sqrt{1-T/T_{QO}}$ of both QOCP amplitude and F_c, in perfect agreement with the experimental data in Figure 5.5(b). These results also underpin that F_c can be used to characterize QO.

We note that in both the experimental and simulational results, a hump shows up at the low-frequency shoulder of the QOCP peak. According to previous Raman spectroscopy results (Rho et al., 2005), all the A_{1g} modes have been identified with energies all above 3.7 THz. Since our isotropic reflectivity measurement can only probe A_{1g} phonons according to symmetry, we can rule out the possibility that this damped mode is a phonon. Also, this mode exists even above T_N but disappears at

T_{QO} [Figure 5.6(b)], indicating that it is not a magnon but should be related to QO. We thus attribute this hump feature to the non-harmonicity of the PES. As SOC smoothens the barrier, the local curvature at the boundary between the two valleys decreases, rendering the PES a local anharmonicity. Therefore, when the system is transiently switched between the valleys, a low energy component emerges from the reduced curvature around the anharmonic part of PES. If this hypothesis is true, we would expect that this low frequency hump should emerge in both $Q_{E\theta}$ and $Q_{E\epsilon}$ only at $T < T_{QO}$ and $F > F_c$. This is indeed corroborated by both our simulation and experiments with good agreement [Figure 5.8]. We would also expect that the amplitude of the hump should increase with F. Our current experimental setup can hardly resolve the dynamics of this mode unambiguously over the entire fluence and temperature range due to unideal SNR. This speculation thus calls for detailed measurements with better SNR in the future.

5.4 Discussion and Outlook

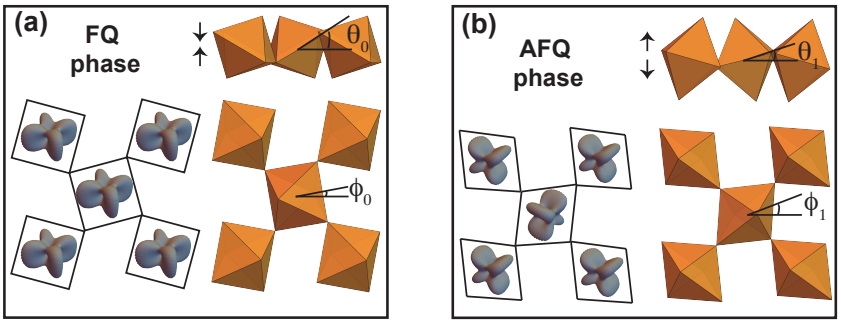

Figure 5.9: Schematic of the collective lattice and pseudospin change. (a),(b) Illustration of the collective pseudospin and lattice configurations of the equilibrium FQ phase and the possible transient AFQ phase.

We now discuss the collective alteration of pseudopsin and lattice of Ca_2RuO_4 when the switch occurs. Since Ca_2RuO_4 lattice is crystallized into an in-plane corner-shared octahedra network with the apical oxygen atoms free to move, the distortion of each octahedron as the QO is switched will generate a collective change of lattice and pseudospin. As $T < T_{QO}$, X-ray spectroscopy confirms a "ferro-quadrupolar" (FQ) order: all the octahedra will favor the d_{xy}-dominated orbital occupation and experience a tetragonal compression along the z-axis [Figure 5.9(a)] (Zegkinoglou et al., 2005). When the QO switch is induced, however, the orbital of each octahedron will transform into either the d_{xz}- or d_{yz}-dominated state and each octahedron will become compressed along the $y-$ or $x-$axis, respectively.

Due to the in-plane isotropy of each octahedron (Braden et al., 1998; Friedt et al., 2001), these two states will be reached with equal possibility. Therefore, the octahedra will potentially form mesoscopic domains with either y- or x-compressed octahedra. Another possible scenario is that the lattice will eventually evolve into a state with "checkerboard" "anti-ferro-quadrupolar" (AFQ) order, i.e., the nearest-neighbor octahedra host opposite lattice distortion and orbital occupation [Figure 5.9(b)]. This kind of QO has been observed in manganites (Tokura and N. Nagaosa, 2000). Previous X-ray diffraction results also show that along with the static Ru-O bond length change as temperature decreases, the octahedron will tilt along an axis bisecting the right angle between x- and y-axes with an angle θ and rotate along the z-axis with an angle ϕ (Braden et al., 1998; Friedt et al., 2001). Therefore, we also foresee that θ and ϕ will change to accommodate the bond length change accompanied by the QO switch. A recent density functional theory calculation indeed reveals that the 3.7 THz QOCP may involve the rotation and tilting of octahedron (M.-C. Lee, C. H. Kim, Kwak, J. Kim, et al., 2018). However, since direct evidence of the hidden QO is missing, we refrain from drawing more detailed conclusion.

Our experimental and theoretical study showcasing an ultrafast switch of QO extensively expands the field of ultrafast order parameter control beyond conventional spin, charge, and orbital orders. Our research not only provides an alternative probe to QO, which broadens the search for multipolar orders, but paves the avenue towards using phonon nonlinearity as fingerprints to detect transient switch of exotic phases that conventional probes cannot directly couple to. In addition, the probe-energy dependent phonon spectroscopy proposed in this work sheds light on decomposing a phonon into orthonormal eigenmodes through scanning probe wavelength to resonantly excite particular electronic transitions.

Chapter 6

Keldysh Tuning and Floquet Band Engineering in Ca_2RuO_4

In the previous chapter, we focused on the phonon dynamics of the transient reflectivity curves at select probe energies and temperatures, which reveals an ultrafast switch of spin-orbit coupled quadrupolar order. However, a detailed analysis of the electronic background of the reflectivity transients remains underexplored. In this chapter, we find that the sign and magnitude of the background exponential terms capture the charge dynamics upon the sub-gap pumping, reflecting the transient electron distribution through nonlinear carrier generation. More specifically, by sweeping the pump fluence, we demonstrate the so-called Keldysh crossover from a multi-photon absorption to quantum tunneling dominated pair production regime associated with a continuous coherent bandwidth renormalization. Our results provide a procedure to control coherent and nonlinear heating processes in Mott insulators, facilitating the discovery of novel out-of-equilibrium phenomena in strongly correlated systems.

6.1 Introduction

The response of a Mott insulator to a strong electric field is a fundamental question in the study of non-equilibrium correlated many-body systems (Martin Eckstein, Oka, and Werner, 2010; W.-R. Lee and Park, 2014; J. Li, Aron, et al., 2015; Oka and Aoki, 2005; Diener et al., 2018; Asamitsu et al., 1997; Hao Chu et al., 2020; S. Wall, Brida, et al., 2011; Okamoto et al., 2007; Martin Eckstein and Werner, 2011). In the DC limit, a breakdown of the insulating state occurs when the field strength exceeds the threshold for producing pairs of doubly-occupied (doublon) and empty (holon) sites by quantum tunneling, in analogy to the Schwinger mechanism for electron-positron pair production out of the vacuum (Schwinger, 1951). Recently, the application of strong low frequency AC electric fields has emerged as a potential pathway to induce insulator-to-metal transitions (Murakami and Werner, 2018; Giorgianni, J. Sakai, and Lupi, 2019; Mayer et al., 2015; Yamakawa et al., 2017), realize efficient high-harmonic generation (Imai, Ono, and Ishihara, 2020; Silva et al., 2018), and coherently manipulate band structure and magnetic exchange interactions in Mott insulators (Mentink, Balzer, and M. Eckstein, 2015; Hejazi, J. Liu, and Balents, 2019; Mikhaylovskiy et al., 2015; Batignani et al., 2015; Claassen et al., 2017; Yao

Wang, Devereaux, and C.-C. Chen, 2018). Therefore there is growing interest to understand doublon-holon (d-h) pair production and their non-thermal dynamics in the strong field AC regime.

Strong AC field induced d-h pair production has been theoretically studied using Landau-Dykhne adiabatic perturbation theory (Oka, 2012) along with a suite of non-equilibrium numerical techniques (Murakami and Werner, 2018; Tsuji et al., 2011; Oka, 2012; Imai, Ono, and Ishihara, 2020; Silva et al., 2018; Takahashi, Itoh, and Aihara, 2008; Tancogne-Dejean, Sentef, and Rubio, 2020). Notably, d-h pairs are primarily produced through two nonlinear mechanisms: multi-photon absorption and quantum tunneling (Oka, 2012; Kruchinin, Krausz, and Yakovlev, 2018). The two regimes are characterized by distinct electric field scaling laws and momentum space distributions of d-h pairs. By tuning the Keldysh adiabaticity parameter $\gamma_K = \hbar\omega_{pump}/(eE_{pump}\xi)$ through unity, where ω_{pump} is the pump frequency, E_{pump} is the pump electric field, e is electron charge, and ξ is the d-h correlation length, a cross-over from a multi-photon dominated ($\gamma_K > 1$) to a tunneling dominated ($\gamma_K < 1$) regime can in principle be induced. However, direct experimental tests are lacking owing to the challenging need to combine strong tunable low frequency pumping fields with sensitive ultrafast probes of non-equilibrium distribution functions.

We devise a protocol to study these predicted phenomena using ultrafast broadband optical spectroscopy in the multiband Mott insulator Ca_2RuO_4. Below a metal-to-insulator transition temperature $T_{MIT} = 357$ K, a Mott gap ($\Delta = 0.6$ eV) opens within its 2/3-filled Ru $4d\ t_{2g}$ manifold (Gorelov et al., 2010; Han and A. Millis, 2018; Fang, Naoto Nagaosa, and Terakura, 2004; Jung et al., 2003), with a concomitant distortion of lattice (Braden et al., 1998). It has recently been shown that for temperatures below T_{MIT}, re-entry into a metallic phase can be induced by a remarkably weak DC electric field of order 100 V/cm (Nakamura, Sakaki, et al., 2013), making Ca_2RuO_4 a promising candidate for exhibiting efficient nonlinear pair production.

6.2 Experiment and Simulation: Nonlinear Carrier Generation and Keldysh Crossover

To estimate the response of Ca_2RuO_4 to a low frequency AC electric field, we calculated the d-h pair production rate (Γ) over the Keldysh parameter space using a Landau-Dykhne method developed by Oka (Oka, 2012). The Landau-Dykhne method combined with the Bethe Ansatz has been used to model the nonlinear d-h pair production process in Mott insulators across the entire Keldysh parameter

space, from the multiphoton regime to the tunneling regime. Although the theory was originally applied to a 1-dimensional (1D) Hubbard model, results and equations therein have been widely referenced by dielectric breakdown experiments on materials with higher dimensions. For a 1D Hubbard model in a time-dependent electric field, the adiabatic perturbative theory expands the time-dependent state into the linear combination of adiabatic eigenstates

$$|\Psi(t)\rangle = a(t)\,|0;\Phi(t)\rangle + b(t)\,|p;\Phi(t)\rangle_{dh}\,, \tag{6.1}$$

where p is momentum, $\Phi(t)$ is the Peierls phase, and $a(t)$ and $b(t)$ are the probability amplitudes for the channel at p to be in the ground state (no pair) or in the excited state (with a pair). The p-dependent transition probability $P_p = [b(t)]^2$ can be calculated as

$$P_p = \exp(-2\mathrm{Im}\mathcal{D}_p), \tag{6.2}$$

where $\mathcal{D}_p$ is the difference between the dynamical phase of the ground state and the excited state. After more treatments, Ref. (Oka, 2012) gives

$$\mathrm{Im}\mathcal{D}_p = \mathrm{Im}\mathcal{D}_{p1} + \mathrm{Im}\mathcal{D}_{p2}, \tag{6.3}$$

and

$$\mathrm{Im}\mathcal{D}_{p1} = \int_p^0 \Delta E(l)\mathrm{Im}\left(\frac{1}{F(p-l)}\right) dl, \tag{6.4}$$

$$\mathrm{Im}\mathcal{D}_{p2} = \int_0^{1/\xi} \Delta E(il)\mathrm{Im}\left(\frac{i}{F(p-il)}\right) dl. \tag{6.5}$$

Here, ΔE is the gap function, $F(\Phi) = \pm\sqrt{F_0^2 - \Omega^2\Phi^2}$ is the time-dependent field with sinusoidal oscillations, ξ is the d-h correlation length, Ω is the pump frequency, and F_0 is the amplitude of F. After P_p is calculated, the total d-h pair production rate can be obtained by an integral

$$\Gamma = \frac{\Omega}{2\pi}\int_{-\pi}^{\pi}\frac{dp}{2\pi}P_p. \tag{6.6}$$

We used the parameters reported in the dynamical mean-field theory calculations for Ca_2RuO_4 (Gorelov et al., 2010), with $U = 3.5$ eV, $\Delta = 0.6$ eV (from optical measurements in (Jung et al., 2003)), $a = 5.6$ Å (in-plane lattice parameter), and $t_{\mathrm{hop}} = 0.23$ eV (the hopping integral between xy orbitals, since joint density of states near the Mott gap is mostly contributed by $d_{xy} \rightarrow d_{xz/yz}$ transitions). The correlation length (Stafford and A. J. Millis, 1993) can be calculated with $\xi =$

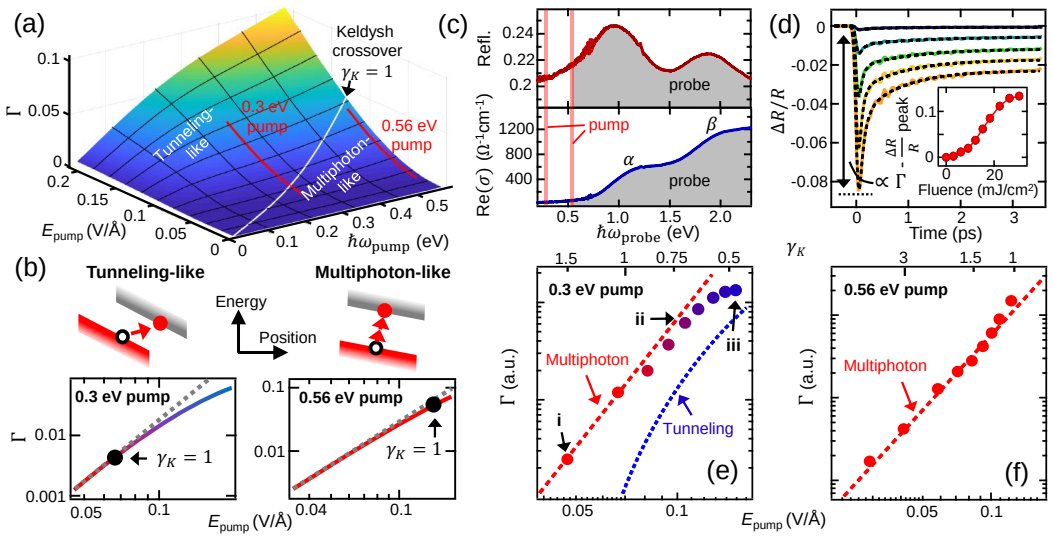

Figure 6.1: Resolving Keldysh tuning using pump-probe spectroscopy. (a) Γ calculated across Keldysh space using the Landau-Dykhne method. (b) Constant energy cuts along the red lines shown in (a) plotted on a logarithmic scale. Black dots mark the Keldysh cross-over. Gray dashed lines: scaling relation in the multi-photon regime. Schematics of the multi-photon and tunneling processes are shown above. (c) Equilibrium reflectivity (top) and conductivity (bottom) spectra of Ca_2RuO_4 at 20 K. The 0.3 eV and 0.56 eV pump energies are marked by vertical red lines. The probe energy range is shaded grey. (d) Select 0.3 eV pump 1.77 eV probe $\Delta R/R$ traces at fluences of 3, 9, 15, 22, and 30 mJ/cm^2 (top to bottom). Dashed lines are fits to double-exponential decay. Inset: Peak $\Delta R/R$ versus fluence showing nonlinearity. (e, f) Experimental cuts through the same regions of parameter space as in (b). Error bars are smaller than data markers. Scaling relations for multi-photon and tunneling behavior are overlaid as red and blue dashed lines respectively.

$[\ln(U/4.377t_{\text{hop}})]^{-1}a$ in the strong-coupling limit (which holds for Ca_2RuO_4 since $U/t_{\text{hop}} = 15$ (Stafford and A. J. Millis, 1993)). We estimate $\xi = 4.45$ Å. This value is the same order of magnitude as $\xi = 2.1$ Å estimated for VO_2 (Mayer et al., 2015), which is another Mott insulator showing a cooperative charge-lattice response across a temperature-driven metal-to-insulator transition.

As shown in Figure 6.1(a), Γ is a generally increasing function of E_{pump} and $\hbar\omega_{\text{pump}}$. For a fixed ω_{pump}, the predicted scaling of Γ with E_{pump} is clearly different on either side of the Keldysh cross-over line ($\gamma_{\text{K}} = 1$), evolving from power law behavior $\Gamma \propto (E_{\text{pump}})^a$ in the multi-photon regime to threshold behavior $\Gamma \propto \exp(-b/E_{\text{pump}})$ in the tunneling regime [Figure 6.1(b)].

At time delays where coherent nonlinear processes are absent, the transient pump-induced change in reflectivity of a general gapped material is proportional to the

density of photo-excited quasi-particles (Gedik et al., 2004; Chia et al., 2006; Demsar, Biljakovi ć, and Mihailovic, 1999), which, upon dividing by a constant pump pulse duration (~100 fs), yields Γ. Differential reflectivity ($\Delta R/R$) transients from Ca_2RuO_4 single crystals were measured at T = 80 K using several different subgap pump photon energies ($\hbar\omega_{\text{pump}} < \Delta$) in the mid-infrared region, and across an extensive range of probe photon energies ($\hbar\omega_{\text{probe}}$) in the near-infrared region spanning both the α and β absorption peaks [Figure 6.1(c)]. These two band edge features can be assigned to optical transitions within the Ru t_{2g} manifold (Das et al., 2018; Jung et al., 2003). Figure 6.1(d) shows reflectivity transients at various fluences measured using $\hbar\omega_{\text{pump}}$ = 0.3 eV and $\hbar\omega_{\text{probe}}$ = 1.77 eV. Upon pump excitation, we observe a rapid resolution-limited drop in $\Delta R/R$. With increasing fluence, the minimum value of $\Delta R/R$ becomes larger, indicating a higher value of Γ within the pump pulse duration. This is followed by exponential recovery as the d-h pairs thermalize and recombine. By plotting Γ against the peak value of E_{pump} (measured in vacuum), we observe a change from power law scaling to threshold behavior when $E_{\text{pump}} > 0.07$ V/Å[Figure 6.1(e)], in remarkable agreement with our calculated Keldysh cross-over [Figure 6.1(a),(b)]. In contrast, measurements performed using 0.56 eV pumping exhibit exclusively power law scaling over the same E_{pump} range [Figure 6.1(f)], again consistent with our model.

A predicted hallmark of the Keldysh cross-over is a change in width of the non-thermal distribution of d-h pairs in momentum space (Oka, 2012). In the multi-photon regime, doublons and holons primarily occupy the conduction and valence band edges respectively, resulting in a pair distribution function (P_p) sharply peaked about zero momentum (p = 0). In the tunneling regime, the peak drastically broadens, reflecting the increased spatial localization of d-h pairs. Using the Landau-Dykhne method, we calculated the evolution of P_p for Ca_2RuO_4 as a function of E_{pump} through the Keldysh cross-over.

To demonstrate how signatures of a changing P_p width are borne out in experiments, we simulate the effects of different non-thermal electronic distribution functions on the broadband optical response of a model insulator. Assuming a direct-gap quasi-two-dimensional insulator with cosine band dispersion in the momentum plane (p_x, p_y), the optical susceptibility computed using the density matrix formalism can be

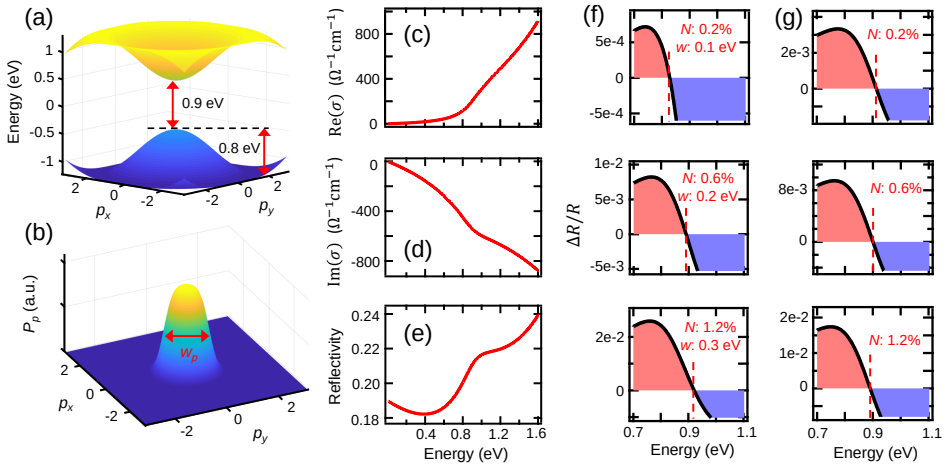

Figure 6.2: Simulation of optical properties of a photoexcited insulator. (a) Band structure. (b) Momentum dependent photocarrier distribution. w_p (w) represents the width of the distribution in the momentum (energy) space. (c)-(e) Equilibrium optical properties calculated from the band structure in (a) with no photocarriers. (f) Differential reflectivity spectrum (spectrum with photocarriers subtracted by that without photocarriers) at various carrier densities (N) and width of distribution w. (g) Same as (f) except that the P_p is adjusted to the 1-eV-pump nonthermal distribution. N changes consistently, while the width of distribution stays constant for the three panels.

expressed as (Rosencher and Vinter, 2002):

$$\chi(\omega) = \sum_{p_x,p_y} \frac{e^2 x_{vc}(p_x,p_y) T_2}{\epsilon_0 \hbar} \frac{[\omega_{\text{probe}} - \frac{\Delta(p_x,p_y)}{\hbar}]T_2 - i}{[\omega_{\text{probe}} - \frac{\Delta(p_x,p_y)}{\hbar}]^2 T_2^2 + 1} [N_v(p_x,p_y) - N_c(p_x,p_y)], \tag{6.7}$$

where e is the electron charge, ϵ_0 is vacuum permittivity, $\hbar$ is Planck's constant divided by 2π, x_{vc} is the matrix element of the vertical interband transition at a particular momentum (assumed to be a constant for all momenta for simplification), T_2 (assume to be constant) is the band dephasing time, ω_{probe} represents probe frequency, $\Delta(p_x, p_y)$ represents the gap energy that respects a cosine dispersion [Figure 6.2(a)], and N_v and N_c are the electron occupations of the valence and conduction bands, respectively. The physical picture of the equation is that the bands are viewed as an ensemble of vertical two-level systems (TLSs) in the p_x-p_y plane with level separations $\Delta(p_x, p_y) = \hbar(\omega_c - \omega_v)$; each TLS contributes a Lorentzian oscillator, weighted by its corresponding occupation factor, to the total susceptibility.

In equilibrium ($N_v = 1$, $N_c = 0$ for all p_x and p_y), we calculated the susceptibility

by Eq. 6.7 and converted it into static real and imaginary parts of conductivity σ and reflectivity, as shown in Figures. 6.2 (c)-(e). The values and trends of the curves are similar to those of Ca_2RuO_4 measured around its α peak onset energy (Mott band edge), but the higher energy transitions that involve multiple orbitals in Ca_2RuO_4, such as the β and γ peaks, are not accounted for by the model.

In the laser-driven case, we used the Gaussian distribution to account for a total of N photoexcited nonthermal carriers

$$N = \sum_{p_x,p_y} N_c(p_x, p_y) = \sum_{p_x,p_y} \frac{A}{w\sqrt{2\pi}} \exp\left\{\frac{-[\omega_c(p_x, p_y) - \omega_0]^2}{2w^2}\right\}, \tag{6.8}$$

where we specified width w, peak center ω_0, and N to determine A and $N_c(p_x, p_y)$ [Figure 6.2(b)]; for 0.3 eV pump experiments, we set ω_0 to be half of the direct gap (assuming zero energy centers the gap), and w progressively increases with N to mimic the width evolution of the γ_K-dependent P_p distribution obtained from the Landau-Dykhne theory, while for 1 eV pumping, we set $\omega_0 = 0.5$ eV, and w remains constant with increasing N. The nonthermal photocarrier distribution affects $N_c(p_x, p_y)$ and $N_v(p_x, p_y) = 1 - N_c(p_x, p_y)$, and therefore, modifies the nonequilibrium σ and reflectivity. By applying the Fresnel equations, we simulated $\Delta R/R$ spectra for various photocarrier densities N and distribution widths w. One detail we noticed was that simply considering the filling-induced optical bleaching will only lead to negative $\Delta R/R$ for all probe energies. To match the experimental fact that positive $\Delta R/R$ regions are present in the experimental data, a term considering the photocarrier-induced band edge redshift has to be included. As will be shown later [Figure 6.5(a)], it is valid to assume that $\Delta(p_x, p_y)$ decreases in proportion to the number of excitations.

Figure 6.3(a) displays P_p curves at three successively larger E_{pump} values corresponding to (i) $\gamma_K = 1.49$, (ii) $\gamma_K = 0.75$ and (iii) $\gamma_K = 0.47$, which show a clearly broadening width along with increasing amplitude. For the Keldysh tuning case [Figure 6.3(b)], as P_p evolves from condition (i) to (iii), we find that the intersection between the non-equilibrium and equilibrium reflectivity spectra shifts to progressively higher energy. For comparison, we also performed simulations under resonant photo-doping conditions using the direct-gap insulator model. Figure 6.3(c) displays three P_p curves at successively larger E_{pump} values, which were chosen such that the total number of excitations match those in Figure 6.3(a). Each curve exhibits maxima at non-zero momenta where $\hbar\omega_{\text{pump}} = \Delta(|p|)$ is satisfied. In stark contrast to the subgap pumping case, the amplitude of P_p increases with E_{pump}

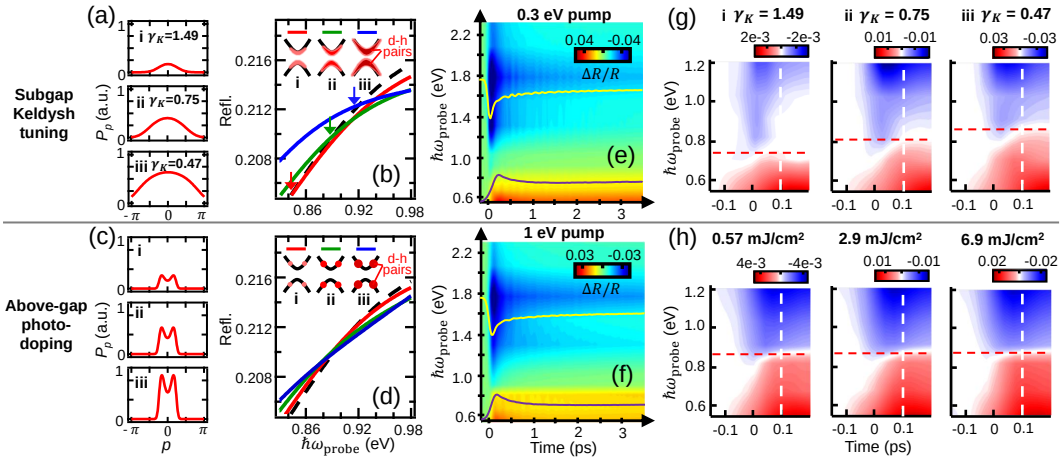

Figure 6.3: Non-thermal pair distribution through the Keldysh crossover. (a) Calculated P_p for conditions **i** to **iii** using the Landau-Dykhne method. (b) Simulated non-equilibrium reflectivity spectra for subgap pumping. (c, d) Analogues of (a) and (b) but simulated for above-gap pumping. Fluence increases from **i** to **iii**. Black curves in (b) and (d) are the equilibrium spectra. Arrows in (b) mark the crossing points between the non-equilibrium and equilibrium curves. Experimental $\Delta R/R$ maps of Ca_2RuO_4 for (e) 0.3 eV pump (fluence: 30 mJ/cm^2) and (f) 1 eV pump (fluence: 7 mJ/cm^2). Two representative constant energy cuts (yellow: 1.77 eV, purple: 0.56 eV) are overlaid. (g) Enlargement of $\Delta R/R$ maps for 0.3 eV pump using three pump fluences [marked in Figure 1(e)] corresponding to conditions (i) to (iii) in (a). (h) Enlargement of $\Delta R/R$ maps for 1 eV pump using three pump fluences indicated above. White dashed lines mark t = 0.1 ps. Red dashed lines: guides to the eye for the $\hbar\omega_{probe}$ where $\Delta R/R$ changes sign at t = 0.1 ps.

but the width remains unchanged. This results in the non-equilibrium reflectivity spectra all intersecting the equilibrium spectrum at the same energy, forming an isosbestic point [Figure 6.3(d)].

This can be further illustrated in Figures 6.2(f) and (g). The simultaneous increase of N and w is for simulating the fluence dependence of our subgap pumping experiment, where pair density increases with fluence, and w increases as γ_K decreases. An apparent expansion of the $\Delta R/R > 0$ region is observed from the top panel to the bottom panel [Figure 6.2(f)]. On the contrary, the simulations which are adapted to the over-gap pumping condition and accounts for both the increase of N and the band edge redshift ($\propto N$) but not the increase of w or any change in the nonthermal probability distribution function, fails to reproduce the expansion of the $\Delta R/R > 0$ region and exhibits an isosbestic point [Figure 6.2(g)]. The presence or absence of an isosbestic point is therefore a key distinguishing feature between Keldysh space tuning and photo-doping.

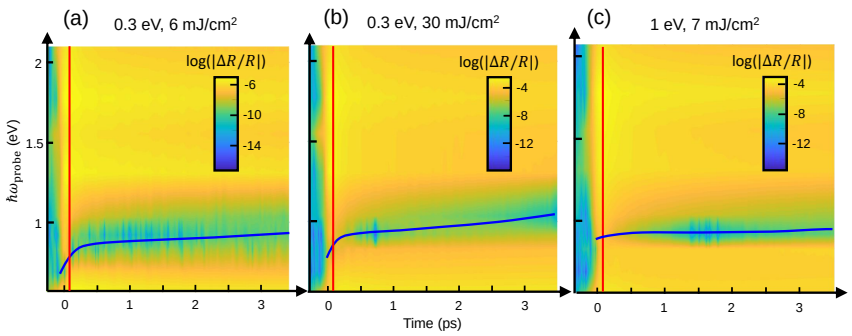

Figure 6.4: Time dynamics of the zero-crossing feature highlighted in the logarithmic plot of $|\Delta R/R|(t)$ map. (a) and (b), Two fluences for the 0.3 eV pump scenario. (c) Highest fluence for the 1 eV pump scenario. Blue lines are guides to the eye for the minimum of $|\Delta R/R|(t)$, highlighting the shift of zero-crossing versus time. Red lines mark the cuts at $t = 0.1$ ps, where the pair distribution is nonthermal.

Time-dependent probe photon energy-resolved $\Delta R/R$ maps of Ca_2RuO_4 were measured in both the Keldysh tuning ($\hbar\omega_{\text{pump}} = 0.3$ eV) and photo-doping ($\hbar\omega_{\text{pump}} = 1$ eV) regimes. As shown in Figures 6.3(e) & (f), the extremum in $\Delta R/R$, denoting the peak d-h density, occurs near a time $t = 0.1$ ps measured with respect to when the pump and probe pulses are exactly overlapped ($t = 0$). Figure 6.3(g) shows $\Delta R/R$ maps acquired in the subgap pumping regime for three different pump fluences corresponding to conditions (i) to (iii) in Figure 6.3(a). Focusing on the narrow time window around $t = 0.1$ ps where the d-h distribution is highly non-thermal, we observe that $\Delta R/R$ changes sign across a well-defined probe energy (dashed red line), marking a crossing point of the transient and equilibrium reflectivity spectra. As γ_K decreases, the crossing energy increases, evidencing an absence of an isosbestic point. Analogous maps acquired in the photo-doping regime [Figure 6.3(h)] also exhibit a sign change. However, the crossing energy remains constant over an order of magnitude change in fluence, consistent with an isosbestic point. These measurements corroborate our simulations and highlight the unique distribution control afforded by Keldysh tuning.

If one closely checks the zero crossing feature at longer timescale, it shows a continuous shift in energy after $t = 0.1$ ps (Figure 6.4), indicating that the optical response of the sample undergoes subsequent stages of evolution, including pair thermalization, interband recombination, and heating, each with a characteristic timescale. A notable example is at $t = 3$ ps, where pairs have mostly recombined and the electronic and the lattice systems have equilibrated at a higher transient

temperature; the energy of the zero-crossing is an indicator of sample heating (M.-C. Lee, C. H. Kim, Kwak, J. Kim, et al., 2018). The fluence of Figure 6.4(b) is higher, and creates more heat than that in Figure 6.4(a), which naturally explains why its zero-crossing is at higher energy at $t = 3$ ps.

6.3 Experiment and Simulation: Coherent Bandwidth Renormalization and Floquet Engineering

To study the d-h thermalization dynamics in more detail, we used a Kramers-Kronig transformation to convert our differential reflectivity spectra into differential conductivity ($\Delta\sigma$) spectra. Considering that the reflectivity spectrum $R(\omega)$ is known, the reflection phase $\theta(\omega)$ can be calculated as

$$\theta(\omega) = \frac{1}{\pi}\int_0^\infty \ln\left|\frac{\omega' + \omega}{\omega' - \omega}\right| \frac{d\ln\sqrt{R(\omega')}}{d\omega'} d\omega', \tag{6.9}$$

without directly measuring it in experiments, and the real and imaginary parts of refractive index $\tilde{n}$ can be calculated by

$$\mathrm{Re}(n) = \frac{1 - R}{1 + R - 2\cos\theta\sqrt{R}}, \tag{6.10}$$

$$\mathrm{Im}(n) = \frac{-2\sin\theta\sqrt{R}}{1 + R - 2\cos\theta\sqrt{R}}. \tag{6.11}$$

The optical conductivity $\tilde{\sigma}$ can be obtained by $\tilde{\sigma} = (\tilde{n}^2 - 1)\omega\epsilon_0/i$.

However, to use Eq. 6.9, $R(\omega)$ must be known from zero to infinite frequencies, which is impractical for experiments. Although there exist various methods that extrapolate $R(\omega)$ within a limited measurement range to high and low frequencies to complete the calculation, we applied a regional Kramers-Kronig transformation to obtain $\tilde{\sigma}$, as the strong resonance at $\omega \sim \omega'$ suggests that frequencies away from the range of interest contribute much less to $\theta(\omega)$.

This method relies on two conditions: (1) the static optical conductivity results should cover a wider range of photon energy than the transient data, and (2) $\Delta R/R(t) \ll 1$. In our case, since the static optical constants of Ca_2RuO_4 from 0.08 eV to 6.5 eV without optical pumping have already been determined by measuring broadband $R(\omega)$, while our transient $\Delta R/R(\omega, t)$ covers a smaller frequency range from 0.5 eV to 2.2 eV, the first condition is satisfied; also note that the temperature-increase-induced $\Delta R/R \ll 1$ and none of the pump-induced change exceeds that induced by temperature increase, the second condition is also fulfilled.

The $\theta(\omega)$ integral can be written as the sum of three frequency ranges, namely, the low-frequency range, the measurement range, and the high-frequency range:

$$\theta(\omega) = -\frac{1}{\pi}\int_{0}^{0.5\text{ eV}} f(R,\omega)d\omega' - \frac{1}{\pi}\int_{0.5\text{ eV}}^{2.2\text{ eV}} f(R,\omega)d\omega' - \frac{1}{\pi}\int_{2.2\text{ eV}}^{\infty} f(R,\omega)d\omega', \tag{6.12}$$

where

$$f(R,\omega) = \ln\sqrt{R(\omega')}\frac{d}{d\omega'}\left(\ln\left|\frac{\omega'+\omega}{\omega'-\omega}\right|\right). \tag{6.13}$$

Applying the generalized mean value theorem to first and third integrals in Eq. 6.12, and defining the second term as ϕ gives

$$\theta(\omega) = A\ln\left|\frac{0.5\text{ eV}+\omega}{0.5\text{ eV}-\omega}\right| + \phi(\omega) + B\ln\left|\frac{2.2\text{ eV}+\omega}{2.2\text{ eV}-\omega}\right|, \tag{6.14}$$

where A and B are coefficients. We fitted A and B from the known static σ data at 20 K. In the nonequilibrium scenario, $\Delta R/R$ due to the optical pump will enter $\phi(\omega)$ to affect $\theta(\omega)$. A and B are also expected to change slightly due to nonzero $\Delta R/R$ in these unmeasured ranges. However, when $\Delta R/R \ll 1$, it is still numerically accurate to keep the nonequilibrium A and B constants to be the same as their equilibrium values, because the first and third terms in Eq. 6.14 are off resonant in frequency. A benchmark test shows a close agreement between regional Kramers-Kronig output and static experimental data between 0.5 and 2.2 eV, demonstrating the validity of our algorithm.

Figure 6.5(a) shows the real part of the transient conductivity measured in the thermalized state (t = 0.5 ps) following an 0.3 eV pump pulse of fluence 26 mJ/cm^2 (γ_K = 0.5), overlaid with the equilibrium conductivity. Subgap pumping induces a spectral weight transfer from the β to α peak and a slight red-shift of the band edge, likely due to free carrier screening of the Coulomb interactions (Gole ž, Martin Eckstein, and Werner, 2015). Unlike in the DC limit, there is no sign of Mott gap collapse despite E_{pump} exceeding 10^9 V/m. To verify that the electronic subsystem indeed thermalizes by t = 0.5 ps, we compare the real parts of $\Delta\sigma_{0.3\text{ eV}}$ (fluence: 26 mJ/cm^2) and $\Delta\sigma_{1\text{ eV}}$ (fluence: 4 mJ/cm^2), the change in conductivity induced by subgap and above-gap pumping respectively, at both t = 0.1 ps and 0.5 ps. A scaling factor A is applied to $\Delta\sigma_{1\text{ eV}}$ to account for any differences in excitation density. As shown in Figure 6.5(b), the t = 0.1 ps curves do not agree within any scale factor. This is expected because the linear and nonlinear pair production processes initially give rise to very different non-thermal distributions. Conversely, by t = 0.5 ps, the curves overlap very well [Figure 6.5(c)], indicating that the system has lost memory of how the d-h pairs were produced and is thus completely thermalized.

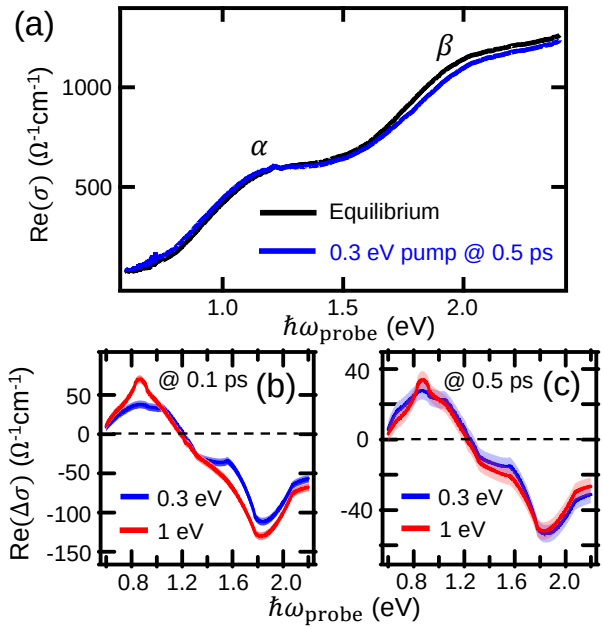

Figure 6.5: Non-equilibrium conductivity transients. (a) Conductivity spectra of Ca_2RuO_4 in the un-pumped equilibrium state at 80 K and the 0.3 eV pumped non-equilibrium state at t = 0.5 ps (fluence: 26 mJ/cm^2). (b) Comparison of differential conductivity spectra between 0.3 eV pump ($\Delta\sigma_{0.3\text{ eV}}$) and scaled 1 eV pump ($A\Delta\sigma_{1\text{ eV}}$) cases at t = 0.1 ps and (c) t = 0.5 ps. Red and blue shades indicate error estimated from the ω_{probe}-dependent fluctuations of the experimental $\Delta\sigma$ spectra.

Based on the observations in Figures 6.5(b) & (c), the non-thermal window can be directly resolved by evaluating the time interval over which the quantity $\Delta(\Delta\sigma) = \Delta\sigma_{0.3\text{ eV}} - A\times\Delta\sigma_{1\text{ eV}}$ is non-zero. Figures 6.6 (a) and (b) show a comparison between $\Delta\sigma_{0.3\text{ eV}}$ and $\Delta\sigma_{1\text{ eV}}$ across all fluences at time zero (t = 0 ps). The probe energy ranges that show apparent modifications in $\Delta\sigma_{0.3\text{ eV}}$ data compared to $\Delta\sigma_{1\text{ eV}}$ are marked by the blue shade, where the positive peak looks flattened out, and the red shade, where a bump appears in the negative portion of the signal. In addition, a robust isosbestic point can be identified in both data sets at the same probe energy (1.2 eV) for all fluences. Generally speaking, for spectroscopic studies, an isosbestic point is usually used as a reference point. In our case, the fact that it lies outside the blue and red shades (where spectral modifications obviously take place) strongly suggests that the probe energy of 1.2 eV, and energies that are right in the vicinity of it, are not influenced by the strong-field modification effect. Therefore, we chose the probe energy range between 1.1 eV to 1.3 eV as the reference, scaled $\Delta\sigma_{1\text{ eV}}$ to obtain the best matching with $\Delta\sigma_{0.3\text{ eV}}$ data in this range, and calculated

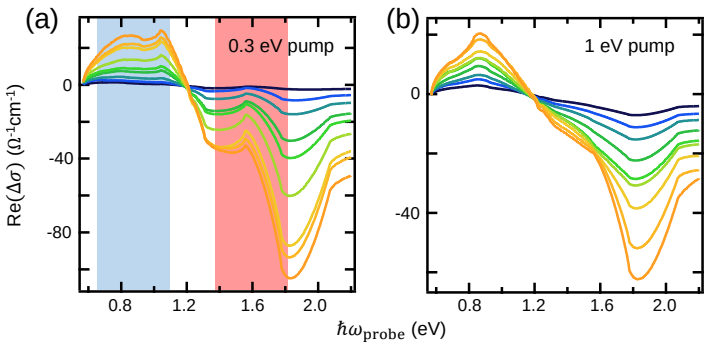

Figure 6.6: Comparison of $\Delta\sigma$ spectra for 0.3 eV pump (a) and 1 eV pump (b) at $t = 0$ ps. Curves from blue to orange represent low to high fluences. 0.3 eV pump fluences range from 3 mJ/cm^2 to 30.4 mJ/cm^2. 1 eV pump fluences range from 0.57 mJ/cm^2 to 6.9 mJ/cm^2. Blue and red shaded regions in (a) highlight spectral ranges where additional modifications develop on the 0.3 eV pump data compared to the 1 eV pump data.

$\Delta(\Delta\sigma) = \Delta\sigma_{0.3\text{ eV}} - A \times \Delta\sigma_{1\text{ eV}}$. This procedure was repeated for all time delays, producing the colormap in Figure 6.7(a). Since both the real and the imaginary parts of $\Delta\sigma_{1\text{ eV}}$ at $t = 0$ ps scale well for all fluences, so the scaling factor can simply account for the amplitude difference and is not important which fluence of $\Delta\sigma_{1\text{ eV}}$ is selected for the subtraction.

Figure 6.7(a) shows the complete temporal mapping of $\Delta(\Delta\sigma)$ spectra. The signal is finite only around $t = 0$ ps and is close to zero otherwise, supporting the validity our subtraction protocol. By taking a constant energy cut, we can extract a thermalization time constant of around 0.2 ps [Figure 6.7(b)]. Interestingly, $\Delta R/R$ and $\Delta\sigma_{0.3\text{ eV}}$, which both track the d-h pair density, peak near 0.1 ps whereas $\Delta(\Delta\sigma)$ peaks earlier at $t = 0$ when the d-h pair density is still quite low. This implies the existence of an additional coherent non-thermal process that scales with E_{pump}, which peaks at $t = 0$, rather than with the d-h density.

To identify the physical process responsible for the $t = 0$ signal, we examined how the electronic structure of Ca_2RuO_4 would need to change in order to produce the $\Delta(\Delta\sigma)$ profile observed at $t = 0$. Using density functional theory (DFT), we performed an *ab initio* calculation of the optical conductivity of Ca_2RuO_4 based on its reported lattice and magnetic structures below T_N. The calculation was set to the spin-polarized mode to take into account the low-temperature antiferromagnetic structure, and to the DFT+U mode to take into account the Coulomb correlation. The real and imaginary parts of the optical conductivity were calculated by the

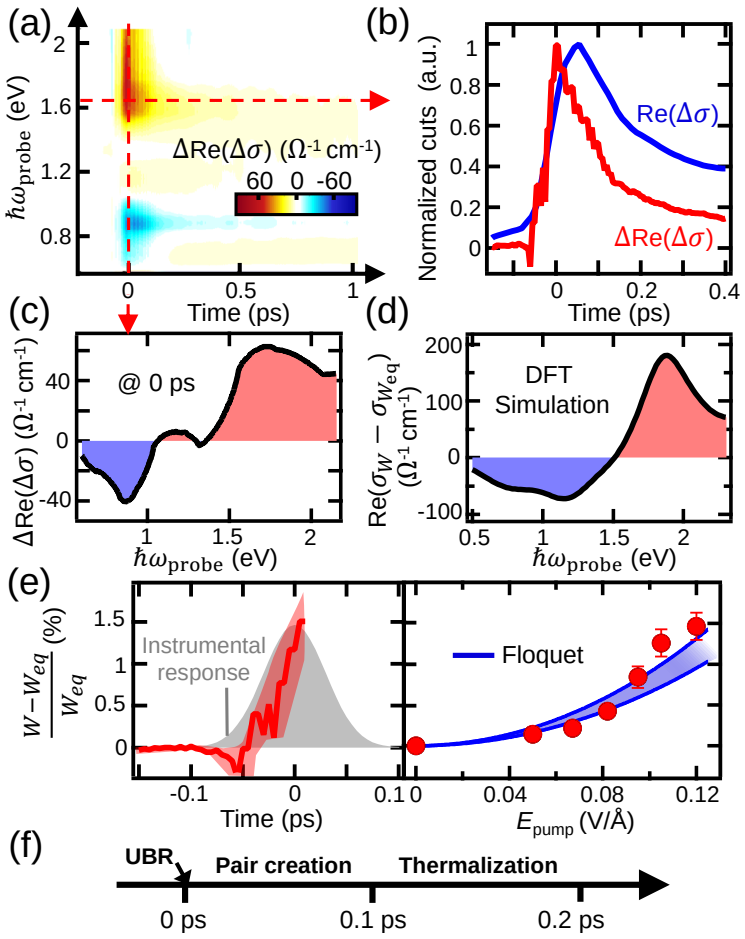

Figure 6.7: Ultrafast coherent bandwidth renormalization. (a) $\Delta(\Delta\sigma)$ map obtained by subtracting scaled $\Delta\sigma_{1\text{ eV}}$ from $\Delta\sigma_{0.3\text{ eV}}$ spectra. (b) A constant probe energy cut at 1.65 eV [dashed horizontal line in (a)] plotted together with $\Delta\sigma_{0.3\text{ eV}}$. (c) A constant time cut at $t = 0$ [dashed vertical line in (a)]. (d) DFT simulation of the spectrum change induced by bandwidth broadening. σ_W ($\sigma_{W_{\text{eq}}}$): conductivity with (without) bandwidth broadening. (e) (left) Quantitative extraction of pump-induced bandwidth modification versus t (with $E_{\text{pump}} = 0.12$ V/Å) and (right) versus E_{pump} (with $t = 0$ ps) based on fitting to DFT calculations. Red shaded region: error bar. Blue shaded region: Floquet theory prediction based on a periodically driven two-site cluster Hubbard model. Upper and lower bounds assume $U = 3$ eV (Jung et al., 2003) and $U = 3.5$ eV (Gorelov et al., 2010) respectively, where U is the on-site Coulomb energy, with no other adjustable parameters. (f) Chronology of non-thermal processes following an impulsive subgap drive.

epsilon.x package with finite interband and intraband smearings to avoid sharp spikes in the spectra caused by numerical issues. The calculated band structure, total density of states, and conductivity spectrum are in agreement with previous DFT and experimental studies (Fang, Naoto Nagaosa, and Terakura, 2004; Jung

et al., 2003).

To simulate the effect of bandwidth broadening, we changed the structural input parameters. In Ca_2RuO_4, each RuO_6 octahedron undergoes two types of distortions compared to the K_2NiO_4 structure (I4/mmm), yielding significant modifications to the in-plane hopping amplitudes, and therefore, the bandwidth. Figure 6.8(a) summarizes the two types of distortions, the rigid rotation of the octahedron around the c axis by the angle ϕ, and the rigid tilting of the octrahedron around an in-plane axis by the angle θ. In the static low temperature AFM state, $\phi = 12°$ and $\theta = 12°$, and the Ru-O-Ru bond angle $\angle$(Ru-O-Ru) = 150.1°. We broadened the bandwidth W in the simulation by reducing the tilting angle θ of the structure [Figure 6.8(a) bottom panel], while keeping all other structural parameters the same; this will make $\angle$(Ru-O-Ru) approach 180°, and broaden the bandwidth according to the empirical formula $W \propto [\cos\angle(\text{Ru-O-Ru})]^2$ (Cao et al., 2000). It is worth noting that keeping ϕ as a constant is based on the well known fact that θ responds much more sensitively to Sr doping (Fang, Naoto Nagaosa, and Terakura, 2004), temperature (Braden et al., 1998), and applied current (Bertinshaw et al., 2019) than ϕ. In addition, the coherent A_g phonon mode at 3.7 THz, which consists majorly of the tilting motion of RuO_6 octahedra, shows robust anomalies across the AFM ordering (M.-C. Lee, C. H. Kim, Kwak, Seo, et al., 2019) and quadrupolar ordering (M.-C. Lee, C. H. Kim, Kwak, J. Kim, et al., 2018) temperatures. These all suggest that the tilting distortion is a crucial structural parameter which responds sensitively to magnetic and electronic ground states, which justifies us adjusting θ for simulating the bandwidth renormalization induced by the strong-field drive, even though the drive does not directly modify θ. The table in Figure 6.8(b) shows examples of combinations of structure parameters, and the resulting ratio of the modified bandwidth to the static equilibrium bandwidth, W/W_{eq}, estimated from $W \propto [\cos\angle(\text{Ru-O-Ru})]^2$. To make sure that W is actually modified, we simulated the nonmagnetic crystal with $U = 0$ eV using the red and blue parameter sets in the table; the calculated bands are shown in the bottom panel of Figure 6.8(b). The nonmagnetic setting with $U = 0$ eV fully collapses the Mott gap, making it easier for us to identify a bandwidth change. As clearly observed in the bottom panel of Figure 6.8(b), the blue parameter set indeed leads to a broadened bandwidth compared to the red parameter set.

We find that both the real and imaginary parts of the measured $\Delta(\Delta\sigma)$ spectrum at $t = 0$ are reasonably well reproduced by our calculations if we assume the bandwidth of

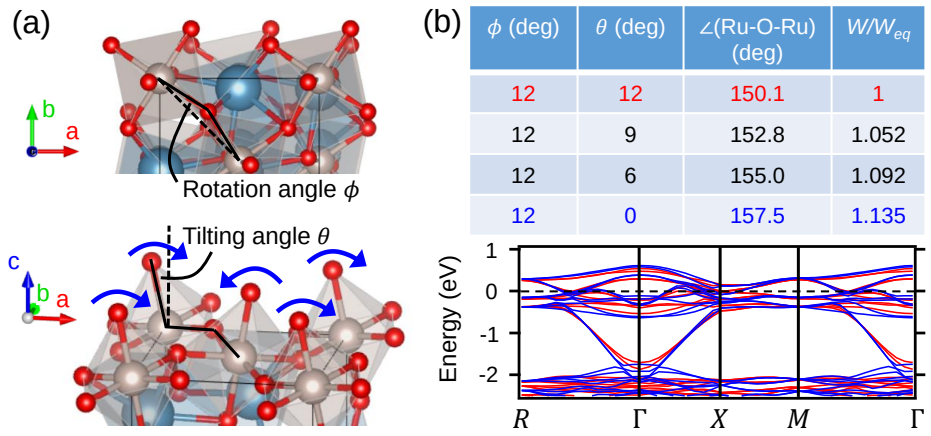

ϕ (deg)	θ (deg)	∠(Ru-O-Ru) (deg)	W/W_{eq}
12	12	150.1	1
12	9	152.8	1.052
12	6	155.0	1.092
12	0	157.5	1.135

Figure 6.8: Method to simulate the effect of bandwidth broadening. (a) There are two angles related to the lattice distortion in Ca_2RuO_4. Top: the rotation angle ϕ about the c axis. Bottom: the tilting angle θ about an in-plane axis. (b) Examples of how tuning θ affects the Ru-O-Ru bond angle and therefore, the bandwidth. Top: table displaying combinations of angles and the resulting modification to the bandwidth W from the equilibrium W_{eq}. Bottom: band structures using the red and blue parameter conditions from the top table with a nonmagnetic structure and $U = 0$ eV. Red (blue) bands correspond to the red (blue) parameter set.

the driven system (W) to exceed that in equilibrium W_{eq} [Figure 6.7(d)]. In contrast, if we consider another scenario where modification to Coulomb correlation U occurs (Tancogne-Dejean, Sentef, and Rubio, 2018), the change in conductivity would look very different, and would not match $\Delta(\Delta\sigma)$; this points to the coherent non-thermal process being a unidirectional ultrafast bandwidth renormalization (UBR) process that predominantly occurs under subgap pumping conditions [Figure 6.7(f)].

Coherent UBR can in principle occur via photo-assisted virtual hopping between lattice sites, which has recently been proposed as a pathway to dynamically engineer the electronic and magnetic properties of Mott insulators (Mentink, Balzer, and M. Eckstein, 2015; Hejazi, J. Liu, and Balents, 2019; Mikhaylovskiy et al., 2015; Batignani et al., 2015; Claassen et al., 2017; Yao Wang, Devereaux, and C.-C. Chen, 2018). To quantitatively extract the time- and E_{pump}-dependence of the fractional bandwidth change $(W - W_{eq})/W_{eq}$, we collected $\Delta(\Delta\sigma)$ spectra as a function of both time delay and pump fluence and fit them to DFT simulations. As shown in Figure 6.7(e), the bandwidth change exhibits a pulse-width limited rise with a maximum $t = 0$ value that increases monotonically with the peak pump field, reaching up to a relatively large amplitude of 1.5 % at $E_{pump} = 0.12$ V/Å, comparable to the bandwidth increases induced by doping (Fang, Naoto Nagaosa, and Terakura, 2004)

and pressure (Nakamura, Goko, et al., 2002).

Independently, we also calculated the field dependence of $(W - W_{\mathrm{eq}})/W_{\mathrm{eq}}$ expected from photo-assisted virtual hopping by solving a periodically driven two-site Hubbard model in the Floquet formalism (Mentink, Balzer, and M. Eckstein, 2015), using the same model parameters for Ca_2RuO_4 as in our Landau-Dykhne calculations [Figure 6.1(a)]. According to Ref.(Mentink, Balzer, and M. Eckstein, 2015), when the Mott insulator is strongly coupled ($U \gg t$), the ratio between the light-modified bandwidth and the static bandwidth is

$$\frac{W}{W_{\mathrm{eq}}} = \sqrt{\sum_{n=-\infty}^{\infty} \frac{J_{|n|}(\mathcal{E})^2}{1 + n\omega/U}}, \tag{6.15}$$

where $\mathcal{E} = eaE_0/(\hbar\omega)$ is the Floquet parameter, a is the lattice constant, E_0 is the field amplitude, ω is the pump frequency, and $J_n(x)$ is the nth Bessel function. We find a remarkable match to the data without any adjustable parameters [Figure 6.7(e)]. Since bandwidth renormalization increases with the Floquet parameter in the case of photo-assisted virtual hopping, this naturally explains why subgap pumping induces the much larger UBR effect compared to above-gap pumping.

6.4 Discussion and Outlook

The ability to rationally tune a Mott insulator *in situ* over Keldysh space enables targeted searches for exotic out-of-equilibrium phenomena such as strong correlation assisted high harmonic generation (Imai, Ono, and Ishihara, 2020; Silva et al., 2018), coherent dressing of quasiparticles (Novelli et al., 2014), Wannier-Stark localization (W.-R. Lee and Park, 2014; Murakami and Werner, 2018), AC dielectric breakdown (Oka, 2012) and dynamical Franz-Keldysh effects (Srivastava et al., 2004; Tancogne-Dejean, Sentef, and Rubio, 2020), which are predicted to manifest in separate regions of Keldysh space. It also provides control over the nonlinear d-h pair production rate - the primary source of heating and decoherence under subgap pumping conditions - in Mott systems, which is crucial for experimentally realizing coherent Floquet engineering of strongly correlated electronic phases. The Floquet engineering of bandwidth also constitutes another pathway toward coherent band modulation in addition to modifying the onsite Coulomb interaction by screening (Tancogne-Dejean, Sentef, and Rubio, 2018).

Appendix A

SHG AS A PROBE OF STRUCTURE OF MAGNETIC WEYL SEMIMETALS

A.1 Introduction

Weyl semimetals are crystalline solids that host bulk relativistic Weyl nodes and surface Fermi-arc states that connect the Weyl nodes with opposite chiralities in their electronic structure. Weyl semimetals must break either spatial inversion symmetry (IS), time-reversal symmetry (TRS), or both, to host the topologically nontrivial Weyl fermions. Ensuing the discovery of the celebrated IS-broken Weyl semimetal family (Ta,Nb)(As,P), magnetic Weyl semimetals with intrinsic TRS breaking stemming from the spin polarization have aroused intense interests. Compared with the Weyl semimetals breaking IS (Hasan et al., 2017), Weyl semimetals with TRS breaking provide a playground to investigate the rich exotic quantum states ranging from anomalous Hall/Nernst effects to axion electrodynamics arising from the interplay between magnetism, electron correlation, and topological orders (Bernevig, Felser, and Beidenkopf, 2022). A vast array of magnetic topological materials have been experimentally established, including magnetic Weyl semimetals with kagome lattice such as M_3X (X = Sn, Ge), $Co_3Sn_2S_2$, RMn_6Sn_6 (R = Tb, Gd, Tm, Lu), and $(Co,Fe)_xSn_y$, antiferromagnetic half-Heusler compound RPtBi (R = Lu, Dy, Gd), antiferromagnetic cubic Weyl semimetals RAlGe (R = Ce, Pr), ferromagnetic nodal line semimetal Co_2MnZ (Z = Ga, Al), and so on. Some of these magnetic Weyl semimetals break both IS and TRS, while the others respect spatial IS.

A.2 SHG measurements of PrAlSi and CeAlGe

CeAlGe belongs to the antiferromagnetic Weyl family RAlGe (R = Ce, Pr) and undergoes an incommensurate multi-k antiferromagnetic transition at T_N =4.4 K (Puphal et al., 2020). However, its analogue PrAlSi orders ferromagnetically at T_c =17.8 K, followed by two reentrant spin-glass transitions at lower temperatures (Lyu et al., 2020). Although the structure of RAlGe (R = Ce, Pr, and La) has been well established, the crystallographic structure of PrAlSi is presently controversial. Specifically, it is difficult to distinguish between a non-centrosymmetric tetragonal space group $I4_1md$ (point group $4mm$) versus a centrosymmetric tetragonal space group $I4_1/amd$ (point group $4/mmm$) with current diffraction-based techniques

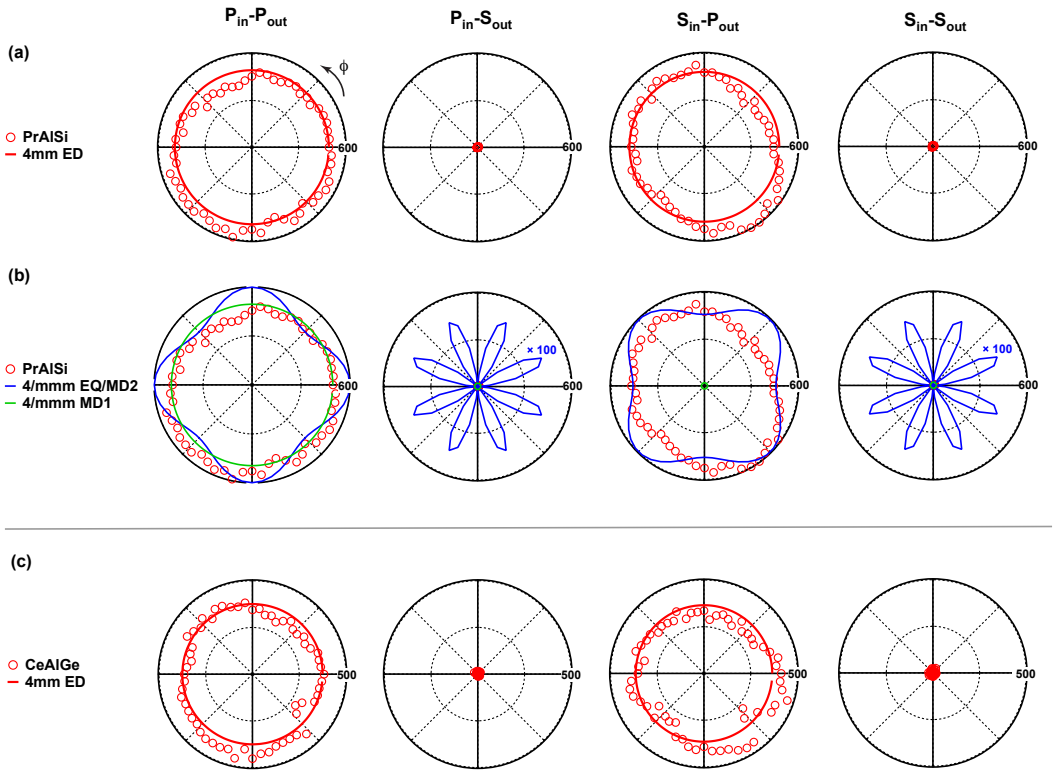

Figure A.1: Polar plots of the SHG-RA data (red circles) from the (001) surface of PrAlSi and CeAlGe for four different incident/outgoing polarization combinations: (a) PrAlSi data with fits to ED SHG (red) from $4mm$ point group. (b) PrAlSi data with fits to MD2 (green) and EQ/MD1 SHG (blue) from a centrosymmetric 4/mmm point group, respectively. (c) CeAlGe data with fits to ED SHG (red) from $4mm$ point group. The radial axis represents the SHG intensity and the azimuthal angle ϕ denotes the rotation angle of the scattering plane.

(Lyu et al., 2020; Yang et al., 2020). However, the presence or absence of inversion symmetry has a profound effect on SHG. Therefore, we seek to resolve this issue by SHG-RA.

The leading order electric dipole (ED) SHG susceptibility tensor vanishes by symmetry in the bulk of centrosymmetric crystals. Nevertheless, higher order SHG processes are still allowed. Therefore, we focus on four possibilities for the origin of any SHG signal from PrAlSi: (1) bulk ED SHG from a non-centrosymmetric $4mm$ point group, (2) surface ED SHG from a centrosymmetric $4/mmm$ point group, (3) bulk magnetic dipole (MD2) SHG from a centrosymmetric $4/mmm$ point group, and (4) bulk electric quadrupole/magnetic dipole (EQ/MD1) SHG processes from a centrosymmetric $4/mmm$ point group.

The SHG-RA data are acquired by selecting the incident (in) and outgoing (out) light polarization to be either parallel (P) or perpendicular (S) to the scattering plane, and then recording the intensity of reflected SHG as the scattering plane is rotated about the (001) axis of PrAlSi. Data taken in the four possible polarization geometries at 300 K are shown in Figure A.1(a). While the signals in the $P_{in} - P_{out}$ and $S_{in} - P_{out}$ channels are strong and isotropic, no signal was detected in the $P_{in} - S_{out}$ and $S_{in} - S_{out}$ geometries. This behavior is in excellent agreement with ED SHG from a $4mm$ point group. However, it cannot be reproduced even qualitatively by either MD2 or EQ/MD1 bulk SHG from a $4/mmm$ point group, as the former will give rise to zero SHG intensity in $S_{in} - P_{out}$ channel while the latter will generate a nonzero SHG pattern with 8 equal petals in $P_{in} - S_{out}$ and $S_{in} - S_{out}$ geometries [Figure A.1(b)]. This definitively rules out the latter two possibilities.

The ED SHG contribution from the (001) surface of a $4/mmm$ point group can produce the same RA patterns as bulk ED SHG from a $4mm$ point group. Therefore the former cannot be ruled out based on symmetry alone. However, we can infer a bulk ED origin based on the absolute SHG intensity. To do so, we also performed SHG-RA measurements on (001) cut CeAlGe whose structure is known to be described by the non-centrosymmetric $I4_1md$ space group and whose SHG response should thus be dominated by the bulk ED contribution (T. Suzuki et al., 2019). We measured the SHG-RA patterns in the four geometries and found that both the SHG-RA patterns and the absolute SHG intensities from PrAlSi and CeAlGe are very similar [Figure A.1(c)]. This indicates that the SHG response from PrAlSi is of predominantly bulk ED origin from a $4mm$ point group, as opposed to surface ED origin which would be much weaker. Therefore, we can conclude that PrAlSi shares the same noncentrosymmetric structural space group with CeAlGe.

A.3 SHG measurements of Co_2MnGa

Co_2MnGa is another interesting ferromagnetic (T_c=690 K) topological nodal-line semimetal where the bulk conduction and valence bands touch along a closed loop of Weyl nodes and the surface states form a "drumhead"-like flat band (Belopolski, Manna, et al., 2019). Moreover, the Weyl node loops form Hopf link which consists of two rings passing through the center of each other and features a topologically nontrivial linking-number invariant (Belopolski, Chang, et al., 2022; Chang, S.-Y. Xu, et al., 2017). It also exhibits giant anomalous Hall and Nernst effects even at room temperature, providing strong evidence of Weyl fermion-induced unconventional transport properties. (Manna et al., 2018; A. Sakai et al., 2018)

Co_2MnGa crystallizes in the centrosymmetric full Heusler structure with a space group $Fm\bar{3}m$ (octahedral point group O_h). As the collinear ferromagnetic order develops far above room temperature, the magnetic structure respects $4/mm'm'$ magnetic point group also with a inversion center. So far, very little is known about the SHG response of magnetic IS-preserved Weyl semimetals. Since both the magnetic and lattice structures respect IS, one would naively expect a very small SHG signal. However, band structure calculations predict resonant excitation can be generated between the surface drumhead flat bands that are spaced by 1.5-2 eV (Chang, S.-Y. Xu, et al., 2017). To this end, we employed an near-IR 800 nm (1.55 eV) light and performed the SHG-RA measurement to investigate the possible enhancement of SHG signal from the resonant excitation of electrons between flat surface bands in Co_2MnGa.

We performed the SHG-RA measurement on the (001) face of Co_2MnGa at 300 K in the four different polarization configurations. The signals in all channels are rather weak and isotropic [Figure A.2(i)]. Since the leading order ED SHG vanishes in the bulk of centrosymmetric crystals, we consider the four possibilities of higher-order processes from both structural and magnetic channels: (1) bulk EQ SHG, (2) bulk MD1, (3) bulk MD2, and (4) surface ED SHG [Figures A.2(a)-(h)]. Apparently a reasonable fit to the data can only be achieved with the coherent addition of bulk MD1 from both structural and magnetic channels, while the other processes either produce zero SHG intensity in particular polarization configurations or fail to reproduce the shape of SHG-RA patterns even qualitatively. The failure of fitting with surface ED process associated with the low SHG intensity indicates that the enhancement of SHG signal purely from the resonant excitation between drumhead states is not achieved at least with a linear 800 nm probe. Further investigation such as changing the light polarization from linear to circular or finely sweeping the light photon energy between 1.5-2 eV is required to draw a conclusion.

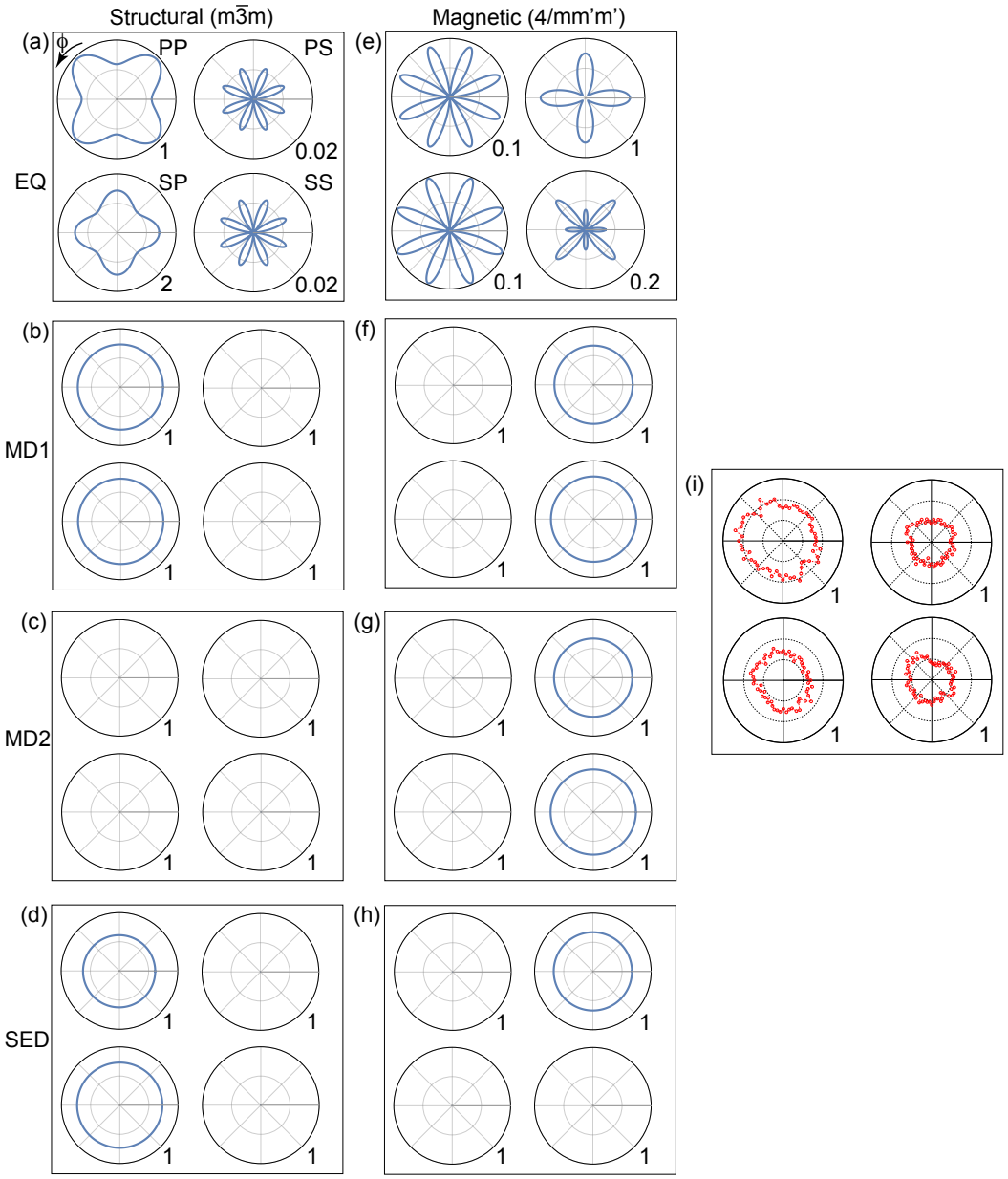

Figure A.2: SHG-RA data and simulation of Co_2MnGa. (a)-(d) Simulation of EQ, MD1, MD2, and surface ED SHG in four different incident/outgoing polarization combinations from $m\bar{3}m$ point group. (e)-(h) Simulation of EQ, MD1, MD2, and surface ED SHG from $4/mm'm'$ point group. The radial axis represents the SHG intensity and the azimuthal angle ϕ denotes the rotation angle of the scattering plane. (i) Polar plots of the SHG-RA data (red circles) from the (001) surface of Co_2MnGa.

BIBLIOGRAPHY

Afanasiev, D. et al. (2021). "Ultrafast control of magnetic interactions via light-driven phonons". In: *Nature Materials* 20.5, pp. 607–611. DOI: 10.1038/s41563-021-00922-7. URL: https://doi.org/10.1038/s41563-021-00922-7.

Agapito, Luis A. et al. (Apr. 2013). "Novel Family of Chiral-Based Topological Insulators: Elemental Tellurium under Strain". In: *Phys. Rev. Lett.* 110 (17), p. 176401. DOI: 10.1103/PhysRevLett.110.176401. URL: https://link.aps.org/doi/10.1103/PhysRevLett.110.176401.

Armitage, N. P. (2009). *Electrodynamics of correlated electron systems*. DOI: 10.48550/ARXIV.0908.1126. URL: https://arxiv.org/abs/0908.1126.

Asamitsu, A. et al. (1997). "Current switching of resistive states in magnetoresistive manganites". In: *Nature* 388.6637, pp. 50–52. ISSN: 1476-4687.

Ashitkov, S. I. et al. (2002). "Ultrafast laser-induced phase transitions in tellurium". In: *Journal of Experimental and Theoretical Physics Letters* 76.7, pp. 461–464. DOI: 10.1134/1.1528702. URL: https://doi.org/10.1134/1.1528702.

Baldini, Edoardo et al. (2020). *The spontaneous symmetry breaking in Ta_2NiSe_5 is structural in nature*. arXiv: 2007.02909 [cond-mat.str-el].

Basov, D. N., R. D. Averitt, and D. Hsieh (2017). "Towards properties on demand in quantum materials". In: *Nature Materials* 16.11, pp. 1077–1088. DOI: 10.1038/nmat5017. URL: https://doi.org/10.1038/nmat5017.

Batignani, G. et al. (2015). "Probing ultrafast photo-induced dynamics of the exchange energy in a Heisenberg antiferromagnet". In: *Nat. Photonics* 9.8, pp. 506–510. ISSN: 1749-4893.

Beaud, P., A. Caviezel, et al. (2014). "A time-dependent order parameter for ultrafast photoinduced phase transitions". In: *Nature Materials* 13.10, pp. 923–927. DOI: 10.1038/nmat4046. URL: https://doi.org/10.1038/nmat4046.

Beaud, P., S. L. Johnson, et al. (Oct. 2009). "Ultrafast Structural Phase Transition Driven by Photoinduced Melting of Charge and Orbital Order". In: *Phys. Rev. Lett.* 103 (15), p. 155702. DOI: 10.1103/PhysRevLett.103.155702. URL: https://link.aps.org/doi/10.1103/PhysRevLett.103.155702.

Beaurepaire, E. et al. (May 1996). "Ultrafast Spin Dynamics in Ferromagnetic Nickel". In: *Phys. Rev. Lett.* 76 (22), pp. 4250–4253. DOI: 10.1103/PhysRevLett.76.4250. URL: https://link.aps.org/doi/10.1103/PhysRevLett.76.4250.

Belopolski, Ilya, Guoqing Chang, et al. (2022). "Observation of a linked-loop quantum state in a topological magnet". In: *Nature* 604.7907, pp. 647–652. DOI: 10.1038/s41586-022-04512-8. URL: https://doi.org/10.1038/s41586-022-04512-8.

Belopolski, Ilya, Kaustuv Manna, et al. (2019). "Discovery of topological Weyl fermion lines and drumhead surface states in a room temperature magnet". In: *Science* 365.6459, pp. 1278–1281. DOI: 10.1126/science.aav2327. eprint: https://www.science.org/doi/pdf/10.1126/science.aav2327. URL: https://www.science.org/doi/abs/10.1126/science.aav2327.

Bernevig, B. Andrei, Claudia Felser, and Haim Beidenkopf (2022). "Progress and prospects in magnetic topological materials". In: *Nature* 603.7899, pp. 41–51. DOI: 10.1038/s41586-021-04105-x. URL: https://doi.org/10.1038/s41586-021-04105-x.

Bersuker, Isaac (2006). *The Jahn-Teller Effect*. Cambridge: Cambridge University Press. DOI: DOI:10.1017/CBO9780511524769. URL: https://www.cambridge.org/core/books/jahnteller-effect/05766FA392314EE9022AA86A53AC52E5.

Bertinshaw, J. et al. (Sept. 2019). "Unique Crystal Structure of Ca_2RuO_4 in the Current Stabilized Semimetallic State". In: *Phys. Rev. Lett.* 123 (13), p. 137204. DOI: 10.1103/PhysRevLett.123.137204.

Bertsch, G. F. et al. (Sept. 2000). "Real-space, real-time method for the dielectric function". In: *Physical Review B* 62.12, p. 7998. DOI: 10.1103/PhysRevB.62.7998. URL: https://doi.org/10.1103%2Fphysrevb.62.7998.

Birss, Robert R. (1966). *Symmetry and magnetism*. North-Holland.

Bloch, Jacqueline et al. (2022). "Strongly correlated electron–photon systems". In: *Nature* 606.7912, pp. 41–48. DOI: 10.1038/s41586-022-04726-w. URL: https://doi.org/10.1038/s41586-022-04726-w.

Bloembergen, N. and P. S. Pershan (Oct. 1962). "Light Waves at the Boundary of Nonlinear Media". In: *Phys. Rev.* 128 (2), pp. 606–622. DOI: 10.1103/PhysRev.128.606. URL: https://link.aps.org/doi/10.1103/PhysRev.128.606.

Boyd, Robert W. (2020). *Nonlinear optics*. Elsevier, AP Academic Press.

Braden, M. et al. (July 1998). "Crystal and magnetic structure of Ca_2RuO_4 : Magnetoelastic coupling and the metal-insulator transition". In: *Phys. Rev. B* 58 (2), pp. 847–861. DOI: 10.1103/PhysRevB.58.847. URL: https://link.aps.org/doi/10.1103/PhysRevB.58.847.

Bretscher, Hope M., Paolo Andrich, Yuta Murakami, et al. (2021). "Imaging the coherent propagation of collective modes in the excitonic insulator Ta_2NiSe_5 at room temperature". In: *Science Advances* 7.28, eabd6147. DOI: 10.1126/sciadv.abd6147. eprint: https://www.science.org/doi/pdf/10.1126/sciadv.abd6147. URL: https://www.science.org/doi/abs/10.1126/sciadv.abd6147.

Bretscher, Hope M., Paolo Andrich, Prachi Telang, et al. (2021). "Ultrafast melting and recovery of collective order in the excitonic insulator Ta2NiSe5". In: *Nature Communications* 12.1, p. 1699. DOI: 10.1038/s41467-021-21929-3. URL: https://doi.org/10.1038/s41467-021-21929-3.

Brodsky, M. H. et al. (1972). "The Raman Spectrum of Amorphous Tellurium". In: *physica status solidi (b)* 52.2, pp. 609–614. DOI: https://doi.org/10.1002/pssb.2220520229. URL: https://onlinelibrary.wiley.com/doi/abs/10.1002/pssb.2220520229.

Bucher, B., P. Steiner, and P. Wachter (Nov. 1991). "Excitonic insulator phase in $TmSe_{0.45}Te_{0.55}$". In: *Phys. Rev. Lett.* 67 (19), pp. 2717–2720. DOI: 10.1103/PhysRevLett.67.2717. URL: https://link.aps.org/doi/10.1103/PhysRevLett.67.2717.

Buzzi, Michele et al. (Mar. 2021). "Higgs-Mediated Optical Amplification in a Nonequilibrium Superconductor". In: *Phys. Rev. X* 11 (1), p. 011055. DOI: 10.1103/PhysRevX.11.011055. URL: https://link.aps.org/doi/10.1103/PhysRevX.11.011055.

Cao, G. et al. (Feb. 2000). "Ground-state instability of the Mott insulator Ca_2RuO_4 : Impact of slight La doping on the metal-insulator transition and magnetic ordering". In: *Phys. Rev. B* 61 (8), R5053–R5057. DOI: 10.1103/PhysRevB.61.R5053. URL: https://link.aps.org/doi/10.1103/PhysRevB.61.R5053.

Cavalleri, A. et al. (Nov. 2001). "Femtosecond Structural Dynamics in VO_2 during an Ultrafast Solid-Solid Phase Transition". In: *Phys. Rev. Lett.* 87 (23), p. 237401. DOI: 10.1103/PhysRevLett.87.237401. URL: https://link.aps.org/doi/10.1103/PhysRevLett.87.237401.

Caviglia, A. D. et al. (Dec. 2013). "Photoinduced melting of magnetic order in the correlated electron insulator $NdNiO_3$". In: *Phys. Rev. B* 88 (22), p. 220401. DOI: 10.1103/PhysRevB.88.220401. URL: https://link.aps.org/doi/10.1103/PhysRevB.88.220401.

Chan, Ching-Kit et al. (Sept. 2016). "Type-II Weyl cone transitions in driven semimetals". In: *Phys. Rev. B* 94 (12), p. 121106. DOI: 10.1103/PhysRevB.94.121106. URL: https://link.aps.org/doi/10.1103/PhysRevB.94.121106.

Chang, Guoqing, Benjamin J. Wieder, et al. (Nov. 2018). "Topological quantum properties of chiral crystals". In: *Nature Materials* 17.11, pp. 978–985. ISSN: 1476-4660. DOI: 10.1038/s41563-018-0169-3. URL: https://doi.org/10.1038/s41563-018-0169-3.

Chang, Guoqing, Su-Yang Xu, et al. (Oct. 2017). "Topological Hopf and Chain Link Semimetal States and Their Application to Co_2MnGa". In: *Phys. Rev. Lett.* 119 (15), p. 156401. DOI: 10.1103/PhysRevLett.119.156401. URL: https://link.aps.org/doi/10.1103/PhysRevLett.119.156401.

Chen, Gang and Leon Balents (Sept. 2011). "Spin-orbit coupling in d^2 ordered double perovskites". In: *Phys. Rev. B* 84 (9), p. 094420. DOI: 10.1103/PhysRevB.84.094420. URL: https://link.aps.org/doi/10.1103/PhysRevB.84.094420.

Chen, Gang, Rodrigo Pereira, and Leon Balents (Nov. 2010). "Exotic phases induced by strong spin-orbit coupling in ordered double perovskites". In: *Phys. Rev. B* 82 (17), p. 174440. DOI: 10.1103/PhysRevB.82.174440. URL: https://link.aps.org/doi/10.1103/PhysRevB.82.174440.

Cheng, Yu-Hsiang, Frank Y. Gao, et al. (Oct. 2017). "Coherent control of optical phonons in bismuth". In: *Phys. Rev. B* 96 (13), p. 134302. DOI: 10.1103/PhysRevB.96.134302. URL: https://link.aps.org/doi/10.1103/PhysRevB.96.134302.

Cheng, Yu-Hsiang, Samuel W. Teitelbaum, et al. (Oct. 2018). "Femtosecond laser amorphization of tellurium". In: *Phys. Rev. B* 98 (13), p. 134112. DOI: 10.1103/PhysRevB.98.134112. URL: https://link.aps.org/doi/10.1103/PhysRevB.98.134112.

Cheng, Meijuan et al. (July 2019). "Large second-harmonic generation and linear electro-optic effect in trigonal selenium and tellurium". In: *Phys. Rev. B* 100 (3), p. 035202. DOI: 10.1103/PhysRevB.100.035202. URL: https://link.aps.org/doi/10.1103/PhysRevB.100.035202.

Chia, Elbert E. M. et al. (Oct. 2006). "Quasiparticle relaxation across the spin-density-wave gap in the itinerant antiferromagnet $UNiGa_5$". In: *Phys. Rev. B* 74 (14), p. 140409. DOI: 10.1103/PhysRevB.74.140409.

Chu, H. et al. (2017). "A charge density wave-like instability in a doped spin–orbit-assisted weak Mott insulator". In: *Nature Materials* 16.2, pp. 200–203. DOI: 10.1038/nmat4836. URL: https://doi.org/10.1038/nmat4836.

Chu, Hao et al. (2020). "Phase-resolved Higgs response in superconducting cuprates". In: *Nat. Commun.* 11.1, p. 1793. ISSN: 2041-1723.

Chuang, Y. D. et al. (Mar. 2013). "Real-Time Manifestation of Strongly Coupled Spin and Charge Order Parameters in Stripe-Ordered $La_{1.75}Sr_{0.25}NiO_4$ Nickelate Crystals Using Time-Resolved Resonant X-Ray Diffraction". In: *Phys. Rev. Lett.* 110 (12), p. 127404. DOI: 10.1103/PhysRevLett.110.127404. URL: https://link.aps.org/doi/10.1103/PhysRevLett.110.127404.

Claassen, Martin et al. (2017). "Dynamical time-reversal symmetry breaking and photo-induced chiral spin liquids in frustrated Mott insulators". In: *Nat. Commun.* 8.1, p. 1192. ISSN: 2041-1723.

Dal Conte, S. et al. (2015). "Snapshots of the retarded interaction of charge carriers with ultrafast fluctuations in cuprates". In: *Nature Physics* 11.5, pp. 421–426. DOI: 10.1038/nphys3265. URL: https://doi.org/10.1038/nphys3265.

Damascelli, Andrea, Zahid Hussain, and Zhi-Xun Shen (Apr. 2003). "Angle-resolved photoemission studies of the cuprate superconductors". In: *Rev. Mod. Phys.* 75 (2), pp. 473–541. DOI: 10.1103/RevModPhys.75.473. URL: https://link.aps.org/doi/10.1103/RevModPhys.75.473.

Das, L. et al. (Mar. 2018). "Spin-Orbital Excitations in Ca_2RuO_4 Revealed by Resonant Inelastic X-Ray Scattering". In: *Phys. Rev. X* 8 (1), p. 011048. DOI: 10.1103/PhysRevX.8.011048.

Dekorsy, T. et al. (Jan. 1995). "Emission of Submillimeter Electromagnetic Waves by Coherent Phonons". In: *Phys. Rev. Lett.* 74 (5), pp. 738–741. DOI: 10.1103/PhysRevLett.74.738. URL: https://link.aps.org/doi/10.1103/PhysRevLett.74.738.

Demsar, J., K. Biljakovi ć, and D. Mihailovic (July 1999). "Single Particle and Collective Excitations in the One-Dimensional Charge Density Wave Solid $K_{0.3}MoO_3$ Probed in Real Time by Femtosecond Spectroscopy". In: *Phys. Rev. Lett.* 83 (4), pp. 800–803. DOI: 10.1103/PhysRevLett.83.800.

Dhar, Lisa, John A. Rogers, and Keith A. Nelson (Jan. 1994). "Time-resolved vibrational spectroscopy in the impulsive limit". In: *Chemical Reviews* 94.1, pp. 157–193. DOI: 10.1021/cr00025a006. URL: https://doi.org/10.1021/cr00025a006.

Diener, P. et al. (July 2018). "How a dc Electric Field Drives Mott Insulators Out of Equilibrium". In: *Phys. Rev. Lett.* 121 (1), p. 016601. DOI: 10.1103/PhysRevLett.121.016601.

Disa, Ankit S. et al. (2020). "Polarizing an antiferromagnet by optical engineering of the crystal field". In: *Nature Physics* 16.9, pp. 937–941. DOI: 10.1038/s41567-020-0936-3. URL: https://doi.org/10.1038/s41567-020-0936-3.

Duan, Shaofeng et al. (2021). "Optical manipulation of electronic dimensionality in a quantum material". In: *Nature* 595.7866, pp. 239–244. DOI: 10.1038/s41586-021-03643-8. URL: https://doi.org/10.1038/s41586-021-03643-8.

Ebihara, Shu, Kenji Fukushima, and Takashi Oka (Apr. 2016). "Chiral pumping effect induced by rotating electric fields". In: *Phys. Rev. B* 93 (15), p. 155107. DOI: 10.1103/PhysRevB.93.155107. URL: https://link.aps.org/doi/10.1103/PhysRevB.93.155107.

Eckardt, André and Egidijus Anisimovas (Sept. 2015). "High-frequency approximation for periodically driven quantum systems from a Floquet-space perspective". In: *New Journal of Physics* 17.9, p. 093039. DOI: 10.1088/1367-2630/17/9/093039. URL: https://doi.org/10.1088/1367-2630/17/9/093039.

Eckstein, Martin, Takashi Oka, and Philipp Werner (Sept. 2010). "Dielectric Breakdown of Mott Insulators in Dynamical Mean-Field Theory". In: *Phys. Rev. Lett.* 105 (14), p. 146404. DOI: 10.1103/PhysRevLett.105.146404.

Eckstein, Martin and Philipp Werner (July 2011). "Thermalization of a pump-excited Mott insulator". In: *Phys. Rev. B* 84 (3), p. 035122. DOI: 10.1103/PhysRevB.84.035122.

Erasmus, N. et al. (Oct. 2012). "Ultrafast Dynamics of Charge Density Waves in $4H_b$−$TaSe_2$ Probed by Femtosecond Electron Diffraction". In: *Phys. Rev. Lett.* 109 (16), p. 167402. DOI: 10.1103/PhysRevLett.109.167402. URL: https://link.aps.org/doi/10.1103/PhysRevLett.109.167402.

Fahy, S. and R. Merlin (Aug. 1994). "Reversal of Ferroelectric Domains by Ultrashort Optical Pulses". In: *Phys. Rev. Lett.* 73 (8), pp. 1122–1125. DOI: 10.1103/PhysRevLett.73.1122. URL: https://link.aps.org/doi/10.1103/PhysRevLett.73.1122.

Fang, Zhong, Naoto Nagaosa, and Kiyoyuki Terakura (Jan. 2004). "Orbital-dependent phase control in $Ca_{2-x}Sr_xRuO_4$ ($0 \leq x \leq 0.5$)". In: *Phys. Rev. B* 69 (4), p. 045116. DOI: 10.1103/PhysRevB.69.045116. URL: https://link.aps.org/doi/10.1103/PhysRevB.69.045116.

Fausti, D. et al. (2011). "Light-Induced Superconductivity in a Stripe-Ordered Cuprate". In: *Science* 331.6014, pp. 189–191. DOI: 10.1126/science.1197294. eprint: https://www.science.org/doi/pdf/10.1126/science.1197294. URL: https://www.science.org/doi/abs/10.1126/science.1197294.

Fiebig, M., D. Fröhlich, B. B. Krichevtsov, et al. (Oct. 1994). "Second Harmonic Generation and Magnetic-Dipole-Electric-Dipole Interference in Antiferromagnetic Cr_2O_3". In: *Phys. Rev. Lett.* 73 (15), pp. 2127–2130. DOI: 10.1103/PhysRevLett.73.2127. URL: https://link.aps.org/doi/10.1103/PhysRevLett.73.2127.

Fiebig, M., D. Fröhlich, G. Sluyterman v. L., et al. (1995). "Domain topography of antiferromagnetic Cr2O3 by second-harmonic generation". In: *Applied Physics Letters* 66.21, pp. 2906–2908. DOI: 10.1063/1.113699. eprint: https://doi.org/10.1063/1.113699. URL: https://doi.org/10.1063/1.113699.

Fiebig, M., Th. Lottermoser, et al. (2002). "Observation of coupled magnetic and electric domains". In: *Nature* 419.6909, pp. 818–820. DOI: 10.1038/nature01077. URL: https://doi.org/10.1038/nature01077.

Fiebig, Manfred, Thomas Lottermoser, et al. (Jan. 2004). "Phase-resolved second-harmonic imaging with nonideal laser sources". In: *Opt. Lett.* 29.1, pp. 41–43. DOI: 10.1364/OL.29.000041. URL: http://ol.osa.org/abstract.cfm?URI=ol-29-1-41.

Fiebig, Manfred, Victor V. Pavlov, and Roman V. Pisarev (Jan. 2005). "Second-harmonic generation as a tool for studying electronic and magnetic structures of crystals: review". In: *J. Opt. Soc. Am. B* 22.1, pp. 96–118. DOI: 10.1364/JOSAB.22.000096. URL: http://opg.optica.org/josab/abstract.cfm?URI=josab-22-1-96.

Först, M. et al. (2011). "Nonlinear phononics as an ultrafast route to lattice control". In: *Nature Physics* 7.11, pp. 854–856. DOI: 10.1038/nphys2055. URL: https://doi.org/10.1038/nphys2055.

Friedt, O. et al. (Apr. 2001). "Structural and magnetic aspects of the metal-insulator transition in $Ca_{2-x}Sr_xRuO_4$". In: *Phys. Rev. B* 63 (17), p. 174432. DOI: 10.1103/PhysRevB.63.174432. URL: https://link.aps.org/doi/10.1103/PhysRevB.63.174432.

Fritz, D. M. et al. (2007). "Ultrafast Bond Softening in Bismuth: Mapping a Solid's Interatomic Potential with X-rays". In: *Science* 315.5812, pp. 633–636. ISSN: 0036-8075. DOI: 10.1126/science.1135009. eprint: https://science.sciencemag.org/content/315/5812/633.full.pdf. URL: https://science.sciencemag.org/content/315/5812/633.

Gao, Shang et al. (June 2020). "Antiferromagnetic long-range order in the $5d^1$ double-perovskite Sr_2MgReO_6". In: *Phys. Rev. B* 101 (22), p. 220412. DOI: 10.1103/PhysRevB.101.220412. URL: https://link.aps.org/doi/10.1103/PhysRevB.101.220412.

Garrett, G. A. et al. (Oct. 1996). "Coherent THz Phonons Driven by Light Pulses and the Sb Problem: What is the Mechanism?" In: *Phys. Rev. Lett.* 77 (17), pp. 3661–3664. DOI: 10.1103/PhysRevLett.77.3661. URL: https://link.aps.org/doi/10.1103/PhysRevLett.77.3661.

Gatti, G. et al. (Nov. 2020). "Radial Spin Texture of the Weyl Fermions in Chiral Tellurium". In: *Phys. Rev. Lett.* 125 (21), p. 216402. DOI: 10.1103/PhysRevLett.125.216402. URL: https://link.aps.org/doi/10.1103/PhysRevLett.125.216402.

Gedik, N. et al. (July 2004). "Single-quasiparticle stability and quasiparticle-pair decay in $YBa_2Cu_3O_{6.5}$". In: *Phys. Rev. B* 70 (1), p. 014504. DOI: 10.1103/PhysRevB.70.014504.

Georges, Antoine, Luca de' Medici, and Jernej Mravlje (2022/01/24 2013). "Strong Correlations from Hund's Coupling". In: *Annual Review of Condensed Matter Physics* 4.1, pp. 137–178. DOI: 10.1146/annurev-conmatphys-020911-125045. URL: https://doi.org/10.1146/annurev-conmatphys-020911-125045.

Gerber, S. et al. (2017). "Femtosecond electron-phonon lock-in by photoemission and x-ray free-electron laser". In: *Science* 357.6346, pp. 71–75. DOI: 10.1126/science.aak9946. eprint: https://www.science.org/doi/pdf/10.1126/science.aak9946. URL: https://www.science.org/doi/abs/10.1126/science.aak9946.

Gerrits, Th. et al. (2002). "Ultrafast precessional magnetization reversal by picosecond magnetic field pulse shaping". In: *Nature* 418.6897, pp. 509–512. DOI: 10.1038/nature00905. URL: https://doi.org/10.1038/nature00905.

Giorgianni, Flavio, Joe Sakai, and Stefano Lupi (2019). "Overcoming the thermal regime for the electric-field driven Mott transition in vanadium sesquioxide". In: *Nat. Commun.* 10.1, p. 1159. ISSN: 2041-1723.

Gole ž, Denis, Martin Eckstein, and Philipp Werner (Nov. 2015). "Dynamics of screening in photodoped Mott insulators". In: *Phys. Rev. B* 92 (19), p. 195123. DOI: 10.1103/PhysRevB.92.195123.

Gorelov, E. et al. (June 2010). "Nature of the Mott Transition in Ca_2RuO_4". In: *Phys. Rev. Lett.* 104 (22), p. 226401. DOI: 10.1103/PhysRevLett.104.226401.

Gorobtsov, O. Yu. et al. (2021). "Femtosecond control of phonon dynamics near a magnetic order critical point". In: *Nature Communications* 12.1, p. 2865. DOI: 10.1038/s41467-021-23059-2. URL: https://doi.org/10.1038/s41467-021-23059-2.

Guan, Meng-Xue et al. (2021). "Manipulating Weyl quasiparticles by orbital-selective photoexcitation in WTe2". In: *Nature Communications* 12 (1). DOI: 10.1038/s41467-021-22056-9. URL: https://doi.org/10.1038/s41467-021-22056-9.

Han, Qiang and Andrew Millis (Aug. 2018). "Lattice Energetics and Correlation-Driven Metal-Insulator Transitions: The Case of Ca_2RuO_4". In: *Phys. Rev. Lett.* 121 (6), p. 067601. DOI: 10.1103/PhysRevLett.121.067601.

Harter, J. W., D. M. Kennes, et al. (Jan. 2018). "Evidence of an Improper Displacive Phase Transition in $Cd_2Re_2O_7$ via Time-Resolved Coherent Phonon Spectroscopy". In: *Phys. Rev. Lett.* 120 (4), p. 047601. DOI: 10.1103/PhysRevLett.120.047601. URL: https://link.aps.org/doi/10.1103/PhysRevLett.120.047601.

Harter, J. W., L. Niu, et al. (Oct. 2015). "High-speed measurement of rotational anisotropy nonlinear optical harmonic generation using position-sensitive detection". In: *Opt. Lett.* 40.20, pp. 4671–4674. DOI: 10.1364/OL.40.004671. URL: http://opg.optica.org/ol/abstract.cfm?URI=ol-40-20-4671.

Harter, J. W., Z. Y. Zhao, et al. (2017). "A parity-breaking electronic nematic phase transition in the spin-orbit coupled metal Cd2Re2O7". In: *Science* 356.6335, pp. 295–299. ISSN: 0036-8075. DOI: 10.1126/science.aad1188. eprint: https://science.sciencemag.org/content/356/6335/295.full.pdf. URL: https://science.sciencemag.org/content/356/6335/295.

Hasan, M. Zahid et al. (2017). "Discovery of Weyl Fermion Semimetals and Topological Fermi Arc States". In: *Annual Review of Condensed Matter Physics* 8.1, pp. 289–309. DOI: 10.1146/annurev-conmatphys-031016-025225. eprint: https://doi.org/10.1146/annurev-conmatphys-031016-025225. URL: https://doi.org/10.1146/annurev-conmatphys-031016-025225.

Hase, M. et al. (1996). "Optical control of coherent optical phonons in bismuth films". In: *Applied Physics Letters* 69.17, pp. 2474–2476. DOI: 10.1063/1.117502. eprint: https://doi.org/10.1063/1.117502. URL: https://doi.org/10.1063/1.117502.

Hase, Muneaki, Tetsuya Itano, et al. (Mar. 1998). "Selective Enhancement of Coherent Optical Phonons Using THz-rate Pulse Train". In: *Japanese Journal of Applied Physics* 37.Part 2, No. 3A, pp. L281–L283. DOI: 10.1143/jjap.37.l281. URL: https://doi.org/10.1143%2Fjjap.37.l281.

Hase, Muneaki, Masahiro Kitajima, et al. (Jan. 2002). "Dynamics of Coherent Anharmonic Phonons in Bismuth Using High Density Photoexcitation". In: *Phys. Rev. Lett.* 88 (6), p. 067401. DOI: 10.1103/PhysRevLett.88.067401. URL: https://link.aps.org/doi/10.1103/PhysRevLett.88.067401.

Hejazi, Kasra, Jianpeng Liu, and Leon Balents (May 2019). "Floquet spin and spin-orbital Hamiltonians and doublon-holon generations in periodically driven Mott insulators". In: *Phys. Rev. B* 99 (20), p. 205111. DOI: 10.1103/PhysRevB.99.205111.

Hejny, C., S. Falconi, et al. (Nov. 2006). "Phase transitions in tellurium at high pressure and temperature". In: *Phys. Rev. B* 74 (17), p. 174119. DOI: 10.1103/PhysRevB.74.174119. URL: https://link.aps.org/doi/10.1103/PhysRevB.74.174119.

Hejny, C. and M. I. McMahon (Nov. 2003). "Large Structural Modulations in Incommensurate Te-III and Se-IV". In: *Phys. Rev. Lett.* 91 (21), p. 215502. DOI: 10.1103/PhysRevLett.91.215502. URL: https://link.aps.org/doi/10.1103/PhysRevLett.91.215502.

– (Nov. 2004). "Complex crystal structures of Te-II and Se-III at high pressure". In: *Phys. Rev. B* 70 (18), p. 184109. DOI: 10.1103/PhysRevB.70.184109. URL: https://link.aps.org/doi/10.1103/PhysRevB.70.184109.

Hirayama, Motoaki et al. (May 2015). "Weyl Node and Spin Texture in Trigonal Tellurium and Selenium". In: *Phys. Rev. Lett.* 114 (20), p. 206401. DOI: 10.1103/PhysRevLett.114.206401. URL: https://link.aps.org/doi/10.1103/PhysRevLett.114.206401.

Hoegen, A. von et al. (2018). "Probing the interatomic potential of solids with strong-field nonlinear phononics". In: *Nature* 555.7694, pp. 79–82. DOI: 10.1038/nature25484. URL: https://doi.org/10.1038/nature25484.

Huang, Yijing et al. (Feb. 2022). "Observation of a Novel Lattice Instability in Ultrafast Photoexcited SnSe". In: *Phys. Rev. X* 12 (1), p. 011029. DOI: 10.1103/PhysRevX.12.011029. URL: https://link.aps.org/doi/10.1103/PhysRevX.12.011029.

Hübener, Hannes et al. (2017). "Creating stable Floquet–Weyl semimetals by laser-driving of 3D Dirac materials". In: *Nature Communications* 8. DOI: 10.1038/ncomms13940. URL: https://doi.org/10.1038/ncomms13940.

Huber, T. et al. (July 2014). "Coherent Structural Dynamics of a Prototypical Charge-Density-Wave-to-Metal Transition". In: *Phys. Rev. Lett.* 113 (2), p. 026401. DOI: 10.1103/PhysRevLett.113.026401. URL: https://link.aps.org/doi/10.1103/PhysRevLett.113.026401.

Hunsche, S., K. Wienecke, T. Dekorsy, et al. (Aug. 1995). "Impulsive Softening of Coherent Phonons in Tellurium". In: *Phys. Rev. Lett.* 75 (9), pp. 1815–1818. DOI: 10.1103/PhysRevLett.75.1815. URL: https://link.aps.org/doi/10.1103/PhysRevLett.75.1815.

Hunsche, S., K. Wienecke, and H. Kurz (1996). "Details of coherent phonon motion in tellurium". In: *Applied Physics A* 62.5, pp. 499–502. DOI: 10.1007/BF01567124. URL: https://doi.org/10.1007/BF01567124.

Ichikawa, Hirohiko et al. (2011). "Transient photoinduced 'hidden' phase in a manganite". In: *Nature Materials* 10.2, pp. 101–105. DOI: 10.1038/nmat2929. URL: https://doi.org/10.1038/nmat2929.

Ideue, Toshiya et al. (2019). "Pressure-induced topological phase transition in noncentrosymmetric elemental tellurium". In: *Proceedings of the National Academy of Sciences* 116.51, pp. 25530–25534. ISSN: 0027-8424. DOI: 10.1073/pnas.1905524116. eprint: https://www.pnas.org/content/116/51/25530.full.pdf. URL: https://www.pnas.org/content/116/51/25530.

Imai, Shohei, Atsushi Ono, and Sumio Ishihara (Apr. 2020). "High Harmonic Generation in a Correlated Electron System". In: *Phys. Rev. Lett.* 124 (15), p. 157404. DOI: 10.1103/PhysRevLett.124.157404.

Iwahara, Naoya, Veacheslav Vieru, and Liviu F. Chibotaru (Aug. 2018). "Spin-orbital-lattice entangled states in cubic d^1 double perovskites". In: *Phys. Rev. B* 98 (7), p. 075138. DOI: 10.1103/PhysRevB.98.075138. URL: https://link.aps.org/doi/10.1103/PhysRevB.98.075138.

Iyer, Vasudevan et al. (Aug. 2019). "Infrared ultrafast spectroscopy of solution-grown thin film tellurium". In: *Phys. Rev. B* 100 (7), p. 075436. DOI: 10.1103/PhysRevB.100.075436. URL: https://link.aps.org/doi/10.1103/PhysRevB.100.075436.

Jain, A. et al. (2017). "Higgs mode and its decay in a two-dimensional antiferromagnet". In: *Nature Physics* 13.7, pp. 633–637. DOI: 10.1038/nphys4077. URL: https://doi.org/10.1038/nphys4077.

Jérome, D., T. M. Rice, and W. Kohn (June 1967). "Excitonic Insulator". In: *Phys. Rev.* 158 (2), pp. 462–475. DOI: 10.1103/PhysRev.158.462. URL: https://link.aps.org/doi/10.1103/PhysRev.158.462.

Jia, Yanyu et al. (2022). "Evidence for a monolayer excitonic insulator". In: *Nature Physics* 18.1, pp. 87–93. DOI: 10.1038/s41567-021-01422-w. URL: https://doi.org/10.1038/s41567-021-01422-w.

Jnawali, Giriraj et al. (2020). "Ultrafast photoinduced band splitting and carrier dynamics in chiral tellurium nanosheets". In: *Nature Communications* 11.1, p. 3991. DOI: 10.1038/s41467-020-17766-5. URL: https://doi.org/10.1038/s41467-020-17766-5.

Johnson, S. L. et al. (Nov. 2009). "Full Reconstruction of a Crystal Unit Cell Structure during Coherent Femtosecond Motion". In: *Phys. Rev. Lett.* 103 (20), p. 205501. DOI: 10.1103/PhysRevLett.103.205501. URL: https://link.aps.org/doi/10.1103/PhysRevLett.103.205501.

Jung, J. H. et al. (July 2003). "Change of Electronic Structure in Ca_2RuO_4 Induced by Orbital Ordering". In: *Phys. Rev. Lett.* 91 (5), p. 056403. DOI: 10.1103/PhysRevLett.91.056403. URL: https://link.aps.org/doi/10.1103/PhysRevLett.91.056403.

Kamaraju, N. et al. (Nov. 2010). "Large-amplitude chirped coherent phonons in tellurium mediated by ultrafast photoexcited carrier diffusion". In: *Phys. Rev. B* 82 (19), p. 195202. DOI: 10.1103/PhysRevB.82.195202. URL: https://link.aps.org/doi/10.1103/PhysRevB.82.195202.

Kampfrath, Tobias et al. (2011). "Coherent terahertz control of antiferromagnetic spin waves". In: *Nature Photonics* 5.1, pp. 31–34. DOI: 10.1038/nphoton.2010.259. URL: https://doi.org/10.1038/nphoton.2010.259.

Kaneko, T. et al. (Jan. 2013). "Orthorhombic-to-monoclinic phase transition of Ta_2NiSe_5 induced by the Bose-Einstein condensation of excitons". In: *Phys. Rev. B* 87 (3), p. 035121. DOI: 10.1103/PhysRevB.87.035121. URL: https://link.aps.org/doi/10.1103/PhysRevB.87.035121.

Katsumi, Kota et al. (Mar. 2018). "Higgs Mode in the d-Wave Superconductor $Bi_2Sr_2CaCu_2O_{8+x}$ Driven by an Intense Terahertz Pulse". In: *Phys. Rev. Lett.* 120 (11), p. 117001. DOI: 10.1103/PhysRevLett.120.117001. URL: https://link.aps.org/doi/10.1103/PhysRevLett.120.117001.

Keimer, B. and J. E. Moore (2017). "The physics of quantum materials". In: *Nature Physics* 13.11, pp. 1045–1055. DOI: 10.1038/nphys4302. URL: https://doi.org/10.1038/nphys4302.

Khaliullin, Giniyat (Nov. 2013). "Excitonic Magnetism in Van Vleck–type d^4 Mott Insulators". In: *Phys. Rev. Lett.* 111 (19), p. 197201. DOI: 10.1103/PhysRevLett.111.197201. URL: https://link.aps.org/doi/10.1103/PhysRevLett.111.197201.

Kim, A. M.-T., C. A. D. Roeser, and E. Mazur (July 2003). "Modulation of the bonding-antibonding splitting in Te by coherent phonons". In: *Phys. Rev. B* 68 (1), p. 012301. DOI: 10.1103/PhysRevB.68.012301. URL: https://link.aps.org/doi/10.1103/PhysRevB.68.012301.

Kim, Kwangrae et al. (2021). "Direct observation of excitonic instability in Ta2NiSe5". In: *Nature Communications* 12.1, p. 1969. DOI: 10.1038/s41467-021-22133-z. URL: https://doi.org/10.1038/s41467-021-22133-z.

Kim, Min-Jae et al. (Dec. 2020). "Phononic soft mode behavior and a strong electronic background across the structural phase transition in the excitonic insulator Ta_2NiSe_5". In: *Phys. Rev. Research* 2 (4), p. 042039. DOI: 10.1103/PhysRevResearch.2.042039. URL: https://link.aps.org/doi/10.1103/PhysRevResearch.2.042039.

Kimel, A. V. et al. (2009). "Inertia-driven spin switching in antiferromagnets". In: *Nature Physics* 5.10, pp. 727–731. DOI: 10.1038/nphys1369. URL: https://doi.org/10.1038/nphys1369.

Kirilyuk, Andrei, Alexey V. Kimel, and Theo Rasing (Sept. 2010). "Ultrafast optical manipulation of magnetic order". In: *Rev. Mod. Phys.* 82 (3), pp. 2731–2784. DOI: 10.1103/RevModPhys.82.2731. URL: https://link.aps.org/doi/10.1103/RevModPhys.82.2731.

Kogar, Anshul, Melinda S. Rak, et al. (2017). "Signatures of exciton condensation in a transition metal dichalcogenide". In: *Science* 358.6368, pp. 1314–1317. ISSN: 0036-8075. DOI: 10.1126/science.aam6432. eprint: https://science.sciencemag.org/content/358/6368/1314.full.pdf. URL: https://science.sciencemag.org/content/358/6368/1314.

Kogar, Anshul, Alfred Zong, et al. (2020). "Light-induced charge density wave in LaTe3". In: *Nature Physics* 16.2, pp. 159–163. DOI: 10.1038/s41567-019-0705-3. URL: https://doi.org/10.1038/s41567-019-0705-3.

Kozina, M. et al. (2019). "Terahertz-driven phonon upconversion in SrTiO3". In: *Nature Physics* 15.4, pp. 387–392. DOI: 10.1038/s41567-018-0408-1. URL: https://doi.org/10.1038/s41567-018-0408-1.

Kruchinin, Stanislav Yu., Ferenc Krausz, and Vladislav S. Yakovlev (Apr. 2018). "Colloquium: Strong-field phenomena in periodic systems". In: *Rev. Mod. Phys.* 90 (2), p. 021002. DOI: 10.1103/RevModPhys.90.021002. URL: https://link.aps.org/doi/10.1103/RevModPhys.90.021002.

Kudryashov, Sergey I. et al. (Feb. 2007). "Intraband and interband optical deformation potentials in femtosecond-laser-excited α−Te". In: *Phys. Rev. B* 75 (8), p. 085207. DOI: 10.1103/PhysRevB.75.085207. URL: https://link.aps.org/doi/10.1103/PhysRevB.75.085207.

Kuznetsov, A. V. and C. J. Stanton (Dec. 1994). "Theory of Coherent Phonon Oscillations in Semiconductors". In: *Phys. Rev. Lett.* 73 (24), pp. 3243–3246. DOI: 10.1103/PhysRevLett.73.3243. URL: https://link.aps.org/doi/10.1103/PhysRevLett.73.3243.

Lambert, C-H. et al. (2014). "All-optical control of ferromagnetic thin films and nanostructures". In: *Science* 345.6202, pp. 1337–1340. ISSN: 0036-8075. DOI: 10.1126/science.1253493. eprint: https://science.sciencemag.org/content/345/6202/1337.full.pdf. URL: https://science.sciencemag.org/content/345/6202/1337.

Larkin, T. I. et al. (May 2017). "Giant exciton Fano resonance in quasi-one-dimensional Ta_2NiSe_5". In: *Phys. Rev. B* 95 (19), p. 195144. DOI: 10.1103/PhysRevB.95.195144. URL: https://link.aps.org/doi/10.1103/PhysRevB.95.195144.

Laurita, N. J. et al. (2019). "Evidence for the weakly coupled electron mechanism in an Anderson-Blount polar metal". In: *Nature Communications* 10.1, p. 3217. DOI: 10.1038/s41467-019-11172-2. URL: https://doi.org/10.1038/s41467-019-11172-2.

Lee, J. J. et al. (2014). "Interfacial mode coupling as the origin of the enhancement of Tc in FeSe films on SrTiO3". In: *Nature* 515.7526, pp. 245–248. DOI: 10.1038/nature13894. URL: https://doi.org/10.1038/nature13894.

Lee, J. S. et al. (Dec. 2002). "Electron and Orbital Correlations in $Ca_{2-x}Sr_xRuO_4$ Probed by Optical Spectroscopy". In: *Phys. Rev. Lett.* 89 (25), p. 257402. DOI: 10.1103/PhysRevLett.89.257402. URL: https://link.aps.org/doi/10.1103/PhysRevLett.89.257402.

Lee, Min-Cheol, Choong H. Kim, Inho Kwak, J. Kim, et al. (Oct. 2018). "Abnormal phase flip in the coherent phonon oscillations of Ca_2RuO_4". In: *Phys. Rev. B* 98 (16), p. 161115. DOI: 10.1103/PhysRevB.98.161115. URL: https://link.aps.org/doi/10.1103/PhysRevB.98.161115.

Lee, Min-Cheol, Choong H. Kim, Inho Kwak, C. W. Seo, et al. (Apr. 2019). "Strong spin-phonon coupling unveiled by coherent phonon oscillations in Ca_2RuO_4". In: *Phys. Rev. B* 99 (14), p. 144306. DOI: 10.1103/PhysRevB.99.144306. URL: https://link.aps.org/doi/10.1103/PhysRevB.99.144306.

Lee, Woo-Ram and Kwon Park (May 2014). "Dielectric breakdown via emergent nonequilibrium steady states of the electric-field-driven Mott insulator". In: *Phys. Rev. B* 89 (20), p. 205126. DOI: 10.1103/PhysRevB.89.205126.

Li, Jiajun, Camille Aron, et al. (June 2015). "Electric-Field-Driven Resistive Switching in the Dissipative Hubbard Model". In: *Phys. Rev. Lett.* 114 (22), p. 226403. DOI: 10.1103/PhysRevLett.114.226403.

Li, Jiajun, Hugo U. R. Strand, et al. (2018). "Theory of photoinduced ultrafast switching to a spin-orbital ordered hidden phase". In: *Nature Communications* 9.1, p. 4581. DOI: 10.1038/s41467-018-07051-x. URL: https://doi.org/10.1038/s41467-018-07051-x.

Li, Tianqi et al. (2013). "Femtosecond switching of magnetism via strongly correlated spin–charge quantum excitations". In: *Nature* 496.7443, pp. 69–73. DOI: 10.1038/nature11934. URL: https://doi.org/10.1038/nature11934.

Li, Xian et al. (2019). "Terahertz field–induced ferroelectricity in quantum paraelectric SrTiO3". In: *Science* 364.6445, pp. 1079–1082. ISSN: 0036-8075. DOI: 10.1126/science.aaw4913. eprint: https://science.sciencemag.org/content/364/6445/1079.full.pdf. URL: https://science.sciencemag.org/content/364/6445/1079.

Li, Xinwei et al. (May 2022). "Keldysh Space Control of Charge Dynamics in a Strongly Driven Mott Insulator". In: *Phys. Rev. Lett.* 128 (18), p. 187402. DOI: 10.1103/PhysRevLett.128.187402. URL: https://link.aps.org/doi/10.1103/PhysRevLett.128.187402.

Lian, Chao et al. (2020). "Ultrafast charge ordering by self-amplified exciton–phonon dynamics in TiSe2". In: *Nature Communications* 11.1, p. 43. DOI: 10.1038/s41467-019-13672-7. URL: https://doi.org/10.1038/s41467-019-13672-7.

Lindner, Netanel H., Gil Refael, and Victor Galitski (2011). "Floquet topological insulator in semiconductor quantum wells". In: *Nature Physics* 7.6, pp. 490–495. DOI: 10.1038/nphys1926. URL: https://doi.org/10.1038/nphys1926.

Liu, Huimei and Giniyat Khaliullin (Feb. 2019). "Pseudo-Jahn-Teller Effect and Magnetoelastic Coupling in Spin-Orbit Mott Insulators". In: *Phys. Rev. Lett.* 122 (5), p. 057203. DOI: 10.1103/PhysRevLett.122.057203. URL: https://link.aps.org/doi/10.1103/PhysRevLett.122.057203.

Liu, M. K. et al. (Aug. 2011). "Photoinduced Phase Transitions by Time-Resolved Far-Infrared Spectroscopy in V_2O_3". In: *Phys. Rev. Lett.* 107 (6), p. 066403. DOI: 10.1103/PhysRevLett.107.066403. URL: https://link.aps.org/doi/10.1103/PhysRevLett.107.066403.

Liu, Mengkun et al. (July 2012). "Terahertz-field-induced insulator-to-metal transition in vanadium dioxide metamaterial". In: *Nature* 487.7407, pp. 345–348. DOI: https://doi.org/10.1038/nature11231.

Liu, Q. M. et al. (2021). "Photoinduced multistage phase transitions in Ta2NiSe5". In: *Nature Communications* 12.1, p. 2050. DOI: 10.1038/s41467-021-22345-3. URL: https://doi.org/10.1038/s41467-021-22345-3.

Lu, L. et al. (2017). "Magnetism and local symmetry breaking in a Mott insulator with strong spin orbit interactions". In: *Nature Communications* 8.1, p. 14407. DOI: 10.1038/ncomms14407. URL: https://doi.org/10.1038/ncomms14407.

Lucchini, M. et al. (2016). "Attosecond dynamical Franz-Keldysh effect in polycrystalline diamond". In: *Science* 353.6302, pp. 916–919. DOI: 10.1126/science.aag1268. eprint: https://www.science.org/doi/pdf/10.1126/science.aag1268. URL: https://www.science.org/doi/abs/10.1126/science.aag1268.

Luo, Liang et al. (2021). "A light-induced phononic symmetry switch and giant dissipationless topological photocurrent in ZrTe5". In: *Nature Materials* 20.3, pp. 329–334. DOI: 10.1038/s41563-020-00882-4. URL: https://doi.org/10.1038/s41563-020-00882-4.

Lv, B. Q., T. Qian, and H. Ding (Apr. 2021). "Experimental perspective on three-dimensional topological semimetals". In: *Rev. Mod. Phys.* 93 (2), p. 025002. DOI: 10.1103/RevModPhys.93.025002. URL: https://link.aps.org/doi/10.1103/RevModPhys.93.025002.

Lyu, Meng et al. (Aug. 2020). "Nonsaturating magnetoresistance, anomalous Hall effect, and magnetic quantum oscillations in the ferromagnetic semimetal PrAlSi". In: *Phys. Rev. B* 102 (8), p. 085143. DOI: 10.1103/PhysRevB.102.085143. URL: https://link.aps.org/doi/10.1103/PhysRevB.102.085143.

Ma, Liguo et al. (2021). "Strongly correlated excitonic insulator in atomic double layers". In: *Nature* 598.7882, pp. 585–589. DOI: 10.1038/s41586-021-03947-9. URL: https://doi.org/10.1038/s41586-021-03947-9.

Mahmood, Fahad et al. (2016). "Selective scattering between Floquet–Bloch and Volkov states in a topological insulator". In: *Nature Physics* 12.4, pp. 306–310. DOI: 10.1038/nphys3609. URL: https://doi.org/10.1038/nphys3609.

Mankowsky, R., A. von Hoegen, et al. (May 2017). "Ultrafast Reversal of the Ferroelectric Polarization". In: *Phys. Rev. Lett.* 118 (19), p. 197601. DOI: 10.1103/PhysRevLett.118.197601. URL: https://link.aps.org/doi/10.1103/PhysRevLett.118.197601.

Mankowsky, R., A. Subedi, et al. (Dec. 2014). "Nonlinear lattice dynamics as a basis for enhanced superconductivity in YBa2Cu3O6.5". In: *Nature* 516, 71 EP -. URL: https://doi.org/10.1038/nature13875.

Manna, Kaustuv et al. (Dec. 2018). "From Colossal to Zero: Controlling the Anomalous Hall Effect in Magnetic Heusler Compounds via Berry Curvature Design". In: *Phys. Rev. X* 8 (4), p. 041045. DOI: 10.1103/PhysRevX.8.041045. URL: https://link.aps.org/doi/10.1103/PhysRevX.8.041045.

Manz, Sebastian et al. (2016). "Reversible optical switching of antiferromagnetism in TbMnO3". In: *Nature Photonics* 10.10, pp. 653–656. DOI: 10.1038/nphoton.2016.146. URL: https://doi.org/10.1038/nphoton.2016.146.

Matsubara, Masakazu et al. (2015). "Magnetoelectric domain control in multiferroic TbMnO3". In: *Science* 348.6239, pp. 1112–1115. ISSN: 0036-8075. DOI: 10.1126/science.1260561. eprint: https://science.sciencemag.org/content/348/6239/1112.full.pdf. URL: https://science.sciencemag.org/content/348/6239/1112.

Matsunaga, Ryusuke, Yuki I. Hamada, et al. (July 2013). "Higgs Amplitude Mode in the BCS Superconductors $Nb_{1-x}Ti_xN$ Induced by Terahertz Pulse Excitation". In: *Phys. Rev. Lett.* 111 (5), p. 057002. DOI: 10.1103/PhysRevLett.111.057002. URL: https://link.aps.org/doi/10.1103/PhysRevLett.111.057002.

Matsunaga, Ryusuke, Naoto Tsuji, et al. (2014). "Light-induced collective pseudospin precession resonating with Higgs mode in a superconductor". In: *Science* 345.6201, pp. 1145–1149. ISSN: 0036-8075. DOI: 10.1126/science.1254697. eprint: https://science.sciencemag.org/content/345/6201/1145.full.pdf. URL: https://science.sciencemag.org/content/345/6201/1145.

Mayer, B. et al. (June 2015). "Tunneling breakdown of a strongly correlated insulating state in VO_2 induced by intense multiterahertz excitation". In: *Phys. Rev. B* 91 (23), p. 235113. DOI: 10.1103/PhysRevB.91.235113.

McIver, J. W. et al. (2020). "Light-induced anomalous Hall effect in graphene". In: *Nature Physics* 16.1, pp. 38–41. DOI: 10.1038/s41567-019-0698-y. URL: https://doi.org/10.1038/s41567-019-0698-y.

Melnikov, A.A., O.V. Misochko, and S.V. Chekalin (2011). "Generation of coherent phonons in bismuth by ultrashort laser pulses in the visible and NIR: Displacive versus impulsive excitation mechanism". In: *Physics Letters A* 375.19, pp. 2017–2022. ISSN: 0375-9601. DOI: https://doi.org/10.1016/j.physleta.2011.03.057. URL: http://www.sciencedirect.com/science/article/pii/S0375960111004427.

Mentink, J. H., K. Balzer, and M. Eckstein (2015). "Ultrafast and reversible control of the exchange interaction in Mott insulators". In: *Nat. Commun.* 6.1, p. 6708. ISSN: 2041-1723.

Mikhaylovskiy, R. V. et al. (2015). "Ultrafast optical modification of exchange interactions in iron oxides". In: *Nat. Commun.* 6.1, p. 8190. ISSN: 2041-1723.

Misochko, O V et al. (Sept. 2007). "Coherent A1phonons in Te studied with tailored femtosecond pulses". In: *Journal of Physics: Condensed Matter* 19.40, p. 406220. DOI: 10.1088/0953-8984/19/40/406220. URL: https://doi.org/10.1088%2F0953-8984%2F19%2F40%2F406220.

Misochko, O. V. and M. V. Lebedev (Nov. 2016). "Coherent lattice dynamics in opaque crystals: Testing the adequacy of two-tensor model". In: *Phys. Rev. B* 94 (18), p. 184307. DOI: 10.1103/PhysRevB.94.184307. URL: https://link.aps.org/doi/10.1103/PhysRevB.94.184307.

Mitrano, M. et al. (2016). "Possible light-induced superconductivity in K3C60 at high temperature". In: *Nature* 530.7591, pp. 461–464. DOI: 10.1038/nature16522. URL: https://doi.org/10.1038/nature16522.

Mizokawa, T. et al. (July 2001). "Spin-Orbit Coupling in the Mott Insulator Ca_2RuO_4". In: *Phys. Rev. Lett.* 87 (7), p. 077202. DOI: 10.1103/PhysRevLett.87.077202. URL: https://link.aps.org/doi/10.1103/PhysRevLett.87.077202.

Möhr-Vorobeva, E. et al. (July 2011). "Nonthermal Melting of a Charge Density Wave in $TiSe_2$". In: *Phys. Rev. Lett.* 107 (3), p. 036403. DOI: 10.1103/PhysRevLett.107.036403. URL: https://link.aps.org/doi/10.1103/PhysRevLett.107.036403.

Mor, Selene, Marc Herzog, Denis Gole ž, et al. (Aug. 2017). "Ultrafast Electronic Band Gap Control in an Excitonic Insulator". In: *Phys. Rev. Lett.* 119 (8), p. 086401. DOI: 10.1103/PhysRevLett.119.086401. URL: https://link.aps.org/doi/10.1103/PhysRevLett.119.086401.

Mor, Selene, Marc Herzog, Johannes Noack, et al. (Mar. 2018). "Inhibition of the photoinduced structural phase transition in the excitonic insulator Ta_2NiSe_5". In: *Phys. Rev. B* 97 (11), p. 115154. DOI: 10.1103/PhysRevB.97.115154. URL: https://link.aps.org/doi/10.1103/PhysRevB.97.115154.

Morrison, Vance R. et al. (2014). "A photoinduced metal-like phase of monoclinic VO2 revealed by ultrafast electron diffraction". In: *Science* 346.6208, pp. 445–448. ISSN: 0036-8075. DOI: 10.1126/science.1253779. eprint: https://science.sciencemag.org/content/346/6208/445.full.pdf. URL: https://science.sciencemag.org/content/346/6208/445.

Murakami, Yuta, Martin Eckstein, and Philipp Werner (Aug. 2018). "High-Harmonic Generation in Mott Insulators". In: *Phys. Rev. Lett.* 121 (5), p. 057405. DOI: 10.1103/PhysRevLett.121.057405.

Murakami, Yuta, Denis Golež, Martin Eckstein, et al. (Dec. 2017). "Photoinduced Enhancement of Excitonic Order". In: *Phys. Rev. Lett.* 119 (24), p. 247601. DOI: 10.1103/PhysRevLett.119.247601. URL: https://link.aps.org/doi/10.1103/PhysRevLett.119.247601.

Murakami, Yuta, Denis Golež, Tatsuya Kaneko, et al. (May 2020). "Collective modes in excitonic insulators: Effects of electron-phonon coupling and signatures in the optical response". In: *Phys. Rev. B* 101 (19), p. 195118. DOI: 10.1103/PhysRevB.101.195118. URL: https://link.aps.org/doi/10.1103/PhysRevB.101.195118.

Murakami, Yuta and Philipp Werner (Aug. 2018). "Nonequilibrium steady states of electric field driven Mott insulators". In: *Phys. Rev. B* 98 (7), p. 075102. DOI: 10.1103/PhysRevB.98.075102.

Murray, É. D. et al. (Aug. 2005). "Effect of lattice anharmonicity on high-amplitude phonon dynamics in photoexcited bismuth". In: *Phys. Rev. B* 72 (6), p. 060301. DOI: 10.1103/PhysRevB.72.060301. URL: https://link.aps.org/doi/10.1103/PhysRevB.72.060301.

Mutch, Joshua et al. (2019). "Evidence for a strain-tuned topological phase transition in ZrTe5". In: *Science Advances* 5.8. DOI: 10.1126/sciadv.aav9771. eprint: https://advances.sciencemag.org/content/5/8/eaav9771.full.pdf. URL: https://advances.sciencemag.org/content/5/8/eaav9771.

Nakamura, Fumihiko, Tatsuo Goko, et al. (May 2002). "From Mott insulator to ferromagnetic metal: A pressure study of Ca_2RuO_4". In: *Phys. Rev. B* 65 (22), p. 220402. DOI: 10.1103/PhysRevB.65.220402.

Nakamura, Fumihiko, Mariko Sakaki, et al. (2013). "Electric-field-induced metal maintained by current of the Mott insulator Ca_2RuO_4". In: *Sci. Rep.* 3.1, p. 2536. ISSN: 2045-2322.

Nakano, Akitoshi et al. (July 2018). "Antiferroelectric distortion with anomalous phonon softening in the excitonic insulator Ta_2NiSe_5". In: *Phys. Rev. B* 98 (4), p. 045139. DOI: 10.1103/PhysRevB.98.045139. URL: https://link.aps.org/doi/10.1103/PhysRevB.98.045139.

Nakayama, K. et al. (Mar. 2017). "Band splitting and Weyl nodes in trigonal tellurium studied by angle-resolved photoemission spectroscopy and density functional theory". In: *Phys. Rev. B* 95 (12), p. 125204. DOI: 10.1103/PhysRevB.95.125204. URL: https://link.aps.org/doi/10.1103/PhysRevB.95.125204.

Němec, P. et al. (2018). "Antiferromagnetic opto-spintronics". In: *Nature Physics* 14.3, pp. 229–241. DOI: 10.1038/s41567-018-0051-x. URL: https://doi.org/10.1038/s41567-018-0051-x.

Nilsen, Gøran J. et al. (Mar. 2021). "Magnetic order and multipoles in the $5d^2$ rhenium double perovskite Ba_2YReO_6". In: *Phys. Rev. B* 103 (10), p. 104430. DOI: 10.1103/PhysRevB.103.104430. URL: https://link.aps.org/doi/10.1103/PhysRevB.103.104430.

Ning, H. et al. (Dec. 2020). "Signatures of Ultrafast Reversal of Excitonic Order in Ta_2NiSe_5". In: *Phys. Rev. Lett.* 125 (26), p. 267602. DOI: 10.1103/PhysRevLett.125.267602. URL: https://link.aps.org/doi/10.1103/PhysRevLett.125.267602.

Nova, T. F., A. Cartella, et al. (Oct. 2016). "An effective magnetic field from optically driven phonons". In: *Nature Physics* 13, 132 EP -. URL: https://doi.org/10.1038/nphys3925.

Nova, T. F., A. S. Disa, et al. (2019). "Metastable ferroelectricity in optically strained SrTiO3". In: *Science* 364.6445, pp. 1075–1079. ISSN: 0036-8075. DOI: 10.1126/science.aaw4911. eprint: https://science.sciencemag.org/content/364/6445/1075.full.pdf. URL: https://science.sciencemag.org/content/364/6445/1075.

Novelli, Fabio et al. (2014). "Witnessing the formation and relaxation of dressed quasi-particles in a strongly correlated electron system". In: *Nat. Commun.* 5.1, p. 5112. ISSN: 2041-1723.

Oka, Takashi (Aug. 2012). "Nonlinear doublon production in a Mott insulator: Landau-Dykhne method applied to an integrable model". In: *Phys. Rev. B* 86 (7), p. 075148. DOI: 10.1103/PhysRevB.86.075148.

Oka, Takashi and Hideo Aoki (Sept. 2005). "Ground-State Decay Rate for the Zener Breakdown in Band and Mott Insulators". In: *Phys. Rev. Lett.* 95 (13), p. 137601. DOI: 10.1103/PhysRevLett.95.137601.

Oka, Takashi and Sota Kitamura (2019). "Floquet Engineering of Quantum Materials". In: *Annual Review of Condensed Matter Physics* 10.1, pp. 387–408. DOI: 10.1146/annurev-conmatphys-031218-013423. eprint: https:

//doi.org/10.1146/annurev-conmatphys-031218-013423. URL: https://doi.org/10.1146/annurev-conmatphys-031218-013423.

Okamoto, H. et al. (Jan. 2007). "Photoinduced Metallic State Mediated by Spin-Charge Separation in a One-Dimensional Organic Mott Insulator". In: *Phys. Rev. Lett.* 98 (3), p. 037401. DOI: 10.1103/PhysRevLett.98.037401.

Okazaki, Kozo et al. (2018). "Photo-induced semimetallic states realised in electron–hole coupled insulators". In: *Nature Communications* 9.1, p. 4322. DOI: 10.1038/s41467-018-06801-1. URL: https://doi.org/10.1038/s41467-018-06801-1.

Orenstein, Joseph (2012). "Ultrafast spectroscopy of quantum materials". In: *Physics Today* 65.9, pp. 44–50. DOI: 10.1063/PT.3.1717. eprint: https://doi.org/10.1063/PT.3.1717. URL: https://doi.org/10.1063/PT.3.1717.

Perez-Salinas, Daniel et al. (2022). "Multi-mode excitation drives disorder during the ultrafast melting of a C4-symmetry-broken phase". In: *Nature Communications* 13.1, p. 238. DOI: 10.1038/s41467-021-27819-y. URL: https://doi.org/10.1038/s41467-021-27819-y.

Petersen, J. C. et al. (Oct. 2011). "Clocking the Melting Transition of Charge and Lattice Order in $1T-TaS_2$ with Ultrafast Extreme-Ultraviolet Angle-Resolved Photoemission Spectroscopy". In: *Phys. Rev. Lett.* 107 (17), p. 177402. DOI: 10.1103/PhysRevLett.107.177402. URL: https://link.aps.org/doi/10.1103/PhysRevLett.107.177402.

Pfeifer, T. et al. (1992). "Generation mechanism for coherent LO phonons in surface-space-charge fields of III-V-compounds". In: *Applied Physics A* 55.5, pp. 482–488. DOI: 10.1007/BF00348337. URL: https://doi.org/10.1007/BF00348337.

Porter, D. G. et al. (Sept. 2018). "Magnetic anisotropy and orbital ordering in Ca_2RuO_4". In: *Phys. Rev. B* 98 (12), p. 125142. DOI: 10.1103/PhysRevB.98.125142. URL: https://link.aps.org/doi/10.1103/PhysRevB.98.125142.

Puphal, Pascal et al. (Jan. 2020). "Topological Magnetic Phase in the Candidate Weyl Semimetal CeAlGe". In: *Phys. Rev. Lett.* 124 (1), p. 017202. DOI: 10.1103/PhysRevLett.124.017202. URL: https://link.aps.org/doi/10.1103/PhysRevLett.124.017202.

Qi, Tingting et al. (June 2009). "Collective Coherent Control: Synchronization of Polarization in Ferroelectric $PbTiO_3$ by Shaped THz Fields". In: *Phys. Rev. Lett.* 102 (24), p. 247603. DOI: 10.1103/PhysRevLett.102.247603. URL: https://link.aps.org/doi/10.1103/PhysRevLett.102.247603.

Radu, I. et al. (2011). "Transient ferromagnetic-like state mediating ultrafast reversal of antiferromagnetically coupled spins". In: *Nature* 472.7342, pp. 205–208. DOI: 10.1038/nature09901. URL: https://doi.org/10.1038/nature09901.

Rau, Jeffrey G., Eric Kin-Ho Lee, and Hae-Young Kee (2016). "Spin-Orbit Physics Giving Rise to Novel Phases in Correlated Systems: Iridates and Related Materials". In: *Annual Review of Condensed Matter Physics* 7.1, pp. 195–221. DOI: 10.1146/annurev-conmatphys-031115-011319. eprint: https://doi.org/10.1146/annurev-conmatphys-031115-011319. URL: https://doi.org/10.1146/annurev-conmatphys-031115-011319.

Rebec, S. N. et al. (Feb. 2017). "Coexistence of Replica Bands and Superconductivity in FeSe Monolayer Films". In: *Phys. Rev. Lett.* 118 (6), p. 067002. DOI: 10.1103/PhysRevLett.118.067002. URL: https://link.aps.org/doi/10.1103/PhysRevLett.118.067002.

Rho, H. et al. (June 2005). "Lattice dynamics and the electron-phonon interaction in Ca_2RuO_4". In: *Phys. Rev. B* 71 (24), p. 245121. DOI: 10.1103/PhysRevB.71.245121. URL: https://link.aps.org/doi/10.1103/PhysRevB.71.245121.

Rini, Matteo et al. (2007). "Control of the electronic phase of a manganite by mode-selective vibrational excitation". In: *Nature* 449.7158, pp. 72–74. DOI: 10.1038/nature06119. URL: https://doi.org/10.1038/nature06119.

Rodriguez, Diego et al. (Mar. 2020). "Two Linear Regimes in Optical Conductivity of a Type-I Weyl Semimetal: The Case of Elemental Tellurium". In: *Phys. Rev. Lett.* 124 (13), p. 136402. DOI: 10.1103/PhysRevLett.124.136402. URL: https://link.aps.org/doi/10.1103/PhysRevLett.124.136402.

Ron, A. et al. (Nov. 2020). "Ultrafast Enhancement of Ferromagnetic Spin Exchange Induced by Ligand-to-Metal Charge Transfer". In: *Phys. Rev. Lett.* 125 (19), p. 197203. DOI: 10.1103/PhysRevLett.125.197203. URL: https://link.aps.org/doi/10.1103/PhysRevLett.125.197203.

Rosencher, Emmanuel and Borge Vinter (2002). *Optoelectronics*. Ed. by P. G.Translator Piva. Cambridge University Press. DOI: 10.1017/CBO9780511754647.

Rudner, Mark S. and Netanel H. Lindner (2020a). "Band structure engineering and non-equilibrium dynamics in Floquet topological insulators". In: *Nature Reviews Physics* 2.5, pp. 229–244. DOI: 10.1038/s42254-020-0170-z. URL: https://doi.org/10.1038/s42254-020-0170-z.

– (2020b). *The Floquet Engineer's Handbook*. arXiv: 2003.08252 [cond-mat.mes-hall].

Runge, Erich and E. K. U. Gross (Mar. 1984). "Density-Functional Theory for Time-Dependent Systems". In: *Physical Review Letters* 52.12, p. 997. DOI: 10.1103/PhysRevLett.52.997. URL: https://doi.org/10.1103%2Fphysrevlett.52.997.

Sakai, Akito et al. (2018). "Giant anomalous Nernst effect and quantum-critical scaling in a ferromagnetic semimetal". In: *Nature Physics* 14.11, pp. 1119–1124. DOI: 10.1038/s41567-018-0225-6. URL: https://doi.org/10.1038/s41567-018-0225-6.

Sakano, M. et al. (Mar. 2020). "Radial Spin Texture in Elemental Tellurium with Chiral Crystal Structure". In: *Phys. Rev. Lett.* 124 (13), p. 136404. DOI: 10.1103/PhysRevLett.124.136404. URL: https://link.aps.org/doi/10.1103/PhysRevLett.124.136404.

Santini, Paolo et al. (June 2009). "Multipolar interactions in f-electron systems: The paradigm of actinide dioxides". In: *Rev. Mod. Phys.* 81 (2), pp. 807–863. DOI: 10.1103/RevModPhys.81.807. URL: https://link.aps.org/doi/10.1103/RevModPhys.81.807.

Schlauderer, S. et al. (2019). "Temporal and spectral fingerprints of ultrafast all-coherent spin switching". In: *Nature* 569.7756, pp. 383–387. DOI: 10.1038/s41586-019-1174-7. URL: https://doi.org/10.1038/s41586-019-1174-7.

Schmitt, F. et al. (2008). "Transient Electronic Structure and Melting of a Charge Density Wave in TbTe3". In: *Science* 321.5896, pp. 1649–1652. ISSN: 0036-8075. DOI: 10.1126/science.1160778. eprint: https://science.sciencemag.org/content/321/5896/1649.full.pdf. URL: https://science.sciencemag.org/content/321/5896/1649.

Schwinger, Julian (June 1951). "On Gauge Invariance and Vacuum Polarization". In: *Phys. Rev.* 82 (5), pp. 664–679. DOI: 10.1103/PhysRev.82.664.

Seki, K. et al. (Oct. 2014). "Excitonic Bose-Einstein condensation in Ta_2NiSe_5 above room temperature". In: *Phys. Rev. B* 90 (15), p. 155116. DOI: 10.1103/PhysRevB.90.155116. URL: https://link.aps.org/doi/10.1103/PhysRevB.90.155116.

Shalygin, V. A. et al. (Jan. 2016). "Circular photon drag effect in bulk tellurium". In: *Phys. Rev. B* 93 (4), p. 045207. DOI: 10.1103/PhysRevB.93.045207. URL: https://link.aps.org/doi/10.1103/PhysRevB.93.045207.

Shan, Jun-Yi et al. (2021). "Giant modulation of optical nonlinearity by Floquet engineering". In: *Nature* 600.7888, pp. 235–239. DOI: 10.1038/s41586-021-04051-8. URL: https://doi.org/10.1038/s41586-021-04051-8.

Shen, Y. R. (2003). *The principles of nonlinear optics*. Wiley-Interscience.

Sie, Edbert J., Chun Hung Lui, et al. (2017). "Large, valley-exclusive Bloch-Siegert shift in monolayer WS₂". In: *Science* 355.6329, pp. 1066–1069. DOI: 10.1126/science.aal2241. eprint: https://www.science.org/doi/pdf/10.1126/science.aal2241. URL: https://www.science.org/doi/abs/10.1126/science.aal2241.

Sie, Edbert J., James W. McIver, et al. (2015). "Valley-selective optical Stark effect in monolayer WS2". In: *Nature Materials* 14.3, pp. 290–294. DOI: 10.1038/nmat4156. URL: https://doi.org/10.1038/nmat4156.

Sie, Edbert J., Clara M. Nyby, et al. (2019). "An ultrafast symmetry switch in a Weyl semimetal". In: *Nature* 565.7737, pp. 61–66. DOI: 10.1038/s41586-018-0809-4. URL: https://doi.org/10.1038/s41586-018-0809-4.

Silva, R. E. F. et al. (2018). "High-harmonic spectroscopy of ultrafast many-body dynamics in strongly correlated systems". In: *Nat. Photonics* 12.5, pp. 266–270. ISSN: 1749-4893.

Singer, Andrej et al. (May 2018). "Nonequilibrium Phase Precursors during a Photoexcited Insulator-to-Metal Transition in V_2O_3". In: *Phys. Rev. Lett.* 120 (20), p. 207601. DOI: 10.1103/PhysRevLett.120.207601. URL: https://link.aps.org/doi/10.1103/PhysRevLett.120.207601.

Sobota, Jonathan A., Yu He, and Zhi-Xun Shen (May 2021). "Angle-resolved photoemission studies of quantum materials". In: *Rev. Mod. Phys.* 93 (2), p. 025006. DOI: 10.1103/RevModPhys.93.025006. URL: https://link.aps.org/doi/10.1103/RevModPhys.93.025006.

Sokolowski-Tinten, Klaus et al. (2003). "Femtosecond X-ray measurement of coherent lattice vibrations near the Lindemann stability limit". In: *Nature* 422.6929, pp. 287–289. DOI: 10.1038/nature01490. URL: https://doi.org/10.1038/nature01490.

Srivastava, Ajit et al. (Oct. 2004). "Laser-Induced Above-Band-Gap Transparency in GaAs". In: *Phys. Rev. Lett.* 93 (15), p. 157401. DOI: 10.1103/PhysRevLett.93.157401.

Stafford, C. A. and A. J. Millis (July 1993). "Scaling theory of the Mott-Hubbard metal-insulator transition in one dimension". In: *Phys. Rev. B* 48 (3), pp. 1409–1425. DOI: 10.1103/PhysRevB.48.1409.

Stamokostas, Georgios L. and Gregory A. Fiete (Feb. 2018). "Mixing of $t_{2g} - e_g$ orbitals in 4*d* and 5*d* transition metal oxides". In: *Phys. Rev. B* 97 (8), p. 085150. DOI: 10.1103/PhysRevB.97.085150. URL: https://link.aps.org/doi/10.1103/PhysRevB.97.085150.

Stanciu, C. D. et al. (July 2007). "All-Optical Magnetic Recording with Circularly Polarized Light". In: *Phys. Rev. Lett.* 99 (4), p. 047601. DOI: 10.1103/PhysRevLett.99.047601. URL: https://link.aps.org/doi/10.1103/PhysRevLett.99.047601.

Stevens, T. E., J. Kuhl, and R. Merlin (Mar. 2002). "Coherent phonon generation and the two stimulated Raman tensors". In: *Phys. Rev. B* 65 (14), p. 144304. DOI: 10.1103/PhysRevB.65.144304. URL: https://link.aps.org/doi/10.1103/PhysRevB.65.144304.

Stojchevska, L. et al. (2014). "Ultrafast Switching to a Stable Hidden Quantum State in an Electronic Crystal". In: *Science* 344.6180, pp. 177–180. ISSN: 0036-8075. DOI: 10.1126/science.1241591. eprint: https://science.sciencemag.org/content/344/6180/177.full.pdf. URL: https://science.sciencemag.org/content/344/6180/177.

Streltsov, Sergey V. and Daniel I. Khomskii (Aug. 2020). "Jahn-Teller Effect and Spin-Orbit Coupling: Friends or Foes?" In: *Phys. Rev. X* 10 (3), p. 031043. DOI: 10.1103/PhysRevX.10.031043. URL: https://link.aps.org/doi/10.1103/PhysRevX.10.031043.

Sun, Zhiyuan, Tatsuya Kaneko, et al. (Sept. 2021). "Second-Order Josephson Effect in Excitonic Insulators". In: *Phys. Rev. Lett.* 127 (12), p. 127702. DOI: 10.1103/PhysRevLett.127.127702. URL: https://link.aps.org/doi/10.1103/PhysRevLett.127.127702.

Sun, Zhiyuan and Andrew J. Millis (May 2020). "Transient Trapping into Metastable States in Systems with Competing Orders". In: *Phys. Rev. X* 10 (2), p. 021028. DOI: 10.1103/PhysRevX.10.021028. URL: https://link.aps.org/doi/10.1103/PhysRevX.10.021028.

Suzuki, T. et al. (2019). "Singular angular magnetoresistance in a magnetic nodal semimetal". In: *Science* 365.6451, pp. 377–381. DOI: 10.1126/science.aat0348. eprint: https://www.science.org/doi/pdf/10.1126/science.aat0348. URL: https://www.science.org/doi/abs/10.1126/science.aat0348.

Suzuki, Takeshi et al. (Mar. 2021). "Detecting electron-phonon coupling during photoinduced phase transition". In: *Phys. Rev. B* 103 (12), p. L121105. DOI: 10.1103/PhysRevB.103.L121105. URL: https://link.aps.org/doi/10.1103/PhysRevB.103.L121105.

Takahashi, Akira, Hisashi Itoh, and Masaki Aihara (May 2008). "Photoinduced insulator-metal transition in one-dimensional Mott insulators". In: *Phys. Rev. B* 77 (20), p. 205105. DOI: 10.1103/PhysRevB.77.205105.

Takayama, Tomohiro, Jiri Chaloupka, et al. (2021). *Spin-orbit-entangled electronic phases in 4d and 5d transition-metal compounds*. arXiv: 2102.02740 [cond-mat.str-el].

Takayama, Tomohiro, Jiří Chaloupka, et al. (2021). "Spin–Orbit-Entangled Electronic Phases in 4d and 5d Transition-Metal Compounds". In: *Journal of the Physical Society of Japan* 90.6, p. 062001. DOI: 10.7566/JPSJ.90.062001. eprint: https://doi.org/10.7566/JPSJ.90.062001. URL: https://doi.org/10.7566/JPSJ.90.062001.

Tanabe, Tetsuhiro, Koudai Sugimoto, and Yukinori Ohta (Dec. 2018). "Nonequilibrium dynamics in the pump-probe spectroscopy of excitonic insulators". In: *Phys. Rev. B* 98 (23), p. 235127. DOI: 10.1103/PhysRevB.98.235127. URL: https://link.aps.org/doi/10.1103/PhysRevB.98.235127.

Tanaka, Yasuhiro, Manabu Daira, and Kenji Yonemitsu (Mar. 2018). "Photoinduced enhancement of excitonic order in the two-orbital Hubbard model". In: *Phys. Rev. B* 97 (11), p. 115105. DOI: 10.1103/PhysRevB.97.115105. URL: https://link.aps.org/doi/10.1103/PhysRevB.97.115105.

Tancogne-Dejean, Nicolas, Michael A. Sentef, and Angel Rubio (Aug. 2018). "Ultrafast Modification of Hubbard U in a Strongly Correlated Material: Ab initio High-Harmonic Generation in NiO". In: *Phys. Rev. Lett.* 121 (9), p. 097402. DOI: 10.1103/PhysRevLett.121.097402.

– (Sept. 2020). "Ultrafast transient absorption spectroscopy of the charge-transfer insulator NiO: Beyond the dynamical Franz-Keldysh effect". In: *Phys. Rev. B* 102 (11), p. 115106. DOI: 10.1103/PhysRevB.102.115106.

Tang, Tangwei et al. (2020). *Non-Coulomb strong electron-hole binding in Ta_2NiSe_5 revealed by time- and angle-resolved photoemission spectroscopy*. arXiv: 2003.00514 [cond-mat.str-el].

Tang, Tianwei et al. (June 2020). "Non-Coulomb strong electron-hole binding in Ta_2NiSe_5 revealed by time- and angle-resolved photoemission spectroscopy". In: *Phys. Rev. B* 101 (23), p. 235148. DOI: 10.1103/PhysRevB.101.235148. URL: https://link.aps.org/doi/10.1103/PhysRevB.101.235148.

Tangney, P. and S. Fahy (May 1999). "Calculations of the A_1 Phonon Frequency in Photoexcited Tellurium". In: *Phys. Rev. Lett.* 82 (21), pp. 4340–4343. DOI: 10.1103/PhysRevLett.82.4340. URL: https://link.aps.org/doi/10.1103/PhysRevLett.82.4340.

– (Jan. 2002). "Density-functional theory approach to ultrafast laser excitation of semiconductors: Application to the A_1 phonon in tellurium". In: *Phys. Rev. B* 65 (5), p. 054302. DOI: 10.1103/PhysRevB.65.054302. URL: https://link.aps.org/doi/10.1103/PhysRevB.65.054302.

Teitelbaum, Samuel W. et al. (Sept. 2018). "Real-Time Observation of a Coherent Lattice Transformation into a High-Symmetry Phase". In: *Phys. Rev. X* 8 (3), p. 031081. DOI: 10.1103/PhysRevX.8.031081. URL: https://link.aps.org/doi/10.1103/PhysRevX.8.031081.

Tobey, R. I. et al. (Nov. 2008). "Ultrafast Electronic Phase Transition in $La_{1/2}Sr_{3/2}MnO_4$ by Coherent Vibrational Excitation: Evidence for Nonthermal Melting of Orbital Order". In: *Phys. Rev. Lett.* 101 (19), p. 197404. DOI: 10.1103/PhysRevLett.101.197404. URL: https://link.aps.org/doi/10.1103/PhysRevLett.101.197404.

Tokura, Y. and N. Nagaosa (2000). "Orbital Physics in Transition-Metal Oxides". In: *Science* 288.5465, pp. 462–468. ISSN: 0036-8075. DOI: 10.1126/science.288.5465.462. eprint: https://science.sciencemag.org/content/288/5465/462.full.pdf. URL: https://science.sciencemag.org/content/288/5465/462.

Topp, Gabriel E. et al. (2018). "All-optical nonequilibrium pathway to stabilising magnetic Weyl semimetals in pyrochlore iridates". In: *Nature Communications* 9 (1). DOI: 10.1038/s41467-018-06991-8. URL: https://doi.org/10.1038/s41467-018-06991-8.

Torchinsky, D. H. et al. (Mar. 2015). "Structural Distortion-Induced Magnetoelastic Locking in Sr_2IrO_4 Revealed through Nonlinear Optical Harmonic Generation". In: *Phys. Rev. Lett.* 114 (9), p. 096404. DOI: 10.1103/PhysRevLett.114.096404. URL: https://link.aps.org/doi/10.1103/PhysRevLett.114.096404.

Torchinsky, Darius H., Hao Chu, et al. (2014). "A low temperature nonlinear optical rotational anisotropy spectrometer for the determination of crystallographic and electronic symmetries". In: *Review of Scientific Instruments* 85.8, p. 083102. DOI: 10.1063/1.4891417. eprint: https://doi.org/10.1063/1.4891417. URL: https://doi.org/10.1063/1.4891417.

Torchinsky, Darius H. and David Hsieh (2017). "Rotational Anisotropy Nonlinear Harmonic Generation". In: *Magnetic Characterization Techniques for Nanomaterials*. Ed. by Challa S.S.R. Kumar. Berlin, Heidelberg: Springer Berlin Heidelberg, pp. 1–49. ISBN: 978-3-662-52780-1. DOI: 10.1007/978-3-662-52780-1_1. URL: https://doi.org/10.1007/978-3-662-52780-1_1.

Torchinsky, Darius H., Fahad Mahmood, et al. (Feb. 2013). "Fluctuating charge-density waves in a cuprate superconductor". In: *Nature Materials* 12, 387 EP -. URL: https://doi.org/10.1038/nmat3571.

Torre, A. de la et al. (2021). "Mirror symmetry breaking in a model insulating cuprate". In: *Nature Physics* 17.7, pp. 777–781. DOI: 10.1038/s41567-021-01210-6. URL: https://doi.org/10.1038/s41567-021-01210-6.

Torre, Alberto de la, Dante M. Kennes, et al. (Oct. 2021). "Colloquium: Nonthermal pathways to ultrafast control in quantum materials". In: *Rev. Mod. Phys.* 93 (4), p. 041002. DOI: 10.1103/RevModPhys.93.041002. URL: https://link.aps.org/doi/10.1103/RevModPhys.93.041002.

Torre, Alberto de la, Kyle L. Seyler, et al. (2022). "Decoupling of static and dynamic criticality in a driven Mott insulator". In: *Communications Physics* 5.1, p. 35. DOI: 10.1038/s42005-022-00813-6. URL: https://doi.org/10.1038/s42005-022-00813-6.

Trigo, M. et al. (Feb. 2021). "Ultrafast formation of domain walls of a charge density wave in $SmTe_3$". In: *Phys. Rev. B* 103 (5), p. 054109. DOI: 10.1103/PhysRevB.103.054109. URL: https://link.aps.org/doi/10.1103/PhysRevB.103.054109.

Tsirkin, Stepan S., Pablo Aguado Puente, and Ivo Souza (Jan. 2018). "Gyrotropic effects in trigonal tellurium studied from first principles". In: *Phys. Rev. B* 97 (3), p. 035158. DOI: 10.1103/PhysRevB.97.035158. URL: https://link.aps.org/doi/10.1103/PhysRevB.97.035158.

Tsuji, Naoto et al. (June 2011). "Dynamical Band Flipping in Fermionic Lattice Systems: An ac-Field-Driven Change of the Interaction from Repulsive to Attractive". In: *Phys. Rev. Lett.* 106 (23), p. 236401. DOI: 10.1103/PhysRevLett.106.236401.

Tudosa, I. et al. (2004). "The ultimate speed of magnetic switching in granular recording media". In: *Nature* 428.6985, pp. 831–833. DOI: 10.1038/nature02438. URL: https://doi.org/10.1038/nature02438.

Tutihasi, Simpei et al. (Jan. 1969). "Optical Properties of Tellurium in the Fundamental Absorption Region". In: *Phys. Rev.* 177 (3), pp. 1143–1150. DOI: 10.1103/PhysRev.177.1143. URL: https://link.aps.org/doi/10.1103/PhysRev.177.1143.

Vahaplar, K. et al. (Sept. 2009). "Ultrafast Path for Optical Magnetization Reversal via a Strongly Nonequilibrium State". In: *Phys. Rev. Lett.* 103 (11), p. 117201. DOI: 10.1103/PhysRevLett.103.117201. URL: https://link.aps.org/doi/10.1103/PhysRevLett.103.117201.

Van Aken, Bas B. et al. (2007). "Observation of ferrotoroidic domains". In: *Nature* 449.7163, pp. 702–705. DOI: 10.1038/nature06139. URL: https://doi.org/10.1038/nature06139.

Vaswani, C. et al. (Apr. 2020). "Light-Driven Raman Coherence as a Nonthermal Route to Ultrafast Topology Switching in a Dirac Semimetal". In: *Phys. Rev. X* 10 (2), p. 021013. DOI: 10.1103/PhysRevX.10.021013. URL: https://link.aps.org/doi/10.1103/PhysRevX.10.021013.

Volkov, P. A. et al. (2021). "Critical charge fluctuations and emergent coherence in a strongly correlated excitonic insulator". In: *npj Quantum Materials* 6.1, p. 52. DOI: 10.1038/s41535-021-00351-4. URL: https://doi.org/10.1038/s41535-021-00351-4.

Wakisaka, Y. et al. (July 2009). "Excitonic Insulator State in Ta_2NiSe_5 Probed by Photoemission Spectroscopy". In: *Phys. Rev. Lett.* 103 (2), p. 026402. DOI: 10.1103/PhysRevLett.103.026402. URL: https://link.aps.org/doi/10.1103/PhysRevLett.103.026402.

Wall, S., D. Brida, et al. (2011). "Quantum interference between charge excitation paths in a solid-state Mott insulator". In: *Nat. Phys.* 7.2, pp. 114–118. ISSN: 1745-2481.

Wall, S., D. Wegkamp, et al. (2012). "Ultrafast changes in lattice symmetry probed by coherent phonons". In: *Nature Communications* 3.1, p. 721. DOI: 10.1038/ncomms1719. URL: https://doi.org/10.1038/ncomms1719.

Wall, Simone et al. (Nov. 2012). "Atomistic Picture of Charge Density Wave Formation at Surfaces". In: *Phys. Rev. Lett.* 109 (18), p. 186101. DOI: 10.1103/PhysRevLett.109.186101. URL: https://link.aps.org/doi/10.1103/PhysRevLett.109.186101.

Wang, Y. H. et al. (2013). "Observation of Floquet-Bloch States on the Surface of a Topological Insulator". In: *Science* 342.6157, pp. 453–457. ISSN: 0036-8075. DOI: 10.1126/science.1239834. eprint: https://science.sciencemag.org/content/342/6157/453.full.pdf. URL: https://science.sciencemag.org/content/342/6157/453.

Wang, Yao, Thomas P. Devereaux, and Cheng-Chien Chen (Dec. 2018). "Theory of time-resolved Raman scattering in correlated systems: Ultrafast engineering of spin dynamics and detection of thermalization". In: *Phys. Rev. B* 98 (24), p. 245106. DOI: 10.1103/PhysRevB.98.245106.

Wang, Ying et al. (2017). "Structural phase transition in monolayer MoTe2 driven by electrostatic doping". In: *Nature* 550.7677, pp. 487–491. DOI: 10.1038/nature24043. URL: https://doi.org/10.1038/nature24043.

Wang, Z. et al. (2016). "Tailoring the nature and strength of electron–phonon interactions in the SrTiO3(001) 2D electron liquid". In: *Nature Materials* 15.8, pp. 835–839. DOI: 10.1038/nmat4623. URL: https://doi.org/10.1038/nmat4623.

Weiner, A. M. et al. (1990). "Femtosecond Pulse Sequences Used for Optical Manipulation of Molecular Motion". In: *Science* 247.4948, pp. 1317–1319. ISSN: 0036-8075. DOI: 10.1126/science.247.4948.1317. eprint: https://science.sciencemag.org/content/247/4948/1317.full.pdf. URL: https://science.sciencemag.org/content/247/4948/1317.

Weiner, Andrew Marc (2009). *Ultrafast Optics*. Wiley-Blackwell.

Werdehausen, Daniel, Tomohiro Takayama, Gelon Albrecht, et al. (July 2018). "Photo-excited dynamics in the excitonic insulator Tasub2/subNiSesub5/sub". In: *Journal of Physics: Condensed Matter* 30.30, p. 305602. DOI: 10.1088/1361-648x/aacd76. URL: https://doi.org/10.1088/1361-648x/aacd76.

Werdehausen, Daniel, Tomohiro Takayama, Marc Höppner, et al. (2018). "Coherent order parameter oscillations in the ground state of the excitonic insulator Ta2NiSe5". In: *Science Advances* 4.3. DOI: 10.1126/sciadv.aap8652. eprint: https://advances.sciencemag.org/content/4/3/eaap8652.full.pdf. URL: https://advances.sciencemag.org/content/4/3/eaap8652.

Witczak-Krempa, William et al. (2021/12/14 2014). "Correlated Quantum Phenomena in the Strong Spin-Orbit Regime". In: *Annual Review of Condensed Matter Physics* 5.1, pp. 57–82. DOI: 10.1146/annurev-conmatphys-020911-125138. URL: https://doi.org/10.1146/annurev-conmatphys-020911-125138.

Wu, Alexander Q. and Xianfan Xu (June 2007). "Coupling of ultrafast laser energy to coherent phonons in bismuth". In: *Applied Physics Letters* 90.25, p. 251111. ISSN: 0003-6951. DOI: 10.1063/1.2750401. URL: https://doi.org/10.1063/1.2750401.

Xiao, Jun et al. (2020). "Berry curvature memory through electrically driven stacking transitions". In: *Nature Physics* 16.10, pp. 1028–1034. DOI: 10.1038/s41567-020-0947-0. URL: https://doi.org/10.1038/s41567-020-0947-0.

Xu, B. et al. (Oct. 2018). "Temperature-Driven Topological Phase Transition and Intermediate Dirac Semimetal Phase in $ZrTe_5$". In: *Phys. Rev. Lett.* 121 (18), p. 187401. DOI: 10.1103/PhysRevLett.121.187401. URL: https://link.aps.org/doi/10.1103/PhysRevLett.121.187401.

Xue, Xiong-Xiong et al. (Feb. 2018). "Strain tuning of electronic properties of various dimension elemental tellurium with broken screw symmetry". In: *Journal of Physics: Condensed Matter* 30.12, p. 125001. ISSN: 0953-8984. DOI: 10.1088/1361-648x/aaaea1. URL: https://doi.org/10.1088/1361-648x/aaaea1.

Yamakawa, H. et al. (2017). "Mott transition by an impulsive dielectric breakdown". In: *Nat. Mater.* 16.11, pp. 1100–1105. ISSN: 1476-4660.

Yan, Binghai and Claudia Felser (2021/10/02 2017). "Topological Materials: Weyl Semimetals". In: *Annual Review of Condensed Matter Physics* 8.1, pp. 337–354. DOI: 10.1146/annurev-conmatphys-031016-025458. URL: https://doi.org/10.1146/annurev-conmatphys-031016-025458.

Yan, Zhongbo and Zhong Wang (Aug. 2016). "Tunable Weyl Points in Periodically Driven Nodal Line Semimetals". In: *Phys. Rev. Lett.* 117 (8), p. 087402. DOI: 10.1103/PhysRevLett.117.087402. URL: https://link.aps.org/doi/10.1103/PhysRevLett.117.087402.

Yang, Hung-Yu et al. (2020). "Transition from intrinsic to extrinsic anomalous Hall effect in the ferromagnetic Weyl semimetal PrAlGe1xSix". In: *APL Materials* 8.1, p. 011111. DOI: 10.1063/1.5132958. eprint: https://doi.org/10.1063/1.5132958. URL: https://doi.org/10.1063/1.5132958.

Yoshikawa, Naotaka et al. (2021). "Ultrafast switching to an insulating-like metastable state by amplitudon excitation of a charge density wave". In: *Nature Physics* 17.8, pp. 909–914. DOI: 10.1038/s41567-021-01267-3. URL: https://doi.org/10.1038/s41567-021-01267-3.

Yusupov, R. V. et al. (Dec. 2008). "Single-Particle and Collective Mode Couplings Associated with 1- and 2-Directional Electronic Ordering in Metallic $R\mathrm{Te}_3$ (R = Ho, Dy, Tb)". In: *Phys. Rev. Lett.* 101 (24), p. 246402. DOI: 10.1103/PhysRevLett.101.246402. URL: https://link.aps.org/doi/10.1103/PhysRevLett.101.246402.

Yusupov, Roman et al. (2010). "Coherent dynamics of macroscopic electronic order through a symmetry breaking transition". In: *Nature Physics* 6.9, pp. 681–684. DOI: 10.1038/nphys1738. URL: https://doi.org/10.1038/nphys1738.

Zegkinoglou, I. et al. (Sept. 2005). "Orbital Ordering Transition in Ca_2RuO_4 Observed with Resonant X-Ray Diffraction". In: *Phys. Rev. Lett.* 95 (13), p. 136401. DOI: 10.1103/PhysRevLett.95.136401. URL: https://link.aps.org/doi/10.1103/PhysRevLett.95.136401.

Zeiger, H. J. et al. (Jan. 1992). "Theory for displacive excitation of coherent phonons". In: *Phys. Rev. B* 45 (2), pp. 768–778. DOI: 10.1103/PhysRevB.45.768. URL: https://link.aps.org/doi/10.1103/PhysRevB.45.768.

Zenker, B., H. Fehske, and H. Beck (Nov. 2014). "Fate of the excitonic insulator in the presence of phonons". In: *Phys. Rev. B* 90 (19), p. 195118. DOI: 10.1103/PhysRevB.90.195118. URL: https://link.aps.org/doi/10.1103/PhysRevB.90.195118.

Zhang, Jingdi et al. (2016). "Cooperative photoinduced metastable phase control in strained manganite films". In: *Nature Materials* 15.9, pp. 956–960. DOI: 10.1038/nmat4695. URL: https://doi.org/10.1038/nmat4695.

Zhang, M. Y. et al. (May 2019). "Light-Induced Subpicosecond Lattice Symmetry Switch in $MoTe_2$". In: *Phys. Rev. X* 9 (2), p. 021036. DOI: 10.1103/PhysRevX.9.021036. URL: https://link.aps.org/doi/10.1103/PhysRevX.9.021036.

Zhang, Nan et al. (May 2020). "Magnetotransport signatures of Weyl physics and discrete scale invariance in the elemental semiconductor tellurium". In: *Proceedings of the National Academy of Sciences* 117.21, p. 11337. DOI: 10.1073/pnas.2002913117. URL: https://doi.org/10.1073/pnas.2002913117.

Zhao, L. et al. (2017). "A global inversion-symmetry-broken phase inside the pseudogap region of YBa2Cu3Oy". In: *Nature Physics* 13.3, pp. 250–254. DOI: 10.1038/nphys3962. URL: https://doi.org/10.1038/nphys3962.

Zhong, Shudan, Joel E. Moore, and Ivo Souza (Feb. 2016). "Gyrotropic Magnetic Effect and the Magnetic Moment on the Fermi Surface". In: *Phys. Rev. Lett.* 116 (7), p. 077201. DOI: 10.1103/PhysRevLett.116.077201. URL: https://link.aps.org/doi/10.1103/PhysRevLett.116.077201.

Zong, Alfred, Pavel E. Dolgirev, Anshul Kogar, Emre Erge çen, et al. (Aug. 2019). "Dynamical Slowing-Down in an Ultrafast Photoinduced Phase Transition". In: *Phys. Rev. Lett.* 123 (9), p. 097601. DOI: 10.1103/PhysRevLett.123.097601. URL: https://link.aps.org/doi/10.1103/PhysRevLett.123.097601.

Zong, Alfred, Pavel E. Dolgirev, Anshul Kogar, Yifan Su, et al. (Nov. 2021). "Role of Equilibrium Fluctuations in Light-Induced Order". In: *Phys. Rev. Lett.* 127 (22), p. 227401. DOI: 10.1103/PhysRevLett.127.227401. URL: https://link.aps.org/doi/10.1103/PhysRevLett.127.227401.

Zong, Alfred, Anshul Kogar, et al. (2019). "Evidence for topological defects in a photoinduced phase transition". In: *Nature Physics* 15.1, pp. 27–31. DOI: 10.1038/s41567-018-0311-9. URL: https://doi.org/10.1038/s41567-018-0311-9.

Zong, Alfred, Xiaozhe Shen, et al. (2018). "Ultrafast manipulation of mirror domain walls in a charge density wave". In: *Science Advances* 4.10. DOI: 10.1126/sciadv.aau5501. eprint: https://advances.sciencemag.org/content/4/10/eaau5501.full.pdf. URL: https://advances.sciencemag.org/content/4/10/eaau5501.